



# COMPUTATIONAL SUPPORT FOR MORPHOLOGY-DRIVEN ANALYSIS OF NEUROVASCULAR PATHOLOGIES

# Dissertation

zur Erlangung des akademischen Grades

# Doktoringenieur (Dr.-Ing.)

angenommen durch die Fakultät für Informatik der Otto-von-Guericke-Universität Magdeburg

#### von

M.SC. LENA SPITZ geb. am 14.07.1995 in München

## GutachterInnen:

Prof. Dr.-Ing. habil. Sylvia Saalfeld Prof. Dr.-Ing. habil. Bernhard Preim Prof. Dr.-Ing. habil Dorit Merhof

Magdeburg 17.07.2025



Stroke is the second most common cause of death and disability worldwide. Neurovascular pathologies disrupt blood supply to the brain, quickly impairing function due to the brain's lack of energy storage. Despite significant progress in recent years, many of the exact mechanisms of these pathologies and how to treat them to achieve the best outcome are not yet fully understood. Analyzing the morphology of the pathologies, like intracranial aneurysms, can lead to new insights, as morphological features are critical in risk assessment and treatment decisions. This thesis aims to provide computational support for morphology-driven analysis to advance research, improve risk assessment, and inform treatment strategies.

The first part of the thesis addresses the necessary preprocessing steps required for analysis. A segmentation pipeline for extraction and 3D reconstruction of the vasculature from medical imaging scans is introduced, and a co-registration, meaning spatial alignment of different scans to enable combination of information from both scans, is developed.

In the second part, morphology-driven analysis for patient-specific research is presented. The impact of mirror aneurysm morphology on hemodynamics is examined, as well as the deformation of intracranial aneurysms following treatment with a novel implant. The deformation analysis is the first to specifically assess the longitudinal effects of the implant on the aneurysm and of the implant itself.

In the third part, cohort-based research is supported by morphology-driven analysis tools for subgroup selection. The tools utilize case-based reasoning and instance selection to identify subgroups within a large dataset of aneurysm cases and various morphological and other parameters. They offer support for research question generation, cohort-matching, and training. Additionally, concepts for how to support cohort-based research in virtual reality are introduced.

The thesis provides computer support for morphology-driven analysis for neurovascular pathologies, from preprocessing to patient-specific and cohort-based research. The analyses demonstrate great potential for generating new insights for research question generation, risk assessment, and treatment decisions. The future holds much promise for addressing the analyses limitations, like lack of data, in combination with advancements in medical imaging, image processing, and novel treatments. Schlaganfälle sind die zweithäufigste Todesursache weltweit und eine häufige Ursache für kognitive Beeinträchtigungen. Neurovaskuläre Erkrankungen stören die Durchblutung des Gehirns und damit dessen Funktion, da das Gehirn keinen Energiespeicher besitzt. Viele der Mechanismen dieser Erkrankungen und deren optimalen Behandlungsmethoden noch nicht vollständig erforscht. Eine Analyse der Morphologie von Erkrankungen wie intrakraniellen Aneurysmen kann neue Einblicke liefern, da morphologische Eigenschaften eine entscheidende Rolle bei der Risikoeinschätzung und Therapieentscheidung spielen. Diese Dissertation stellt Computerunterstützung für morphologiegetriebene Analysen zur Verfügung, um die Forschung voranzutreiben, die Risikoeinschätzung zu verbessern, und Therapieentscheidungen zu optimieren.

Der erste Teil der Arbeit befasst sich mit der notwendigen Vorverarbeitung. Eine Segmentierungspipeline wird vorgestellt, die es ermöglicht, Gefäße aus bildgebenden Scans zu extrahieren und in 3D zu rekonstruieren. Außerdem wird ein Registrierungsverfahren entwickelt, das Informationen aus verschiedenen Bildgebungsscans kombiniert.

Im zweiten Teil geht es um morphologiegetriebene Analyse für patientenspezifische Forschung. Der Einfluss der Morphologie auf die Hämodynamik in Spiegelaneurysmen wird untersucht, sowie die Veränderung von intrakraniellen Aneurysmen nach der Behandlung mit einem neuartigen Implantat. Die Deformationsanalyse ist die erste, die Veränderung und den Einfluss des Implantats auf das Aneurysma über Zeit untersuchen.

Im dritten Teil wird die kohortenbasierte Forschung durch die Entwicklung von Werkzeugen zur Auswahl von Untergruppen aus einem Datensatz mit vielen Aneurysmen und morphologischen Parametern unterstützt. Diese Werkzeuge können bei der Formulierung von Forschungsfragen, beim Kohortenmatching und bei der Ausbildung helfen. Darüber hinaus werden Konzepte für die Unterstützung von kohortenbasierter Forschung durch virtuelle Realität vorgestellt.

Die vorliegende Dissertation bietet computergestützte Lösungen für die morphologiegetriebene Analyse neurovaskulärer Erkrankungen sowohl für die Vorverarbeitung als auch für die patientenspezifische und kohortenbasierte Forschung. Die Analysen zeigen großes Potenzial, neue Erkenntnisse zu generieren, die zur Entwicklung neuer Forschungsfragen, zur Verbesserung der Risikoabschätzung und zur Optimierung von Therapieentscheidungen beitragen können. Die Zukunftsaussichten sind vielversprechend, insbesondere angesichts der derzeitigen Einschränkungen, wie z.B. der geringen Datenmenge, vor allem in Kombination mit Fortschritten in der Bildgebung, Bildverarbeitung und neuen Behandlungsmethoden.

# CONTENTS

Ι	AN INTRODUCTION TO COMPUTATIONAL SUPPORT FOR MORPHOLOGY-							
	DRIVEN ANALYSIS OF NEUROVASCULAR PATHOLOGIES 1							
1	INT	RODUC	TION	3				
	1.1	Motiva	ation	3				
	1.2	Structi	ure	3				
	1.3	Contri	ibution	4				
2 MEDICAL BACKGROUND								
	2.1	Cerebi	ral vasculature	7				
	2.2	Cerebi	ral small vessel disease	9				
	2.3	Intraci	ranial aneurysms	10				
		2.3.1	Risk factors	12				
		2.3.2	Diagnosis and Imaging	13				
	2.4	Treatn	nent of intracranial aneurysms	14				
		2.4.1	Surgical Treatment	15				
		2.4.2	Endovascular Treatment	16				
		2.4.3	Flow Diverters	17				
	2.5	Intrasa	accular Flow Disruptors	19				
		2.5.1	WEB™Embolization System	19				
		2.5.2	The Contour Neurovascular System	22				
	2.6	Aneur	ysm rupture risk prediction	25				
		2.6.1	Metadata	26				
		2.6.2	Morphology	26				
		2.6.3	Hemodynamics	28				
		2.6.4	Scores	29				
	2.7	Medic	al background summary	29				
II			ESSING OF NEUROVASCULAR STRUCTURES	31				
3	SEG		TION OF VASCULAR STRUCTURES	33				
	3.1		ical background on vessel segmentation	33				
	3.2	Segme	entation pipeline	35				
		3.2.1	Preprocessing	36				
		3.2.2	Mesh extraction and postprocessing	37				
		3.2.3	Centerline extraction	37				
		3.2.4	Outcome	39				
	3.3	Concl	usion on vessel segmentation	39				
4	CO-	REGIST	RATION OF NEUROVASCULATURE	41				

	4.1	Technical background on neurovascular co-registration	43
	4.2	A hybrid approach for co-registration of neurovasculature	45
	4.3	Related work on hybrid neurovascular co-registration	45
	4.4	Hybrid co-registration method for neurovasculature	46
		4.4.1 Medical Image Data	46
		4.4.2 Extraction of Vessels	47
		4.4.3 Hierarchical hybrid approach	47
		4.4.4 Coarse-to-fine hierarchical strategy	49
			52
	4.5	Results and discussion of neurovascular co-registration	53
	4.6	Conclusion on neurovascular co-registration	56
Ш	МО	RPHOLOGY-DRIVEN ANALYSIS OF INTRACRANIAL ANEURYSMS FOR	
	PAT	FIENT-SPECIFIC RESEARCH	57
5	MOR		59
	5.1	,	60
	5.2	•	62
	5.3	• • • • • • • • • • • • • • • • • • •	64
	5.4	Conclusion on mirror IA analysis	66
6	ANA	LYSIS OF INTRACRANIAL ANEURYSM DEFORMATION AFTER CNS TREAT-	
	MEN	JT (	67
	6.1	·	67
	6.2		69
		6.2.1 Results of preliminary study on IA deformation after CNS treat-	
			71
		6.2.2 Discussion of preliminary study on IA deformation after CNS	
			72
		6.2.3 Conclusion on the preliminary study on IA deformation after	_6
	6.2		76 -6
	6.3		76 
		,	77 80
			84
		· · · · · · · · · · · · · · · · · · ·	04 87
	6.4		88
	°.4	Concension on unualysis of foliations unless years decreasing the con-	
IV		PRPHOLOGY-DRIVEN ANALYSIS OF INTRACRANIAL ANEURYSMS FOR HORT-BASED RESEARCH	89
_			
7			91
	7.1		92 04
		7.1.1 Related work on CBR for IA subgroup selection	94

		7.1.2	Method for CBR for IA subgroup selection	95
		7.1.3	Evaluation of CBR for IA subgroup selection	100
		7.1.4	Conclusion on CBR for IA subgroup selection	102
	7.2	Subgr	oup selection of intracranial aneurysms via instance selection	103
		7.2.1	Materials and methods for IS in IA subgroup selection	104
		7.2.2	Results of IS in IA subgroup selection	107
		7.2.3	Discussion on IS in IA subgroup selection	108
		7.2.4	Conclusion on IS in IA subgroup selection	109
	7.3	Concl	usion on subgroup selection for IA analysis	109
8	VIR	TUAL R	REALITY CONCEPTS FOR MORPHOLOGICAL ANALYSIS	111
	8.1	A VR	concept for CBR for IAs	111
		8.1.1	Related Work for a VR concept for CBR for IAs	112
		8.1.2	Virtual data shelf as a VR concept for CBR for IAs	114
		8.1.3	Evaluation of a VR concept for CBR for IAs	118
		8.1.4	Results of a VR concept for CBR for IAs	122
		8.1.5	Discussion of a VR concept for CBR for IAs	125
		8.1.6	Conclusion on a VR concept for CBR for IAs	127
	8.2	Excer	pt: A VR concept for CoW exploration	127
	8.3	Concl	usion on VR concepts for morphologic analysis	130
v	СО	NCLUS	IONS ON MORPHOLOGY-DRIVEN ANALYSIS OF NEUROVASCU-	
	LA	R PATE	HOLOGIES	133
9	CON	ICLUSI	ON	135
	9.1	Limita	ations	139
	9.2	Future	e work	140
BI	BLIO	GRAPH	TY.	145

# **ACRONYMS**

AComA anterior communicating artery

AED Artisse Embolization Device

AOI aneurysm of interest

AR aspect ratio

ASSD average symmetric surface distance

AWSS average wall shear stress

CBR case-based reasoning

CH convex hull

CFD computational fluid dynamics

CNS Contour neurovascular system

CoW circle of Willis

CSVD cerebral small vessel disease

CTA computed tomography angiography

DAPT dual antiplatelet therapy

DBSCAN density-based spatial clustering of applications with noise

DL deep learning

DOF degrees of freedom

DSA digital subtraction angiography

EDIS egocentric distance-based item sizing

EI ellipticity index

FD flow diverter

GUI graphical user interface

HD Hausdorff distance

IA intracranial aneurysm

ICA internal carotic arteries

ICI inflow concentration index

IEL internal elastic lamina

IFD intrasaccular flow disruptor

#### X ACRONYMS

IS instance selection

LOF local outlier factor

LRD local reachability distance

LSA low shear area

MCA middle cerebral artery

MCS Monte Carlo simulations

MED Medina Embolization Device

MRA magnetic resonance angiography

MRI magnetic resonance imaging

NQS NEQSTENT

NCI non-circularity index NSI non-sphericity index

nWSS normalized wall shear stress

OPTICS ordering point to identify clustering structure

OSI oscillatory shear index

PC phase-contrast

PCA principle component analysis
PCC Pearson correlation coefficient
PComA posterior communicating artery

RIS reverse instance selection RMSE root mean squared error

RndS randomly sampled RQ research question

SAH subarachnoid hemorrhage

SEAL Saccular Endovascular Aneurysm Embolization System

SimS most similar sampled

T Tesla

TOF time-of-flight
UI undulation index
VR virtual reality

WSS wall shear stress

WEB Woven EndoBridge

WNBA wide-necked bifurcation aneurysm

# Part I

AN INTRODUCTION TO COMPUTATIONAL SUPPORT FOR MORPHOLOGY-DRIVEN ANALYSIS OF NEUROVASCULAR PATHOLOGIES

INTRODUCTION

#### 1.1 MOTIVATION

The human brain is dependent on sufficient and constant blood flow to supply it with necessary nutrients [83]. This is because the brain has no energy storage, and thus brain function is reliant on the careful regulation of blood flow to manage its requirements [83].

The main part of the neurovascular unit, which supplies blood flow to the brain, is the intracranial vasculature. Therefore, any pathology of the intracranial vasculature affects its function in providing sufficient blood flow and can lead to cognitive deficits or death [64].

Pathologies of the vasculature can lead to strokes, the second most common cause of death and disability worldwide [171]. Strokes are either ischemic or hemorrhagic, meaning either caused by a thrombosis of a vessel, or vessel damage that causes bleeding within the brain [171].

However, many of the exact mechanisms of vascular pathologies and how they can be treated most successfully are not yet fully understood.

As morphology drives both risk assessment and treatment decisions, an in-depth analysis of neurovascular pathologies and their morphology can aid in understanding and treating those pathologies. Image processing methods help reveal and extract features that aid this analysis. Therefore, this thesis presents different image processing methods and other computer support to facilitate the morphology-driven analysis of neurovascular pathologies, especially intracranial aneurysms, to aid in research, risk assessment, and treatment.

#### 1.2 STRUCTURE

The structure of the thesis is depicted in Figure 1.1.

Before diving into the exact methodologies of analysis, Chapter 2 introduces the main pathologies this thesis is focused on, that focus being intracranial aneurysms (IAs). It covers general information about the disease, as well as risk factors and treatment options.

Neurovascular pathologies are usually visible in medical imaging scans done via various modalities. To extract the neurovasculature, along with the pathologies, from these scans to analyze them, several preprocessing steps are required. These steps are covered in Chapter 3 and Chapter 4 (Figure 1.1, yellow).

#### 4 INTRODUCTION

After preprocessing, analysis can begin. This thesis focuses on two aspects of analysis: patient-specific analysis, where morphology of individual patients is assessed, and analysis that supports cohort-based research.

For patient-specific analysis, Chapter 5 (Figure 1.1, blue) gives a brief insight into general morphology-driven assessment of individual cases by showing the impact of morphology on hemodynamics. Then, Chapter 6 (Figure 1.1, purple) presents how deformation of morphology can be quantified via analyzing the pathology over time before and after deployment of a novel implant. The longitudinal morphological change of the implant itself is also analyzed.

For cohort-based analysis, Chapter 7 (Figure 1.1, green) introduces two strategies for subgroup selection. These methods serve to identify research questions, to match cohorts, and in the selection of a training set for surgical training. The subgroups are found via extensive analysis of the pathology and its morphology. Then, Chapter 8 (Figure 1.1, orange) explores how cohort-based analysis can further be supported by virtual reality (VR).

Finally, Chapter 9 summarizes the thesis, discusses its limitations, and presents future work.

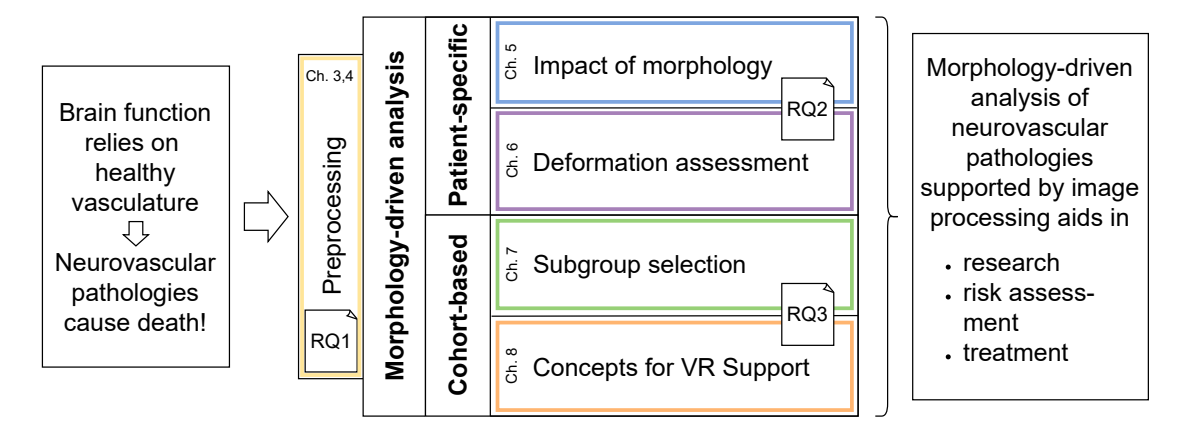


Figure 1.1: Structure of the presented thesis. Colors indicate chapters (Ch.). Research questions (RQs) and the chapters that answer them are indicated. Own figure.

#### 1.3 CONTRIBUTION

This thesis aims to provide computer support for the analysis of neurovascular pathologies. The analysis can aid in the research, risk assessment and treatment of those pathologies, help prevent disruptions to the intracranial blood flow and thus save lives.

Before analysis can be provided, preprocessing is required. One part of preprocessing, aside from the extraction of features, is the process of making information from

different modalities comparable. This is a highly specialized process where the methods must be tailored to the specific modalities and desired structures and features. In this area, methods to make vascular information from 7Tesla (T) modalities comparable are lacking, and the thesis aims to answer the question of how information from these different modalities can be combined (RQ 1).

Once preprocessed, analysis can be done on patient-specific data, where individual cases are examined, and their results are collected. As research of neurovascular pathologies is an active field, new treatments are developed, including implants. Any implant means a foreign object being inserted into the human body, which will inevitably have effects on the structure where it was inserted. The morphology of the structure as well as treatment success therefore must be observed and analyzed, particularly over time, to ensure robustness of the implant and give insights into best practices for treatment success. Further, morphology has an impact on blood flow, meaning changed morphology may have consequences for blood supply. This thesis aims to answer the question of how the morphological deformation of a neurovascular pathology treated with a novel implant can be analyzed (RQ 2).

Lastly, this thesis looks beyond patient-based analysis and aims to support analysis of cohorts. Looking at large groups of patients, pathologies, and their features, can be overwhelming for physicians and researchers. Computer support can help in identifying subgroups among a large number of patients, while keeping in mind a large amount of features from individual pathologies. It can further provide visualizations to aid researchers and physicians in identifying features or interesting cohorts. This thesis aims to answer the question of to what extent computer-supported morphology-driven analysis can support cohort-based research questions (RQ 3).

The three core research questions (RQs) of this thesis are thus:

- RQ 1 How can information about vascular pathologies from multiple 7T MRI scans be combined?
- RQ 2 How can longitudinal morphological deformation be analyzed, using the example of a novel implant?
- RQ 3 To what extent can morphology-driven analysis support cohort-based research?

#### 2.1 CEREBRAL VASCULATURE

The cerebral vasculature is a complex system of blood vessels that supplies the brain with oxygen and nutrients. It consists of multiple components, including arteries, capillaries, veins and the blood-brain barrier. Due to its function of sustaining the brain, it is extremely important to normal human cognition, and disruptions of it lead to serious cerebrovascular diseases that can lead to stroke, cognitive deficits, and death. To highlight the importance of the brain's blood supply: despite making up only 2% of body mass, the brain takes up almost 50% of the body's glucose [51].

The arterial system supplies the brain with blood and drains interstitial fluids and proteins. It is made up from the anterior and posterior circulation, where the anterior circulation supplies the front parts of the brain, and the posterior, also called vertebrobasilar, supplies the back parts of the brain as well as the brainstem [51].

The anterior and posterior circulations meet in the circle of Willis (CoW), a circular arterial system named by Thomas Willis, who first described it in 1664. It is depicted in Figure 2.1 and is made of the following cerebral arteries [51, 235]:

- Internal carotic arteries (ICA): Supplies anterior circulation
- Basilar artery: Supplies posterior circulation
- Anterior cerebral artery: Supplies medial part of the brain hemispheres
- Anterior communicating artery (AComA): Connects the two anterior cerebral arteries
- Anterior choroidal artery: Branch of the ICA
- Ophthalmic artery: Branch of the ICA
- Middle cerebral artery (MCA): Largest and most complex cerebral artery
- Posterior cerebral artery: Supplies occipital and parts of the temporal and parietal lobe
- Posterior communicating artery (PComA): Connects ICA and posterior cerebral artery

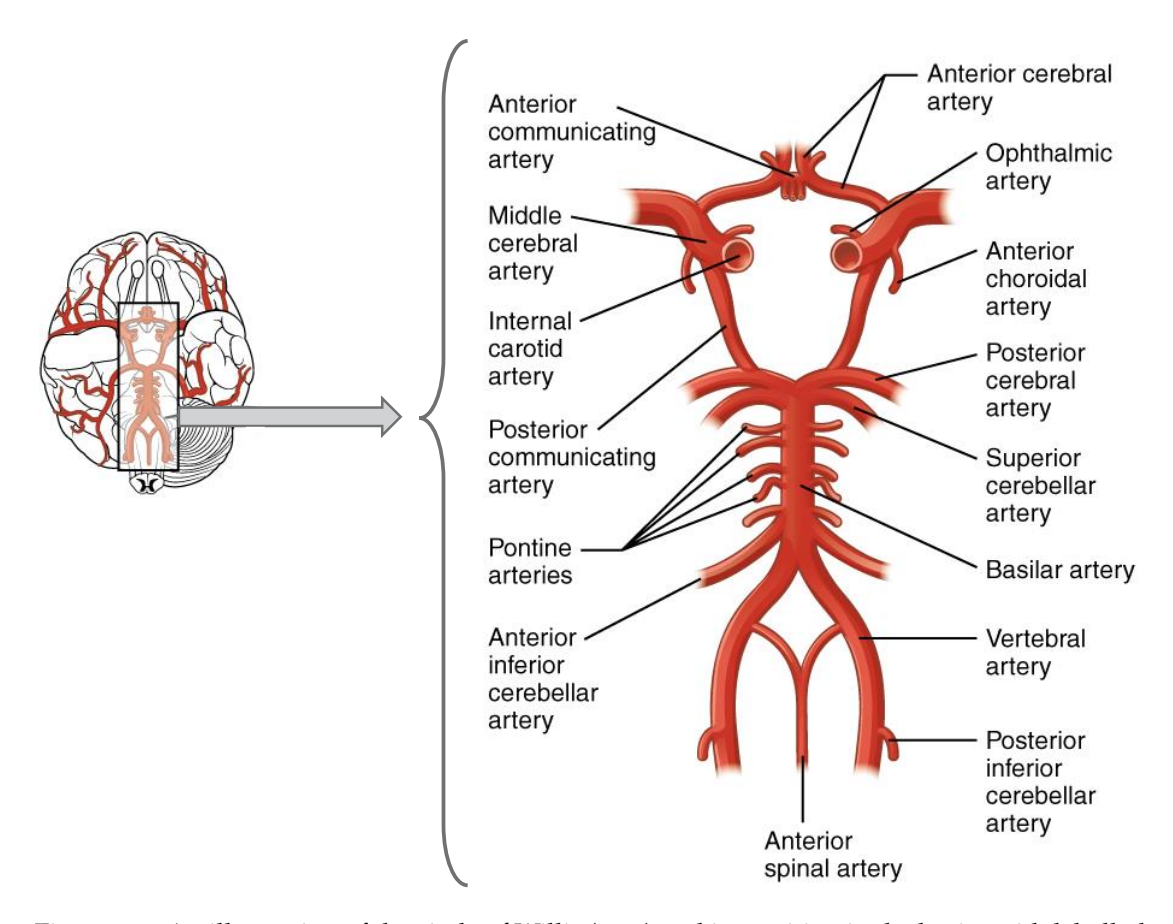


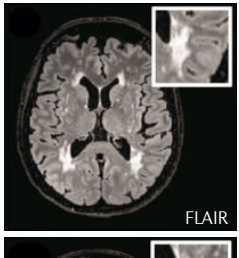
Figure 2.1: An illustration of the circle of Willis (CoW) and its position in the brain, with labelled arteries. Image adapted from [182] and available under a CC BY 4.0 license.

While general CoW illustrations as depicted in Figure 2.1, show the listed arteries, a wide range of variations can exist in individuals, including additional vessels and branches, different branching points, or complete lack of some vessels. Some variants may increase the risk for ischemic events [51, 246].

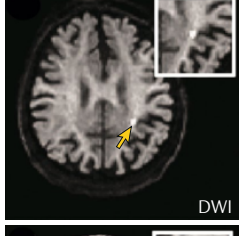
The exact function of the CoW is an active research field. The circular nature of the arteries in the CoW is thought to act as a fallback system in case of stenosis of one artery [51, 170, 246]. Larger disruptions of blood flow may further lead to stroke, brain damage, and death, so having alternative ways for blood to reach the rest of the brain when one artery fails may be beneficial [51, 246]. However, as several animal species also have a CoW-like vasculature despite not generally experiencing fatal consequences from cerebrovascular diseases, the CoW may not only serve a compensatory function [246]. The wide range of variations in the CoW in humans, which can include complete lack of some structures, also speaks against this purpose. Instead, the CoW and its many branchings may serve as a passive way to exchange pressure and protect the blood-brain barrier from hemodynamic stresses [235, 246].

#### 2.2 CEREBRAL SMALL VESSEL DISEASE

Many diseases affect the neurovasculature. One of the most commonly found ones, as well as one of the most relevant ones due to its association with dementia, is cerebral small vessel disease (CSVD). CSVD is an umbrella term that describes a remodeling of the smallest vessels in the brain which supply the white matter and deep structures of grey matter [57]. CSVD can be responsible for a variety of negative medical outcomes, including strokes, difficulties with walking, depression, cognitive impairment, incontinence, mood instability, and dementia. 20% of all strokes are caused by CSVD, including 25% of ischemic strokes, and 45% of dementia [57, 142, 158, 216, 241].



White matter hyperintensities Bilateral hyperintensities (often symmetrical) visible on T2-weighted sequences (e.g. FLAIR). They are of variable size and are mostly located in the periventricular and deep white matter.

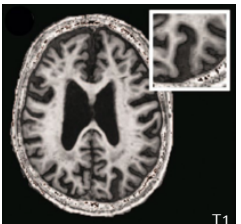


Recent small subcortical infarcts Can be revealed by DWI as a small (<20 mm on axial slice) hyperintensity in the territory of a single perforating arteriole. Lesions <5 mm (that is, subcortical microinfarcts) are detectable only with high-resolution (3T and higher field strengths) imaging<sup>65</sup>.



Lacunes

Round or ovoid subcortical cavitations (3–15 mm in diameter) presumed to be of vascular origin. Lacunes have a signal intensity similar to CSF and often, although not always, have a surrounding hyperintensive rim. They are thought to result from acute, small subcortical infarcts or haemorrhages in the territory of a single perforating artery.



Brain atrophy

Cortical or subcortical brain volume loss unrelated to large traumatic injuries or infarctions.



Enlarged perivascular spaces

Extensions of extracerebral fluid space surrounding the perforating vessels. These features are visible on MRI as CSF-like fluid-filled spaces that follow the course of penetrating vessels, with a linear or round shape depending on whether imaged parallel or perpendicular to the vessel orientation, respectively.



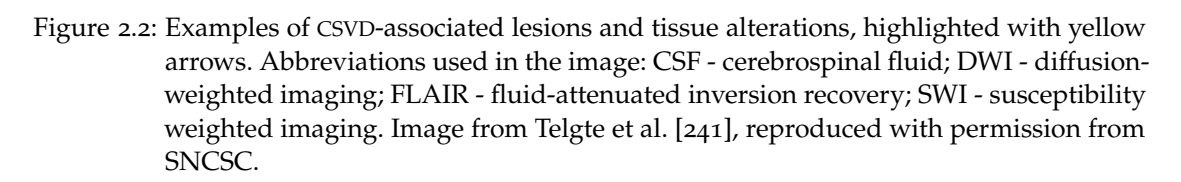
Cortical microinfarcts

Small ischaemic lesions varying between 50 µm and a few millimetres<sup>139</sup> that are revealed on high-resolution structural MRI and DWI



Cerebral microbleeds

Small depositions of haemosiderin consistent with blood cell leakage into brain tissue. Microbleeds are detectable on paramagnetic resonance sequences (e.g. T2\*-weighted sequences or SWI), as small (2–10 mm in diameter) hypointense lesions.



CSVD is diagnosed mainly with magnetic resonance imaging (MRI). Typical signs of CSVD include [142, 146, 158, 216]:

- White matter hyperintensities: lesions in the white brain matter, which are visible as bright white areas in MRI
- Lacunar infarcts/Lacunes: fluid-filled hollows in the brain caused by stenosis of small arteries
- Increase of perivascular spaces: more tissue surrounding arteries
- Cerebral microbleeds
- Decrease in brain volume: sign of advancing age but more common and severe in CSVD patients

What these signs and more looks like on MRI can be seen in Figure 2.2.

The mechanisms of CSVD are an active research field, not least because there is no direct treatment. One of the biggest hurdles in CSVD research is imaging resolution, as the small vessels that are affected are hard to capture in state-of-the-art MRI, the most common imaging method for CSVD. Instead, it is usually the effects of CSVD that are captured [248]. High-field MRI with 7 Tesla (T) imaging, for example with phase-contrast (PC)- or time-of-flight (TOF)-MRI, has been opening new research potential in this area. PC-MRI can measure hemodynamics like blood flow velocity though it is limited in its resolution when with 7T [248]. TOF-MRI captures small vessels thanks to its high resolution of 40  $\mu$ m [89, 249]. A detailed depiction of the small vessels and their morphology can aid in CSVD research, especially in addition to flow information. These two modalities first have to be made comparable and combined through a process called co-registration, where one dataset is transformed to be aligned with the other. This requires a complex methodology that needs specific adaptations for every use case. A registration for PC-MRI and TOF-MRI is not widely available at this time.

## 2.3 INTRACRANIAL ANEURYSMS

IAs are dilatations of the intracranial blood vessel walls. With a prevalence of around 3.2% they are relatively common [127, 211, 240]. Their risk lays in the possibility of rupture, which leads to a subarachnoid hemorrhage (SAH), a type of hemorrhagic stroke, which is often fatal. However, most IAs never rupture, and they can be unpredictable in risk factors and growth [36, 94, 127, 211, 240]. Yearly aneurysm rupture risk ranges from 0.1 to 3.1% based on multiple factors [211, 240]. Women are at a higher risk of IAs, and the general risk rises with age [18, 36, 250, 257].

Due to the high prevalence and high risk when ruptured, IA management is an active research field. With an annual incidence of 6.1 to 10 in 100 000, SAH has one of the highest rates of neurological disorders, including brain tumors and multiple sclerosis.

Patients suffering from SAH after IA rupture die in 25-50%, 12% before receiving medical attention, and 40% die within a month of hospitalization. Further, only a third of all SAH patients have a positive outcome, as half of the survivors will suffer permanent complications [127, 211].

Unruptured IAs remain asymptomatic in 85-90%. Symptoms are mainly caused by mass effect, meaning a large IA causing pressure or irritation, and include headaches, seizures, ischemic cerebrovascular disease, and others, depending on the location of the IA, most commonly palsy of the third nerve, brain-stem dysfunction and visual-field defects [127, 211]. Due to the high number of asymptomatic IAs, they are either discovered after rupture due to SAH symptoms, or, most commonly, incidentally during other procedures [94].

85% of aneurysms occur within the CoW. Within the CoW, the statistical distribution of IAs is 30-35% at the AComA, 30% at the ICA (including PComA and ophthalmic artery), 22-30% at the MCA (bifurcation), and 8-10% in the posterior circulation, most commonly basilar artery tip [36, 127].

IAs come in four main types: saccular, fusiform, dissecting and mycotic.

- Saccular IAs (see Figure 2.3 A) are the most common, making up 90% of IAs [94, 211]. They are prominent bulges of the cerebral artery walls, forming a sac either at a bifurcation or on the sidewall. They are caused by a combination of hemodynamic stresses and deficiency of collagen in the internal elastic lamina (IEL), which separates the tunica intima and the tunica media, which are the two internal of the three layers making up the normal arterial structure. Collagen deficiency of the IEL causes a breakdown of the tunica media, which causes the other two layers, tunica intima and tunica adventitia, to dilate in an outpouching, the IA sac, through the affected area of the IEL [36, 127, 240]. This thesis focusses on saccular IAs.
- Fusiform IAs (see Figure 2.3 B) do not develop a saccular dilation but instead dilate the entire vessel circumference.
- *Dissecting IAs* (see Figure 2.3 C) are rare and are technically false IAs, or pseudoaneurysms. They develop through a tear in the tunica intima and IEL, leading to an intramural hemorrhage, and the pseudoaneurysm forms between the layers of the vessel walls [36].
- *Mycotic IAs* (see Figure 2.3 D), also called infectious IAs, cover 2-4% of IAs and are common in patients with infective endocarditis or HIV. Mycotic IA sacs are formed by necrosis of the tunica intima and inflammation of the other vessel wall layers. As such, they are fragile and usually rupture within weeks after formation and are associated with high morbidity and mortality [36].

Multiple IAs found in one patient occur in 20-30% of IA patients [127, 211, 240]. Of those, 40% are placed at identical locations in the right and left hemispheres, making

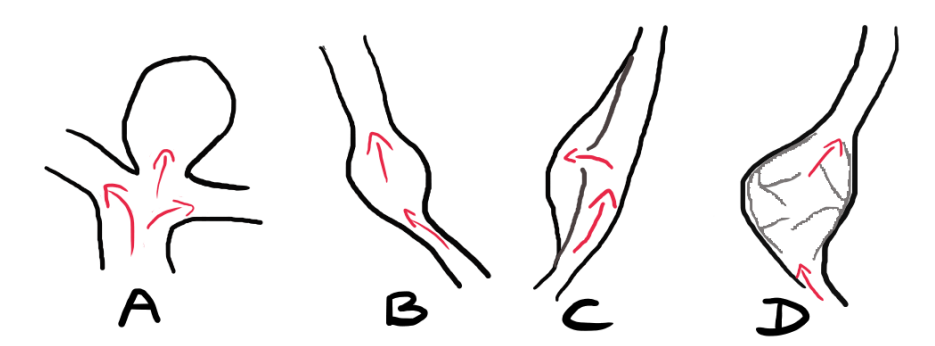


Figure 2.3: Illustration of IA types: A) saccular (at a bifurcation), B) fusiform, C) dissecting, D) mycotic. Own figure.

them mirror aneurysms [162]. This rare subgroup makes up only 5% of IAs [247], leading to a small amount of data that has not been exhaustively researched yet in regard to causes, risks, and development, making analysis of mirror IAs an active research field [162].

Some research points towards genetic predisposition as main cause for mirror aneurysms [15, 44, 247], though the exact predisposition could not be identified. Many genetic diseases known to heighten aneurysm formation risk, including various connective tissue diseases, occur only rarely in patients with mirror aneurysms. Baccin et al. [15] found that a significant amount of mirror aneurysm patients had first-degree family members with ruptured IAs in similar locations. Hormonal factors might also play a role, as more women than men have mirror aneurysms [15].

# 2.3.1 Risk factors

Risk factors of IAs formation and rupture can be patient-specific (genetic and acquired) and aneurysm-specific.

Genetic risk factors for IA formation include various diseases, particularly those affecting connective tissue: autosomal dominant polycystic kidney disease, Ehlers-Danlos syndrome, neurofibromatosis, and antitrypsin deficiency. 4-20% of IA patients have a first or second degree relative who has suffered from SAH [127, 211, 240]. People with Japanese or Finnish heritage are also at a higher risk [250].

Acquired risk factors include advancing age, hypertension, smoking, alcohol abuse, estrogen deficiency, hypercholesterolemia, and carotid artery stenosis, and previous SAHs [127, 211, 240]. Women are 1.6-2 times more likely to get an SAH, particularly above age 50, most likely caused by estrogen deficiency after menopause [127].

Rupture risk is particularly important to assess in combination with treatment decisions, as only few IAs rupture in patients' lifetimes. Details on rupture risk assessment follow in Section 2.6.

# 2.3.2 Diagnosis and Imaging

Several imaging modalities can be utilized for IA diagnosis. The most employed method is *digital subtraction angiography* (*DSA*), where a series of images is taken with and without contrast agent and subtracted from each other. The resulting images depict the lumen of the arteries with good contrast and decreased spatial resolution. DSA is carried out as a single projection, but can be accomplished using 3D rotational angiography, providing a 3D volume. In contrast to other imaging methods, DSA can depict even very small IAs with a size <3 mm, for which the sensitivity of other methods drops. While DSA is considered the gold standard for IA diagnosis, it is an invasive and costly procedure and has a complication rate of 1-4% with 0.5% of patients suffering permanent neurological complications [94, 127, 211, 240].

Computed tomography angiography (CTA) is a CT scan with contrast agent, thus highlighting the vessels and allowing for 3D reconstruction of the vasculature [127].

Magnetic resonance angiography (MRA) can be done without contrast agent, as it relies on a magnetic pulse aligning protons and those protons returning to the pre-agitated state at different rates based on tissue properties. As blood moves through the image, the aligned protons are no longer in the image to be captured, resulting in a lack of signal and a "void" in the final image, thus visualizing the vessels [127]. MRA can also be done with contrast agent based on gadolinium, which is an advantage for patients unable to take the iodine contrast agent necessary for DSA and CTA. High-field MRI scans are a more recent development that offers opportunities for even more finely resolved images down to 40  $\mu$ m, thus also enabling depictions of small vessels and thus small aneurysms [104, 249]. The long acquisition time is a disadvantage, however [94, 127, 240].

Lastly, *transcranial doppler sonography* has also been proposed for IA diagnosis but is limited by its resolution [127].

A drawback of DSA is that it only provides information about the lumen of the vessel and not the vessel walls, which are captured in CTA and MRA. A thrombus or wall calcification will therefore be better visualized in the latter two modalities [127]. There are many debates about which modality is best for IA diagnosis, with DSA considered as gold standard, but ultimately the results of each vary not just in resolution and costs, but also in suitability based on the IA itself, e.g., with IA size [127].

As each modality has its benefits and drawbacks, there is also the option to combine two or more scans from different modalities. This process of making two or more scans comparable to combine them is called co-registration and has to be specifically tailored to each individual use case. For such individual cases it raises the question of how this combination, in the form of co-registration, can be achieved. We aim to answer this question for the specific case of neurovasculature from 7T MRI with RQ 1.

#### 2.4 TREATMENT OF INTRACRANIAL ANEURYSMS

The number of asymptomatic aneurysms that are discovered incidentally, meaning during screenings for other reasons, is rising, which raises the question of how to treat them [200]. As not every IA ruptures and any intervention also comes with complication risks, the treatment of an IA always has to be carefully weighed against its individual rupture risk. Especially for asymptomatic, incidental IAs, treatment is not always recommended, as they are unlikely to rupture in a patient's lifetime, making potential treatment complications an unnecessary risk [200, 230]. This makes rupture risk analysis an important part of the treatment strategy, where computer support can aid the physicians. However, the knowledge of having an IA often presents a significant mental burden to the patient, meaning they may request treatment regardless of rupture risk [200, 230]. The selection of the treatment methods presents a challenging task for physicians that does not have a straightforward solution, giving potential for computer support.

For treatment, there are three possibilities: observation, surgery, or endovascular treatment.

Observation is recommended for IAs with a low rupture risk, for patients who do not want treatment, and for patients who are particularly at risk for treatment complications, especially older patients. It entails regular screening of the IA for changes like IA growth, which is often unpredictable [211]. Additionally, patients are advised to lower acquired risk factors for rupture and IA growth, e.g., quit smoking and reduce hypertension [240].

The choice between surgical and endovascular treatment is also not solely dependent on the risk or complication factors but can also be based on patient condition and IA parameters like location or morphology [94].

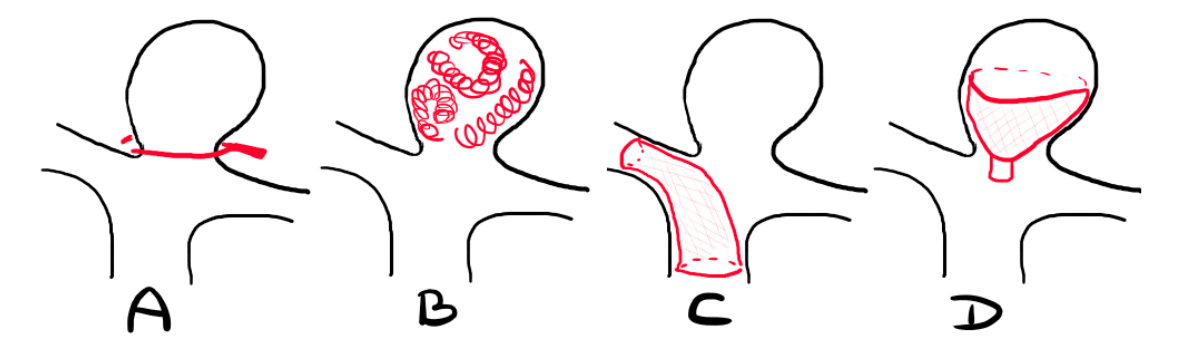


Figure 2.4: Illustrated examples of IA treatments: A) surgical clipping, B) endovascular coiling, C) flow diverter, D) flow disruptor. Own figure.

The importance of morphology in treatment decisions is illustrated by the hard-totreat wide-necked bifurcation aneurysms (WNBAs). WNBAs are a subtype of IAs defined by their wide neck in comparison to the IA dome. An IA counts as a WNBA if its neck diameter is larger than 4 mm, or its dome-to-neck ratio is less than 1.6 [11, 106]. A bifurcation IA is an IA located at the separation point where one vessel branches into two or more child vessels. The neck of an IA is the area where the parent vessel (Figure 2.5 D) opens into the IA sac (Figure 2.5 C), defined by the neck curve (Figure 2.5 A), the line that separates the IA sac from the parent vessel. Treating that neck curve as a surface results in the ostium(Figure 2.5 B).

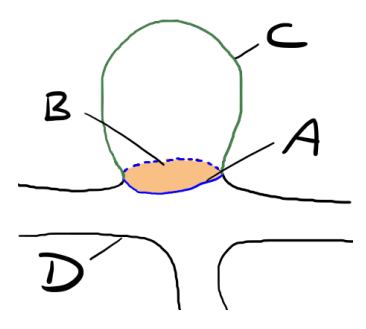


Figure 2.5: Illustrated bifurcation aneurysm with neck curve (A, blue), ostium (B, orange), dome/sac (C, green), and parent vessel (D, black). Own figure.

WNBAs are particularly hard to treat. The wide neck can lead to the prolapse of endovascular devices like coils, while the bifurcation placement complicates stent assistance as it branches into child vessels that need to be protected. This means high retreatment rates for traditional treatments [106], which have an average full occlusion of only 45%, adequate occlusion of 60 %, and complication rates of 19 % [78].

Instead of coiling alone, balloon- and stent-assisted coiling is done more commonly [187, 188]. Flow diverters (FDs) are not recommended for treatment of WNBAs due to the high rate of 43% ischemic complications because of parent artery occlusion, though dual antiplatelet therapy (DAPT) could improve this [43]. More recently, intrasaccular flow disruptors (IFDs) have shown promising results in WNBA treatment. The Woven EndoBridge (WEB) is the most well-researched, but the Contour neurovascular system (CNS) is showing much promise as well. Details about the treatment of WNBAs with IFDs follow in Section 2.5

## 2.4.1 Surgical Treatment

The most common surgical treatment for IAs is clipping (see Figure 2.4 A), where a craniotomy is performed to open the skull and brain for access to the IA. Subsequently, at least one metal clip is placed over the IA neck to stop blood flow into the sac [20, 257].

Clipping has a very high occlusion rate combined with a low retreatment rate and as such can be used after other treatments failed. The International Subarachnoid Aneurysm Trial [168] reports a 94.0% adequate occlusion rate, with only 2 rebleed-

ing cases in 1070 clipped IAs. A large study from South Korea [130] assessed over 13 thousand clipped IAs and found all-cause mortality at seven years to be 3.6%. Another study also found a 3.4% mortality rate for clipping after one year [251]. A meta-analysis from 2019 [5] found a pooled complication rate of 8.34% for surgical treatment, with associated complication risk factors to be similar to rupture risk factors, namely advanced age, sex (female), smoking, hypertension, and location (posterior circulation) as well as diabetes, congestive heart failure, coagulopathy, use of anticoagulation, and IA calcification.

Craniotomies are, however, associated with seizures, leading to endovascular treatments having a significantly lowered risk in comparison [168].

#### 2.4.2 Endovascular Treatment

Endovascular treatment does not require open surgery, instead accessing the IA via catheters through the patient's peripheral artery. Overall, a meta-analysis [5] assessing various endovascular treatments found a pooled complication rate of 4.96%, with a fatality rate of 0.3%. Associated complication risk factors were similar to rupture risk factors, including sex (female) and location (posterior circulation), as well as diabetes, hyperlipidemia, cardiac comorbidity, wide IA neck, stent-assisted coiling, and stenting.

## Coiling

Among endovascular treatment options, coiling (see Figure 2.4 B) is the most used method [186]. Starting with the detachable Guglielmi coil in the 1990s, coils are thin metal wires that are inserted into the IA sac to induce embolization [19, 20, 257].

Many studies have been done to assess the safety and effectiveness of coiling. A review from 2009 including 46 studies with 8161 treated IAs reported 91.2% adequate occlusion [77]. The International Subarachnoid Aneurysm Trial treated ruptured aneurysms and found a 92% adequate occlusion rate for coils [168].

Risks of coiling include thromboembolic events, intraoperative rupture, and recanalization, meaning a worsening of the IA occlusion which can lead to rebleeding, and about half of reopened cases require retreatment [77].

Recanalization rates range from 11.0% to 29.5% [77, 160, 186], and are associated with rupture status, smoking, IA size (>10mm), wide necks, and location (MCA, posterior circulation) [77, 186].

Thromboembolic event rates differ between studies. A study on unruptured IAs reports 7.1% and one on ruptured ones 13.3% of coiling patients [30, 60]. A study with both ruptured and unruptured IAs reports thromboembolic complications in 10.4%, of which 25.7% had a poor clinical outcome [185].

The probability of coil-related mortality and morbidity, as well as long-term rupture, is very low, with one study reporting 0.9% rupture rate at seven years post-coiling [130].

A big study from South Korea [130] with over 26 thousand treated IAs found an all-cause mortality of 3.8% of patients with coiled IAs. 10.8% of coiled IAs need to be retreated [77, 160].

Additional coiling techniques include:

- *Balloon-assisted coiling* uses a non-detachable balloon which is temporarily inflated in the neck of the aneurysm to aid in coil deployment, allowing treatment of complex IAs with unfavorable morphology by stabilizing the IA neck, allowing for greater packing attenuation [60, 257].
- Stent-assisted coiling entails the deployment of a stent along the parent vessel and over the IA neck, aiding in preventing coil prolapse and stabilizing the vasculature [20, 257]. Despite stent-assisted coiling generally being used for IA cases with difficult morphology, meaning wider necks and lower dome-to-neck ratio, it has similar outcomes to coiling on its own [109]. The use of a stent requires an additional DAPT.

The coiling techniques predominantly perform the same [23, 77, 109, 160].

An advantage of coiling, particularly in comparison to surgical treatment, is the comparatively short hospital stay. One study reported a median hospital stay of four days for patients treated with coils, compared to eleven days for patients treated with a clip, with a hospital transfer or more than 30-day hospital stay rate of 0.4% for coils and 1.4% for clips [20, 130].

In comparison to clipping, coiling has a better long-term result for ruptured IAs, but a higher chance of rebleeding [168]. Coiling reduces the risk of death or dependency by 23.9%, meaning an absolute risk reduction of 7.4%, thus being rated as having a better clinical outcome despite a higher rebleeding rate [140, 168]. Some imaging methods, like CTA, have strong artifacts when imaging coiled IAs [240].

Overall, despite clipping having higher occlusion and lower recanalization rates, coiling is rated as having a better clinical outcome [20, 140]. However, clipping is still considered a valid alternative to coiling when the coiling procedure fails.

## 2.4.3 Flow Diverters

FDs, also called flow-diverting stents (see Figure 2.4 C), are flexible stents that isolate the IA sac from the parent vessels by utilizing recanalization. They self-expand within the parent vessel to divert blood flow away from the IA, causing the blood within the IA to thrombose. They were developed for the treatment of challenging IAs that may be difficult to treat with coiling or clipping, like fusiform, giant, or wide-necked IAs [155, 257].

A meta-analysis of 29 studies done between 2005 and 2012 with 1654 treated IAs, found a 76% complete occlusion rate with a procedure-related morbidity of 5% and

mortality of 4% while SAH, ischemic stroke and other complication rates were between 3-6% [38].

A study with 514 IAs found that 18% of patients had a minimum of one neurological complication after treatment with an FD, most of which occurred within 30 days after the procedure [52]. While other studies support the high risk within the periprocedural period [22], others emphasize the risk of long-term complications as well and highlight the importance of long-term follow-up after FD treatment [100].

Another risk of FD treatment is the occlusion of the parent artery through the stent itself. While this can be treated when occurring during the procedure, a delayed parent artery occlusion was observed in 21% of cases in one study [155].

FD treatment requires DAPT to reduce thromboembolic events and to keep small side branches from being occluded by the stent. DAPT however also raises the risk of hemorrhage and complicates the treatment of ruptured IAs. Further, there is no recorded guideline for the length or exact dosage of DAPT, though research is ongoing [22, 244].

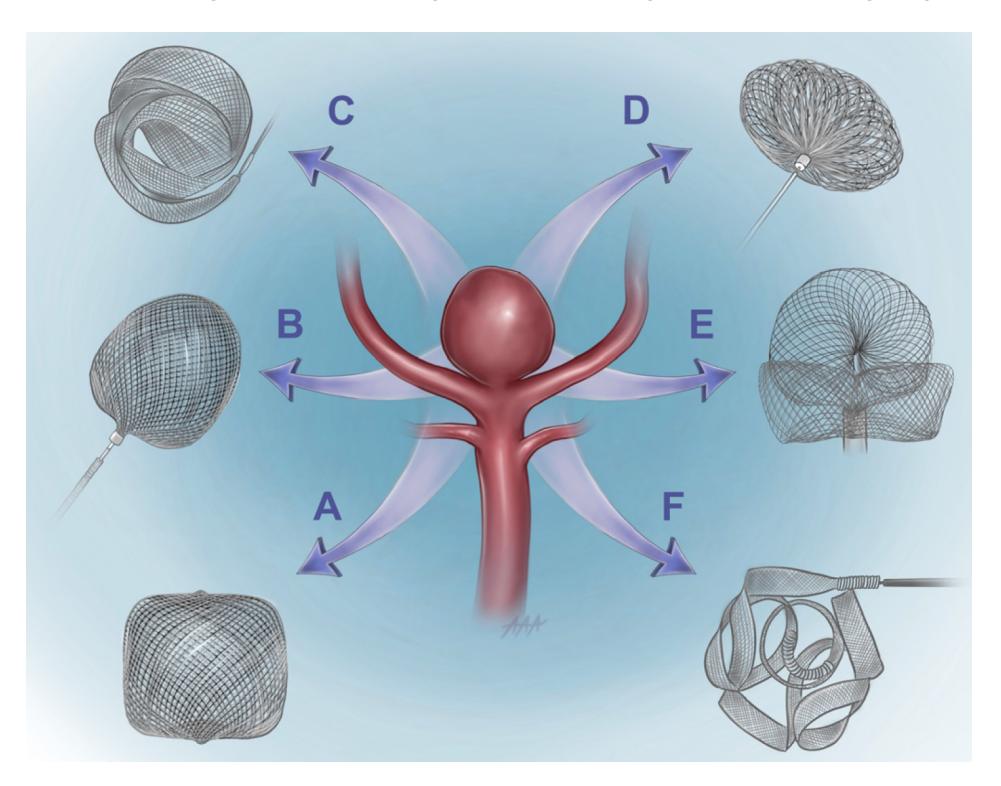


Figure 2.6: IFDs. A: WEB, B: Artisse Embolization Device (AED), C: Medina Embolization Device (MED), D: CNS, E: Saccular Endovascular Aneurysm Embolization System (SEAL), F: Trenza. Image from Shao et al. [214] and available under a CC BY 4.0 license. No changes were made.

#### 2.5 INTRASACCULAR FLOW DISRUPTORS

IFDs (see Figure 2.4 D) are a newer alternative to FDs that are specifically well-suited to treat WNBAs. They are deployed inside of the IA sac, thus potentially not requiring DAPT and lowering the risk of parent artery occlusion [30, 106]. IFDs come in various shapes, generally achieving a high mesh density deployed at or in the IA neck region to disrupt blood flow within the sac and divert it from the IA neck.

IFDs that are currently being used, developed or researched include the WEB<sup>TM</sup>(Terumo Neuro, Aliso Viejo, California, USA), CNS (Stryker, Kalamazoo, MI, USA), NEQSTENT (NQS) (Stryker, Kalamazoo, MI, USA), Trenza (Stryker, Kalamazoo, MI, USA), SEAL (Galaxy Therapeutics Inc, Milpitas, CA, USA), MED (Medtronic, Irvine, CA, USA) and the AED (formerly known as LUNA; Medtronic, Dublin, Ireland).

Generally, adequate occlusion for these devices ranges between 77.9% to 96.4% [79, 95, 99, 117, 189]. A comparison of all devices is presented in Table 2.1 and all devices are depicted in Figure 2.6. The two most popular and successful ones are the WEB and the CNS. This thesis will focus more on the CNS, the newer and less well-researched device. The WEB will also be introduced in detail to highlight the areas where the CNS still needs to be researched.

## 2.5.1 WEB<sup>TM</sup>Embolization System

The WEB<sup>TM</sup> Embolization System (Terumo Neuro, Aliso Viejo, California, USA), is an IFD meant to specifically treat WNBAs. Introduced in 2010 as a dual-layer mesh, each layer made of 144 braided wires, it has since evolved into two single-layer options, one roughly cylindrical, and one spherical (Figure 2.7). The manufacturer offers various size configurations in the range from  $4 \times 3$  mm to  $11 \times 9$  mm. Sizing of the WEB is generally 1 mm oversized in neck diameter and 1 mm smaller than IA height as the WEB should brace against the IA wall [47, 98], and knowledge of morphology and hemodynamics around the IA can be beneficial before treatment, as it may affect occlusion success [47].

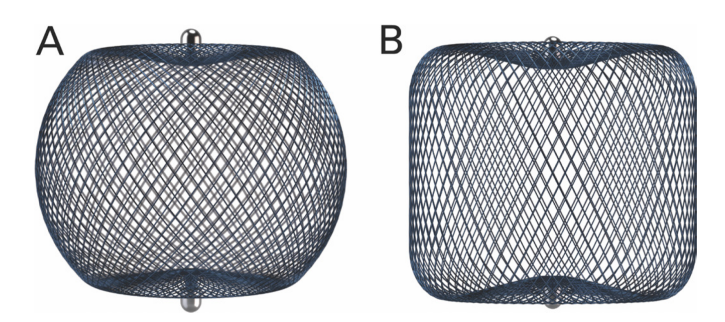


Figure 2.7: The WEB, in single layer (B) and single layer spherical (A) options. Reproduced from Fiorella et al. [79] with permission from BMJ Publishing Group Ltd.

Table 2.1: Comparison of IFDs currently being researched and developed. Sources for the individual IFDs are: WEB [40, 79, 151, 184, 189], CNS [95, 99, 105, 117], Trenza [39, 197, 214], SEAL [183, 214], NQS [72, 116, 143], AED/LUNA [190, 191, 214] and MED [29, 85, 214].

Devices	Shape	Occlusion	Complica-	Retreat-	Use and issues
		rates	tion rates	ment rates	
WEB	Cylindrical +	77.9-81%	6%	11.6-15.5%	Compression
	spherical				phenomenon
	shapes				
CNS	Cup shape	85-91.5%	4.7-7.2%	2.5-3.2%	
Trenza	Braided loops	83%	25%	17%	No FDA/CE
	in Omega				Mark yet
	shape				
SEAL	Bridging	81.5%	-	-	Not FDA/CE
	component				Mark yet
	(+ ovoid loop)				
NQS	less dense	80.6-94.1%	10%	-	Only used with coils,
	CNS				Higher recurrence
					than CNS
AED/	Spheroid and	57.1-79-2%	9.6%	4.8%	
LUNA	ovoid shapes				
MED	Loops around	71.4-90%	23.1%	-	Not available to
	core wire				market, difficulty
					in covering neck

RESULTS OF WEB TREATMENT Generally, the WEB is seen as safe and effective. Multiple studies have been conducted with up to 5-year follow-ups. Across these studies, including multiple European and US-centric trials, the WEB reached an adequate occlusion ranging from 77.9 to 81% at last follow-up, with most cases remaining stable or improving over time. Retreatment rates ranged from 11.6 to 15.5%. No deaths were associated with the WEB [79, 151, 184, 189].

Notably, in one study with 150 patients, none of the treating physicians had deployed the WEB prior to the study, though they received a training program. Occlusion status did not correlate with clinician experience, though adverse events correlated with IA sac size (>= 8 mm) and clinician experience (1-3 procedures more adverse events than 4-6 than >6) [79].

One systematic review noted a learning curve where morbidity decreased from 5% to 1% from data before and after 2013, and thromboembolic complication was 10% before and 6% after 2013 [151].

ADVANTAGES OF THE WEB The WEB does not necessitate DAPT, making it viable for treatment of ruptured IAs [151]. One study with 60 treated patients found a rebleeding rate of 0% [218] of ruptured IAs treated with the WEB, in comparison to rebleeding rates of 1.9% for IAs treated with coils [168].

COMPLICATIONS WITH THE WEB The most common complications of the generally safe WEB treatment are thromboembolic with 6% [151], with the following factors lowering complication risk and raising the chance for complete occlusion: anterior circulation, neither narrow nor wide neck, and use of newer generation WEB [256]. Studies about the WEB report no to few adverse events after one year, in contrast to studies about FDs [22, 52, 100, 155, 189]. The ARETA coiling study reported a 29.5% recanalization rate for coiled IAs [186]. FDs are still seen as the most efficacious treatment, however, with complete occlusion of 95.2% and adequate occlusion of 96.8% [19], despite their higher complication rates than the WEB's [189].

COMPRESSION PHENOMENON Some studies mention the compression phenomenon, where the WEB shrinks over time, in 24% to 65% of cases [30, 40, 61, 108]. The exact reason for this compression is not clear, but it may be related to arterial blood pressure called the water-hammer effect, or retraction of the WEB due to clot formation [29, 40, 108]. Some studies attribute lower occlusion rates to WEB compression and shape change, and while adequate occlusion rates do not seem to be affected, complete occlusion rates were statistically significantly lower in cases with compression than in cases without (25.0% versus 76.9%) [61, 108]. These results could not be confirmed in other studies, though [40]. Notably, there are a lot of studies that do not report any compression phenomenon [30, 184, 189].

WEB SIZING While oversizing the WEB is recommended, there can be complications due to misplacement, sizing and touching of the IA dome [63, 95]. Nawka et al. [174] assessed IA morphology and occlusion rates, and found no association between sizing (correct sizing, under- and oversizing) and occlusion, thus questioning the importance of oversizing. They also noted average diameters as being superior to single measurements of length, as they found an association between small differences of WEB width and average aneurysm neck diameter [174].

# 2.5.2 The Contour Neurovascular System

The Contour Neurovascular System (CNS; Stryker, Kalamazoo, MI, USA) is a relatively new flow diverter meant to specifically tackle the challenge of treating WNBAs. It achieved FDA Breakthrough Device designation in 2021 [105]. It is a dual-layer mesh made from 144 nitinol wires that unfolds to sit directly in the aneurysm neck, where it diverts and disrupts blood flow into the aneurysm sac (see Figure 2.8 and Figure 2.9). It comes in five sizes and can treat aneurysms sized between 2 and 10.5 mm (see Table 2.2.).

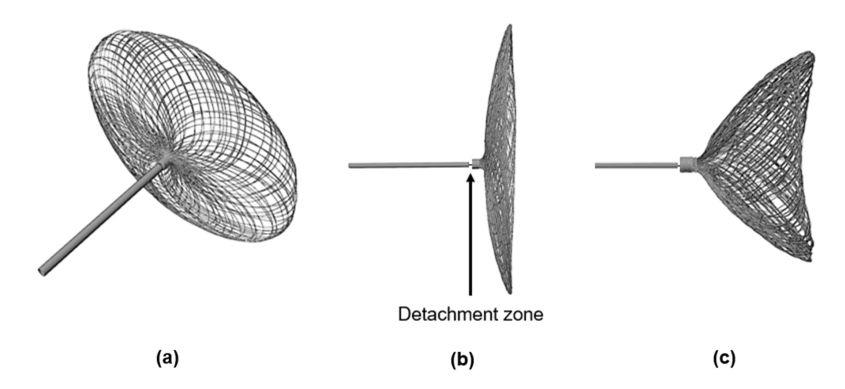


Figure 2.8: The CNS unfolded (a), proximum platinum radiopaque marker connected to wire (b), and adapted to inside of aneurysm (c). Image from Lyu et al. [152] and available under a CC BY 4.0 license. No changes were made.

Table 2.2: Available CNS sizes	and their	sizing	recommendations,	as	provided	by	Stryker
(Stryker, Kalamazoo,	MI, USA).						

Product number	Microcatheter	Device	Maximum	Maximum
		diameter	aneurysm	aneurysm
			width	neck
CNS21005-15	0.021"	5.0 mm	2.0-3.5 mm	2.0-3.0 mm
CNS21007-15	0.021"	7.0 mm	3.0-5.5 mm	3.0-5.0 mm
CNS21009-15	0.021"	9.0 mm	5.0-7.5 mm	4.0-6.0 mm
CNS011-15	0.027"	11.0 mm	7.0-8.5 mm	5.0-8.0 mm
CNS014-15	0.027"	14.0 mm	8.0-10.5 mm	7.0-10.0 mm

RESULTS OF CNS TREATMENT Due to the novelty of the CNS, long-term effects and safety are still being assessed, but results so far have been promising. There is currently one meta-analysis and review [95] and its update [117] with retrospective analysis of

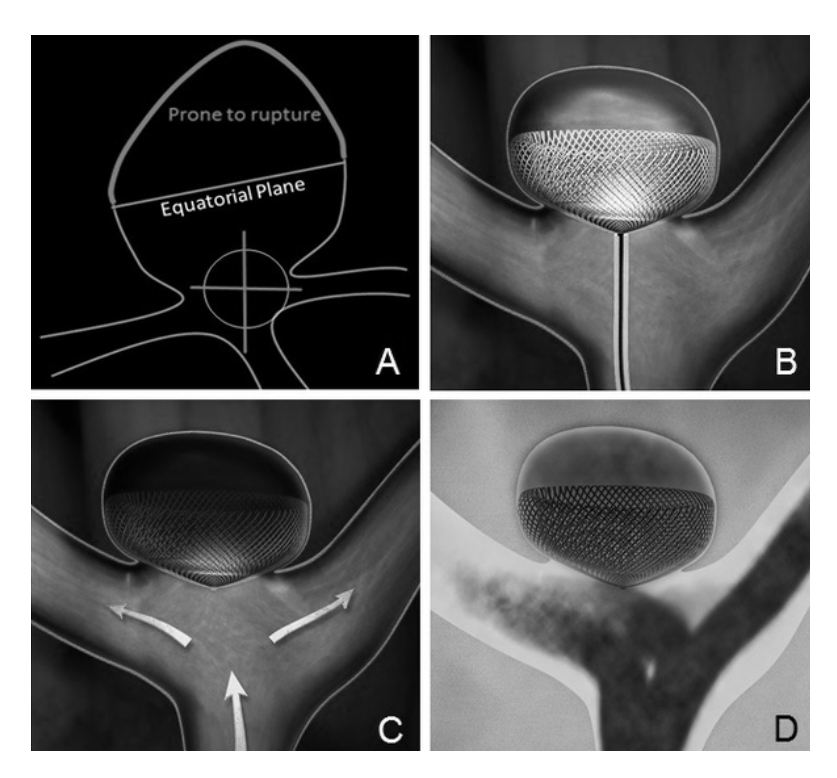


Figure 2.9: Illustrated Examples of how the CNS sits in an IA. A) Target zone of the CNS, B) deployed CNS with catheter, C) schematic flow diversion of deployed CNS, D) angiographic view. Image from Akhunbay-Fudge et al. [4] and available under a CC BY 4.0 license. No changes were made.

206 IAs, and one multi-center study [99] with 279 treated IAs, which comprise the most comprehensive analyses of the efficacy and safety of the CNS. Many smaller reports on singular and small number of treated cases exist.

The adequate occlusion in the reviews ranges from 85% [117] to 91.5% [99], with other studies finding similar results [4, 33, 105, 144, 169, 252]. Adequate occlusion rate generally seems to grow over time, as multiple studies showed rising occlusion rates over the course of multiple follow-up scans [4, 33, 90, 105]. Hecker et al. [105] observed 40 IAs and report 87.5% adequate occlusion at 6 months, 87.5% at 12 months, and 90% at last follow-up. Gallo-Pineda et al. [90], who observed a total of 25 IAs treated with CNS, reported 41.6% adequate occlusion at the initial postprocedural scan, 58.3% at the 6-month follow-up, and 65.5% after one year.

Retreatment rates in the mentioned studies ranged from 2.5 to 3.16% [95, 99, 105]. In the reviews and multi-center studies, complications rates were 4.7 and 7.2% [95, 99].

Flow assessment studies are rare at this point in time. A first in vitro and in silico study done by Korte et al. [133] compared 14 combinations of IA models at the basilar tip with and without CNS in different sizes and positions. It found that the CNS significantly reduced flow velocity inside the IA sac by 67% and time-averaged wall shear

stress (WSS) by 87%, as well as reductions of the neck inflow rate, kinetic energy and inflow concentration index. Another study by Lyu et al. [152] found an average inflow reduction ability of 91%.

While long-term effects remain to be seen, in the studies done so far, the CNS appears to be stable over the time observed [4, 33, 63]. One study [90] found complete coverage of the IA neck with the CNS to be helpful for full occlusion, as without full coverage of the neck they observed reperfusion. Branches directly located at the IA neck further complicated successful treatment.

A detailed analysis of how the CNS affects IA morphology has not yet been done. One study found a correlation between pre-treatment IA height and occlusion, however, due to interactions with the age distribution on the cohort, it was ultimately concluded that there is no correlation with rupture state or morphology [99]. This study did however not assess morphology after CNS deployment or deformation over time. Further, no study has yet analyzed if there is any deformation of the CNS itself. This raises RQ 2: how can longitudinal morphological deformation be analyzed?

TREATMENT OF RUPTURED INTRACRANIAL ANEURYSMS The CNS can be used to treat both ruptured [72, 101, 105, 252] and unruptured IAs [4, 29, 72, 144].

One study examined 25 IAs [90], of which 15 (65.5%) had an adequate occlusion one year after treatment. Three patients experienced device displacement during the procedure and five as a late complication, while three patients had to be retreated using stenting, coiling or a flow diverter. Of those 25 aneurysms, three were ruptured and the CNS was deployed as a scaffold for assisted coiling.

Another study [252] reported on 18 ruptured cases from their 55 treated IAs, were 17 reached full occlusion despite complications in four cases. Five cases received additional coiling.

13 ruptured IAs were treated in another study [63] with the CNS as primary device. Two IAs required additional coiling, but there were no procedural complications, and all IAs showed adequate occlusion at three-month follow-up.

Griessenauer et al. [99] also reported on 31 ruptured IAs. They found no correlation between CNS treatment outcome with rupture. Adequate occlusion was achieved in 91% of ruptured cases, as compared to an overall adequate occlusion of 91.5% for all 279 cases. Thromboembolic and hemorrhagic complication rates were 16% and 3.2%, respectively, for ruptured, and 6.8% and 0.4% for all IAs.

Therefore, ruptured IAs treated with the CNS show more complications during the procedure, but similar occlusion rates.

COMBINED AND OTHER USES Despite being intended as a single device [4, 29, 169], the CNS can be used together with other devices such as coils or stents [72, 105, 252]. In case of coils, some studies say there is little difference in outcome with or without coils [95], while other studies use coils in combination with CNS to specifically

prevent recurrence [45] or accelerate thrombus formation and stabilize the CNS [253], particularly in cases of complex neck morphology. Stents are generally used in cases of failed CNS [105, 206].

The CNS was originally derived for the treatment of WNBAs, however, a recent study also demonstrates its feasibility for narrow-necked aneurysms, meaning IAs with a high dome-to-neck ratio [169].

ADVANTAGES OF THE CNS The CNS shares multiple advantages with other IFDs like the WEB, which are both single- or double-layered meshes made from braided nitinol wires that are deployed via a microcatheter and sit in the IA neck to disrupt flow into the IA sack. Both are single devices that are easily deployed and electrolytically detachable from their delivery system. They are meant to treat the same size of challenging WNBAs, need no DAPT, and both are unsuitable for MRA for follow-up scans due to the artifacts of their radiopaque markers [105].

The CNS does however have advantages over the WEB. As it is not a volumetric device, it does not touch the potentially fragile IA dome [4, 105, 144]. It can also be used for coil jailing [90, 253].

Instead, the CNS further is considered easy to size, as only the size of the neck of the IA is necessary to know [4, 33, 63, 101, 105, 144, 206] and can be used for asymmetric deployment [243].

Some studies have directly compared the CNS against the WEB or other devices and found it to be faster to deploy and thus take less intervention time [101, 105, 169]. This time advantage was observed even in a study where the interventional team had no previous experience with the CNS [101]. While that particular study observed no learning curve in regard to time, other studies report a learning curve that is comparable to that reported in the early days of the WEB [95]. The CNS also had a smaller radiation dose, and fewer intra-procedural device changes [101, 169]. An in silico study found that while all IFDs lead to an effective reduction of the rupture risk, the CNS leads to more flow reduction and less child vessel occlusion than other IFDs [152]. Disadvantages of the WEB, like migration and compression phenomenon, meaning shrinking over time, have no yet been described in any CNS study [105]. However, no study has done a comprehensive analysis of CNS shape after deployment yet, a research gap this thesis looks to fill.

#### 2.6 ANEURYSM RUPTURE RISK PREDICTION

Rupture risk prediction is an important aspect of the decision of how to treat an unruptured aneurysm. Due to the high fatality and little chance of a positive SAH outcome, prevention of rupture is of highest priority. However, the low rate of rupture and the risk of an intervention has to be weighed against the risk of rupture. An accurate assessment of the rupture risk is thus important [96, 120].

The treatment decision should always be individually tailored to an aneurysm, as endovascular and surgical interventions always bear risks, including rupture [71]. An over-treatment of IAs should also be avoided, however, so patients with a high risk of rupture where treatment prevents a rupture need to be identified [41]. Meanwhile, the knowledge of having an unruptured IA is also a mental burden for patients, and correct rupture risk prediction can aid in patient education and lower the fear of rupture [240].

Multiple factors influence IA rupture, including metadata, IA morphology, and hemodynamics.

#### 2.6.1 Metadata

Metadata, also called clinical parameters, cover patient-specific factors or clinical data relating to the patient or IA. Many of these were already mentioned in Section 2.3.1. Important metadata include:

- Location: IAs in the posterior circulation are thought to have a higher rupture risk, as well as IAs at the AComA, particularly small ones [69, 240, 250].
- Age: higher ages have a higher risk [66, 240, 250].
- Sex: women have a higher risk [66, 240, 250].
- Ethnicity: people with Finnish or Japanese heritage have a higher risk [240, 250].
- Smoking: heightens risk [2, 120, 240].
- Hypertension: heightens risk. Patients with unruptured IAs were found to be more likely to be taking antihypertensive medication [2, 120, 240].
- Family history: patients with a family history of IAs seem to experience rupture at a younger age and smaller size [240].
- Presence of blebs: outpouchings on the IA sac, also called daughter-aneurysms [240].

#### 2.6.2 *Morphology*

Morphology assesses the size and shape of IAs. Size is often simply referring to general maximum diameter measured on the imaging scans, dividing IAs into small (<7 mm), large (>7 mm), and giant (>25 mm). The exact cutoff values are debated in literature, some studies list the cutoff between small and large IAs as 10 mm [36]. Large size is generally seen as risk factor for rupture, though based on location, even small IAs are said to be high risk, causing size alone to be seen as an outdated risk factor [240].

Shape can be simplified as regular and irregular, the latter being defined by blebs or sac wall protrusions [16]. Irregular shape and blebs are both rupture risk factors.

There is a variety of morphological parameters that assess size and shape in great detail. They utilize both the entire IA sac and surrounding vasculature, but also abstractions, such as the neck curve, which separates the parent vessel from the IA sack, the ostium, which is the surface made by the neck curve, the convex hull (CH) of the IA sac, or the centerline of the parent vessel.

Some of the most important morphological parameters include:

- Size: maximum distance between dome and neck perpendicular to neck plane [69].
- Aspect ratio (AR): ratio between maximum height to average neck diameter. High AR indicates higher risk, though exact threshold differs in literature [2, 69, 172].
- Size ratio: ratio between maximum IA diameter to parent vessel diameter. Higher size ratio indicates higher risk [2, 69, 120].
- Undulation index (UI): measures concavity of the surface of the IA sac via volume (V) of the sac and volume of the IA sac convex hull (V<sub>CH</sub>). Higher UI indicates higher risk. Calculated via: 1 \frac{V}{V\_{CH}} [69, 196].
- Ellipticity index (EI): measures IA elongation by comparing the CH of the IA sac to a perfect hemisphere. Calculated with  $V_{CH}$  and surface area of the CH ( $S_{CH}$ ):  $1-(18\pi)^{1/3}\frac{V_{CH}}{S_{CH}}$  [69].
- Non-sphericity index (NSI): combines EI with UI, by utilizing IA sac measurements instead of CH measurements, therefore also factoring in concavity:  $1 (18\pi)^{1/3} \frac{V^{2/3}}{S}$  [69, 196].
- Vessel angle: angle between neck plane and parent vessel centerline [69, 196].
- Aneurysm inclination angle: angle between neck plane and IA inclination determined by the line from neck plane centroid to max distance dome point [69].

Variations on the measurements and parameters exist, some of them are illustrated in Figure 2.10.

Aneurysm growth, meaning a change in size, is generally thought to be an indicator of impending rupture. Growth itself also has risk factors. Metadata relevant for IA growth are sex (female), hypertension, smoking, multiple IAs, and IA location (posterior circulation), while morphological parameters include irregular shape and large size. IA growth is generally sporadic, non-linear, and unpredictable, though periods of stability are more common [240]. The ELAPSS score can be used to predict IA growth, as it rates easily checked risk factors such as Earlier SAH, Location, Age, Population and simple morphology like Size and regularity of Shape [16].

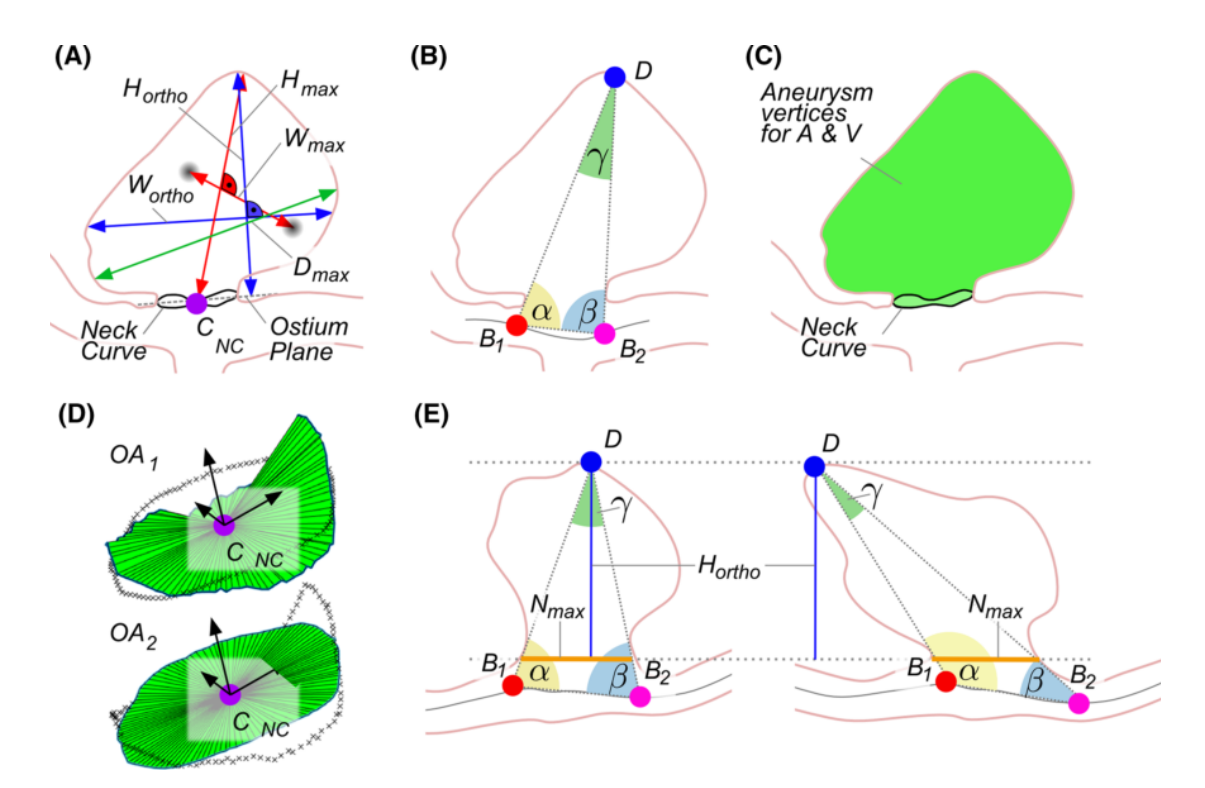


Figure 2.10: Illustration of a variety of morphological parameters and how they are measured. A) orthogonal and maximum height ( $H_{ortho}$  and  $H_{max}$ ) and width ( $W_{ortho}$  and  $W_{max}$ ), and maximum diameter ( $D_{max}$ ). B) angles  $\alpha$ ,  $\beta$  and  $\gamma$  between base points  $B_1$ ,  $B_2$  and dome point D. C) neck curve (NC) and aneurysm volume (V) and area (A) in green. D) Ostium area surface ( $C_{NC}$ ) for reconstructed ( $OA_1$ ) and projected ostium ( $OA_2$ ). E) Angle parameters account for tilting of and IA, showing two IAs with identical AR (here based on  $H_{ortho}$  and maximum neck diameter ( $N_{max}$ ) but different angles). Image from Saalfeld et al. [209], reproduced with permission from Springer Nature.

#### 2.6.3 Hemodynamics

Hemodynamics measure blood flow within the IA and parent vessels. Morphology is thought to affect hemodynamics, though as hemodynamic parameters also play a role in rupture risk and IA formation, they might in turn also affect morphology [36].

Important hemodynamic parameters for the determination of rupture risk include:

- Impact force: measures force acting perpendicular to the vessel wall [36].
- Wall shear stress (WSS): measures force acting parallel to the vessel wall. High WSS is associated with IA formation as it may lead to vessel deterioration, while low WSS is associated with rupture due to thrombus formation [41, 66, 120].

- Low shear area (LSA): area on the IA wall with low WSS, high LSA means higher risk [41, 120, 254].
- Oscillatory shear index (OSI): measures temporal variations in the direction of blood flow and magnitude of WSS fluctuation. High OSI indicated rupture risk [66, 120].

Many further hemodynamic parameters exist. Generally, unstable flow patterns as well as high, concentrated pressure inside the IA sac are seen rupture risk factors [36, 69].

#### 2.6.4 Scores

Just as the ELAPSS score presents a simple scoring for IA growth, scores for rupture risk assessment exist. Their aim is to compress the wide variety of features and risk factors down to a few measurable ones. The most commonly known is the PHASES score. It assesses the 5-year rupture risk by looking at Population (Japanese or Finnish), Hypertension, Age, Size of IA, Earlier SAH, and Site of IA [2, 17]. A critique of the PHASES score is its heavy weighting of IA size [2, 178, 240].

The UIA treatment score, in comparison to the PHASES score, is not based on the pooled analysis of prospective cohort studies but instead is based on expert opinions. As such, it reflects how experts would treat a patient with an unruptured IA [240].

The Triple-S risk prediction model assesses rupture risk after growth was observed by assessing location (Site), Size, and Shape [124].

#### 2.7 MEDICAL BACKGROUND SUMMARY

Here are the main takeaways from the medical background:

- The neurovasculature, at the center of which is the circle of Willis (CoW) supplies the brain with blood. Disruptions to that blood flow through neurovascular pathologies often end in strokes and death.
- Diagnosis, research, and treatment benefit from segmentation and extraction of 3D models of the vasculature. They further benefit from the combination of information of multiple modalities, which can be achieved with co-registration, that transforms one scan to align with the other.
- Intracranial aneurysms (IAs) are dilations of the intracranial vessel walls. Most are asymptomatic and discovered incidentally, but their rupture, though rare, is often fatal. Rupture risk assessment and how to decide the best treatment strategy for the best outcome are active research fields, as more and more IAs are treated.

- A large number of parameters exist to assess IA rupture risk and treatment decision, divided into clinical metadata (about the patient), morphological parameters (IA shape and size), and hemodynamics (blood flow in the IA). Keeping an overview of all the parameters, and deciding on which ones are the most relevant to guide treatment and diagnosis, is a challenge for clinicians.
- The Contour neurovascular system (CNS) is a novel implant for hard-to-treat wide-necked bifurcation aneurysms (WNBAs). Outcomes of the CNS are promising, but no study has yet assessed if and how it deforms after deployment over time.

# Part II PREPROCESSING OF NEUROVASCULAR STRUCTURES

As technology advances, imaging scans get more and more detailed, revealing a better view inside the human body and its functions. However, with more details, the process of identifying and isolating relevant structures within these images and extracting their models, called segmentation, becomes more sophisticated as well.

The segmentation and 3D reconstruction of blood vessels and extraction of their morphological features is important in medical image analysis for diagnosis, therapy planning, and clinical outcome assessment [3, 166, 237]. It is a crucial step for vessel analysis, as it enables the extraction of a 3D model of the vessels and of morphological features, including centerlines, furcations, or diameters, as well as the identification of pathologies of stenoses, aneurysms, and more [3, 237, 242].

As segmentation is an integral preprocessing step for morphological analysis, we needed an in-house segmentation to analyze the intracranial vasculature and answer the RQs. This chapter will give a brief overview of segmentation techniques and the segmentation pipeline used for most projects.

#### 3.1 TECHNICAL BACKGROUND ON VESSEL SEGMENTATION

The challenge of vessel segmentation arises from the complexities of the intracranial vasculature, multiple branchings, and small details, as well as imaging noise, artifacts, and lack of contrast and resolution [3, 97]. Insufficient resolution and other imaging factors can lead to the fusing of small, separate vessels into one bigger vessel in the segmentation [3]. Similarly, overlapping structures, in combination with low contrast and noise, make it difficult to separate the vessels from the surrounding structures, requiring multi-scale approaches [3, 24]. Since intracranial vasculature varies in diameter, one method often does not work for all vessels, making it necessary for a segmentation to scale accordingly [3]. The addition of pathologies and their changes to the vasculature can further complicate segmentation [166].

Vessel segmentation methods can be divided into four categories:

- Region-based: Divide the image into different areas based on voxel properties.
   Methods include region-growing, watershed, and threshold-based methods [3, 229].
- Active contour-based: Utilize curves or surfaces that deform based on energyminimizing terms and connective properties. Methods include parametric mod-

els, models that utilize edges and statistical homogeneity in the image values, and geometric models based on level sets that can use topology [3, 97, 166].

- Statistical-based: Classify voxels as belonging to vessels or other classes based on homogeneity and material properties. Methods include the Expectation Maximization algorithm and intensity-based approaches like Particle Swarm Optimization [3, 97].
- Hybrid: Combine two or more segmentation techniques [3].

Deep learning (DL) is a technique to automatically extracts structures from high-dimensional data by utilizing multiple processing layers, each of which adds a new level of abstraction, similar to multi-scale approaches. Other than machine learning, it does not require manual feature extraction but instead uses a training stage to automatically identify features in the data [137]. While many DL segmentation models exist, they necessitate a large amount of annotated and pre-segmented data to train the models [97, 242]. DL reaches high segmentation accuracy, but may miss small details [111], making it not ideal for the presented use-case of small vessel segmentation. Due to this use case, lack of access to the necessary amount of annotated data and data and class imbalance, meaning unequal amounts of healthy and pathologic patients, as well as imbalance in recorded features and classes, combined with the variety of different modalities used, are the reasons why no DL methods were used for the segmentation tasks, and others, in this thesis.

Regardless of segmentation method, many images require preprocessing to increase the quality of the subsequent segmentation. Common preprocessing steps for the segmentation of intracranial vasculature include, but are not limited to:

- Noise reduction: can be done via conventional filters like the median or low-pass filter, as well as via adaptive filters, or filters that highlight tubular structures like the Hessian- or Frangi-filters and their extensions [3, 84, 97, 123].
- Contrast enhancement: for better contrast between vessels and the surrounding structures [3, 97].
- Brain stripping: removes the skull from the imaging scans [3, 97].

The choice of preprocessing steps and methods is highly dependent on the given modality and its specific parameters, as well as the requirements and desired results of the segmentation.

Similarly, postprocessing is a common and often necessary step for vessel segmentation. It refines and improves the segmentation as well as preparing the extracted model for subsequent steps. Typical postprocessing steps include (some depicted in Figure 3.1):

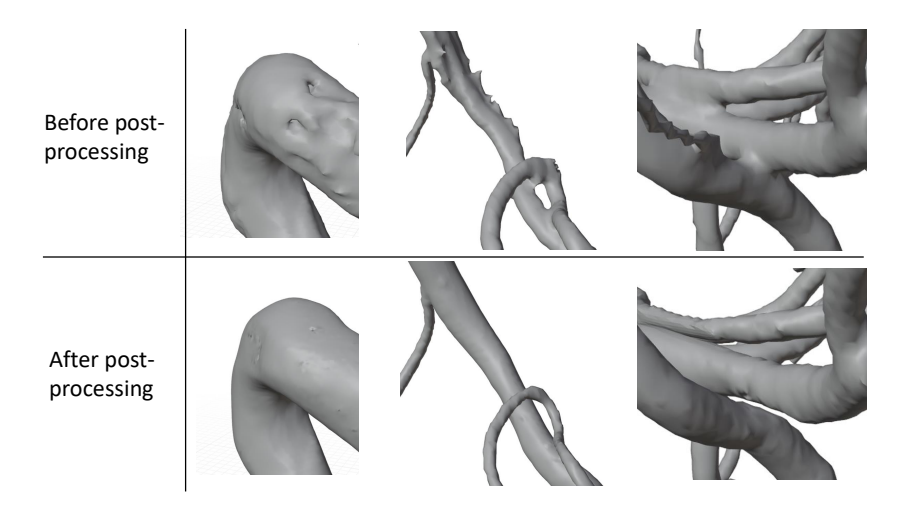


Figure 3.1: Examples of postprocessing, including smoothing, removal of holes in the vessel lumen, and separating fused vessels. Own figure.

- Smoothing: The surface of the vessel segmentation may include bumps or spikes, which require smoothing. While filters like, e.g., Laplacian-Kernel or Gauss-Filter, exist, they may remove small vessels or destroy connectivity. Instead, other methods utilize convolution surfaces to reconstruct the vasculature from a skeleton and vessel radius or reconstruct the vessel model with MPU implicits [181, 213].
- Removal of false positives: Small areas close to the vessel boundaries may be wrongly included in the segmentation and require removal [166].
- Connecting severed vessels: Vessels may be fragmented or broken during the segmentation process and require reconnection to reinstate continuity [166].
- Removal of holes: The segmentation may cause holes or hollow spaces within the vessels that disrupt the vessel lumen. These require filling or removal [97].
- Separating fused vessels: Small overlapping vessels may be segmented as one vessel and require separation.

Most of the postprocessing steps aid in reestablishing the topological structure of the complex vasculature to remain true to the patient anatomy, as well as to prepare for following analysis steps. It is not uncommon to require manual corrections, particularly for complex structures such as the CoW [3, 97, 166, 209].

#### 3.2 SEGMENTATION PIPELINE

7 T TOF-MRI is a state-of-the-art imaging method, though it is not part of clinical routine yet. It yields high-resolution scans that can show even very small vessels with a

### Publication

Section 3.2 is based on:

[220] L. Spitz, M. Allgaier, and A. Mpotsaris, D. Behme, B. Preim, and S. Saalfeld. "Segmentation of Circle of Willis from 7T TOF-MRI data and immersive exploration using VR." In: Curr Dir Biomed Eng 8.1 (2022), 129-132. doi: 10.1515/cdbme-2022-0033. The segmentation was conceptualized and implemented by L. Spitz.

diameter of 40 µm [249]. Such small vessels are important for the exploration of various pathologies, including ones that still need more research to be understood, such as CSVD [249]. Further, a segmentation of small vessels is important, as complexity of the vessel model affects blood flow [88]. We therefore present a segmentation pipeline for a detailed model of the CoW (see Figure 3.2). As per Hsu et al. [111]'s taxonomy, use raw input data, our task is to accurately segment the vessel for a subsequent quantification, though this quantification is not part of the pipeline. For this, we combine approaches for volumetric data including surface mesh generation and surface mesh methods, which are best for later morphological analysis [111].

We worked with volunteer data which was obtained with a 7T whole-body MRI system (Siemens Healthineers, Erlangen, Germany) with a 32-channel head coil (Nova Medical, Wilmington, MA, USA). The parameters were set for high-resolution angiograms, yielding a final resolution voxel size ranging from 0.26 mm to 0.39 mm.

#### 3.2.1 Preprocessing

To prepare for vessel segmentation and get rid of surrounding tissue, the MRI DICOM files were loaded into MeVisLab 3.4.2 [201]. After adjusting page size for faster handling, a vesselness filter was applied to highlight both larger and smaller vessels. To account for the extreme variations of vessel size, we tested different filtering strategies. Although a vesselness filter with six scales ( $\sigma$ ={1, 2,..., 6}) yields best results, we combined the resulting image again with a filtered image focusing on small vessels ( $\sigma$ ={1, 1.5}, 2 scales) and with a filtered image focusing on large vessels ( $\sigma$ ={6}, 1 scale).

Next, a mask was created. The highlighted vessels were segmented with region growing, and a convex hull and dilation were applied to the result. This mask was then saved and applied to the vessel image again.

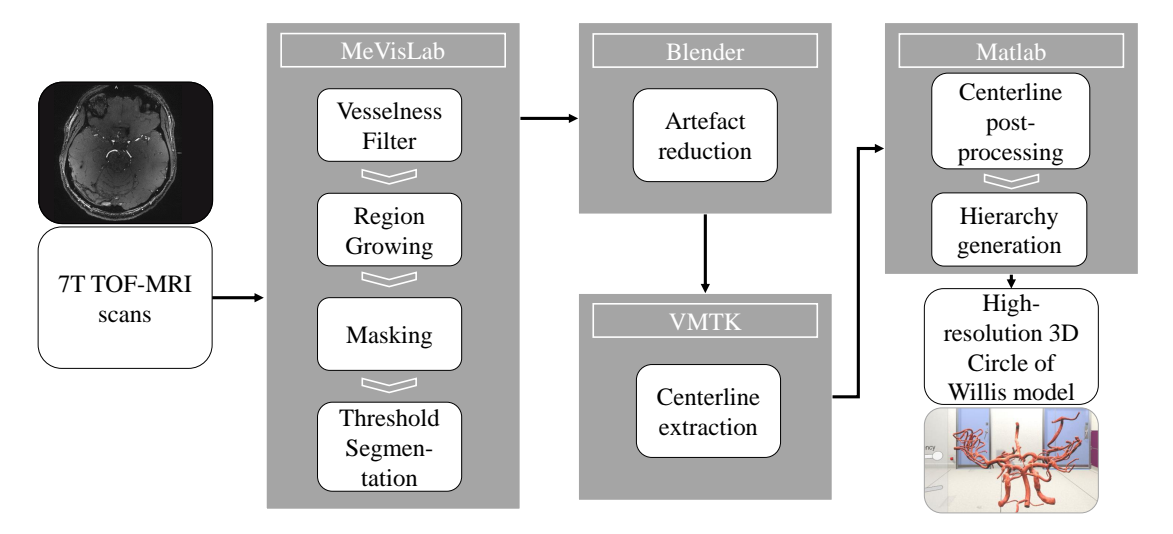


Figure 3.2: The segmentation pipeline from the imaging scans to the segmented CoW model, including centerline. Image from **Spitz** et al. [220] and available under a CC BY 4.0 license. No changes were made.

#### 3.2.2 Mesh extraction and postprocessing

The background filtered image was then loaded into our in-house software MERCIA, where mesh extraction is carried out as described by Saalfeld et al. [208, 209]. There, a threshold-based segmentation on the background-filtered image is followed by region growing and connected component analysis to extract the CoW. Special attention was paid to segmenting the PComA in its entirety, as it is a small vessel important in the CoW.

The resulting segmentation was then postprocessed by manual editing in Blender 2.93.4 (The Blender Foundation, Amsterdam, Netherlands) to account for vessel fusion, staircase, and noise bleeding artifacts from the region growing [208]. Additionally, the periphery was trimmed, and inlets and outlets were cut to be approximately perpendicular to the vessel centerline. Finally, the mesh was smoothed manually in Blender's sculpting workspace.

#### 3.2.3 Centerline extraction

To prepare for centerline extraction, the CoW's complex 3D model was split at the AComA and PComAs into three vessel trees to eliminate cycles. The centerline was then extracted for each of the three subtrees with the Vascular Modelling Toolkit (VMTK) 1.4.0 [10]. The resulting .vtp file was converted into .vtk in Paraview v4.2 (Kitware Inc. and Los Alamos National Laboratory). The .vtk file saves the centerline points, as well

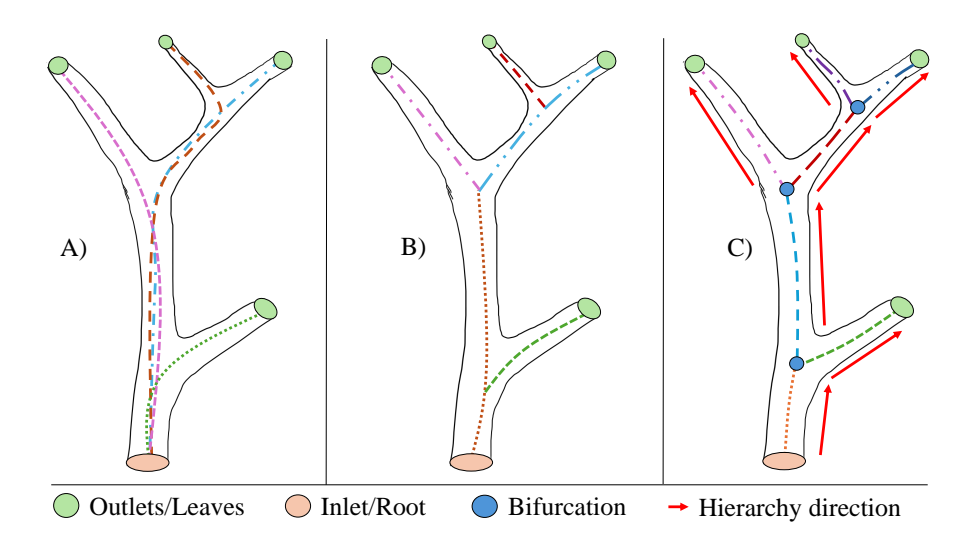


Figure 3.3: Centerline processing: A) initial centerline going from all outlets to the inlet. B) centerline after first preprocessing, splitting it into segments based on distance. C) final centerline with segments between bifurcations and hierarchy from inlet/root to outlets/leaves. Red arrows indicate hierarchy. Colors of centerlines only indicate different segments. Own figure.

as which point is part of which segment, and the maximum inscribed sphere radius for each point.

Matlab R2021a (The MathWorks Inc., Natick, MA, USA) was used to further work with the centerline. VMTK extracts the centerline going from outlet to inlet, meaning each segment ends in the inlet (Figure 3.3 A). We algorithmically adjusted number and length of the segments so that there is only one segment between two furcations or inlet/outlet. Further postprocessing included cleaning up the way segments meet at furcations, deleting wrongly detected segments, and deleting points with less than 0.1 mm between them as well as unused points. Unused points refer to points that are not part of any segment (Figure 3.3 B and C).

The hierarchy between the segments was determined, meaning each segment (except the root segment) was assigned a parent vessel. Child vessels were assigned for all non-leaf segments similar to Saalfeld et al.'s [207] flow-splitting approach. Hierarchy direction goes from inlet to outlets, thus following the vessel tree from root to leaves. This included recombining the three subtrees into one tree again. Here, the hierarchy direction from root to leaves was followed (Figure 3.3 C).

#### 3.2.4 Outcome

The segmentation was evaluated qualitatively with two experienced neuroradiologists and the think-aloud method [82].A quantitative evaluation was not possible as there is no gold standard.

The experts rated the segmentation as realistic and more detailed than other models they previously had access to. They noted that a high-resolution CoW that includes centerlines and hierarchies is useful, e.g., for computational fluid dynamics (CFD), possibly in combination with a prior phase-contrast MRI scan registration. This can help explore hemodynamic parameters and blood flow in patient-specific intracranial vasculature.

In terms of drawbacks, our pipeline relies on user experience, both with CoW anatomy and the four different tools used. Especially the step in Blender requires time-intensive manual work. A streamlined and more automatic approach integrating these programs into a single framework would be desirable.

While the introduced pipeline was developed for 7T TOF-MRI, it can be easily adapted for other modalities. The adaptation is possible by adjusting the parameters of the preprocessing, and the manual steps can easily be tailored to the individual segmentation and dataset.

#### 3.3 CONCLUSION ON VESSEL SEGMENTATION

The segmentation of vascular structures in a complex problem, especially when the goal is a high-quality 3D model of the vasculature for subsequent morphological analysis or blood flow simulations. An automatic segmentation for every modality is beyond the scope of this thesis, so it presents the introduced pipeline with its largely manual postprocessing to gain the best results for the different analysis tasks.

In the future, the pipeline can be automatized and extended in different ways. DL support is feasible, as well as more automatization in the postprocessing steps, and a combination of centerline extraction and other steps into one software rather than several ones.

In the previous chapter, the creation of a single segmentation was described. In clinical research and practice, multimodal image data or different sequences are required for diagnosis and research. One such scenario is the analysis of cerebral blood vessels based on PC-MRI and TOF-MRI. While PC-MRI contains valuable information about blood flow within the scanned volume, it is limited in resolution [104, 228]. In contrast, TOF-MRI can be of high resolution when scanned with a 7T MR scanner and can yield a highly detailed 3D vessel model [104, 249]. Combining two such images of a patient to make them comparable enables access to PC-MRI's hemodynamic information within the high-resolution TOF-MRI model.

Small vessels only visible in higher resolutions are of interest for medical research, e.g., in the case of CSVD, treatment of IAs, and explorations of neurovascular implants. Visible small vessels enable the extraction of more detailed morphology, enabling a more detailed analysis. To briefly recap Section 2.2, CSVD is tied to Alzheimer's disease, but their exact connection is an active research field with many open questions remaining [215, 249].



Figure 4.1: Segmented CoW and surrounding vasculature of the same volunteer acquired from TOF-MRI (left) and PC-MRI (right). Image from **Spitz** et al. [219, 221] and available under a CC BY 4.0 license. No changes were made.

PC-MRI data provides blood flow measurements that CFD simulations can utilize, enabling an in-depth analysis of shear stress and pressure values. For these simulations to be as realistic as possible, patient-specific boundary conditions and a 3D model of the patient's vessel morphology is needed [26, 46]. PC-MRI offers such patient-specific

conditions, but their resolution is not sufficient to detect small vessels [215]. TOF-MRI, however, can provide a detailed segmentation of even small vessels with a diameter of 40 µm [249]. Figure 4.1 illustrates the differences in the level of detail of segmentations from PC- and TOF-MRI.

Although both imaging techniques rely on MRI, artifacts occur, and the information from both modalities, even if from the same patient, cannot be simply combined for data assimilation [89]. This raises

RQ 1: How can information about vascular pathologies from these 7T MRI scans be combined?

We answer this RQ by presenting a sophisticated, specialized co-registration tailored to the two specified modalities and the neurovasculature [87].

# Publication

Chapter 4 is based on:

[221] L. Spitz, F. Gaidzik, D. Stucht, H. Mattern, B. Preim, and S. Saalfeld. "A hybrid hierarchical strategy for registration of 7T TOF-MRI to 7T PC-MRI intracranial vessel data." In: Int J Comput Assist Radiol Surg 18.1 (2023), 837–844. doi: 10.1007/s11548-023-02836-y,

which in turn is based on:

[219] L. Spitz, "Multi-modal co-registration of high-resolution 7T MRI vessel data." Masterthesis, Otto-von-Guericke University Madgeburg (2020).

Both works were conceptualized, designed, implemented and written by L. Spitz.

Co-registration, also called registration, is the process of spatially aligning two images to make them pixel-wise (or voxel-wise, in 3D cases) comparable by transforming one image (called the moving image) to the other (called the fixed image). This can also be done for more than two images. In a medical context, registration is needed to compare images from different patients, or images from the same patient taken at different time points, or with different modalities. Inter-patient registration can be used to create an atlas, while intra-patient registration is useful for movement artifact correction or medical research [103, 118, 121, 159]. Depending on the data and artifacts, co-registration can be error-prone and requires highly adapted algorithms that are specialized to their respective use-case, as no one approach fits all [167]. For simplicity, this thesis will keep referring to the objects that are being registered as images in the following.

#### 4.1 TECHNICAL BACKGROUND ON NEUROVASCULAR CO-REGISTRATION

When the registration is based on the images the RMSElves, meaning based on their voxel (or pixel) intensities, it is called image-based, intensity-based, or image-to-image registration [149, 159]. Registration can however also be done on segmentations, objects, landmarks, or other features derived from the images, in which case it is called feature-based or feature-to-feature registration [121, 159, 217]. Image-based registration is generally considered to have a high accuracy as it takes each pixel into account [161]. As they directly take the intensities of the image to register, they do not rely on feature extraction methods [159]. However, they can be cost-intensive, and in case of vascular registration, the vessel pixels only make out a small percentage of the entire image [159, 161]. For multimodal co-registration, meaning when registering images from multiple modalities, there may not be enough shared intensity information between the images [121]. Feature-based registration has the advantage of being more cost-efficient as it only relies on the extracted features rather than the entire image, meaning they can also focus on those extracted features, such as the vessel centerline, or bifurcations as landmarks [159, 161]. However, those features need to be extracted first, meaning additional image analysis which may need sophisticated methods to be precise and robust [167]. This means that the registration is only ever as good as its feature extraction [161, 217].

Intensity- and feature-based registration methods can also be combined into hybrid or *feature-to-image registration*, where, e.g., one image's features are registered to another image's intensities [159]. Hybrid registration thus combines the advantages and disadvantages of the two other types.

TRANSFORMATION The transformation that registers the moving image to the fixed image can be done in different ways. Traditionally, a transformation matrix can be used, in which case the transformation can be rigid or affine. A *rigid transformation* does not change the shape of the image and only uses rotation and translation, resulting in a four degrees of freedom (DOF) transformation in a three-dimensional space. An *affine transformation* adds scaling and shearing, thus altering the shape of the image and enabling a twelve DOF transformation [121, 149, 159]. Both rigid and affine transformations are generally used globally but can also be applied locally by only transforming selected regions [217].

Deformable registration instead allows for local deformations of the image or object shape. Local deformations are particularly important for medical registration, as patient movement, breathing, and surgical treatments can cause deformations in soft tissues and organs [13, 103]. Deformable registration can be facilitated through B-Splines or thin plate splines, which rely on manipulating the image through control points and by finding a surface that smoothly fits through given points, e.g. landmarks, respec-

tively [159, 203, 205]. Deformable registration is however computationally complex and difficult to validate [205, 217].

Because of this difficulty to validate, affine transformations are often used in registration [118]. While many changes in vessel data are non-rigid, they can be sufficiently approximated with local rigid transformations [13, 217]. For inter-subject applications, it is argued that higher-order deformable transformations are needed to resolve vascular registration problems [118, 205]. However, in this thesis, we register data from the same patient.

COST FUNCTION The best transformation for registration is usually found by optimizing (often minimizing) a *cost function*, also called metric, that calculates the dissimilarity between the moving and the fixed image. This cost function is dependent on what features or image properties the registration is based on [118, 159, 203]. As such, it can be based on voxel intensities, correlation, mutual information, sum of squared difference, or distance metrics, among many others [103, 118, 149, 159].

OPTIMIZATION An optimal result of the cost function thus identifies the best transformation for the best registration result. To find this best result, an *optimization* technique is employed. Most registration problems, particularly ones with local transformations, have multiple local optima that local optimization functions can get stuck in without identifying the global optimum [118]. Strategies like multi-scale, coarse-to-fine, or multi-start approaches all aim at finding the global optimum instead of converging at the first local one [14, 118]. The multi-scale approach, also called multi-resolution, starts the registration at a low resolution and gradually raises the resolution in subsequent registrations [167]. The coarse-to-fine approach similarly iteratively performs the optimization and refines the parameters of the registration in each step, e.g., DOF of the transformation, or sampling size, in each step [13, 121, 167]. The multi-start approach also repeats the registration multiple times, each time starting with different starting parameters for the cost function [159]. All these approaches also have benefits for runtime [118].

Many optimization strategies rely on the derivative of the cost function. As the calculation of the derivative may be computationally expensive or impossible, there are also derivative-free methods, like the established and commonly used Powell's method [149, 193]. It utilizes the concept of conjugate directions and is often extended with Brent's method, a 1D optimization strategy [159], and performs well in related algorithms [203]. DL methods are becoming more popular for the optimization step of registrations [103, 141]. However, a comparison of iterative optimization and DL reveals that they are highly competitive regarding runtime and accuracy. Iterative methods further perform better with respect to robustness and parameter changes without needing long supervised training procedures, and are not dependent on a large training set [103]. In the medical context, in particular, large training sets are often not

available and often unbalanced. This was also the case for this thesis, which was part of the decision as to why no DL method was pursued.

#### 4.2 A HYBRID APPROACH FOR CO-REGISTRATION OF NEUROVASCULATURE

In this thesis, we want to co-register vascular structures, specifically vessels of the entire CoW for research into CSVD by combining a high-resolution segmentation from TOF-MRI and the blood flow information from PC-MRI. Since vessels make up only a small part of the entire image, an image-to-image registration approach may focus on irrelevant information and may thus be error-prone [13, 49, 50]. Therefore, many vessel-focused strategies use vessel segmentations for feature-to-feature registration instead, and for our subsequent goal of blood flow simulation through data assimilation after registration, a segmentation of the detailed TOF-MRI data is provided. However, there is no fully automatic segmentation for PC-MRI data available, and even manual segmentation would not include relevant vessels as they are not visible in the image data. Further, there is no existing strategy for registering high-resolution 7T PC-MRI (voxel size 0.26-0.39 mm,) and TOF-MRI (voxel size 0.64-0.79 mm) data, raising RQ 1.

This thesis thus presents a hybrid approach for registration, meaning segmented vessels from TOF-MRI shall be registered to the image values of the pre-processed PC-MRI. In this work,

- we developed a co-registration for high-resolution 7T TOF-MRI to 7T PC-MRI intracranial vessel data,
- we implemented a hybrid hierarchical strategy based on centerline fit,
- our metric guides the registration with three components that consider a weighted sum of scaled intensities, a penalty based on gradients on the normal plane, and manually placed landmarks,
- during optimization, parameters are decoupled for local affine transformations, and
- we include a *representation* of the smallest vessels, which allows them to be registered despite not being recognizable within the PC-MRI data.

This can aid further exploration of blood flow in and morphological analysis of smaller vessels that can be critical to analyze for various neurological pathologies.

#### 4.3 RELATED WORK ON HYBRID NEUROVASCULAR CO-REGISTRATION

Hybrid co-registration that includes both feature- and image-based information has been used for co-registration of vessels for different modalities [159]. It combines the

benefits of and thus eliminates many of the drawbacks of both intensity- and feature-based registration. For example, it does not require as many expensive operations and feature storage [141]. They are also seen as more precise and robust and more flexible in terms of imaging modality [159].

In the area of 3D-2D registration, hybrid registration has been used by Rivest-Hénault et al. [203] and Liu et al. [149] for cardiac vessel registration. Rivest-Hénault et al. [203] extracted the 3D centerlines of the vasculature and registered them, augmenting the images during intervention in real time. Pre-processing included a vesselness filter before segmentation. For registration, a progressively refined affine transformation and a non-rigid method with thin plate splines were used [203]. Liu et al. [149] also extracted the centerlines and registered them to the 2D images of angiographic scans. They utilized the tree-like structure of the vasculature by matching corresponding bifurcations [149].

Other studies also employ the entire vessel graph. Aylward et al. [13] performed a centerline segmentation in one image to rigidly register to another image that required no segmentation. This hybrid approach works under the assumption that vessels in the second image are recognizable as intensity ridges, i.e., they exhibit a large gradient. When the two sets of data are registered, all centerline points lie within these ridges and a weighted sum of scaled intensities metric will be maximized. Results were found to be accurate and robust even for non-rigid deformations and only partial overlap of the images [13].

Other hybrid methods use hierarchical relationships between the vessels by considering the direction of blood flow and parent-child relations of branching vessels. Jomier and Aylward [121] registered centerlines to intensities hierarchically from root to leaf vessel segments. Furthermore, they use a coarse-to-fine approach and first apply a global rigid, then a local rigid, and finally a local non-rigid transformation. To guide the registration, the normal plane perpendicular to each centerline point is calculated, and the surrounding gradients within the vessel radius are projected on it. An iterative optimizer maximizes the intensity sum metric.

Given this precedent of hybrid co-registration of vascular structures, this thesis implemented a hybrid method for the new task of co-registering PC- and TOF-MRI.

#### 4.4 HYBRID CO-REGISTRATION METHOD FOR NEUROVASCULATURE

In the following we briefly describe our medical image data before explaining feature extraction and the developed hybrid co-registration method for PC- and TOF-MRI.

#### 4.4.1 Medical Image Data

A 7T whole-body MRI system (Siemens Healthineers, Erlangen, Germany) was utilized to acquire both sets of MRI data from volunteers. For TOF-MRI, the parameters were

set to obtain high-resolution angiograms, which yielded a voxel size ranging from 0.26-0.39 mm, while PC-MRI scans ranged from 0.64-0.79 mm. A spoiled gradient echo sequence that featured quantitative flow encoding in all three spatial dimensions was used [86, 157]. Each time frame had three maps as well as one magnitude image. The velocity encoding value varied among the datasets and was set accordingly to match the highest uniquely resolvable velocity that was assumed by the medical experts [157].

#### 4.4.2 Extraction of Vessels

Both sets of data underwent several pre-processing steps. The PC-MRI data were treated according to Bock et al. [35] and then combined into a single dataset by creating a temporal maximum intensity projection of the magnitude image.

TOF-MRI data were segmented according to Chapter 3, including the generation of centerlines. A graph including parent-child relationships was built, representing the vessel as a tree with root vessels (inlets) that branch out into leaves (outlets). These inherent hierarchical relations were later used for traversal in the optimization strategy.

As mentioned in Chapter 3, the CoW had to be split to eliminate cycles. This split was done at the PComA and AComAs.

#### 4.4.3 Hierarchical hybrid approach

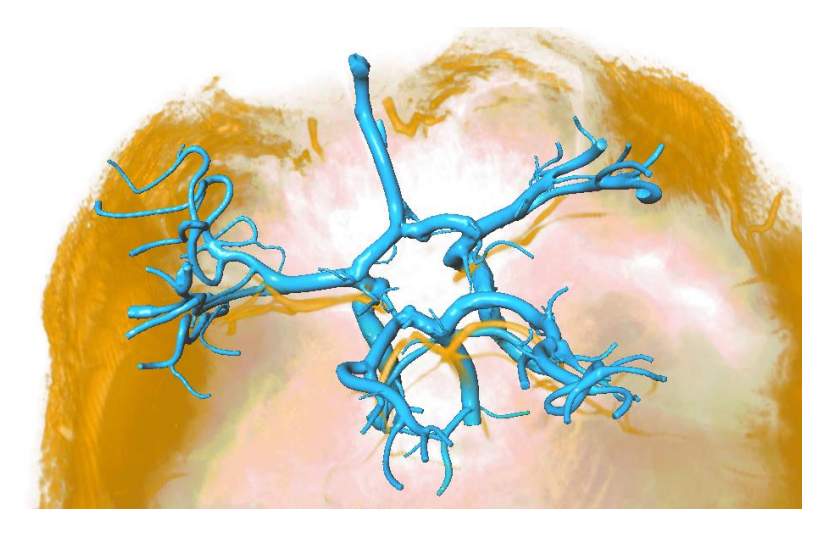


Figure 4.2: Illustration of differences of a patient's CoW for PC-MRI and TOF-MRI data. The segmented TOF data is depicted in blue, whereas PC-MRI data is depicted in orange (high intensities are drawn in orange to indicate the intensity ridges, low intensities are mapped transparently). Image from **Spitz** et al. [219, 221] and available under a CC BY 4.0 license. No changes were made.

The co-registration was implemented in Matlab R2021a (The MathWorks Inc., Natick, MA, USA). To register and thus combine high-resolution PC- and TOF-MRI for subsequent analysis of the vasculature, we developed a hierarchical hybrid method. A hierarchical hybrid model-image approach inspired by Aylward et al. [13] was developed for registration, meaning the TOF-MRI centerline was fit to the intensity ridges representing the vessels within the PC-MRI volume (illustrated in Figure 4.2). A first concept that added hierarchical vessel tree traversal and a higher degree of deformation was introduced in [219] and evaluated with one dataset. Subsequently, we added two new components to the metric, reworked the code to run more smoothly, and evaluated on a bigger database [221]. The entire registration pipeline is illustrated in Figure 4.3, which is described in the following.

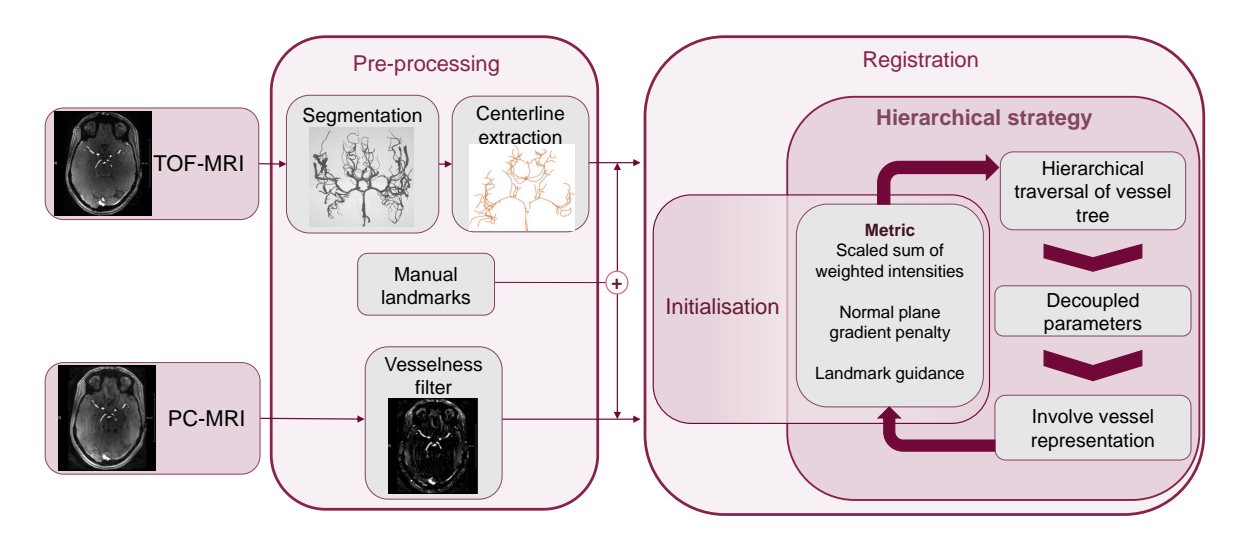


Figure 4.3: Registration pipeline: Input are TOF- and PC-MRI data. The TOF data are preprocessed according to Chapter 3, and the PC data with a vesselness filter. Landmarks are identified manually. Registration is initialized, followed by an iterative hierarchical strategy that traverses the vessel tree top-down. Parameters are decoupled for a bottom-up strategy. Representation, meaning visibility, of the vessels is considered throughout the process. Own figure.

The registration metric had multiple components. The first component was a scaled sum of weighted intensities, which sums up the intensities of the voxels of the PC-MRI volume in which the TOF-MRI centerline points lie after a transformation step. This sum shall be maximized, so that all centerline points lie within the intensity ridges (Figure 4.4, right). The intensities are weighted according to the corresponding vessel radius, derived from the maximum inscribed sphere at the current centerline point. The sum of intensities is scaled based on the weight and amount of centerline

points currently considered (Section 4.4.4). This first part of the metric  $\mathfrak{m}_1(T)$  is thus calculated:

$$m_1(T) = \frac{1}{\sum_{i=1}^{n} w(r_i)} \sum_{i=1}^{n} w(r_i) I_{\kappa \sigma_i}(x_i T)$$
(4.1)

where  $x_i$  is a centerline point, T the transformation, I the interpolated intensity value in which the centerline point lies, n the number of centerline points, and  $w(r_i)$  is a given point's weight depending on radius  $r_i$  of a given point. This was the only part that was introduced in [219]. The other two parts were newly added in [221].

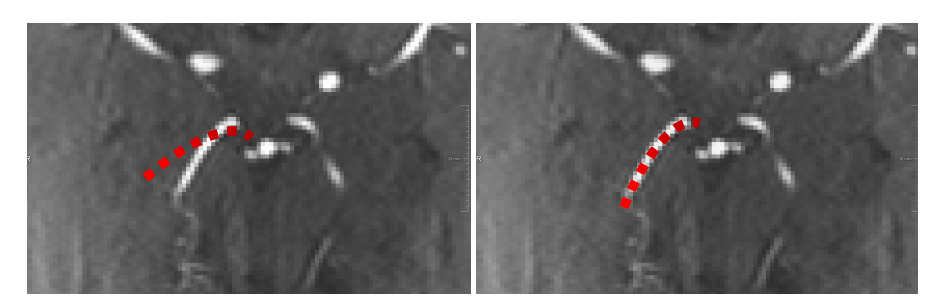


Figure 4.4: Alignment of red dashed centerline within the intensity ridges. Right picture maximizes the scaled sum of weighted intensities, thus resulting in a good metric, while left picture does not. Image from **Spitz** et al. [221] and available under a CC BY 4.0 license. No changes were made.

The second component of the metric is a penalty that ensures the centerline points fit to the middle of the intensity ridge, inspired by Jomier and Aylward [121]. We extended their approach to prevent a centerline point from being registered to a wrong vessel with a larger or smaller radius by first calculating the perpendicular normal plane at current centerline points within the PC-MRI data. Then, the directions of the gradients on the normal plane within the current vessel radius were examined to see how they correspond to the centerline point position, which ideally would lay within the highest intensity value (illustration in Figure 4.5).

The last component uses landmarks that are set at vessel branching points to provide additional guidance for vessel start- and endpoints.

#### 4.4.4 Coarse-to-fine hierarchical strategy

TREE HIERARCHY When finding the right fit of the centerlines to the intensity ridges, the registration strategy made use of a coarse-to-fine approach by utilizing the tree-like hierarchy of the vessels [121]. The inlets and outlets are considered roots and leaves, respectively. Vessel bifurcations represent the nodes of the tree. Registration is executed from the roots to the leaves.

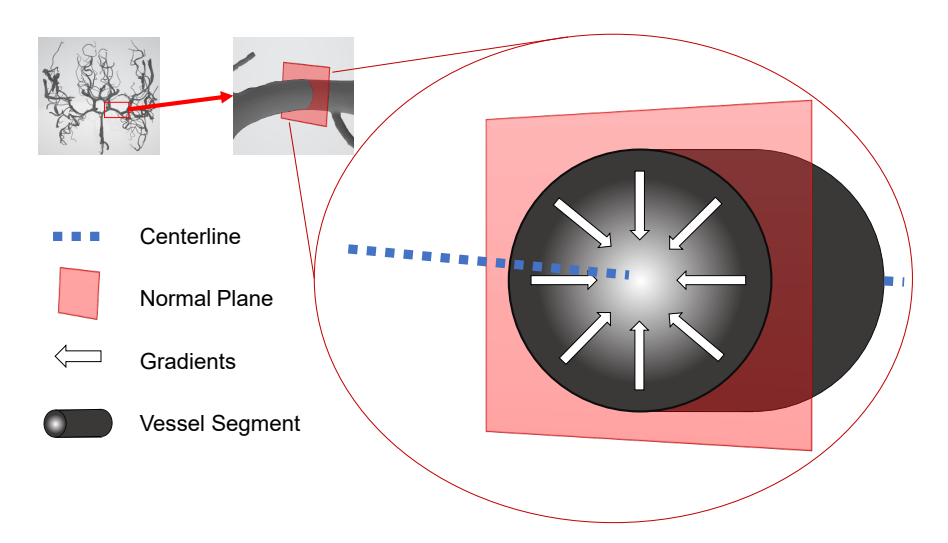


Figure 4.5: Illustration of how the centerline (blue) shall optimally be placed in an intensity ridge. Own figure.

Then, the roots' immediate children are considered the new roots but remain anchored to their parent vessels during transformation. This keeps the tree together, as well as registering the smallest vessels, which are visible in the TOF-MRI data, but not recognizable in the lower-resolution PC-MRI data. The assumption is that the alignment of children vessels benefits from the alignment of parent vessels.

REPRESENTATION CONCEPT In a variable called *representation* we record which vessel segments are recognizable in PC-MRI data. This was determined via a vessel segment's radius, as visibility is determined by vessel size. Thus, represented segments are considered for metric calculation and will eventually become roots for the hierarchical tree traversal. Non-represented vessel segments do not count towards metric calculation and will only be transformed with their parent vessels. Because there are no intensity ridges they can be matched to, including them in the calculation of the metric and having them transform on their own would lead to them being wrongly transformed to fit into other vessels' intensity ridges.

MULTI-START DECOUPLING OF PARAMETERS Another aspect of the coarse-to-fine strategy was a multi-start implementation and decoupling of transformation parameters.

Affine transformations were chosen for most of the registration, though a rigid registration is carried out for initialization. The rigid registration is performed in the same manner as the following affine registration, just stopping after a 4 DOF rigid transformation instead of carrying on with more DOF. The registration steps are based on the

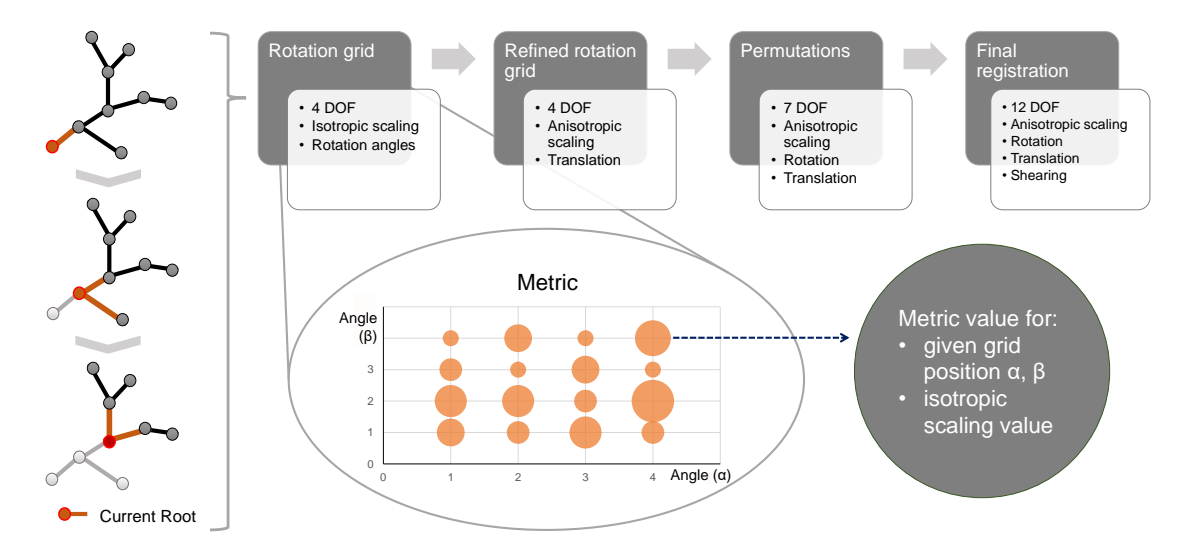


Figure 4.6: 2D illustration of hierarchical top-down strategy and decoupling of parameters: The vessel tree is traversed top-down from root to leaves, each segment becoming the new root and being iteratively registered. Each subtree finds the local affine transformation parameters bottom-up. Rotation angles are resolved via multi-start initialization. Best metric results are taken and refined up to a twelve DOF transformation. Image adapted from **Spitz** et al. [221] and available under a CC BY 4.0 license.

observation that rigid transformations are heavily dependent on rotation, which are therefore resolved first [118]. Each registration step goes as follows:

- 1. Starting with rotations only, a rotation grid is spanned over a set of rotation angles ranging from o° to 30° in steps of 3° to suit our data. Each point on the grid represents a possible start for the optimization progress.
- 2. After applying the rotation of one grid point to the data, a four DOF optimization is run to find the isotropic scaling and translation parameters. The resulting metric of each point is saved.
- 3. The grid is then refined through interpolation, inserting a grid point between each two existing ones.
- 4. From the refined grid, the three best sets of parameters are chosen, and every transformation parameter is permutated based on brain radius and voxel size [118], yielding further starting points for a higher seven DOF optimization.
- 5. The best set is chosen and will be the starting point for the final twelve DOF optimization featuring three translations three rotation, three scaling, and six shearing parameters (see scheme in Figure 4.6).

All steps are repeated for each subtree within the hierarchical vessel tree traversal. For optimization, we used Powell's method [193], a gradient-free iterative optimizer commonly used in registration with good performance [159, 163, 203]. We used a step size of 0.1 and a maximum number of iterations of 1000.

# 4.4.5 Evaluation

For validation, we considered metric results that shall be maximized, as well as error measures based on landmarks placed at branching points of the vessel trees. Landmark placement was conducted manually on natural peculiarities (e.g., bifurcations) that could be identified in both sets of data (see Figure 4.7). Different sets of landmarks were used for training and validation.

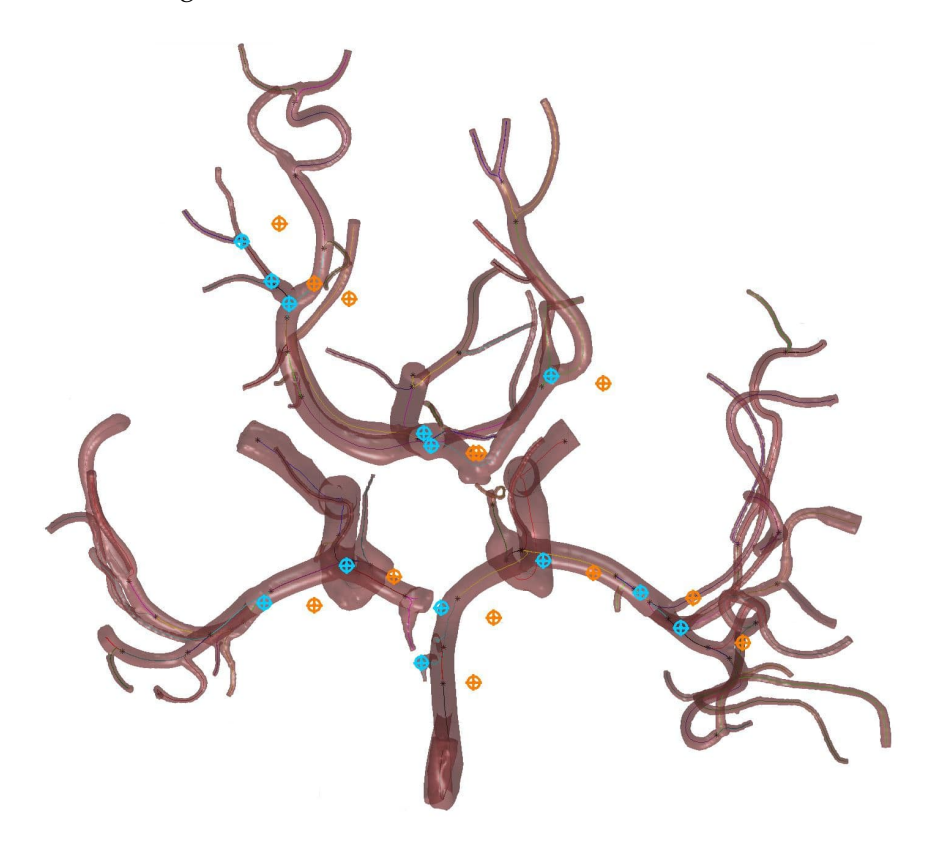


Figure 4.7: Examples of landmark placement. Orange are PC-MRI landmarks, blue TOF-MRI landmarks. Image from **Spitz** et al. [221] and available under a CC BY 4.0 license. No changes were made.

Root mean squared error (RMSE) and Hausdorff distance (HD) served as error measures, both of which shall be minimized to be optimized, and were recorded before and after registration.

Since 7T MRI is not part of the clinical routine and datasets are rare, we could only use seven paired TOF and PC-MRI scans from healthy volunteers. To get meaningful validation, we artificially transformed them to increase the data size. We opted for Monte Carlo simulations (MCS), i.e., we randomly transformed the TOF-MRI data and registered each of those transformations to their respective (untransformed) PC-MRI data [13, 159].

The strength and number of transformations were adjusted such that the results simulate differences between the original TOF- and PC-MRI data. We chose both rigid and non-rigid transformations to observe our method's performance for both sets of transformations, and due to the discussion of affine transformations being able to solve non-rigid deformations [13]. Each of the seven patient datasets was transformed 20 times, ten times each with rigid and non-rigid transformations.

#### 4.5 RESULTS AND DISCUSSION OF NEUROVASCULAR CO-REGISTRATION

Registration and validation were carried out on a device with an Intel core i7-10850H CPU @ 2.70GHz 2.71GHz processor, 32GB working RAM and an NVIDIA GeForce RTX 2080 Super graphics card. A single registration took between 20 and 40 minutes based on size and image quality of the data and complexity of the vessel tree.



Figure 4.8: Fit of centerline from TOF-MRI segmentation (orange) to a PC-MRI segmentation done by a clinical expert (black). Left shows pre-registration, right post-registration. Image from **Spitz** et al. [221] and available under a CC BY 4.0 license. No changes were made.

Before registration, the centerline is misaligned with the vessels of the PC-MRI segmentation. After registration, the vessels in the center of the CoW minimize error measures and maximize the metric, though vessels in the periphery seem to be more skewed (see Figure 4.8).

Every MCS led to a maximization of the metric, meaning the metric was larger than zero and had a valid final value. On average, the RMSE was reduced from 27.82 mm to 13.59 mm. There are outliers in the upper ranges, as the median final RMSE is 8.90 mm (see Table 4.1).

Table 4.1: Overall results for MCS. RMSE and HD are given in mm.

	initial RMSE	final RMSE	initial HD	final HD
Average	27.82	13.59	31.21	15.20
Median	25.78	8.90	30.51	13.51
Std. Deviation	19.95	17.74	9.64	13.68

RMSE was minimized in 99.93% and HD was minimized in 99.91% of MCS, meaning that only a very small number of outlier registration cases lead to the error measures, specifically distances between landmarks, worsening rather than improving.

HD was reduced from 31.21 mm to 15.20 mm on average, with the gap to median values not being as high with an average reduction from 30.51 mm to 13.51 mm. Standard deviation, however, was 13.68 mm.

There is a trend of non-rigid transformations yielding better registration results, with an average final HD and RMSE of 16.91 mm and 14.90 mm for rigid and 13.49 mm and 12.14 mm for non-rigid MCS transformations, respectively (see Table 4.2 and Table 4.3). This is likely due to the rigid transformations leading to a stronger deformation of the data, as the initial HD and RMSE is higher for rigid MCS transformations, too.

Table 4.2: Results for rigid MCS. RMSE and HD are given in mm.

	initial RMSE	final RMSE	initial HD	final HD
Average	28.65	14.90	33.61	16.91
Median	27.93	10.45	32.59	15.25
Std. Deviation	20.94	18.17	11.72	13.31

Table 4.3: Results for non-rigid MCS. RMSE and HD are given in mm.

	initial RMSE	final RMSE	initial HD	final HD
Average	26.97	12.14	28.82	13.49
Median	25.10	7.16	28.70	10.84
Std. Deviation	18.61	17.15	6.08	13.83

However, rigid MCS on average minimized their HD to 50.32% and their RMSE to 27.03%, while non-rigid MCS reduced their HD to 46.81% and their RMSE to 20.28%. This supports our hypothesis that local affine transformations can approximate the non-rigid deformations in the data that shall be co-registered.

While HD is the maximum distance across all minimum distances of landmark pairs, an average result of around 1.4 cm is large for cranial structures. However, the error depends strongly on landmark placement, which was done manually, meaning that even small displacements in landmark placement can lead to higher errors.

In comparison, Rivest-Hénault et al. [203] achieved a maximum 3D replacement of 7.416 mm, while Jomier et al. [121]'s algorithm registers 87% of the centerline within two voxels of each other, and Aylward et al. [13] reached a 0.1-0.2 voxel standard deviation. This shows that while our method reduces the error significantly, we have further work to do in our method's accuracy, for which ideas are presented below. It shall be noted that none of these related works use the exact same data or method.

Registration of non-rigid transformation MCS leads to better results than rigid transformations MCS (see Table 4.2 and Table 4.3). We used local affine transformations for the registration itself, which can only approximate non-rigid deformations. Therefore, replacing them with free deformable transformations could lead to better results. This could also be achieved by adding another registration step, for example with thin-plate splines like Rivest-Hénault et al. [203].

Since we used MCS by applying transformations to the TOF data, which already features changes to its corresponding PC-MRI scans, we added further transformations and thus made the registration problem harder. However, when registering the seven real-world scans from volunteers, no significant differences are present, other than lower standard deviation (see Table 4.4).

Table 4.4. Results for original data. Rivise and the are given in film.					
	initial RMSE	final RMSE	initial HD	final HD	
Average	23.75	10.23	27.98	16.34	
Median	23.00	9.89	29.78	16.61	
Std. Deviation	17.45	7.59	6.41	5.79	

Table 4.4: Results for original data. RMSE and HD are given in mm.

The runtime of 20 to 40 minutes was measured after acceleration by vectorization. This relates to a pre-processing step, not a step in an interactive process. Nevertheless, additional runtime benefits may be gained by GPU acceleration by high memory throughput, parallelism, and specialized hardware [81]. Another approach to accelerated runtimes could be a DL strategy, though for that more data and a ground truth would be necessary, which are not available at this time.

#### 4.6 CONCLUSION ON NEUROVASCULAR CO-REGISTRATION

Per the data-specific characteristics, we presented a hybrid approach to register TOF-MRI data to PC-MRI scans to answer *RQ 1*, thus combining the 7T TOF-MRI segmentation with the blood flow information available in the 7T PC-MRI data. This enables the combined use of both modalities, for example for data assimilation in hemodynamic analysis [89]. Thanks to the registration, both the detailed morphology of the TOF-MRI and the blood flow information of the PC-MRI can be used in combination for patient-specific insights.

Our registration fits the centerlines of the TOF-MRI data to the intensity ridges of the PC-MRI volume via a weighted sum of scaled intensities metric dependent on radius and vessel normal, and further guidance via landmarks.

We employ information on the recognizability of vessel segments in the TOF data but not in the PC-MRI, yielding a *representation* status. Thus, non-represented segments are treated differently in the registration strategy and are aligned via their parent vessels rather than on their own. Separate landmarks from the ones used to guide registration served for validation purposes.

With an average HD of 15.20 mm and an RMSE of 184.73 mm there is potential for improvement. Future work will include the addition of deformable transformations and possibly a non-iterative optimizer via DL for higher performance. Similarly, we aim to improve the runtime by GPU acceleration. Furthermore, we see potential for improvements through optimizing pre-processing by including motion correction inscan, and by utilizing the PC-MRI phase data. An automatization of the segmentation could address concerns about user variability.

With this presented co-registration strategy for 7 T TOF- and PC-MRI, we answer RQ 1 about how to combine the neurovascular information from multiple 7T scans.

# Part III

MORPHOLOGY-DRIVEN ANALYSIS OF INTRACRANIAL ANEURYSMS FOR PATIENT-SPECIFIC RESEARCH

# MORPHOLOGY-DRIVEN ANALYSIS OF INTRACRANIAL MIRROR ANEURYSMS

After presenting relevant preprocessing steps, morphology-driven analysis for patient-specific research can be performed. This chapter demonstrates morphology-driven analysis using the example of how mirror aneurysms can be analyzed, and how morphology can affect hemodynamics, thus highlighting the relevance of and setting a basis for

#### RQ 2, how can longitudinal morphological deformation be analyzed?

As discussed in Section 2.3, mirror aneurysms are a rare subgroup of IAs where multiple aneurysms appear at identical locations in the left and right hemispheres of the CoW. Due to rarity, their specific risk factors are not yet well researched. Mirror aneurysms have the same location and the same metadata, meaning patient-specific parameters, making their location and patient-based risk factors are identical. As the metadata and location for mirror aneurysms in one patient are the same, we use their morphology to guide the analysis. During data collection, there were patients who, at the time of the scan, had one ruptured and one unruptured mirror aneurysm. This may potentially highlight the importance of morphology during risk analysis. The thesis therefore aims to explore what may lead to the differences between mirror aneurysms that have identical locations and patient-related risk factors yet differing sizes, shapes, and rupture states, and focuses its analysis on morphology.

# Publication

Chapter 5 is based on:

[225] **L. Spitz**, J. Schmidt, J. Korte, P. Berg, D. Behme, B. Neyazi, B. Preim, and S. Saalfeld. "Morphologic and hemodynamic analysis of intracranial mirror aneurysms." In: Curr Dir Biomed Eng 10.2, pp. 87-90. doi: 10.1515/cdbme-2024-1074.

This work was conceptualized by L. Spitz and S. Saalfeld, written by L. Spitz, and designed, implemented and simulated by J. Schmidt as part of a Master Thesis.

#### 5.1 MATERIAL AND METHODS OF MIRROR IA ANALYSIS

Hemodynamics of both the IA itself as well as the upstream parent vessel were assessed, and their relations and influences on each other. Virtual stitching was performed, meaning separating the IA domes from their parent vessels and placed them onto the opposing parent vessel in the other hemisphere (see Figure 5.1). We then compare hemodynamics of the original and stitched anatomies and analyze similarities and differences.

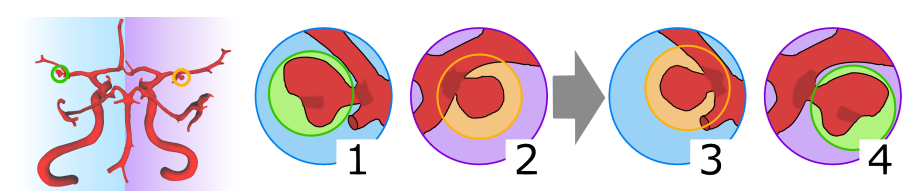


Figure 5.1: Illustration of stitching. 1) and 2) are the original mirror aneurysms and 3) and 4) the stitched ones. 3) is the left parent vessel with the right IA dome, and 4) the right parent vessel with the left IA dome. Image from **Spitz** et al. [225] and available under a CC BY 4.0 license. No changes were made.

DATA From a database of 300 IAs from approximately 200 patients, we selected eight patients with a total of 16 mirror aneurysms at the same location in the right and left hemispheres that still showed morphological variety and different rupture states. We used pre-segmented IA surface meshes from 3D rotational angiography data from the University Hospital Magdeburg and the Clinic Nordstadt in Hannover. Morphological parameters were extracted semi-automatically with the help of Saalfeld et al.'s [209] tool.

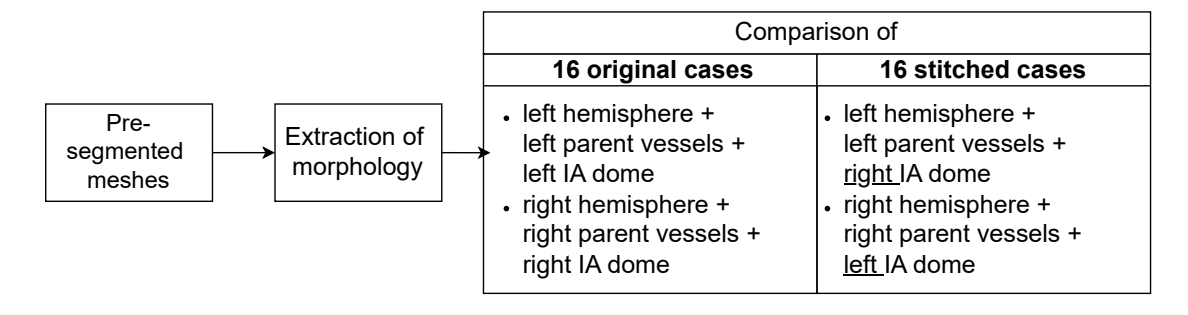


Figure 5.2: Pipeline of the stitching process. Image from **Spitz** et al. [225] and available under a CC BY 4.0 license. No changes were made.

STITCHING Stitching of the IA domes to the opposite parent vessel was performed manually in Blender 2.82 (Blender Foundation, Amsterdam, Netherlands) and Sculp-

tris Alpha 6 (Sculptris, Pixologic ZBrush, Inc, Los Angeles, USA). This yielded a total of 32 IA models: the 16 original IA models, and the additional 16 stitched models. The stitching pipeline is illustrated in Figure 5.2.

BLOOD FLOW SIMULATION To get hemodynamic parameters, we had to simulate the blood flow with CFD, as the original imaging data had not measured any blood flow parameters, and many hemodynamic parameters cannot be captured with imaging. To simulate the blood flow, the surface meshes of the IAs required further preprocessing.

All 32 segmented surfaces were re-meshed in STAR-CCM+ 2020.1 (SimcenterTM STAR-CCM+, Siemens Product Lifecycle Management Software Inc., Plano, USA) using a base mesh size of 0.15 mm for a trade-off between resolution and computational effort [48]. An unstructured mesh with polyhedral cells was chosen and three prism layers with a stretch factor of 1.3 were set for a more accurate solution for flow close to walls.

As there was no information available about the patient-specific inlet boundary conditions, generalized values were chosen from literature [27]. Velocity at the inlets was based on the estimated velocity at the respective arteries, ranging from 0.25-0.5  $\frac{m}{s}$  [125, 173]. Inlets and outlets were extruded to six times their diameter to allow a realistic formation of the flow profile, and walls were assumed to be rigid [27]. For the outlet boundary conditions, zero pressure boundary conditions and advanced flow-splitting were applied [207]. For the simulation of blood flow, the following fluid parameters were chosen:

- Incompressible fluid with a density of  $\rho = 1055 \frac{kg}{m^3}$
- Newton fluid with constant viscosity of  $\eta = 4$  mPa·s
- Laminar flow behavior was assumed based on low Re < 1000

The Finite-Volume method was used to approximate Navier-Stokes equations iteratively, with a continuity criterion of  $10^{-5}$ . The commercial flow solver STAR CCM+ was used to solve the 32 steady simulations of original and stitched IAs.

Based on Oeltze-Jafra et al. [180]'s taxonomy for visual exploration of medical flow data, our approach is categorized as IAs for application domain, vessel lumen as the spatial scope and near context. As for visual exploration tasks, we performed a spatial overview, probing by focusing on the IA sac, the parent vessel, or the neck area, and comparison via the stitching.

RECORDED PARAMETERS For calculation and visualization of the hemodynamics we used EnSight 2019 R2; (Ansys, Inc., USA). They comprised: velocity, average wall shear stress (AWSS), normalized wall shear stress (nWSS), LSA, inflow concentration index (ICI), and flow rate [48].

<u> </u>	· · · · · · · · · · · · · · · · · · ·				
Morphological parameters		Hemodynamic parameters			
Hortho	size / height	Q	flow rate		
AR	aspect ratio	V	velocity		
EI	ellipticity index	AWSS	average wall		
NSI	non-sphericity		shear stress		
	index	nWSS	normalized wall		
UI	undulation index		shear stress		
$\alpha, \beta, \gamma$	angles*	LSA	low shear area		
$N_{avg}$	average neck	ICI	inflow concentration		
	diameter		index		

Table 5.1: Overview over measured parameters [48, 209]. \*Angles between parent vessel centerline, IA neck, and IA dome point.

Morphological parameters included: size in the form of orthogonal height in mm, AR, EI, NSI, UI, angles between IA dome and parent vessel, and neck diameter [209]. All parameters are listed in Table 5.1.

#### 5.2 RESULTS OF MIRROR IA ANALYSIS

Blood flow was simulated, and hemodynamics were measured in both original and stitched mirror aneurysms to compare the influence of aneurysm morphology and parent vessel anatomy on hemodynamics. Additionally, the morphology of the initial mirror aneurysms was evaluated for variations between hemispheres and rupture status.

There were differences between left and right mirror aneurysms in size, AR, and one shape index. On average, IAs on the left hemisphere were 0.61 mm larger and exhibited 70% higher UI, see Table 5.2. Other parameters were comparable on both sides. In regard to rupture status, ruptured IAs were 2.01 mm larger on average and had approximately 40% higher AR and NSI. Out of the six ruptured IAs, four were on the left side.

In the hemodynamic analysis of the original cases, the left-side IAs showed higher average velocities, flow rates, AWSS, and nWSS. For the latter two parameters, the left side was always higher, which might be due to left-side IAs having a higher neck diameter on average [239]. Consequently, the right side had higher LSA values, which might be related to the lower AWSS values.

An example of streamlines, which visualize the velocity, of original and stitched cases can be seen in Figure 5.4. While differences in streamline behavior were observed

Table 5	.2: Overvie	w of average	and standard	deviation of	f relevant parameters.
iubic )	.2. 0 101 110	W OI WYCIUSC	aria stariaare	a actiunion of	. Icic varit parameters.

Parameter	All	Ruptured	Unruptured	
	(n=16)	(n=10)	(n=6)	
Size (mm)	4.74±1.93	5.99±1.83	3.98±1.64	
AR	1.30±0.41	1.58±0.20	1.13±0.42	
NSI	0.19±0.07	0.24±0.06	0.17±0.05	
UI	0.14±0.07	0.15±0.10	0.13±0.06	
Velocity $(\frac{m}{s})$	0.23±0.12	0.18±0.06	0.25±0.13	
AWSS (Pa)	7.64±4.65	6.33±2.91	8.43±5.27	
Parameter	Left	Di alat	Critale and last dames	C('( 1 1 1 1 1 1
1 didilictei	Leit	Right	Stitched left dome	Stitched right dome
- urumeter	(n=8)	(n=8)	(n=8)	(n=8)
Size (mm)		· ·		e
	(n=8)	(n=8)		e
Size (mm)	(n=8) 5.04±2.38	(n=8) 4.43±1.45		e
Size (mm) AR	(n=8) 5.04±2.38 1.28±0.53	(n=8) 4.43±1.45 12.3±0.28		e
Size (mm) AR NSI	(n=8) 5.04±2.38 1.28±0.53 0.20±0.09	(n=8) 4.43±1.45 12.3±0.28 0.19±0.03		e

more often than similarities when comparing stitched and original, half of the cases showed a comparable average velocity in original and stitched. This might be due to streamlines not being a reliable tool to assess flow behavior or velocity. They do, however, illustrate the influence of the IA angle, meaning the orientation in which the IA sits on the parent vessel. In Figure 5.4 b) and c), which show the left parent vessel, the streamlines enter in a more straight, upward motion into the IA dome, whereas in a) and d), which use the right parent vessel, they exhibit a flatter inflow angle.

Figure 5.3 shows an example of AWSS of original and stitched IAs. WSS developed similarly in each hemisphere regardless of IA morphology. Furthermore, right IA domes stitched on left hemisphere vessels had a higher AWSS on average than left IA domes stitched on right hemisphere vessels (see Table 5.2). However, when looking at individual patients, IA domes showed a comparable AWSS and nWSS both on original and opposite parent vessels.

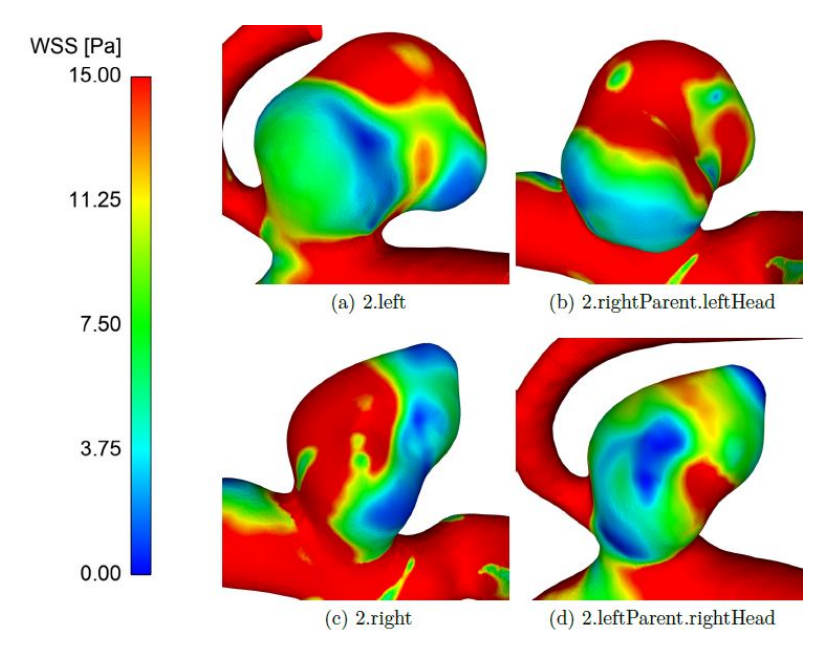


Figure 5.3: Depiction of AWSS for Case 2. a) and c) are the original aneurysms and b) and d) the stitched ones. Image from **Spitz** et al. [225] and available under a CC BY 4.0 license. No changes were made.

#### 5.3 DISCUSSION OF MIRROR IA ANALYSIS

We observed a correlation between rupture, size, and shape, which is in accordance with related studies about IA rupture, size, and shape correlations in general [69], and mirror aneurysms in particular [247, 255]. The majority of ruptured cases were in the left hemisphere, which goes against Wang et al.'s [247] findings of no dominant side for rupture. These differences in rupture behavior are particularly interesting to observe, as the patient-specific risk factors like age, sex, lifestyle, and genetics are the same for both mirror aneurysms of one patient. It illustrates the importance of morphological analysis in rupture risk assessment. In the following, we analyze these differences in morphology and hemodynamics.

We defined IA angle as a morphological feature of the IA. It could also be counted as a feature of the upstream parent vessel, as streamlines in Figure 5.4 show similar angles for identical parent vessels regardless of IA dome.

Our observations oppose another study about symmetrical flow behavior [247], as we found hemodynamic differences in the left and right hemispheres. ICI was the most consistent parameter, save for two outliers on the left side.

Both stitched and original cases have similar average values and distributions of WSS. This points to a higher influence of the upstream parent vessel, even though, when looking at the domes individually, they had similar values on either hemisphere.

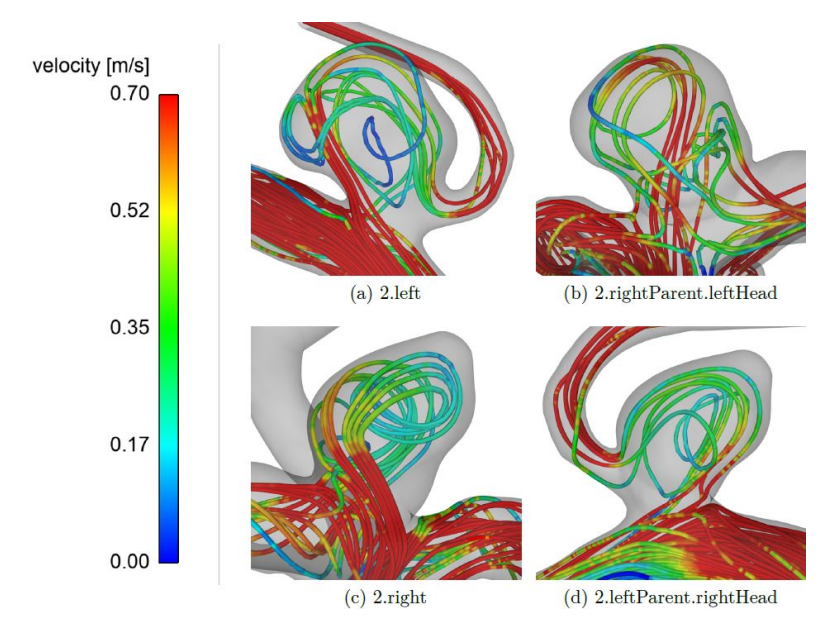


Figure 5.4: Depiction of streamlines for Case 2. a) and c) are the original aneurysms and b) and d) the stitched ones. Image from **Spitz** et al. [225] and available under a CC BY 4.0 license. No changes were made.

To analyze rupture behavior and risk, we only selected patients with one ruptured and one unruptured mirror aneurysm, or patients where mirror aneurysms had strongly differing morphology. Rupture analysis of the stitched IAs was still purely speculative, but as dome morphology does not change, we assume the correlations between size, AR, and NSI still stand. As AWSS and nWSS of one dome remain comparable regardless of the parent vessel, we concluded a comparable rupture risk. However, as illustrated in Figure 5.4 and Figure 5.3, flow behavior and distribution of WSS are dependent on the parent vessel, and we did not investigate possible changes in morphology based on changed blood flow after stitching.

Due to mirror aneurysms only making up a small percentage of all IAs and selecting only patients with differing morphology or one ruptured and one unruptured mirror aneurysm, we had a small sample set and could not investigate the possible influence of localization. Ultimately, we found that both upstream parent vessel as well as IA morphology seem to influence hemodynamics. The exact relations were not clear in our study, though it confirms Yuan et al.'s [255] findings about the close connection between morphological and hemodynamic parameters.

In future studies, more patients and IAs in more diverse locations should be included. We want to extract and analyze more morphological parameters, not just of the IA but also of the parent vessel anatomy to further explore its influence on rupture risk. We also want to perform a more realistic and precise transient simulation to get patient-specific hemodynamics and achieve a higher degree of realism. For patient-specific

hemodynamics, selecting patients who underwent flow imaging like PC-MRI would add more realism.

Tools like AmniVis [177] can help in a more detailed qualitative analysis of the near wall hemodynamics, providing further support through their focus and classification widgets, potentially providing more insights.

We also want to investigate changes in morphology through changed blood flow behavior after stitching through deformable models.

#### 5.4 CONCLUSION ON MIRROR IA ANALYSIS

16 mirror aneurysms were analyzed based on their morphology and hemodynamics and found that left and right hemisphere IAs exhibit differences. Left-side IAs tended to be larger, with higher AR and UI. Their blood flow showed higher velocities, flow rates, and WSS. We also found a correlation between rupture, size, and NSI, and accordingly, ruptured IAs were more prevalent in the left hemisphere.

When stitching the IA domes to the opposite parent vessel, both the IA morphology as well as the upstream parent vessel influence hemodynamics. IA size and UI seemed to be the most influential parameters, along with the angle of the IAs on the parent vessel. The difference between hemispheres and original and stitched IAs highlights the importance of morphological analysis of IAs.

This study serves as an introduction to patient-specific morphology-driven analysis before longitudinal deformation is taken into account. It illustrates how morphology can be analyzed and sets the basis for answering RQ 2, as well as illustrating the relevance of IA morphology-driven analysis, and how morphology influences hemodynamics. Further, it shows how patient-specific morphology, even beyond metadata, is relevant for individual rupture risk prediction and should be considered for treatment planning.

# ANALYSIS OF INTRACRANIAL ANEURYSM DEFORMATION AFTER CNS TREATMENT

After demonstrating how vascular morphology can be analyzed, and how a change in morphology can affect blood flow, the thesis now explores how to analyze longitudinal changes in morphology.

Introduced in Section 2.5.2, the CNS is a novel IFD for WNBAs, for which conventional treatment options have relatively high recurrence rates [78, 106]. The CNS is a dual-layered mesh device that unfolds into a cup-like shape, sitting in the neck of the intracranial aneurysm (IA) to disrupt blood flow into the aneurysm sac.

In the short-term, various studies show good results, and while longitudinal studies are ongoing, the results so far are promising. No in-depth analysis of the effect of CNS deployment on IA morphology over time has been done yet.

Further, few studies have assessed the influence of IA morphology on CNS success compared to other IFDs [47]. This is an important aspect of device safety, as post-therapeutic changes in aneurysm morphology possibly influence the healing process and recurrence rates, as well as blood flow. One study assessed pre-treatment IA morphology and rupture state but found no correlation with treatment outcome [99].

This thesis aims to fill this gap in research, and answer

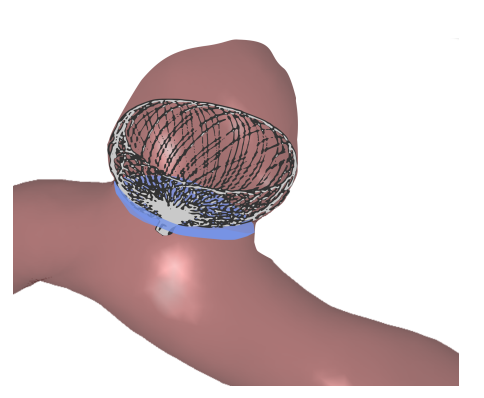
RQ 2: how longitudinal morphological deformation can be analyzed?

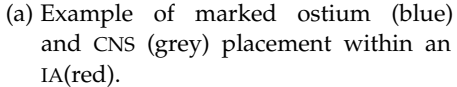
using the example of the CNS. We therefore present a preliminary study that serves as first comparison of neck curves and ostia of IAs before and after treatment with the CNS, and a following study that gives a first assessment of the CNS's robustness to deformations over time, as well as a longitudinal deformation analysis of the IA neck curve and the CNS itself.

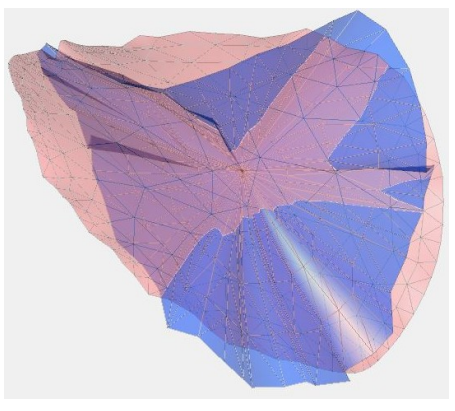
#### 6.1 RELATED WORK ON ANEURYSM DEFORMATION

Aneurysms may deform, or change in size or shape, either through natural causes in case of aneurysm growth or through insertion of an implant. In both cases, a quantification of the deformation is necessary, as aneurysm growth indicates an increase rupture risk [240], and changes in shape have an influence on hemodynamics.

In case of growth, the most common clinical method of measuring the deformation is through measuring maximum aneurysm diameter in angiography scans [31]. Another method is the comparison of morphological parameters extracted from 3D reconstruction of the vasculature, as presented in the previous chapters, and analyzing their







(b) Example of registered pre-treatment (pink) and follow-up (blue) ostia models.

Figure 6.1: Examples of ostium, CNS and ostia. Images from **Spitz** et al. [223] and available under a CC BY 4.0 license. No changes were made.

relative differences [34]. Another option is using co-registration utilizing non-rigid warping of the IAs and analyzing the deformation field [34]. To measure elongation, which is a risk factor for thoracic aortic aneurysms, Bian et al. [31] used deformable image-based registration, followed by segmentation and surface mesh and centerline extraction, to utilize the Jacobian determinant and its differences in directional components to quantify the directional change and thus elongation. Spatial change can also be assessed via distance measurements between the non-deformed IAs, such as HD [62].

For deformation after treatment, the visual inspection of angiographic scans taken before and after treatment through experienced clinicians is also common [53]. This, however, does not provide a quantification of the deformation. A common treatment deformation is vessel-straightening after treatment with a FD stent, where the inserted stent bends the parent vessel of the IA to be more straight [21]. Through the change in angle, hemodynamics in the IA sac can change significantly, and hemodynamics, in turn, can affect IA growth, thrombus formation, and rupture risk [113, 119, 245]. To measure vessel straightening, the change in angle can be determined using the centerline of the parent vessel [53]. For coiling, the volume of recurrence can be measured via rigid image-based co-registration of MRA scans and calculating the change in volume from the difference images [236].

As surface meshes are most well suited for morphological analysis [111], and we had access to different modalities, we decided against the use of image-based coregistration. Further, in the post-treatment angiographies, the IA sac is no longer visible, as the CNS hinders blood flow into the IA. Therefore, we could not perform a deformable co-registration on the IA meshes. We therefore analyze the deformation of

IA after CNS treatment by focussing on the neck curve and ostium and their respective morphological parameters. Further, we use distance measurements between the rigidly co-registered parent vessels (not the IA) to assess spatial change.

#### 6.2 PRELIMINARY STUDY ON IA DEFORMATION AFTER CNS TREATMENT

# **Publication**

Section 6.2 is based on:

[223] L. Spitz, J. Korte, F. Gaidzik, N. Larsen, B. Preim, and S. Saalfeld. "Assessment of intracranial aneurysm neck deformation after Contour deployment." In: Int J Comput Assist Radiol Surg 19 (2024), 2321–2327. doi: 10.1007/s11548-024-03189-w. This work was conceptualized, designed, and implemented by L. Spitz.

The preliminary study is meant to give a first comparison of the IA neck curve and ostia from before and after CNS deployment.

Our data included seven IAs treated with the CNS (example case in Figure 6.1a). We compared in vivo scans taken pre-treatment (Pre) to follow-up (FU) 3D rotational angiographic images (3D RA) on an Allura Xper FD 20/10 (Philips, Best, The Netherlands), all with a spatial resolution of 384×384×384 and an isotropic voxel size ranging from 0.16 to 0.33 mm after reconstruction. The time between Pre and FU scans ranged from two months and three weeks to two years and two months, with a mean of 10 months and two weeks.

All IA images were segmented into 3D models using the segmentation pipeline from Chapter 3, with the approach extended to work for 3D RA by adjusting pre-processing parameters manually. The models were then manually cut to the region of interest comprising mainly the IA with parent vessels and a few child vessels, and ostia were extracted automatically [209]. This was possible for all Pre datasets and for three of the FU datasets. For the other four FU datasets, the aneurysm sack was not visible after treatment and automatic extraction failed, thus the ostium was extracted manually.

A global rigid iterative closest point registration was performed (using Meshlab v2o22.o2 [59]) to align the Pre and FU models (IAs and surrounding vasculature) of each case, which automatically registered the ostia (Figure 6.1b). Automatic registration failed for one case, which was then manually registered, globally and rigidly. For qualitative deformation analysis of the ostia, we utilized arrow visualizations based on correspondences and minimal distances to illustrate areas of low and strong deformations. For quantitative analysis we used morphological parameters, namely size and shape indices, the first describing the size of the IA, and the latter size-independent

shape that relates to the ellipticity and concavity of the ostia. Derivation of all parameters was implemented in Matlab 2023a (The MathWorks Inc., Natick, MA, USA) or they were extracted with its internal functions.

IA size indices included:

- area of neck curve,
- width of neck curve, determined by maximum diameter, which determines CNS sizing,
- mean diameter of neck curve
- convex hull (CH) volume of the ostium,
- distance between registered Pre and FU ostia calculated by symmetric surface distance.

IA shape indices included:

- EI
- UI
- NSI
- mean curvature of ostium surface
- Gaussian curvature of the ostium surface

Shape indices were used as defined by [196] and described in Section 2.6.2. However, as the ostium is a surface and does not have a volume, we used surface adaptations of UI and NSI [165]. Instead of volume V they utilize area A and circumference C, and the NSI thus becomes the non-circularity index (NCI) [165]:

$$UI_{2D} = 1 - \frac{A}{A_{CH}} \tag{6.1}$$

$$NCI = 1 - 2\sqrt{\pi} \frac{A^{\frac{1}{2}}}{C}$$
 (6.2)

Where necessary, we projected the ostia onto a 2D plane based on principle component analysis (PCA) for minimum information loss. Low values of the indices close to zero describe a shape close to a perfect circle, while high values close to 1 describe high ellipticity or concaveness.

The rate of change was calculated by dividing the absolute change ( $\Delta$ ) of a parameter by the number of days between Pre and FU scans and multiplying the daily rate of change by 365 to reach the rate of change per year ( $\frac{\Delta}{\text{year}}$ ).

We did not assess deformations of the entire aneurysm sack, because the IA dome is not visible in the underlying angiographic data as the contrast agent does not uniformly opacify the IA sack after CNS deployment.

#### 6.2.1 Results of preliminary study on IA deformation after CNS treatment

Size indices can be compared in Table 6.1. Pre ostia had an average area of  $15.52 \pm 3.51 \,\mathrm{mm^2}$ , with values ranging from 9.14 to  $20.61 \,\mathrm{mm^2}$ , and FU ostia had an average area of  $13.30 \pm 2.27 \,\mathrm{mm^2}$ , ranging from 10.18 to  $16.55 \,\mathrm{mm^2}$ . Three out of seven ostia were larger after treatment (Table 6.2 and Table 6.3), but on average, the ostium area of the FU data was 10% smaller than Pre data, with an average absolute shrinkage of  $2.22 \pm 4.22 \,\mathrm{mm^2}$  and an average yearly shrinkage rate of  $0.58 \pm 4.88 \,\mathrm{mm^2}$ , which makes  $-2 \pm 0.26 \,\%$  per year.

Pre ostia had an average width of 5.01  $\pm$ 0.54 mm and FU ostia 4.49  $\pm$ 0.45 mm, with an average difference of 0.51  $\pm$ 0.68 mm, making FU ostia width 9% smaller than that of Pre ostia. This mirrors the results for mean diameter, where the average difference was 0.39  $\pm$ 0.62 mm, and FU had an 8% smaller mean diameter on average. For yearly rate of difference, max diameter had one of -0.59  $\pm$ 0.87 mm, making -12  $\pm$ 19%, and the mean diameter had one of -0.24  $\pm$ 0.78 mm, making -4  $\pm$ 18%.

Distances denoted by mean SSD between the Pre and FU ostia ranged from  $0.35 \, \text{mm}$  to  $1.69 \, \text{mm}$ , with a mean of  $0.74 \pm 0.42 \, \text{mm}$ . The strength of deformation from Pre to FU ostia varied between individual cases, where some cases had a maximum deformation of  $2.32 \, \text{mm}$ , and others had one of  $0.78 \, \text{mm}$  (Figure 6.2). Deformation seemed to be bigger around the edges of the neck curve and smaller in the middle of the ostium.

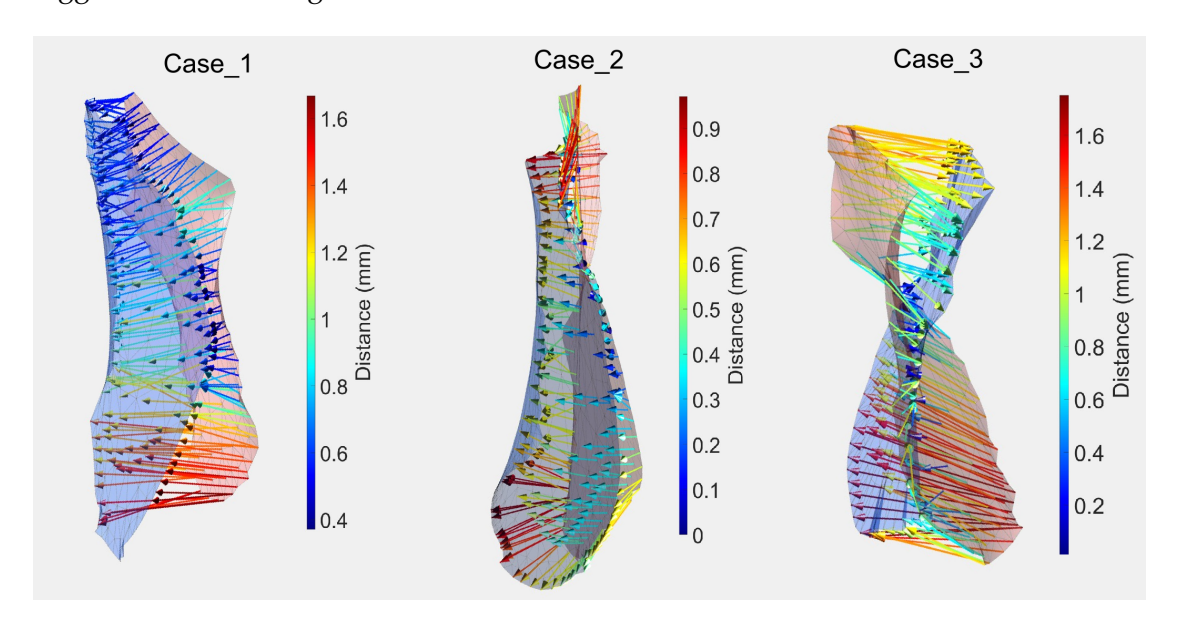


Figure 6.2: Example of the deformation of the ostia of three ostia from Pre (pink) to FU (blue) scans. Color-coded arrows pointing from Pre to FU data highlight areas of low (blue) and high (red) deformations. Image from **Spitz** et al. [223] and available under a CC BY 4.0 license. No changes were made.

Correlating the time passed between the Pre and FU scans with the rate of change, we found a positive correlation between time passed and changes in area, width, and mean diameter. The Pearson correlation coefficient (PCC) for time and area change was 0.80, and had a p-value of 0.03, making it the only correlation with p-value < 0.05. PCC for width and mean diameter was 0.68 and 0.69, respectively.

As ostia are complex shapes that can be concave, we started the comparison of shape indices with the CHs. Here, we observed an average absolute increase in volume of  $0.43 \pm 3.08 \,\mathrm{mm^3}$  and a rate of  $1.11 \pm 3.02 \,\mathrm{mm^3}$  per year. However, when looking at average relations between Pre and FU scans, CHs of FU ostia were 4% larger. Average CH volume was  $6.81 \pm 2.41 \,\mathrm{mm^3}$  and  $6.38 \pm 1.83 \,\mathrm{mm^3}$  for Pre and FU ostia, respectively.

The Pre ostia EI was higher than FU ostia EI in four out of seven cases (Table 6.2 and Table 6.3), with respective average EIs of 0.59  $\pm$ 0.02 and 0.54  $\pm$ 0.07 (Table 6.1). On average, the Pre EI was 8% larger than the FU EI, with a yearly rate of change of -0.06  $\pm$ 0.15, which is -10  $\pm$ 26% per year. This means that ostia were more elongated before treatment with the CNS.

We applied the 2D-adapted formula for  $\rm UI_{2D}$  (Equation 6.1) to both the original ostium data and to the 2D-projected data, as the latter would lose information about convexity in the z-dimension. For projected ostia, both Pre and FU ostia had small values, 0.01  $\pm$ 0.01 and 0.03  $\pm$ 0.02, respectively, meaning they were overall convex shapes with low changes after treatment. The original ostia had a nearly identical  $\rm UI_{2D}$  of 0.53  $\pm$ 0.01, with an average difference of 0.004 and FU ostia being 0.7% less convex on average.

The projected Pre ostia had an average NCI of 0.04  $\pm$ 0.02, and FU ostia 0.06  $\pm$ 0.04. The non-projected ostia showed a similar trend, with Pre ostia having an average NCI of 0.08  $\pm$ 0.02 and FU ostia having one of 0.10  $\pm$ 0.04. These differences seem small, but when put in relation, the NCI of projected FU ostia was three times larger on average than for Pre ostia, and the 3D NCI 52% larger. Overall, both Pre and FU ostia's NCI is close to 0 and therefore rather circular, but slightly less so for FU ostia.

Lastly, we assessed the mean and Gaussian curvature of the ostia. Pre ostias' mean curvature was 0.02, and FU was 0.00. While an average difference of 0.02  $\pm$ 0.06 is small, the differences in individual ostium curvature from Pre to FU ostia go up to seven times larger. Gaussian curvature was -0.09  $\pm$ 0.07 for Pre ostia and -0.16  $\pm$ 0.13 for FU ostia on average, with an average difference of 0.08  $\pm$ 0.17, and FU observations being three times larger.

#### 6.2.2 Discussion of preliminary study on IA deformation after CNS treatment

With an average SSD of 0.74 mm, which is 15% of the average ostium width, changes in ostia after treatment with the CNS are subtle but present. SSD compares vertices on the ostia surface mesh, and a meshing-independent distance measure could yield further information in future studies.

Table 6.1: Mean and standard deviation ( $\sigma$ ) of all calculated parameters, as well as difference ( $\Delta$ ) and rate of change per year ( $\frac{\Delta}{y \, e \, \alpha \, r}$ ), for pre-treatment and FU ostia, as averages of all seven cases.

	Pre		FU		$\Delta$		$\frac{\Delta}{ ext{year}}$	
Parameter	Mean	σ	Mean	σ	Mean	σ	Mean	σ
SSD (mm)	0.74	0.42	-	-	-	-	-	-
Area (mm²)	15.52	3.51	13.30	2.27	2.22	4.22	-0.58	4.88
Max diameter(mm)	5.01	0.54	4.49	0.45	0.51	0.68	-0.59	0.87
Mean diameter (mm)	4.35	0.46	3.96	0.40	0.39	0.62	-0.24	0.78
CH Volume (mm <sup>3</sup> )	6.81	2.41	6.38	1.83	0.43	3.08	1.11	3.02
EI	0.59	0.02	0.54	0.07	0.05	0.08	-0.06	0.15
$_{ m 2D}$ UI $_{ m 2D}$	0.01	0.01	0.03	0.02	-0.02	0.03	0.01	0.04
$_{ m 3D}$ UI $_{ m 2D}$	0.53	0.01	0.53	0.01	0.00	0.01	0.00	0.02
2D NCI	0.04	0.02	0.06	0.04	-0.03	0.06	0.00	0.10
3D NCI	0.08	0.02	0.10	0.04	-0.02	0.06	0.00	0.08
Mean curvature	0.02	0.03	0.00	0.08	0.02	0.06	-0.01	0.08
Gaussian curvature	-0.09	0.07	-0.16	0.13	0.08	0.17	-0.26	0.64

We found that on average, ostia were smaller after treatment in comparison to pretreatment, as reflected by their area and diameters (Table 6.1). We also found a high positive correlation (PCC 0.80) between time passed between Pre and FU scans and shrinking of the ostium area, with a p-value of 0.03, pointing towards a significant correlation. This is supported by the yearly shrinkage rate of 0.58 ±4.88 mm², which is 2% area shrinkage per year on average. Shrinking of width and mean diameter showed a moderately positive correlation with time passed as well, but no statistical significance. Our small case number needs to be kept in mind, however. The shrinking of the ostia could be related to the healing process of the aneurysm after treatment, possibly including advancing fibrosis which has been described to be a feature of aneurysm healing [135], one of the goals of the CNS [29].

However, we also observed that on average, CH volume increased by 4%. At the same time, CH volume was, on average, 0.43 mm<sup>3</sup> smaller for FU data. This is likely due to individual cases. Five of seven cases were larger after treatment, but their average growth (1.41 mm<sup>3</sup>) was overall less than the other two cases' average shrinking (5.03 mm<sup>3</sup>).

This might be due to shape changes after treatment. We found FU ostia to be slightly less elongated than Pre ones, based on the average EI decreasing from 0.59 to 0.54, which makes a shrinkage of 10% per year. UI<sub>2D</sub> and NCI meanwhile increased, mean-

Table 6.2: All observations of parameters for cases 1 through 4, including differences between Pre and FU data ( $\Delta$ ) and rate of change per year ( $\frac{\Delta}{year}$ ).

(	Case 1		Case 2		Case 3		Case 4	
Parameter	Pre	FU	Pre	FU	Pre	FU	Pre	FU
Area (mm²)	13.47	16.42	16.31	12.40	15.50	16.55	19.22	12.59
Max diameter(mm)	4.78	5.29	4.70	4.07	5.24	4.85	5.74	4.66
Mean diameter (mm)	4.07	4.59	4.53	3.76	4.45	4.44	4.82	4.00
CH Volume (mm <sup>3</sup> )	5.43	8.24	6.39	8.41	6.73	7.09	10.05	4.15
EI	0.59	0.55	0.61	0.42	0.59	0.60	0.56	0.62
$_{ m 2D}$ UI $_{ m 2D}$	0.02	0.01	0.00	0.04	0.01	0.02	0.01	0.01
$3D UI_{2D}$	0.54	0.53	0.52	0.55	0.53	0.53	0.53	0.52
2D NCI	0.05	0.03	0.01	0.07	0.05	0.03	0.03	0.04
3D NCI	0.11	0.07	0.06	0.11	0.11	0.08	0.07	0.08
Mean curvature	0.03	0.02	-0.02	-0.10	0.01	0.03	0.02	0.04
Gaussian curvature	-0.26	-0.05	-0.05	-0.12	-0.11	-0.21	-0.05	-0.02
	Δ	$\frac{\Delta}{\text{year}}$	Δ	$\frac{\Delta}{\text{year}}$	Δ	$\frac{\Delta}{\text{year}}$	Δ	$\frac{\Delta}{\text{year}}$
Days	170	-	196	-	165	-	802	-
Area (mm²)	-2.95	6.34	3.91	-7.29	-1.05	2.33	6.63	-3.02
Max diameter(mm)	-0.51	1.09	0.63	-1.18	0.39	-0.86	1.08	-0.49
Mean diameter (mm)	-0.51	1.10	0.77	-1.44	0.01	-0.02	0.82	-0.37
CH Volume (mm <sup>3</sup> )	-2.81	6.04	-2.02	3.76	-0.35	0.87	5.89	-2.68
EI	0.04	-0.09	0.19	-0.36	-0.01	0.03	-0.06	0.03
${ m 2D~UI_{2D}}$	0.01	-0.03	-0.03	0.06	0.00	0.01	0.00	0.00
$3D UI_{2D}$	0.01	-0.02	-0.02	0.04	0.00	0.00	0.01	0.00
2D NCI	0.02	-0.04	-0.06	0.10	0.01	-0.03	-0.01	0.01
3D NCI	0.04	-0.08	-0.05	0.10	0.03	-0.06	0.00	0.00
Mean curvature	0.01	-0.02	0.08	-0.14	-0.02	0.03	-0.03	0.01
Gaussian curvature	-0.20	0.44	0.07	-0.13	0.09	-0.21	-0.03	0.02

ing after treatment, ostia were more concave and less circular. This increase, however, was very small, with yearly rates of change not above 0.01. 2D-projected ostia were overall very convex, Pre ostia  $\mathrm{UI}_{2D}$  being on average 0.01 and 0.03 for FU ostia. Despite such small changes,  $\mathrm{UI}_{2D}$  increased five times from Pre to FU on average. For the non-2D-projected  $\mathrm{UI}_{2D}$ , changes in Pre and FU were minuscule. The concavity, however,

Table 6.3: All observations of parameters for cases 5 through 7, including differences between Pre and FU data ( $\Delta$ ) and rate of change per year ( $\frac{\Delta}{y \, e \, \alpha \, r}$ ).

	Case 5		Case 6		Case 7	
Parameter	Pre	FU	Pre	FU	Pre	FU
Area (mm²)	9.14	10.18	14.40	13.74	20.61	11.19
Max diameter(mm)	4.37	3.99	4.42	4.51	5.78	4.07
Mean diameter (mm)	3.46	3.54	4.22	3.94	4.93	3.46
CH Volume (mm <sup>3</sup> )	3.24	3.25	5.39	7.23	10.47	6.31
EI	0.57	0.61	0.61	0.50	0.58	0.48
${ m 2D~UI_{2D}}$	0.02	0.01	0.00	0.03	0.01	0.08
$3D UI_{2D}$	0.53	0.53	0.52	0.52	0.53	0.55
2D NCI	0.08	0.04	0.01	0.07	0.02	0.16
3D NCI	0.10	0.07	0.04	0.11	0.06	0.19
Mean curvature	0.08	0.11	0.01	0.02	0.02	-0.13
Gaussian curvature	-0.06	-0.45	-0.03	-0.09	-0.04	-0.21
	Δ	$\frac{\Delta}{ ext{year}}$	Δ	<u> </u>	Δ	$\frac{\Delta}{ ext{year}}$
Days	81	-	263	-	554	-
Area (mm²)	-1.04	4.68	0.66	-0.91	9.42	-6.21
Max diameter(mm)	0.38	-1.72	-0-09	0.13	1.71	-1.12
Mean diameter (mm)	-0.08	0.35	0.26	-0.35	1.47	-0.97
CH Volume (mm <sup>3</sup> )	-0.01	0.06	-1.84	2.55	4.16	-2.74
EI	-0.04	0.17	0.11	-0.15	0.10	-0.07
$_{ m 2D}$ UI $_{ m 2D}$	0.01	-0.04	-0.03	0.04	-0.08	0.05
3D UI <sub>2D</sub>	0.01	-0.02	0.00	0.00	-0.03	0.02
2D NCI	0.04	-0.19	-0.06	0.09	-0.13	0.09
3D NCI	0.02	-0.11	-0.07	0.10	-0.12	0.08
Mean curvature	-0.03	0.12	-0.01	0.01	0.15	-0.10
Gaussian curvature	0.39	-1.75	0.07	-0.10	0.17	-0.11

was higher in 3D overall, averaging at 0.53 for both Pre and FU, confirming that information loss through projection is noteworthy. We conclude that ostia are in general quite concave, and only by projecting to their principal component, become convex. NCI achieved similar results, with a small absolute increase from Pre to FU ostia (as

little as 0.03), but a high increase in relation (up to three times larger). This supports the increase in curvature, with a three-time increase from Pre to FU ostia.

The cases with the highest EI and NCI pre-treatment also had the highest reduction rate of the respective index (see Table 6.2 and Table 6.3), but there were several cases where EI and NCI increased. Interestingly, in the case of NCI, four out of seven cases were less circular after treatment, on average three times less circular. Intuitively, one would expect increasing circularity after implantation of the circular CNS. The absolute changes in NCI were small, however, with 0.03 on average, and EI only increased by 0.05 on average.

The results of this study hint at complex interactions between the device and the aneurysm wall and their respective mechanical behaviors. With a sample size of seven cases, we can however not make any statements about statistical significances.

#### 6.2.3 Conclusion on the preliminary study on IA deformation after CNS treatment

While we cannot make a decisive statement about the change of the ostium shape after treatment with the CNS, we found that generally ostia sizes reduce over time according to size indices, with stronger shrinking as more time passed. This might enable faster endothelialization of the ostium and promote aneurysm healing [135]. We hypothesize this shrinking is related to the healing process of the vessel wall. We did not assess morphologic changes of the aneurysm sac in this study, which may complement the analysis of overall post-treatment changes in aneurysm morphology.

The results of this preliminary study provide valuable first insights into morphologic changes in IAs after CNS implantation which could be further used in hemodynamic and clinical studies to investigate their clinical impact.

#### 6.3 DEFORMATION ANALYSIS OF IA AND CNS AFTER TREATMENT

# Publication

Section 6.3 is based on:

[222] L. Spitz, J. Korte, F. Gaidzik, N. Larsen, D. Behme, B. Preim, and S. Saalfeld. "Deformation analysis of intracranial aneurysms after treatment with the Contour neurovascular system." Manuscript submitted for publication. Institute of Simulation and Graphics, Otto-von-Guericke University Magdeburg.

This work was conceptualized, designed, and implemented by L. Spitz.

As our preliminary study with 7 aneurysms found a shrinkage of the IA neck after CNS deployment of approximately 0.5  $\frac{mm}{year}$ , we meant to further confirm those findings by analysis the deformation longitudinally, as well as the CNS's deformation and correlations with time and recurrence.

This study thus presents a comprehensive longitudinal deformation analysis of

- the IA neck and ostium after CNS deployment over time
- the CNS itself

as well as investigating the correlation of IA morphology and recurrence.

Thus, we assess consistency and robustness of the CNS over time. Our null hypothesis  $H_0$  is therefore that there is no effect of the CNS on IA ostium morphology after deployment and over time, and no effect of the CNS itself over time.

#### 6.3.1 Materials and methods for IA and CNS deformation analysis

We had retrospective access to 13 IAs treated with the CNS from two German hospitals. Each IA was scanned between 2 and 5 times, resulting in a total of 48 scans (see 6.3).

IMAGING Each IA was scanned at least once before and once after CNS deployment, with scans being either 3D rotational DSA or 3D CTA scans. Examinations were performed on biplane angiography systems (Allura Xper FD 20/10, Philips, The Netherlands, or Axiom Artis Q, Siemens Healthcare, Germany), where spatial resolution ranged from  $384 \times 384 \times 384 \times 512 \times 512 \times 355$ , and isotropic voxel size ranged from 0.16 to 0.47 mm after reconstruction.

LONGITUDINAL DATA Most IAs had multiple follow-up scans after treatment, and extra scans taken during CNS deployment, amounting to a total of 48 scans (see Fig. 6.3). Pre-treatment scans were done for three IAs. All thirteen IAs had a pre-interventional scan taken right before deployment, and eight had a postprocedural scan right after deployment. Those that did not have a postprocedural scan taken had at least one follow-up scan. Nine IAs had a second follow-up, and two had a third.

The average time between scans not taken on the same day was seven months, and average time between first and last scan was 16 months, with a minimum of six and a maximum of 26 months.

#### Data processing

We followed and expanded the data processing from Section 6.2, resulting in the pipeline in Figure 6.4.

Patient	CNS Size	Reper- fusion	-	Intervention (I)		Months passed since intervention Subscript x <sub>i</sub> are scans used for group i											
			ment scan	Pre-I scan	Post-I scan	* Tw	o sc	ans o			day 9	12	1	5	18	21	26
01	7	no		X <sub>1,2,4</sub>	x <sub>1</sub>			x <sub>2</sub>								x <sub>2</sub>	
02	11	no	X <sub>4</sub>	x <sub>0,1,2</sub>	X <sub>1</sub>			X <sub>2</sub>	2			x <sub>2</sub>					
03	7	yes		x <sub>2,4</sub>						<b>X</b> <sub>2</sub>							
04	11	no		X <sub>2,4</sub>											x <sub>2</sub>		
05	9	no		X <sub>1,2,4</sub>	<b>x</b> <sub>1</sub>				<b>x</b> <sub>2</sub>					X	2		
06	7	no		X <sub>1,2,4</sub>	<b>x</b> <sub>1</sub>			<b>X</b> <sub>0,</sub>	,2				X <sub>2</sub>	2			
07	9	no		X <sub>1.2,4</sub>	x <sub>1</sub>			X <sub>0,2</sub>	*					x <sub>2</sub>			
08	5	no	X <sub>4</sub>	x <sub>0,2</sub>			<b>x</b> <sub>2</sub>										
09	9	yes		X <sub>1,2,4</sub>	<b>x</b> <sub>1</sub>			)	× <sub>2</sub>				x <sub>2</sub>				
10	9	yes	X <sub>4</sub>	X <sub>0,1,2</sub>	<b>x</b> <sub>1</sub>		<b>x</b> <sub>2</sub>				<b>x</b> <sub>2</sub>						
11	11	no		X <sub>2,4</sub>				X <sub>2</sub>	2								X
12	7	no		X <sub>1,2,4</sub>	x <sub>1</sub>			x <sub>2</sub>									
13	7	no		X <sub>2,4</sub>		<b>x</b> <sub>2</sub>											x <sub>2</sub>
		•	1	·				6m	cas	es		1y-	+ ca	ises			

Figure 6.3: List of cases, their CNS size and whether they have a recurrence, along with scans taken and which group they were assigned for deformation analysis. The "i" in  $x_i$  denotes group. \* marks dates on which two scans were taken. Group explanation to be found in Sec. 6.3.2. Own figure from **Spitz** et al. [222].

SEGMENTATION AND MESH POST-PROCESSING An initial segmentation of the vasculature was adapted from Chapter 3. As the IA sac was not visible in post-treatment scans due to the CNS disrupting flow of the contrast agent, the IA sac of the pre-treatment scan was manually stitched onto the neck remnant of the post-treatment IAs.

The CNS was roughly segmented from the scans via the same methods. Due to the scan resolution, artifacts were present, and no wires were visible. A CAD model of the CNS, courtesy of Cerus Endovascular (acquired by Stryker in 2023), was then manually registered via the radiopaque markers, and smoothly deformed via a Lattice modifier (Blender 3.6.4, The Blender Foundation, The Netherlands) to fit to the CNS segmentation and into the vasculature. For later processing and due to the size of the original CAD model the deformed CNS models were reduced to 5% of their original size via quadric edge collapse [93], which did not affect deformation analysis.

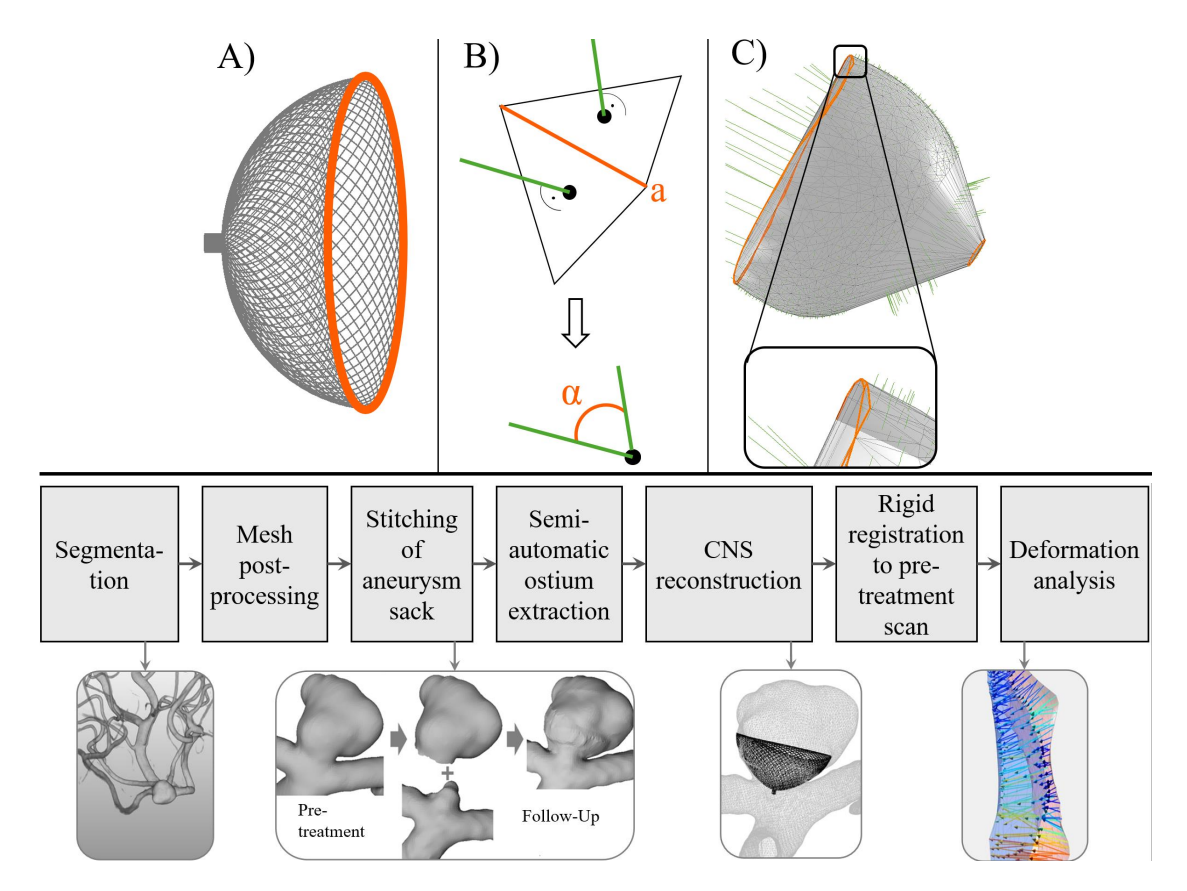


Figure 6.4: Upper: A) CNS with highlighted edge ring (orange). B) Angle  $\alpha$  of edge a (orange), determined by face normals (green). C) CH of a CNS, with face normals (green) and candidate edges for edge ring (orange). Lower: Data processing pipeline, inspired by and expanding upon [223]. Own figures from **Spitz** et al. [222].

EXTRACTION OF MORPHOLOGY IA ostium and pre-treatment IA morphological parameters were extracted semi-automatically as part of the segmentation pipeline.

Size and shape parameters of the ostia as well as the CNS were calculated in Matlab 2023a. As the CNS is a complex double-layered wire mesh, we calculated size parameters based on its convex hull (CH) and its edge ring (see Fig. 6.4 A), meaning the top rim of the CNS. The triangulated mesh of the CNS convex hull was examined for edges where the connecting triangles had an angle >15°. Angle was determined via the adjacent faces' normals (see Fig. 6.4 B). Due to CNS shape, most edges had an angle close to o°, and only the radiopaque marker edge and edge ring of the CNS remained with less flat edge angles. However, the top ring edges were not perpendicular, necessitating a smaller threshold to capture a completed ring of candidate edges (see Fig. 6.4 C). These edges were connected to the edge ring.

MORPHOLOGICAL PARAMETERS Size and shape of the CNS edge ring were assessed with the same parameters as the IA ostium: area, width (defined as maximum diameter), mean diameter, CH volume, and the shape indices EI, NCI, and UI. For NCI and UI, 2D adaptations of the non-sphericity index and UI that do not require volume measurements were used, same as in Section 6.2 [165].

For all parameters, yearly rate of change was calculated  $(\frac{\Delta}{year})$  due to inconsistent intervals between scans.

All scans of one IA were rigidly co-registered using ICP via point-based alignment in Meshlab v2o22.o2 [59]. After registration, average symmetric surface distance (ASSD), the mean distance of all points of one mesh to all points on the other mesh and vice versa was calculated for ostium and CNS.

#### 6.3.2 Results of IA and CNS deformation analysis

Using the co-registered meshes, we analyzed ASSD and morphological parameters of the ostium, CNS, and CNS edge ring (see Figure 6.5). Parameters were grouped and compared based on when the scans were taken or if they had a recurrence. The groups were:

- **Group o: Intra-patient variance.** Assesses deformation of scans taken on the same day or with little time passing and without intervention in between, determining range of observed deformation due to patient movement, segmentation ambiguity, resolution, etc. Acts as control group. Five patients: 02, 06, 07, 08, 10.
- **Group 1: Postprocedural changes.** Assesses deformation from pre- to postprocedural scans. Eight patients: 01, 02, 05, 06, 07, 09, 10, 12.
- **Group 2: Longitudinal changes.** Assesses deformation between pre-treatment and last follow-up scan. For CNS parameters, postprocedural scan was used as first scan. All 13 patients.
- **Group 3: Changes over 6 months versus after years.** Assesses differences in rates of change within the first 6 months (6m) and after more than one year (1y+). 6m: Eight patients: 01, 02, 05, 06, 07, 09, 11, 12. 1y+: Nine patients: 01, 02, 04, 05, 06, 07, 09, 11, 13.
- **Group 4: Correlation with recurrence.** Assesses correlation between morphology and recurrence, and morphological differences of IAs with and without recurrence, as well as correlation of deformation with time passing across all groups. All 13 patients.
- **Group 5: Spatial changes.** Assesses position changes of the CNS via ASSD. All 13 patients.

Results of groups o to 4 are displayed in Tab. 6.5.

#### Statistical analysis

For statistical analysis, we used RStudio 2024.04.2 (vPosit Software, PBC, USA). A paired student t-test was done for pairwise comparison. Normality was assessed with Shapiro-Wilk's method, as well as visually confirmed using QQ-plots. Homogeneity of variance was assessed with the Levene test. In case of non-normality or inhomogeneity, a Mann-Whitney-Wilcoxon test was used.

#### Group o: Intra-patient variance

Group o assesses the range of observed deformation due to patient movement, different scanning devices, segmentation ambiguity, scan resolution, etc. While we use "shrinking" and "increase", the intra-patient variance is meant to assess the entire range of deformation that can occur due to the mentioned reasons.

The range of relevant parameter changes was as follows:

- Ostium area  $\Delta$ : -8.99 to 4.56 mm<sup>2</sup>
- Ostium width  $\Delta$ : -1.87 to 0.74 mm
- Ostium mean diameter  $\Delta$ : -1.27 to 0.56 mm
- Ostium EI Δ: -0.22 to 0.11
- Ostium UI Δ: -0.04 to 0.04
- Ostium NCI Δ: -0.11 to 0.06

Two pairs of scans featuring a CNS were taken on the same day. One CNS grew by 23.65 mm², the other shrank by 18.05 mm². One patient CNS parameter increasing while the other's shrank continued for the rest of the size parameters. For CNS ring area, one case grew by 2.02 mm², and the other shrank by -10.89 mm². Shape parameters UI and NCI of the CNS ring showed no change, while both scans showed a small ring EI increase.

Intra-patient variance was not statistically significant.

### Group 1: Postprocedural changes

Ostium size increased after CNS deployment. EI shrank and had the widest range of all shape indices, ranging from 0.46 to 0.73. UI stayed between 0.52 to 0.57. NCI stayed low, ranging between 0.05 and 0.17.

EI change was statistically significant with a p-value of 0.01 and NCI change with a p-value of 0.04.

Figure 6.5: Average results of all groups. Vol stands for volume, Dia for diameter. Cursive numbers marked with \* have a statistically significant difference. Own figure from **Spitz** et al. [222].

Group 0	Scan 1	Scan 2	Δ		Scan 1	Scan 2	Δ
Ostium Param	eters $(n = 5)$			CNS Parameters	s(n=2)		
Area	24.02 ±8.92	25.15 ±10.25	1.14 ±5.20	Area	111.10 ±42.66	113.90 ±21.81	2.80 ±20.37
Width	$6.56 \pm 1.41$	$6.40 \pm 1.24$	-0.16±0.92	CH Vol	87.05 ±49.52	$86.50 \pm 26.23$	-0.55 ±23.29
Mean Dia	$5.38 \pm 1.05$	$5.46 \pm 1.16$	$0.07 \pm 0.69$	Ring Area	30.45 ±13.87	26.01 ±7.41	-4.44 ±6.64
CH Vol	14.89 ±6.36	$15.88 \pm 3.45$	$0.99 \pm 5.81$	Ring Width	$6.84 \pm 1.48$	5.47 ±0.86	$-0.38 \pm 0.61$
EI	$0.57 \pm 0.07$	$0.52 \pm 0.09$	$-0.04 \pm 0.11$	Ring Mean Dia	$6.16 \pm 1.41$	$5.80 \pm 0.85$	$-0.36 \pm 0.57$
UI	$0.55 \pm 0.01$	$0.54 \pm 0.01$	$0.00 \pm 0.02$	Ring EI	$0.59 \pm 0.01$	$0.68 \pm 0.02$	$0.09 \pm 0.01$
NCI	$0.14 \pm 0.03$	$0.12 \pm 0.04$	$-0.02 \pm 0.06$	Ring UI	$0.50 \pm 0.00$	$0.50 \pm 0.00$	$0.00 \pm 0.00$
				Ring NCI	$0.02 \pm 0.01$	$0.02 \pm 0.00$	$0.00 \pm 0.00$
Group 1	Scan 1	Scan 2	Δ				
Ostium Param	eters $(n = 8)$						
Area	20.75 ±9.76	22.04 ±10.29	1.29 ±4.77				
Width	$5.79 \pm 1.30$	$6.03 \pm 1.32$	$0.24 \pm 0.91$				
Mean Dia	$5.01 \pm 1.08$	$5.06 \pm 1.18$	$0.05 \pm 0.55$				
CH Vol	$10.45 \pm 6.00$	$15.45 \pm 8.92$	$5.00 \pm 7.74$				
EI	0.59 ±0.08	$0.51 \pm 0.07$	-0.07 ±0.06*				
UI	$0.53 \pm 0.01$	$0.55 \pm 0.02$	$0.01\pm0.01$				
NCI	0.10 ±0.03	$0.13 \pm 0.04$	0.04±0.04*				
Group 2	Scan 1	Scan 2	Δ/year		Scan 1	Scan 2	Δ/year
Ostium Param	eters $(n = 13)$		•	CNS Parameters	s(n=13)		•
Area	18.97 ±8.37	18.78 ±8.58	-1.09 ±6.07	Area	74.25 ±15.91	87.12 ±27.12	9.75 ±26.50
Width	$5.56 \pm 1.13$	$5.68 \pm 1.46$	$0.03 \pm 1.20$	CH Vol	87.98 ±42.83	94.71 ±34.44	$1.96 \pm 24.56$
Mean Dia	$4.76 \pm 0.96$	$4.73 \pm 1.04$	$-0.10\pm0.79$	Ring Area	31.29 ±9.55	$35.53 \pm 11.30$	$4.69 \pm 6.64$
CH Vol	$9.65 \pm 5.28$	$10.52 \pm 6.51$	$0.08 \pm 6.60$	Ring Width	6.85 ±1.09	$7.28 \pm 1.04$	$0.30 \pm 0.86$
EI	$0.58 \pm 0.07$	$0.56 \pm 0.08$	$-0.01 \pm 0.12$	Ring Mean Dia	6.29 ±0.98	$6.78 \pm 1.05$	$0.40 \pm 0.62$
UI	$0.53 \pm 0.01$	$0.54 \pm 0.02$	$0.01 \pm 0.02$	Ring EI	$0.66 \pm 0.11$	$0.75 \pm 0.08$	$0.10 \pm 0.17$
NCI	$0.09 \pm 0.04$	$0.11 \pm 0.04$	$0.01 \pm 0.06$	Ring UI	$0.50 \pm 0.00$	$0.50 \pm 0.01$	$0.00 \pm 0.00$
				Ring NCI	$0.01 \pm 0.01$	$0.01 \pm 0.00$	$0.00 \pm 0.00$
Group 3	6m Δ/year	1y+ ∆/year			6m Δ/year	1y+ ∆/year	
Ostium Param	eters			CNS Parameters	\$		
Area	1.81 ±14.22	$0.66 \pm 3.50$		Area	57.97 ±92.94	-2.33 ±34.00	
Width	$0.31 \pm 2.20$	$0.62 \pm 1.27$		CH Vol	-19.61 ±24.36	20.52 ±34.05*	
Mean Dia	$0.53 \pm 1.81$	$0.13 \pm 0.55$		Ring Area	$9.94 \pm 8.93$	$7.89 \pm 8.98$	
CH Vol	-1.88 ±20.55	$-3.82 \pm 5.79$		Ring Width	$0.82 \pm 1.20$	$0.71 \pm 0.81$	
EI	$0.12 \pm 0.21$	$0.05 \pm 0.11$		Ring Mean Dia	$0.91 \pm 0.86$	$0.72 \pm 0.77$	
UI	$-0.02 \pm 0.05$	$0.00 \pm 0.02$		Ring EI	-0.12 ±0.06	$0.05 \pm 0.11$	
NCI	$-0.07 \pm 0.13$	$0.02 \pm 0.05$		Ring UI	$0.00 \pm 0.00$	$0.00\pm0.00$	
				Ring NCI	$0.00 \pm 0.01$	$0.00\pm0.00$	
Group 4	All	Full occlusion	Reperfusion				
IA Parameters	. ,	(n=9)	(n=3)				
Area	$168.29 \pm 86.91$	166.54 ±78.33	$173.54 \pm 108.51$				
Width	$9.39 \pm 2.31$	$9.47 \pm 2.00$	$9.15 \pm 3.06$				
CH Vol		$240.70 \pm 153.93$					
Aspect Ratio	$1.57 \pm 0.68$	$1.53 \pm 0.52$	$1.69 \pm 1.01$				
EI	$0.25 \pm 0.01$	$0.25 \pm 0.01$	$0.26 \pm 0.02$				
UI	$0.09 \pm 0.04$	$0.10 \pm 0.04$	$0.07 \pm 0.002$				
NSI	$0.18 \pm 0.05$	$0.19 \pm 0.03$	$0.16 \pm 0.11$				

#### Group 2: Longitudinal changes

Ostium size changed very little over time. More ostia decreased in size than increased, but one patient showed a particularly strong increase in ostium size, ostium area alone increasing by a total of  $16.89\,\mathrm{mm}^2$ , while total area change of all other ostia ranged between  $\pm 0.41$  to  $\pm 7.46\,\mathrm{mm}^2$ . The same patient increased by  $2.74\,\mathrm{mm}$  in width and  $2.19\,\mathrm{mm}$  in mean diameter, where the rest of the IAs width and mean diameter change ranged from  $\pm 0.01$  to  $1.39\,\mathrm{mm}$  and  $\pm 0.01$  to  $1.03\,\mathrm{mm}$ , respectively. Excluding this patient would result in mean changes of  $-2.20\,\pm 4.15\,\frac{\mathrm{mm}^2}{\mathrm{year}}$  for area,  $-0.15\,\pm 1.00\,\frac{\mathrm{mm}}{\mathrm{year}}$  for width, and  $-0.24\,\pm 0.55\,\frac{\mathrm{mm}}{\mathrm{year}}$  for mean diameter. Changes of ostium shape indices were small.

The CNS and its edge ring size increased over time in the averages. Half of the ten patients with more than one CNS scan showed an increase in CNS area. Those whose area shrank, however, shrank by a range of -2.10 to -14.07 mm², while the range of increase of those whose area grew was 6.95 to 72.07 mm². The CNS edge ring only shrank in three of the ten patients. The CNS edge ring changed little in shape.

We found no statistically significant longitudinal changes.

#### Group 3: Changes over six months versus after years

For most parameters, the 6m  $\frac{\Delta}{y\,e\,a\,r}$  was larger than the 1y+  $\frac{\Delta}{y\,e\,a\,r}$ , with the exceptions of ostium CH volume, NCI, CNS width, and CNS ring EI. We found a statistically significant difference in the differences of CNS CH volume (p-value = 0.02), which, on average, initially decreases by -19.61  $\pm$ 24.36  $\frac{m\,m^3}{y\,e\,a\,r}$  at 6m, but then increases by 20.52  $\pm$ 34.05  $\frac{m\,m^3}{y\,e\,a\,r}$  at 1y+.

#### Group 4: Correlation with recurrence

Looking at pre-treatment parameters of the IAs (including the IA sac), one of the cases with recurrence was a small IA (area: 43.61 mm², width: 5.27 mm, CH volume: 37.90 mm³, AR: 0.66) while another was a large aneurysm (area: 309.21 mm², width: 12.74 mm, CH volume: 488.02 mm³, AR: 3.06). That first IA is the smallest IA of all cases, while there was one case with full occlusion that was the largest IA (area: 316.36 mm², width: 13.62 mm, CH volume: 543.12 mm³, AR: 2.56). There was no statistically significant correlation between recurrence and any of the morphological pre-treatment IA parameters, or in the average differences between recurrence and full occlusion cases.

In group 2, longitudinal change, two parameters had statistically significant differences between recurrence and full occlusion cases:  $\frac{\Delta}{y \, e \, ar}$  of ostium EI (p-value: 0.02) and of ostium NCI (p-value: 0.03).

Ostium EI change for recurrence cases was -0.05  $\pm$ 0.04  $\frac{\Delta}{year}$ , and 0.08  $\pm$ 0.08  $\frac{\Delta}{year}$  for full occlusion cases. Of the recurrence cases, two cases had a decrease in EI of -0.08 and -0.07, while the last had a small increase of 0.01. From the full occlusion cases, only

two had a decrease in EI, both being very small, -0.02 and -0.01. Change of ostium NCI was 0.05  $\pm$ 0.03  $\frac{\Delta}{y\,e\,a\,r}$  for recurrence cases and -0.03  $\pm$ 0.05  $\frac{\Delta}{y\,e\,a\,r}$  for full occlusion cases. All three recurrence cases' NCI increased, while of the full occlusion cases all but two showed an NCI decrease.

We found no statistical significance or correlations.

#### Group 5: Spatial changes

Ostia had an average ASSD of  $0.54 \pm 0.29$  mm and the CNS had an average ASSD of  $0.63 \pm 0.33$  mm. ASSD of group 0, intra-patient variance, was  $0.55 \pm 0.33$  mm for ostia, and  $0.47 \pm 0.23$  mm for CNS. For group 2, longitudinal change, ASSD was  $0.55 \pm 0.26$  mm on average for ostia, and  $0.64 \pm 0.35$  mm for CNS for all patients. The three IAs with a recurrence had an average ASSD of  $0.44 \pm 0.27$  for ostia, and  $0.55 \pm 0.33$  mm for CNS, while the ten IAs with full occlusion had an average ASSD of  $0.58 \pm 0.25$  mm for ostia and  $0.69 \pm 0.36$  mm for CNS.

One recurrence case had a low ASSD of 0.25  $\pm$ 0.12 mm, and the other two cases with recurrence also had below-average ASSD. Overall, ostia ASSD ranged between 0.23 and 0.88 mm. The case with smallest ostium ASSD was a case with full occlusion with ostium ASSD 0.23  $\pm$ 0.10 mm. One full occlusion case had a high ASSD of 1.39  $\pm$ 0.89 mm, while the rest of CNS ASSD ranged from 0.35 to 0.74 mm. Both highest and lowest CNS ASSD cases were full occlusion cases.

We found no statistically significant spatial changes.

### 6.3.3 Discussion of IA and CNS deformation analysis

We compared a variety of morphological parameters of IAs treated with the CNS over multiple follow-up scans.

Comparison to intra-patient variance

Group 0, intra-patience variance, was generally smaller than postprocedural changes (group 1). The ranges were comparable save for ostium CH volume, which was 5.00  $\pm$ 7.74 mm<sup>3</sup> in group 1 and 0.99  $\pm$ 5.81 mm<sup>3</sup> in group 0. There was no statistically significant difference between the groups.

CNS deformation of group 0 and group 2 was very different, developing in different directions for CNS CH volume, CNS ring area, CNS ring width, and mean diameter. The absolute change was generally bigger in group 2, and a limitation of group 0 is the small number of cases with CNS (n = 2), which markedly also deformed in different directions. Group 2 deformations were overall within observed intra-patient variance.

Differences between group o and all other groups were not statistically significant. Combined with the lack of correlation between time and recurrence and any of the parameters, we are unable to reject the null hypothesis of the CNS having no effect on

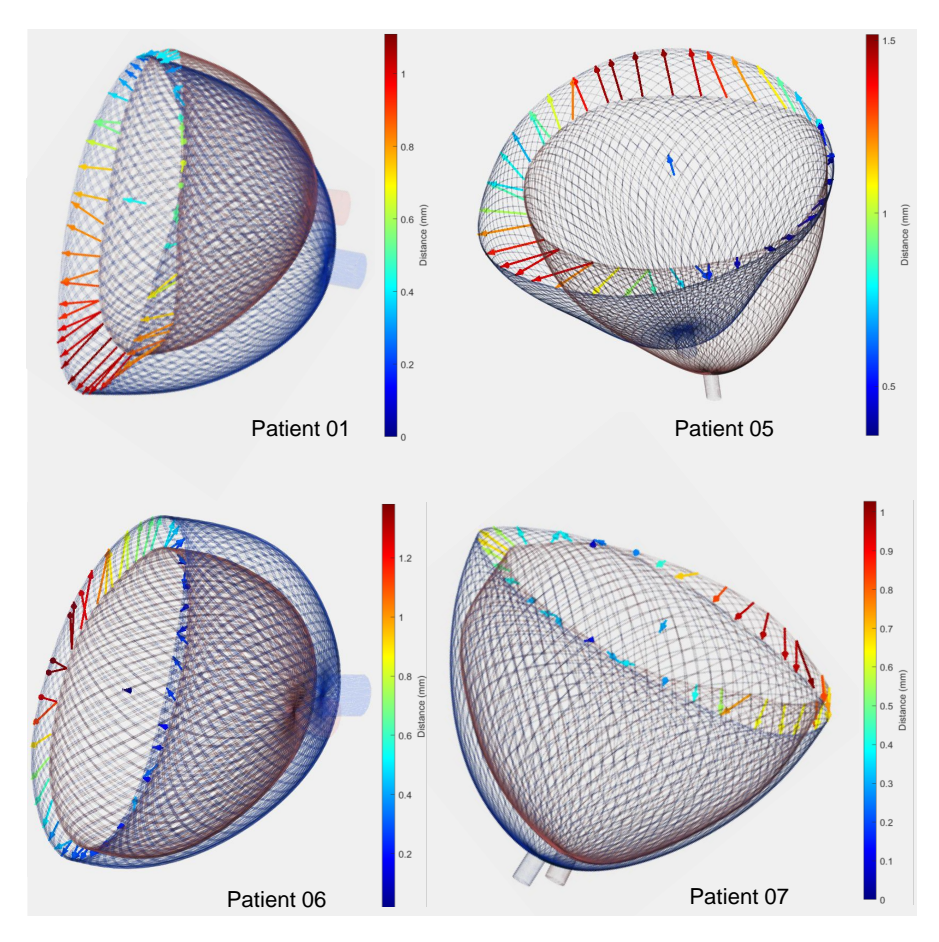


Figure 6.6: Example cases of CNS, registered and with color-coded arrows highlighting deformation at the edge ring. Red CNS are postprocedural, blue CNS are latest follow-up. Own figure from **Spitz** et al. [222].

the ostium of the IA after deployment, and the CNS shape not changing over time. This may indicate the robustness of the CNS over time, however, lack of statistically significance does not mean a lack of deformation, so a study to confirm this is necessary. We theorize that due to the lack of statistical significance or observed changes between recurrence and full occlusion cases, recurrence cannot be predicted by IA morphology, or the observed CNS parameters. This is in line with another recent study that assessed correlation with IA morphology and rupture [99].

#### Comparison of observations

The strongest deformations occurred in group 1, postprocedural changes.

The statistical significance of postprocedural changes of ostium EI and NCI point towards the CNS deforming the ostium. EI decreased on average and in six out of eight

cases. The two other cases showed a very small increase (<0.01) and were also the only cases where NCI decreased. Most aneurysms had a less elliptical ostium after CNS deployment, while the ostium was also less perfectly circular.

Group 1's changes are stronger than group 2's. The direction of the deformation was the same for all parameters except for ostium area. This may be due to an initial postprocedural deformation that leads to an increase in area, whereas over time, the healing process facilitated by the CNS leads to a decrease in area. However, neither change was statistically significant.

In group 3, 6m and 1y+ changes, we found that 6m  $\frac{\Delta}{year}$  is almost always stronger than 1y+  $\frac{\Delta}{year}$ , indicating that the strongest changes happen in the time after deployment with the CNS settling and becoming more stable the more time passes. We, however, only observed statistically significant changes when comparing 6m and 1y+  $\frac{\Delta}{year}$  for CNS CH volume. CNS CH volume shrinks and then grows 1y+ later. The growing in the year later may be due to thrombus formation expanding the visible CNS. However, the CNS ring CH volume grows more strongly in the first 6m and then less in 1y+, which would imply a stronger deformation or thrombus formation in the first 6 months rather than a year later. This was, however, not statistically significant.

#### Comparison to preliminary study

The preliminary study from Section 6.2 performed a longitudinal comparison of seven ostia with one pre-interventional scan and one follow-up scan. In group 2, longitudinal change, we found similar ostium area shrinkage over time, namely a yearly shrinkage of -1.09  $\pm 6.07 \, \frac{\text{mm}^2}{\text{year}}$ , compared to the preliminary study's -0.58  $\pm 4.88 \, \frac{\text{mm}^2}{\text{year}}$ . Here, however, an increase of ostium width was found, though, upon exclusion of a case with a particularly high ostium size increase after treatment, average ostium width decreases to -0.15  $\pm 1.00 \, \frac{\text{mm}}{\text{year}}$ , compared to -0.59  $\pm 0.87 \, \frac{\text{mm}}{\text{year}}$  in the preliminary study. Mean diameter decrease in our longitudinal analysis was comparable to the preliminary study's. Our results for shape changes are comparable with the preliminary study.

Unlike in the preliminary study, here we found no correlation or statistical significance between time passing and ostium area shrinkage, or any other parameters.

#### Comparison to other device deformations

Other IFDs and FDs are subject to deformations. For the WEB, the major alternative of the CNS, the compression phenomenon is discussed, where the entire device seems to shrink within the IA sac. Median shrinkage is about 50% of WEB height [40]. Exact causes of the deformation are unclear, but studies report this occurring in 25 to 57.2% of cases [30]. The compression seems to not affect occlusion rate [30, 40].

Deformations have also been reported for stents, affecting the struts of the stent, porosity and pore density, altering blood flow through the stent after deployment [32]. Another concern is vessel straightening, where the radius of curvature of the parent

vessel increases 3.6  $\pm$ 2.7 mm after stent deployment, which is more than 50% of the pre-deployment value [131].

The changes we observed in CNS deformation were much smaller, and not statistically significant. Even our ASSD of the CNS is under 1 mm. The CNS thus shows a promising robustness to deformation over time.

#### Limitations

The changes we observed may partially be due to scan resolution and segmentation ambiguity. Scan resolution ranged from 0.16 to 0.47 mm, which is partially larger than the changes observed. Additionally, scans are subject to noise. While segmentation was performed as consistently as possible by an experienced user, there is ambiguity during the segmentation process. The same case may have a range of segmentation parameters that may appear as a valid segmentation, without a definite ground truth. For CNS segmentation, overexposure of the radio-opaque marker proved an additional challenge. This, along with patient movement as well as the brain not being a static object, may partially be the reason for the observed deformations.

An automatic segmentation would be desirable, however, there is no segmentation available for the CNS, and not enough data was available to train a DL network. To address this, the use of pipelines that automatize the aneurysm detection and morphology extraction from a presented vessel mesh, like the one presented by Lawonn et al. [136] would be feasible. While that approach does not segment and extract a 3D surface mesh from imaging scans, instead using a surface mesh geometry as input, the approach can handle a level of noise on the mesh, meaning it could be used together with an automatic surface mesh generation [136].

Deformation also varied strongly from patient to patient. 13 aneurysms may not be able to represent every possible deformation case, and a larger study should confirm our results. This may also be why the study resulted in a lack of statistically significant results. While this may seem promising, a lack of statistically significant deformation does not mean there is no deformation. Further studies are necessary to confirm the results.

# 6.3.4 Conclusion on IA and CNS deformation analysis

The presented study showed no statistically significant influence of the CNS on IA morphology over time. We found no correlation between recurrence and morphology and no differences in recurrence and full occlusion cases. This is a promising result for the consistency of the CNS and it robustly disrupting blood flow into the IA sac over time. The non-significant observed changes may occur due to too low imaging resolution and ambiguity in model segmentation. Due to limitations, a larger study is necessary to gain statistically significant results. We showed first proof of a lack

of statistically significant IA morphological change, and a lack of correlation between morphology and recurrence.

#### 6.4 conclusion on analysis of longitudinal aneurysm deformation

We closed the gap in CNS research by performing a detailed analysis of how the CNS affects IA morphology over time after treatment, as well as assessing deformation of the CNS itself. At the same time, we answered RQ 2: how to analyze longitudinal morphological deformation.

We did this by presenting a study and its preliminary study of the effect of treatment with the CNS on the IA neck curve, ostium, and the CNS itself, as well as correlations with recurrence. While the smaller preliminary study found a small but statistically significant reduction of ostium area, the larger study found no significant changes of the ostium over time. Together with no significant deformations of the CNS over time, we conclude that the CNS may be robust in its shape and does not generally significantly deform the IA, though further studies are necessary.

We further found no correlation between morphology and recurrence, meaning IA morphology pre-treatment and IA and CNS morphology post-treatment do not seem to influence treatment success.

While more studies with more patients that observe a longer timeframe are necessary, these results are promising and pave the way for future studies that will further establish the CNS for treatment of WNBAs, and possibly other IAs. None of these studies would be possible without in-depth analysis of IA morphology.

# Part IV

MORPHOLOGY-DRIVEN ANALYSIS OF INTRACRANIAL ANEURYSMS FOR COHORT-BASED RESEARCH

# ANALYSIS OF INTRACRANIAL ANEURYSMS FOR SUBGROUP SELECTION

Careful consideration of treatment is particularly important for IAs, as both endovascular treatment and microsurgical clipping may entail unnecessary complications for the patients, especially for asymptomatic, incidental aneurysms with a low rupture risk [127]. Various features, including morphologic parameters describing their size and shapes and hemodynamic parameters describing the blood flow within them, as well as metadata referring to the patient-related characteristics, are relevant in IA research, rupture assessment, and determining treatment options [69, 102]. Rupture risk assessment and subgroup selection therefore are of high value in this area [68, 69, 127, 179].

When researching pathologies and their causalities, matching cohorts and finding cases with similar features, i.e., identifying certain patient subgroups, is an important step in determining possible risk factors. Looking beyond research at treatment decisions, where patient-specific analysis is essential, there are cases where multiple patients or entire cohorts must be considered.

This thesis wants to answer

RQ 3: to what extent can morphology-driven analysis support cohort-based research questions?

by providing computational support to match cohorts and identify subgroups. This is not only relevant for research, but also for clinical practice, as finding similar features of incoming patients to those of already treated ones can support physicians in diagnosis and treatment decisions.

The identification of such subgroups is not trivial. The complexity of the task rises with the number of both patients and features based on which similarity shall be determined, and with the different types of features that shall be considered. With manual selection of similar cases, it is often only possible to select few features that shall match, and these matches often have to be exact or are based on a threshold, making no use of the distances of continuous variables [126, 138, 178]. Another issue is that individual hospitals generally only rely on their own experience, or the experience of individual surgeons, to draw on for treatment decisions. Automatic subgroup selection that takes into account the various features that affect rupture risk and treatment success, as well as the experience from multiple clinics and surgeons, is thus potentially valuable.

Another area that may benefit from automatic subgroup selection is training simulations for trainee surgeons. Training simulations enable trainees to gather experience, gain spatial skills, and learn the procedure of an intervention in a safe environment.

Especially for surgical IA treatment, where there are fewer cases to train on, training simulations can be crucial [122]. As more and more training simulations are developed, the question of training case selection arises. The IAs a student trains on should be realistic and representative of the scenarios they may encounter in real patients.

This thesis presents two approaches to subgroup selection for IAs:

- For research and to support rupture risk assessment and treatment decisions, utilizing case-based reasoning (CBR), to find a subgroup of similar cases, in Section 7.1
- For training case selections in training simulations, utilizing instance selection (IS), to find subgroup representative of the entire database, in Section 7.2

With these two subgroup selection methods, we aim to answer RQ 3, as the subgroup selection, which relies on analysis, can match cohorts as well as reveal new avenues for research.

#### 7.1 SUBGROUP SELECTION OF INTRACRANIAL ANEURYSMS VIA CASE-BASED REA-SONING

# Publications

Section 7.1 is based on:

[226] **L. Spitz**, V. M. Swiatek, B. Neyazi, I. E. Sandalcioglu, B. Preim, and S. Saalfeld. "An interactive tool for identifying patient subgroups based on arbitrary characteristics for medical research." In: Curr Dir Biomed Eng 7.1 (2021), pp. 43–46. doi: 10.1515/cdbme-2021-1010,

which in turn is based on:

[224] **L. Spitz**, U. Niemann, O. Beuing, B. Neyazi, I. E. Sandalcioglu, B. Preim, and S. Saalfeld. "Combining visual analytics and case-based reasoning for rupture risk assessment of intracranial aneurysms." In: Int J Comput Assist Radiol Surg 15.9 (2020), pp.1525-1535. doi: 10.1007/s11548-020-02217-9

Both works were conceptualized, designed, and implemented by L. Spitz.

Case-based reasoning (CBR) is a method that applies experiences from previously solved cases to a newly presented case, mimicking how a domain-expert would solve a problem. The cycle of CBR is displayed in Figure 7.1, and comprises the following steps:

- When a new case is presented, previously solved cases are *retrieved* from a database
- The solutions of the previously solved cases are *reused* to solve the new case
- The solution is *revised* to fit the new case
- The new, now solved, case is now *retained* in the database to be used for more new cases in the future.

Using experience to solve a new case is reminiscent of how physicians chose to treat a newly discovered pathology, inspiring the use of CBR for IAs with its varied parameters and treatment options.

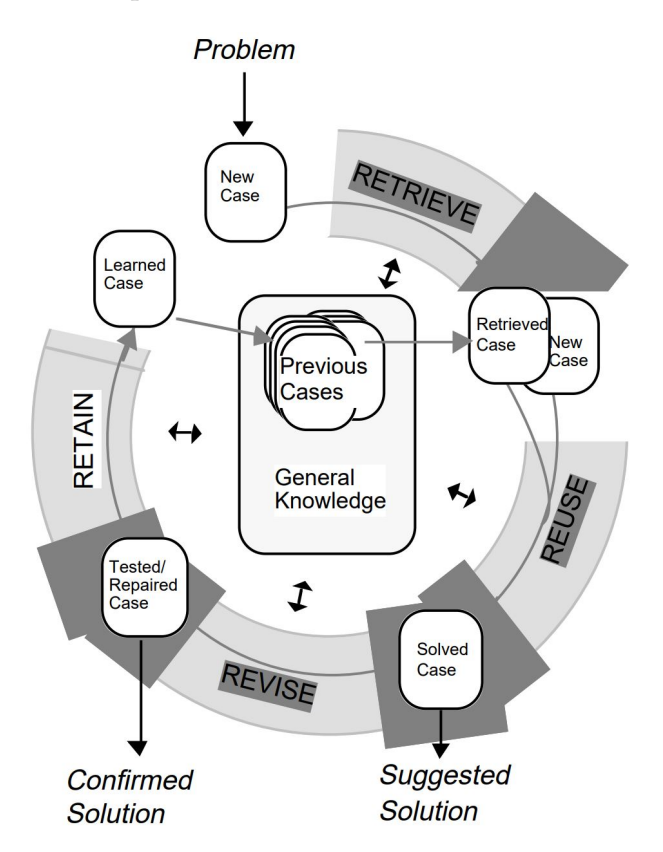


Figure 7.1: The CBR cycle: to solve a new case, already solved cases are retrieved from a database and their solutions are reused on the new case. The solutions are revised to fit the new problem, before this new case is retained in the database. Image from Aamodt and Plaza [1], reprinted by Permission of Sage Publications.

#### 7.1.1 Related work on CBR for IA subgroup selection

Chuang [58] used CBR as well as various data mining methods, such as back-propagation neural networks, classification and regression trees, or logistic regression, to diagnose liver diseases that are difficult to detect. For CBR, each case was defined as a feature vector containing patient data and individual results from biochemical tests of the liver. The feature vector could be weighted and normalized to calculate the Euclidean distance between cases to find the most similar ones. A classification as healthy or diseased was made by calculating the overall similarity to all diseased and all healthy cases and comparing the two. This CBR approach was then combined with data mining methods which increased sensitivity and specificity compared to the performance of each method on its own. By itself, CBR had an accuracy of 89%, a sensitivity of 90% and a specificity of 88%. The overall best model was the CBR combined with back-propagation neural networks with an accuracy of 95%, a sensitivity of 98%, and a specificity of 94%, which could be increased by another 1% by weighing the features. The weights were assigned using an analytic hierarchy process as described in detail by Lin and Chuang [145], where liver experts were consulted to help determine a feature's significance. The back-propagation neural networks on their own performed with 93% accuracy and 91% sensitivity. It was concluded that CBR brings a significant benefit to the diagnosis of liver diseases [58].

In the context of IA, CBR has been used for their detection in MRA images [132], and for IA rupture risk evaluation in the context of a statistical model [65, 68].

When analyzing the IA rupture risk, many studies evaluated their morphology with respect to the rupture state [55, 69, 153]. Niemann et al. [179] investigated the potential of 22 morphological features for aneurysm rupture risk prediction. Although the best model had an accuracy of only 69%, several features showed a high association towards rupture risk.

Detmer et al. [67] introduced an aneurysm rupture probability model trained on 1631 IAs and based on patient characteristics, i.e., age and gender, aneurysm location, morphology and hemodynamics. They found rupture risk to be associated with higher hemodynamic parameters, complex IA shape, younger patient age, and male sex. A study by Ishibashi et al. [115] further cemented the influence of an aneurysm's location and size on the rupture risk, as well as a patient's medical history. In addition, the Multiple Aneurysms AnaTomyCHallenge 2018 (MATCH) was conducted to provide an overview of state-of-the-art blood flow simulations as well as rupture risk prediction [28]. As a result, the simulation setups of the participating groups revealed very similar boundary conditions of the simulations, but clear differences were reported regarding morphological and hemodynamic parameters of the aneurysms.

In contrast to these approaches, in this thesis we focus on the concept of similarity, highlighting the individual aneurysm cases and illustrating their similarities in graph layouts, all to facilitate cohort-based research.

#### 7.1.2 Method for CBR for IA subgroup selection

REQUIREMENTS In dialogue with neurosurgeons, the end users of the tool, three criteria were determined to be crucial for the tool to fulfill:

- *Reliability*: the tool shall reliably return the most similar cases to a new case, the aneurysm of interest (AOI). Similarity shall be defined by the closest possible match within the user-selected features.
- Appropriate feedback: The output of the tool shall correspond to the selected features.
- *Clear visualization*: The visualizations shall put the numerical results into context, and it shall be immediately clear which cases are most similar.

BASE TOOL Using Matlab R2020a (MathWorks, Natick, U.S.), we extended a previously developed tool for case-based reasoning and rupture risk assessment support for IAs based on their morphological parameters [224]. The base tool loads a database of IAs and their morphological parameters, normalizes them, and then calculates distances between them, with special consideration given to one AOI. The distances represent how similar two IAs are based on the input features, here morphological parameters, and thus the most similar IAs to the AOI have the smallest distances. Features were normalized into a range of zero to one.

All distances d calculated make use of the Euclidean distance measure:

$$d(p,q) = \sqrt{\sum_{i=n}^{n} (q_i - p_i)^2}$$
 (7.1)

where p and q are features of two IAs, i is the current feature and n is the total number of features. For categorical or normal values, which the base tool could not handle, the distance of that feature is automatically set to zero if they are equal, and to one if they are not.

CLASSIFICATION Another functionality of the base version is a classification of rupture status: using the most similar IAs, three different k-nearest-neighbor classifiers predict if the AOI's morphology is more like that of ruptured or unruptured IAs. Since the IAs in the database have already been treated, the classification result can support the rupture risk assessment and treatment decision for the AOI. We extend the described tool to patient subgroup identification. This includes the use of arbitrary features in the database and no longer limiting similarity calculation to morphological parameters and classification of rupture status. Instead, nominal and numerical features with categorical and continuous values can be part of the database, and classification can be done for an arbitrary parameter. To further make the tool more suitable and robust

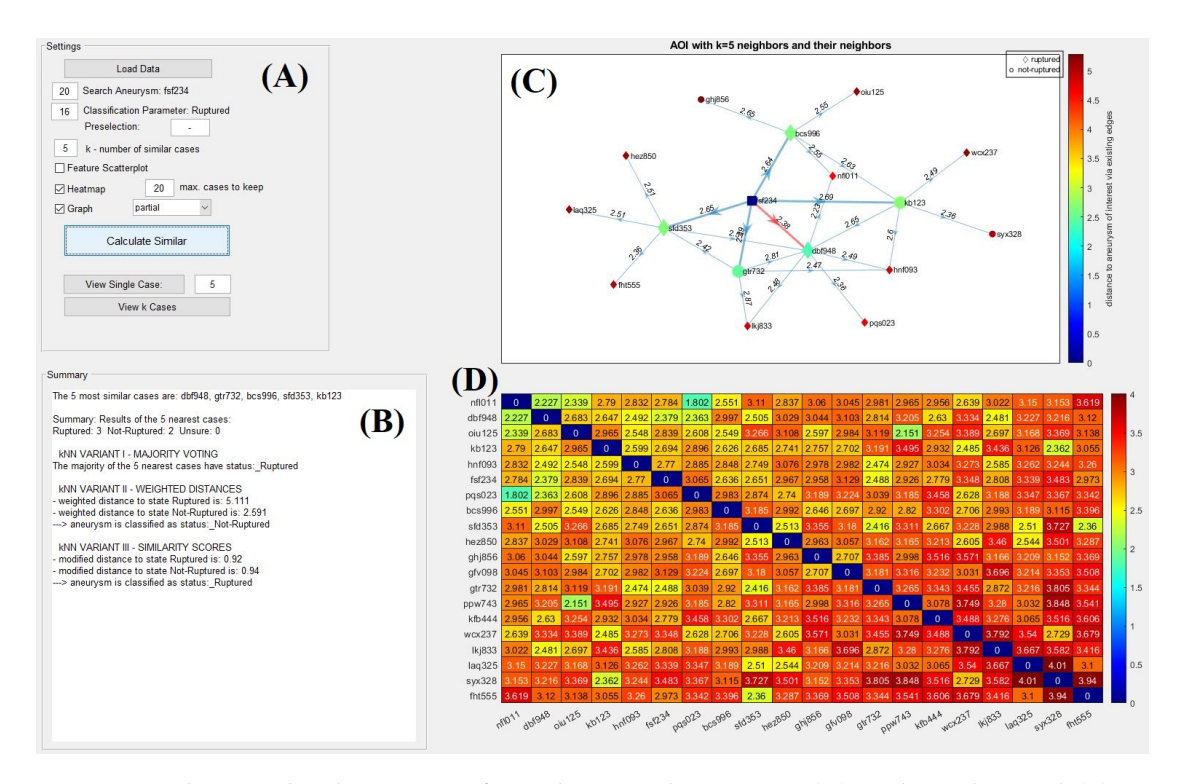


Figure 7.2: The Graphical User Interface, showing the settings (A) and result panel (B) as well as the graph (C) and heatmap (D) visualization. Image adapted from **Spitz** et al. [226] and available under a CC BY 4.0 license.

for use in clinical practice, it also accounts for missing data values by treating them as non-equal categorical values.

FILTERING AND OTHER NEW FEATURES Another new functionality is preselection. Here, the user can select any feature that is part of the database and select a value. Similarity calculation and subgroup identification will then only be executed within the preselected subgroup that has the value in the selected feature.

Other additions include direct feedback to user-defined variables and a more user-friendly and intuitive input via a comma-separated value format (csv table, e.g. Figure 7.3) rather than having to manually load multiple individual files.

DATA All data and features used are anonymized patient data of verified IA diagnoses, acquired during clinical routine at the neurosurgery department at the university hospital in Magdeburg, Germany. Thus, we gain image data, manual annotations, and derived data, including metadata and pathology and treatment developments as categorical data, as well as hemodynamic and morphological values as continuous data.

	A	В	С	D	E	F	G	Н	1	J
1	Sex	Age	Date	Diabetes	pAVK	Stroke	Birth control	AspectRatio	CHSurface	EI
2	1: male 2: female			1: Type 1 2: Type 2 3: none	1: yes 1 2: no	1: yes 2: no	1: yes 2: no			
3	2	76	30.11.2010	3	2	1	2	1,12885909	85,370461	0,2685
4	2	51	16.06.2007	2	1	. 2	2	0,68864899	111,15713	0,3261
5	2	76	09.12.2009	3	1	2	1	0,922457	116,7903	0,2728
6	1	42	03.01.2013	1	1	2	2	1,32605265	280,4328	0,2489
7	1	46	31.12.2014	3	2	. 2	2	1,21632752	256,48678	0,2365
8	1	81	28.04.2009	1	2	1	2	0,72081902	74,011244	0,2697

Figure 7.3: An example database with categorical and numerical metadata and continuous morphological parameters. Image adapted from **Spitz** et al. [226] and available under a CC BY 4.0 license.

GUI The graphical user interface (GUI), visible in Figure 7.2, of the tool includes a settings panel (A) that handles all user input, and three output panels. The result panel is a text field that returns the defined subgroup and patient names, as well as the results of the classification (B). The two other panels (C and D) are visualizations that illustrate the similarity relationships of the patients based on their calculated distances across the defined features. The user furthermore has the option to view segmented 3D models of the AOI and its most similar IAs, as well as view a scatterplot matrix visualization that gives information about the correlations and information gain of the individual features used for similarity calculation.

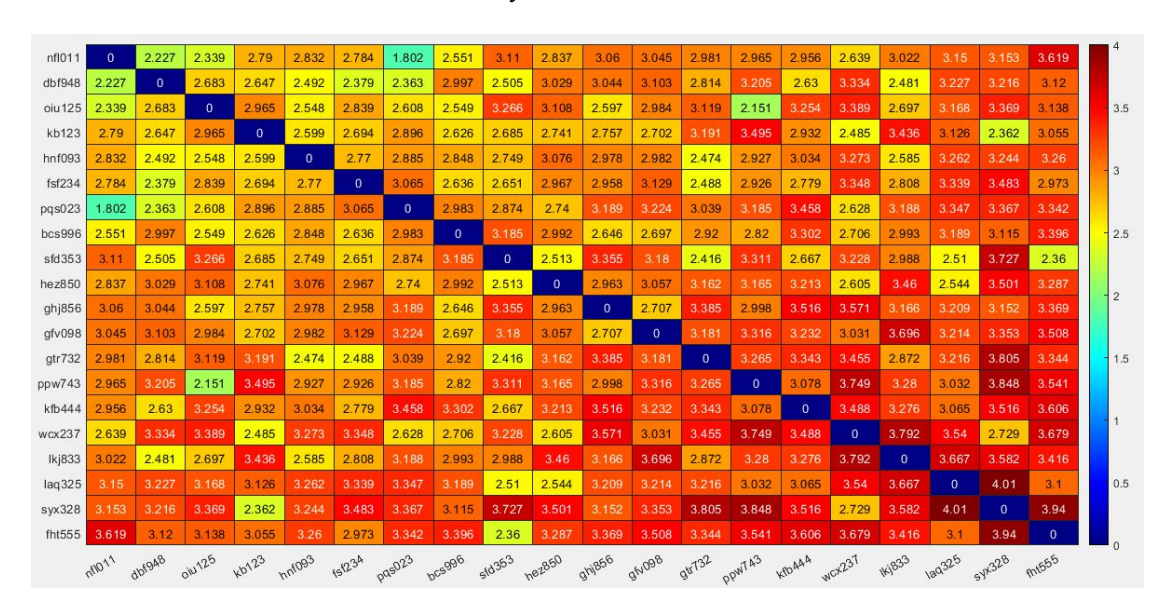


Figure 7.4: Heatmap visualization. Each entry encodes the distance between the row and column IA. Image adapted from **Spitz** et al. [226] and available under a CC BY 4.0 license.

HEATMAP The first visualization in the GUI is a heatmap (see Figure 7.4). It uses Matlab's heatmap function. Here, each row and column represent one IA in the database, and each corresponding entry of the heatmap represents the similarity between them. The similarities are color-coded based on similarity according to a rainbow color map selected by the end users. Hovering or clicking on the entries highlights row and column IAs and a pop-up appears that shows the X and Y values, which here is the index of the IAs, as well as their similarity. Further basic interaction is possible, like dragging single columns or rows across the map to directly compare to others or re-sorting the entire heatmap according to one specific IA. To cope with larger database sizes, we do automatically keep only a user-defined number of IAs. However, the user can still reject a single IAs due to low similarity or just keep all datasets for the subsequent analyzes.

The second visualization is a graph (see Figure 7.5), done with Matlab's GRAPH graph function, that illustrates information about similarity within the defined subgroup and the IAs immediately outside of it as a partial graph. Each node is an IA, and the edges between nodes represent their similarity by distance. Smaller distances mean more similarity than larger distances. The AOI and its most similar IAs are highlighted, and the classification feature is encoded in node shape. Node colors again encode similarity to the AOI, using the same color scheme as in the heatmap. The graph can be shown as a partial graph (as in Figure 7.2), or a full graph with all IAs in the database and their similarity to the AOI being visible. The user can switch between two graph layouts: circle and force layout. The circle layout puts the AOI in the center and all other IAs on a set radius around it, regardless of them being nearest neighbors or not. The force layout (which is chosen for all figures) arranges the nodes according to attracting and repelling forces. It matches the length of the edges to their weight, i.e., an edge's length matches the similarity between the two nodes that it connects. These edge weights also determine the forces used to place the nodes; connected nodes with more dissimilarity have a stronger repelling force between each other than more similar nodes.

scatterplot matrix By checking the "Feature Scatterplot" checkbox in the settings panel (see Figure 7.2 A), the user can optionally open a window depicting a scatterplot matrix (done with the Matlab function) where each row and each column represent a morphological feature (see Figure 7.6). The upper triangle of the matrix shows pairwise scatterplots of the morphological features. Each point in the scatterplots represents an IA color-coded by its rupture status class. The features are sorted according to their information gain  $\Delta_{\rm info}$  towards the rupture status. Here, the infor-

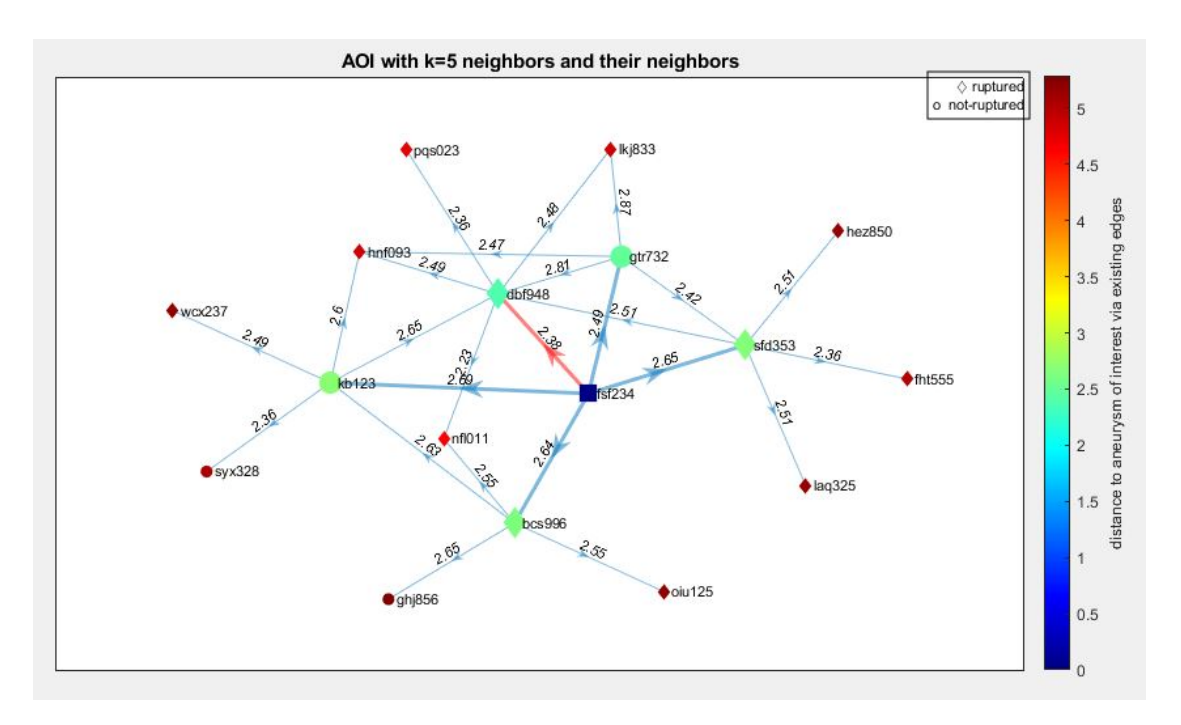


Figure 7.5: Graph visualization. Each node represents an IA and their connecting edges how similar they are. Only the most similar IAs are depicted by edges. Own figure.

mation gain of feature f measures the decrease in impurity H of D towards the rupture status when splitting D into R partitions, and is calculated as

$$\Delta_{info}(f) = H(D) - \sum_{r=1}^{R} \frac{M_r}{M} H(D_r), \tag{7.2}$$

where D is the dataset, R is the number of partitions, and  $D_r$  is the r-th partition with  $\bigcup_{r=1}^R D_r = D$ . The impurity H of a partition  $D_r$  is measured using Shannon entropy as

$$H(D_r) = -\sum_{j} p(j|D_r) \log_2 p(j|D_r),$$
 (7.3)

where  $p(j|D_r)$  is the ratio of IAs of class j in  $D_r$ .

For categorical features, each partition  $D_r$  represents the set of IAs where all IAs exhibit the same value, i.e.,  $\forall q \in D_r : q_f = \nu_r$ , with  $\bigcup_{r=1}^R \nu_r = \nu \text{alues}(f)$  and  $\forall o, p \in D, o \in D_r, p \in D_s, r \neq s : o_f \neq p_f$ .

Each continuous feature is split into R=2 partitions, with  $\forall q \in D_1: q_f \leqslant \tau_f$  and  $\forall q \in D_2: q_f > \tau_f$ , where  $\tau_f$  is the cutoff value for f that yields the highest  $\Delta_{info}(f)$  over all unique values of f.

The lower triangle of the scatterplot matrix shows the pairwise color-coded PCC of the row and column feature. The PCC between two morphological parameters is visualized via color and saturation. PCC measures the linear correlation between the two features, meaning how one feature can be expressed by another through linear operations. A PCC of 1 means perfect positive correlation, a PCC of -1 means perfect negative correlation and a PCC of 0 means no correlation. The fields are colored based on the PCC, increasing in saturation with stronger correlation, with the color itself reflecting if it is a positive or negative correlation. Through  $\Delta_{info}$ , PCC and the distribution of the scatterplots, the scatterplot matrix gives the user a sense of which features might be important for the classification of the AOI, and they can choose to exclude single features for the similarity calculations. While this description used rupture status as classification target feature, any other feature can be chosen as well.

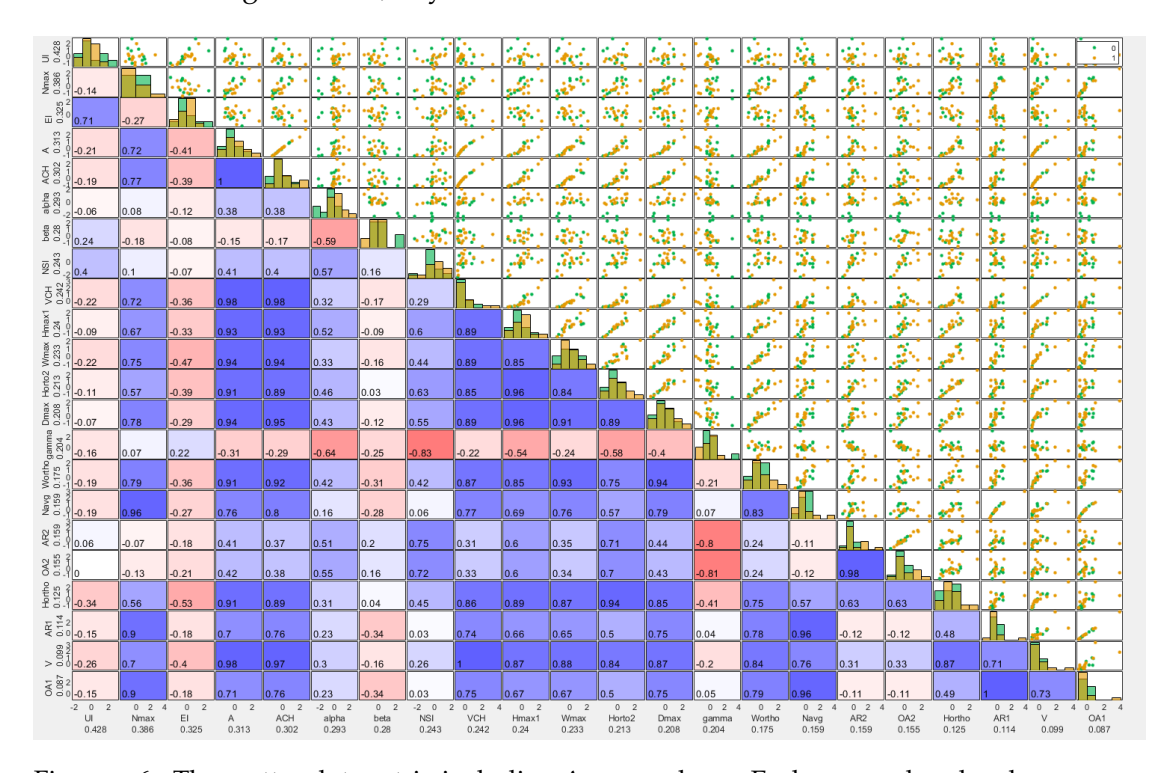


Figure 7.6: The scatterplot matrix including  $\Delta_{info}$  and PCC. Each row and each column represent a morphological feature. Labels provide the name of the feature and its  $\Delta_{info}$ . The upper triangle matrix shows pairwise scatterplots, the lower triangle matrix the color-coded PCC (red = 1; white = 0; blue = -1). Image from **Spitz** et al. [224] and available under a CC BY 4.0 license. No changes were made.

#### 7.1.3 Evaluation of CBR for IA subgroup selection

The tool was assessed based on the three criteria previously determined by neurosurgeons: reliability, appropriate feedback, and clear visualization.

PHANTOM DATABASE To assess reliability, a phantom database of IAs based on patient data was created by a medical engineer familiar with the field. In this phantom database, the resulting subgroups were known, providing a ground truth.

Within the phantom database, several clusters around example AOIs were created to check if the tool identified them as subgroups, and if the order of most to least similar cases would be recognized. There were five AOIs with corresponding subgroups.

The most similar IA was found reliably for all AOIs. In two cases, one of the IAs that belonged to the subgroup was not identified, however, in both of those cases, the IA that was not assigned to the subgroup was the one that was the least similar to the AOI. The order from most to least similar IA within the identified subgroup was not always correct, but errors within the order were only found towards the least similar ones, never within the most similar IA. Out of the five subgroups, two had perfect orders. The discrepancy in the order of similar IAs may be due to the differences in how the medical engineer ranked similarity, and the similarity metric developed by the tool. For example, at the time of evaluation, all features were weighed equally, while someone experienced with IAs may weight some parameters higher than others based on their knowledge about risk factors. In many of the research questions posed during discussion with clinicians, finding the most similar case or a subgroup was sufficient, rather than finding the specific order of similarity within a subgroup. The tool can therefore reliably identify the most similar IA to an AOI.

SURVEY For feedback and visualization evaluation, a survey was presented to clinicians where they could rate the different components of the tool and its output. The survey was sent to eight medical researchers within the fields of neurosurgery and medical engineering. This included two practicing doctors, and all participants had experience with IA research ranging from one to ten years. The participants were asked to rate the different outputs and visualizations on their intuitiveness, helpfulness, and appropriateness, as well as how likely they would be to use the visualization for research, on a five-point Likert scale.

Overall, the tool's output was rated as appropriate, with an average of 4.6 out of 5. The heatmap received the best ratings, it was deemed the most helpful and appropriate. The result panel was rated as the least intuitive, but more participants said they would use it when considering a research question than the graph, though the classifier results need elaboration to be understood. It is important to note that preferences varied significantly between users. This was illustrated when the participants were asked for their favorite of the outputs, where answers were non-conclusive. Overall, the graph was mentioned the most when asked for the most helpful, intuitive and appropriate output, despite the heatmap receiving the most favorable rating. The tool's evaluation in regard to reliability, appropriate and clear feedback was therefore positive.

LIMITATIONS AND FUTURE WORK The graph visualization, while receiving good ratings, was mentioned to be confusing. This is because only the distances between nodes connected by edges have meaning, and even these distances are not always true to scale due to Matlab's internal handling. While the distances between nodes are supposed to reflect the similarity value between the IAs the nodes represent, the repelling and attracting forces that the graph uses to be drawn skew the actual distances of the edges, to not overlap. Additionally, the graph is not always readable. Completely re-working the graph to make all distances meaningful would be desired, especially in combination with a state-of-the-art dimension reduction that could reduce the distances to a 2D problem.

As we use mixed data with both categorical and numerical features, dimension reduction is not trivial, as most dimension reduction algorithms either handle one or the other. This can be solved by encoding categorical values as numerical (each category is one number), which is how we handled categorical values in the Euclidean distance. Another option is one-hot-encoding, where each category becomes a binary variable, but this heightens dimensionality. Additionally, this can lead to a loss of information as all categories have the same Euclidean distance to each other, which is also a limitation of our tool [25, 110]. Another option is using a distance hierarchy to extend methods like t-SNE by including a unified measurement of the distance between categorical and numerical features by including domain knowledge [110].

Another valuable addition could be an overview of the similar and non-similar features of the identified subgroup. Such additions could be made in the results panel.

Since the development of the tool, DL has risen in popularity, and can feasibly be used for quantification of rupture risk and clustering. Ru et al. [204] present a framework that segments imaging scans automatically, extracts the IA and its morphological parameters, and assesses correlations and relations between morphological parameters and rupture via linear and non-linear models. The result is an evaluation of rupture risk. While they analyze less parameters than the tool we represent, they also calculate the centerline, so our parameters could be added. Ru et al. [204] do not calculate similarity, visualization for exploration, or subgroup selection, but those could feasibly be added as well in the future.

## 7.1.4 Conclusion on CBR for IA subgroup selection

An interactive tool for patient subgroup identification based on arbitrary characteristics was developed. The tool supports a mix of categorical and continuous features and includes a classification feature as well as visualizations of the most similar cases to the case of interest. It can account for missing values and automatically identify subgroups of patients according to their similarities in user-defined features. It can thus not only find an arbitrary number of cases for a subgroup but also find the most similar case to the one of interest. It was tested in context of IAs and grants sufficient

results to support clinicians in research questions. As features and cases are arbitrary, the tool can be used for any pathology or even outside of the medical research field.

Future work will include a suitable, state-of-the-art dimension reduction to address the curse of dimensionality. In this context, a weighting of different parameters shall additionally be enabled as different parameters have different impacts on research questions [178], which shall also be visualized. This will also lead to an overworking of the graph visualization to give all distances within it a meaning, rather than just the ones encoded via an edge.

In medical IA research, the tool is already actively being used for subgroup identification and cohort matching, resulting in joint research publications. One study compared the rupture risk and clinical outcomes of IAs at the AComA and the basilar tip. From 1062 patients, a cohort of 32 basilar tip IAs was matched with 32 AComA IAs using the presented tool. The study found a comparable rupture risk for the two locations [232].

Another study compared two surgical approaches for AComA IAs, specifically pterional craniotomy and the interhemispheric approach. From 129 AComA IAs, 14 cases with each approach were matched based on morphology and clinical parameters using the developed tool. The study found that the interhemispheric approach led to improved clinical outcomes depending on IA angulation [233].

A third study investigated the influence of patient sex on IA rupture rate, severity of bleeding, outcome, complications, and IA location, as well as the effect on multiple IAs. The tool was used to match female patients with male patients based on morphology and metadata, from a database with 511 IAs. The study found a significant difference in rupture rate between the observed variables [231].

A fourth study compared the outcomes of surgical clipping and endovascular treatment of AComA IAs. Using the tool and morphological and clinical parameters and scores, 24 surgically clipped IAs were matched with 116 endovascularly treated IAs, from a database with 1496 IAs. The clipped IAs achieved a significantly higher rate of complete occlusion, but also a higher rate of postoperative ischemic complications. Clinical outcomes, however, showed no statistically significant difference [234].

All four studies highlight the value of the developed tool for IA research. The results of the studies further highlight the need for individualized treatment based on IA parameters, which include morphology.

#### 7.2 SUBGROUP SELECTION OF INTRACRANIAL ANEURYSMS VIA INSTANCE SE-LECTION

The thesis presents a framework for the selection of a subgroup of training cases for IA treatment. In this framework, there are two options for training case selection: general training, and training for a specific scenario. General training describes training cases representing a variety of different IAs that a physician may need to treat. A specific

# ■ Publication

Section 7.2 is based on:

[227] L. Spitz, S. C. Umeh, D. Behme, B. Neyazi, I. E. Sandalcioglu, B. Preim, and S. Saalfeld. "Subset selection for intracranial aneurysms for training simulations." In: Curr Dir Biomed Eng 10.1, pp. 73–76. doi: 10.1515/cdbme-2024-0119.

This work was conceptualized and written by L. Spitz, designed by L. Spitz and S. C. Umeh, and implemented by S. C. Umeh as part of a Master Thesis.

training scenario describes training that is specialized based on IA features of a specific case.

For general training, instance selection (IS) can be utilized. IS is the process of reducing the size of a dataset while preserving quality and variance. Thus, it can be used to select a subset of representative and diverse IAs from a large database of IAs. IS can be done in a variety of ways, popular models including prototype selection, training set selection, and sampling, clustering, and prototyping [92, 199]. In the medical context, IS has also been used, for example, via clustering approaches for medical relations [129], or in a divide-and-conquer based strategy to tackle the specific issues of medical datasets [112].

For training for specific cases, we introduce reverse instance selection (RIS), a novel approach where a representative and diverse subset is chosen with one specified IA in mind. Here, the subset shall be like the specified IA, without losing the variance of the entire database.

## 7.2.1 Materials and methods for IS in IA subgroup selection

The framework (overview in Figure 7.7) was implemented in Python 3.10.12. Two databases were provided in the form of tabular data. The first database, for which we had access to 3D models, had 76 IAs from 54 patients collected from three clinics, with a total of 37 parameters (7 metadata, 23 morphological [209], 7 hemodynamic [48]). After preprocessing, which included data correction by removal of missing entries, feature aggregation, and Boolean encoding, 70 IAs with 29 features remained. The second database had 406 IAs with 106 parameters, though after preprocessing, 351 IAs and 12 parameters (metadata and morphological) remained. During preprocessing, duplicate records or features with very high correlation were removed, as well as entries with missing data. Categorical and Boolean features were encoded numerically, and all features were scaled to have a mean of zero and a standard deviation of one. PCA

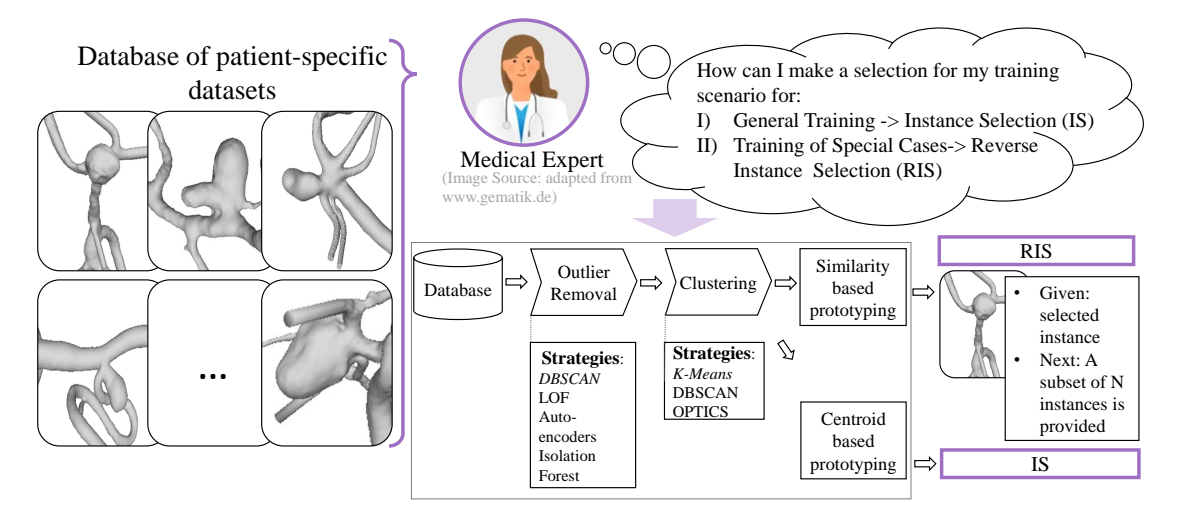


Figure 7.7: Overview over subset selection for training, including the framework for RIS and IS. Image adapted from **Spitz** et al. [227] and available under a CC BY 4.0 license.

served as dimension reduction, and the first three principal components were used to continue calculations, as they covered a sufficiently explained variance of at least 88%.

We determined three criteria necessary for subgroup selection: inlierness, diversity, and, for RIS, similarity.

The inlierness criterion ensures that there are no outliers in the selected subset. This is achieved through outlier removal. We tested density-based spatial clustering of applications with noise (DBSCAN) [76], local outlier factor (LOF) [37], autoencoders [134] and isolation forest [147]. DBSCAN (minPts = 4, eps = 1.6, determined empirically) was the best candidate as it requires few hyperparameters, no input number of outliers like autoencoders, and no clearly defined clusters like LOF.

The diversity criterion ensures variance and low redundancy in the selected subset. It is fulfilled via clustering. We tested DBSCAN, ordering point to identify clustering structure (OPTICS) [9], and k-means [154]. The latter was selected for our application as it showed similar results for our database with and without PCA.

Prototyping selects the candidates in the subgroup, and in the case of RIS meets the similarity criterion for the specified IA. It describes an iterative process of choosing candidates from the clusters. For RIS, the candidates are chosen based on how similar they are to the specified case. For IS, the candidates closest to the centroids of the clusters are chosen.

As we present RIS as a new concept, we also introduce its evaluation score which is made up of three weighted metrics for a selected subset: similarity, redundancy, and anomaly. Similarity ensures the representation of the specified IA case in the selected subset. One part of the similarity metric thus calculates how similar two aneurysms

are based on their parameters or PCs (denoted as vectors p, q), utilizing Euclidean distance dist(p,q) and some modifications:

$$sim(p,q) = \frac{1}{1 + dist(p,q)}$$
(7.4)

Similarity for an entire subset thus is the mean similarity of all IAs in the subset S to the specified case A:

$$Sim(A,S) = \frac{\sum_{s_i \in S} sim(A, s_i)}{|S|}$$
(7.5)

Redundancy assures diversity by punishing similarity within the selected subset. It can be calculated using Equation 7.4, and thus the redundancy of one IA  $s_i$  to an extracted subset S is:

$$Red(s_i, S) = 1 - \frac{\sum_{s_j \in S} sim(s_i, s_j)}{|S| - 1}$$
(7.6)

The overall redundancy of one subset is therefore:

$$Red(S) = \frac{\sum_{s_i \in S} Red(s_i, S)}{|S|}$$
(7.7)

Anomaly, or outlierness, of an IA punishes inclusion of outliers in a subset. It can be calculated using local reachability distance (LRD), which is the local density based on neighboring instances within the database. LRD is defined by:

$$LRD_{k}(s_{i}) = \frac{1}{\frac{1}{k} \sum_{q \in N_{k}} reachDist_{k}(s_{i}, q)}$$
(7.8)

where  $N_k(s_i)$  are the k nearest neighbors to IA  $s_i$ , and reachDist $_k(p,q)$  is the reachability distance, which is the maximum of the distance between two points and the distance to the point's kth neighbor. For the overall anomaly of a subset, the LRD of each point is normalized, and the average is taken:

$$Anom_{k}(S) = \frac{\sum_{s_{i} \in S} norm(LRD_{k}(s_{i}))}{|S|}$$
(7.9)

The value of k can be adjusted based on individual use case, but for our case we empirically determined and set k to four.

Similarity, redundancy and anomaly metrics can then be combined into an overall score, where each metric can additionally be weighted based on domain knowledge or use case.

$$Score(S) = w_1 Sim(A, S) + w_2 Red(S) + w_3 Anom_k(S)$$
(7.10)

As we are working on a sparse dataset with a focus on representation and diversity, we set the weights to favor similarity and redundancy over anomaly:  $w_1 = 0.4$ ,  $w_2 = 0.4$ ,  $w_3 = 0.2$ .

## 7.2.2 Results of IS in IA subgroup selection

We compared our RIS approach to subsets consisting of the most similar sampled (SimS) (as in, most similar IAs to the specified IA), and to randomly sampled (RndS) subsets. We tested with six randomly selected specified IAs, and with two subset sizes, one equaling the number of clusters in the dataset (N=3) and a bigger one (N=5) (Table 7.1).

Table 7.1: Results of comparing RIS with SimS and RndS models. Metrics are averages over six experiments with randomized specified IAs. Best performing models and metrics are highlighted in bold.

Database	Model	Metrics					
		Sim	Red	Anom	Score		
1	RIS	0.399	0.744	0.252	0.508		
(N = 3)	Similarity	0.568	0.446	0.449	0.506		
	Random	0.225	0.809	0.234	0.455		
1	RIS	0.392	0.715	0.239	0.495		
(N = 5)	Similarity	0.529	0.500	0.432	0.505		
	Random	0.245	0.777	0.276	0.463		
2	RIS	0.397	0.701	0.638	0.567		
(N = 3)	Similarity	0.528	0.485	0.595	0.524		
	Random	0.201	0.832	0.632	0.540		
2	RIS	0.385	0.694	0.622	0.556		
(N = 5)	Similarity	0.486	0.552	0.610	0.537		
	Random	0.138	0.814	0.630	0.531		

RIS outperformed SimS and RndS subsets in 79% of experiments, though SimS also performed well, as visible in the mean results of Table 7.1. In the evaluation metrics, SimS performed best for the Sim metric in all experiments, and RndS best for Red metric in all but one experiment. Results for Anom metric were more scattered, SimS performed best in 50%, RndS best in 29% and RIS best in 21% of experiments. While RIS did not outperform in any one metric, it aims to strike a balance between the weaknesses of SimS and RndS. However, for both datasets, we observed that when subset size exceeded cluster size within the database, RIS performance grew worse, and SimS subset selection performed better.

To evaluate our IS approach, we used the common IS evaluation method of comparing the classification accuracy of a model trained on the complete dataset and on

the extracted subset [112]. Using XGBoost [54] and a 80/20 training/testing split, we trained several models with different subset sizes (based on a percentage of training data) and compared IS subsets results to those of RndS subsets. For each subset size, five experiments were performed. We utilized database 2 and the Iris dataset [8, 80]. The classification accuracy of the model trained on the complete dataset was 100%.

Table 7.2: Averages of results of comparing the accuracy of a classification model trained on subsets extracted with IS and random sampling, tested on two databases. Subset sizes are percentages of the complete dataset.

Database	Model	Accuracy per subset size (%)				
		12.5%	30%	50%		
Iris	IS	83.3	96.7	96.7		
	Random	77.3	94.7	99-3		
2	IS	45.1	53.5	54.9		
	Random	49.9	56.3	56.6		

For subset sizes 12.5% and 30% of the Iris dataset, RIS outperformed the RndS selection. For a subset size of 50% and all sizes of database 2, RndS achieved a higher accuracy than RIS. However, for database 2, RndS accuracy did not get higher than 57%, and differences to RIS were always smaller than 5%.

## 7.2.3 Discussion on IS in IA subgroup selection

The results in Table 7.1 and Table 7.2 show that our presented approach for RIS and IS performs best for small subset sizes close to or equal to the number of ideal clusters in the database. In the case of IS, where RndS achieved better results, database 2, even when sampled at 12.5%, may simply be too big to emphasize the strengths of the presented IS approach. Even so, RndS only performed 5% better at most.

Our IS approach and our novel method of RIS can easily be adapted in parameters and are flexible in which machine learning techniques it utilizes in the anomaly detection, clustering and prototyping steps. They can thus be adapted to many different datasets if domain knowledge is available. The same flexibility is applicable to our presented evaluation method for RIS, where the weights of each metric can be adjusted based on which metric is more favored.

The currently chosen implementation of the approach has limitations in that it is based on distance metrics and needs a minimum subset size equal to the number of clusters. The latter may be problematic for databases with a lot of clusters but can be solved by using another clustering method, or by not utilizing all clusters through

weighting or rating clusters before prototyping. Distance metrics could also be replaced by other metrics that do not rely on distance.

The adjustment of weighting the metrics in our evaluation is an advantage due to adaptability, but this also meant no ideal weights were determined. A dimension reduction method that can handle categorical features without numerical encoding as we did for PCA would be desirable in the future.

We discussed the IS and RIS approach with clinical experts, who highlighted the importance of adequate IS and which were interested in using the tool to quickly and automatically identify initial subsets. However, we could not conduct a qualitative user study due to a missing ground truth which is difficult to determine and additionally highly dependent on each medical application scenario.

#### 7.2.4 Conclusion on IS in IA subgroup selection

In this work, we present an approach for IS, the novel concept and approach of RIS, and a metric score for its evaluation, for training simulations of IA treatment. Both IS and RIS are useful for selecting a subset of training cases for IA treatment. RIS can select a subset of IAs like one specified case that shall be trained for in particular, whereas IS selects a diverse and representative subset of the entire database, so trainees can gain proficiency in a variety of IAs.

#### 7.3 CONCLUSION ON SUBGROUP SELECTION FOR IA ANALYSIS

IA cohort-based research is dominated by a wide variety of parameters that describe both patient and IA risk factors that influence treatment possibilities and clinical outcomes. While the weighting of these parameters can differ between clinics and research is ongoing, it is impossible for even experienced radiologists to keep all the parameters in mind, especially when comparing more than two IAs. We therefore want to answer RQ 3: to what extent can morphology-driven analysis support cohort-based research?

This thesis provides two tools for analysis of IAs based on a variety of parameters, both specifically powerful for subgroup selection in the context of cohort-based research as well as training applications.

One tool utilizes CBR, where a database of IAs can be compared based on their similarity to an AOI. The tool can aid in detecting outliers, subgroup selection, finding correlations, and cohort matching. It provides multiple visualizations for exploration of the database and similarities to the AOI, and is actively being used in clinical research, resulting in multiple joint research papers [231–234]. Specifically, the tool is being used for research on rupture risk and medical outcome based on IA location [232], for the comparison of different surgical approaches based on IA angulation and treatment outcome [233], for the influence of patient sex on rupture risk and treatment outcome [231], and for comparison of surgical and endovascular treatment outcomes [234].

In these studies, the tool was used to match cohorts, i.e., to find the most similar case to a case-of-interest based on a wide variety of parameters and enable statistical analysis.

The other tool presents a framework for selecting a training group out of a database of IAs, with functionalities for two training scenarios: one for general training, and one for training of a specific case. This framework is based on IS, where a database is reduced while retaining variance. IS is utilized for general training subset selection, whereas the novel RIS is used for specific case training, where variance is retained based on the case that shall be trained.

Automatic subgroup selection, both for subgroups defined by similarity and for representation of a bigger database, thus is a versatile and relevant addition to patient-specific IA analysis by providing computer support for cohort-based research and education.

# VIRTUAL REALITY CONCEPTS FOR MORPHOLOGICAL ANALYSIS

An important aspect of analysis is visualization, as even numeric or quantitative (as well as qualitative) data can be processed more easily when displayed appropriately. The CBR tool introduced in Section 7.1 demonstrated the benefit of visualizations via its heatmap visualization, which enabled outlier detection, and the graph visualization, which showed relationships between similar IAs in a database based on a wide variety

of parameters. This tool demonstrated to what extent analysis can support cohort-based research, answering RQ 3. We now want to extend this answer by looking at a particularly immersive way to visually analyze neurovasculature, namely via virtual reality (VR).

VR offers more and different possibilities to visualize and explore data than conventional monitors. It enables better examination of three-dimensional object shapes using improved depth perception and intuitive interactions [107]. The benefits of VR when dealing with anatomical 3D models were demonstrated in different medical applications [114, 258].

This chapter gives insights into how morphological analysis can benefit from VR, not just in cohort-based research to extend RQ 3, but also individual patient and physician education.

#### 8.1 A VR CONCEPT FOR CBR FOR IAS

## Publication

Section 8.1 is based on:

[7] M. Allgaier\*, L. Spitz\*, D. Behme, A. Mpotsaris, P. Berg, B. Preim, and S. Saalfeld. "Design of a virtual data shelf to effectively explore a large database of 3D medical surface models in VR." In: Int J Comput Assist Radiol Surg 18.1 (2023), pp. 2013–2022. doi: 10.1007/s11548-023-02851-z. \*These authors contributed equally. This work was conceptualized in equal parts by L. Spitz and M. Allgaier. M. Allgaier designed and implemented the VR application. L. Spitz designed and implemented the CBR functionality.

As discussed in Chapter 7, medical research often involves the investigation and evaluation of large medical databases, for which we developed the CBR tool. To facilitate a link between the numerical data of the parameters and the actual anatomy as well as visual analysis, 3D surface models of the pathology's morphology should be integrated. VR offers the previously mentioned benefits of three-dimensional exploration, immersion, and intuitive interactions. Thereby, meaningful arrangement of the models is desirable.

To exploit benefits of VR, we introduce a *virtual data shelf* to intuitively arrange 3D objects, including functionalities to support the user in generating new hypotheses. We were inspired by Schott et al. [212], who presented virtual organ shelves motivated by shelves in surgical departments. We further wanted to extend our interactive tool for patient subgroup identification that we introduced in Section 7.1 by utilizing its CBR functionality and visualizing the database in VR and enable visual exploration of IA morphology.

Medical researchers must often deal with an abundance of patient data comprising various medical parameters that influence whether and how treatment should be carried out. After getting an overview of the relevant data, various characteristics of the patient data can be explored, and researchers can come up with new hypotheses. Working with the database, e.g., finding similar cases, gets more and more difficult the more parameters and patient data are included. These tasks are enabled by our shelf through a head-mounted display.

However, to facilitate these tasks, the anatomical objects must be visually arranged in a proper way. To provide the most suitable visual arrangement, we introduced three layouts: *flat*, *curved* and *spherical*. These are compared within studies in an immersive VR environment based on two main tasks: Overview and Exploration. A pilot study determined suitable shelf characteristics. A quantitative study investigates the suitability of the layouts regarding the two tasks using an attentive and a pre-attentive task to simulate them. In a qualitative study we aim at identifying medical use cases and their requirements, thus adding to the answer to *RQ 3: to what extent morphology-driven analysis can support cohort-based research*.

#### 8.1.1 Related Work for a VR concept for CBR for IAs

Ens et al. [74] present a *personal cockpit* including horizontal and vertical curvature, where the user can switch between several everyday applications. A  $40^{\circ}$  field of view was deemed sufficient as the tasks rely on the eyes' foveal region, which is even smaller. The *cockpit* layout was a  $4 \times 4$  world-fixed matrix of displays, with which the participants were significantly faster than with view-fixed techniques. Furthermore, the *cockpit* was easy and fast to navigate.

Gao et al. [91] present an amphitheater with varying egocentric distance-based item sizing (EDIS), where item size is adjusted according to the distance. Besides comparing

different levels of EDIS based on a retrieval and recall task, they found that additional location-fixed and user-defined visual landmarks are useful for a set of 54 items. They used a 110° field of view.

Cao et al. [42] propose to display a 2D dataset on a curved display where the single items are both arranged in a circular layout and curved by themselves. This work solely used 2D information.

In contrast, Liu et al. [148] compared arrangements of small multiples using the *shelf metaphor* [139] to enhance spatial memory by providing a clear horizontal and vertical alignment. Small multiples are arranged as a tiled display of multiple of the same visualization, and a metaphor describes the use of main attributes of real-world objects, like a shelf, in another context to ease usability through the integration of familiar interactions. In two studies, they compared flat, quarter-, half-, and full-circle layouts with horizontal curvature. The flat shelf was faster and more accurate with a small number of multiples, and while the half-circle layout was preferred, there were no differences with many multiples. Our layouts include no curvature, horizontal curvature, and vertical curvature, which was mentioned but not implemented by Liu et al. [148]. The shelf metaphor was also used to display livers in a VR anatomy training application [212]. Here, several virtual shelves can be stacked to build up a *library*.

Another work in immersive analytics, where visual analytics and virtual reality is combined [73], is presented by Satriadi et al. [210]. They used a qualitative approach to investigate how users arrange hierarchical views. As a result, a spherical cap layout is preferred by most users.

A recent study from Takashina et al. [238] evaluated curved virtual interactive surfaces and their operational efficiency with varying curvature, size (up to  $27 \times 15$ ), and presentation distance. Based on those parameters they analyzed target selection speed and error rate. Curved surfaces performed best regarding speed, and a larger curvature radius meant a larger error. A flat surface performed worst due to perspective distortion at the edges, but when a search task was added, it performed fastest, possibly due to seeing all objects at once, whereas curved surfaces have out-of-sight targets.

In contrast to the above-mentioned approaches, our *virtual data shelf* provides three layouts to display complex 3D objects in an immersive environment. The comparison to related work is presented in Table 8.1. The shelf is scalable by scrolling, providing an uncluttered way to work with a larger database since a manageable subset is displayed. The user is also supported by, e.g., filtering and sorting as well as automatically finding similar objects. Furthermore, the *virtual data shelf* is specialized for medical research in the area of IAs but might also be adapted to other medical applications or non-medical applications. This adaptation necessitates a requirement analysis of the respective use case.

Authors	Concept	Content	Number of items	Curvature
Ens et al. [74]	personal cockpit	2D interfaces in 3D environment	4x4	horizontal + vertical
Gao et al. [91]	EDIS	2D icons in	6x9	horizontal
Cao et al. [42]	curved display	3D environment 2D interface elements in 3D environment	N/A	horizontal
Liu et al. [148]	small multiples shelf metaphor	3D statistical visualizations	12 (3x4, 4x3,2x6)	none, horizontal
Takashina et al. [238]	curved virtual interfaces	2D grid on surface in 3D environment	27x15	none horizontal
This work [7]	virtual data shelf	3D anatomical models	6x11	none, horizontal, horizontal + vertical

Table 8.1: Comparison of related work approaches.

#### 8.1.2 Virtual data shelf as a VR concept for CBR for IAs

The *virtual data shelf* can facilitate medical research and hypothesis generation by showing and interacting with previously treated cases in a 3D environment. IAs, with their wide variety of metadata, morphologic and hemodynamic parameters that can be relevant for research, are the example use case for which we developed the *virtual data shelf*. As such, we used the same database for it as for the CBR tool from Section 7.1, meaning a csv file with metadata, hemodynamic, and morphological parameters for each IA.

For each case, a 3D surface model of the IA and its relevant surrounding vascular structures was available.

#### Metaphorical Design

The use of metaphors is a widespread concept in user interface design. Metaphors are applied in the target domain (the envisioned software) while drawing on users' knowledge and experiences in the source domain of the metaphor. A well-known example is the desktop metaphor with representations of documents, folders or paperbins (see e.g., [175]).

In medical applications, the virtual scalpel or the virtual resection plane are examples for metaphors where surgery is the source domain [195]. Ritter et al. [202] discussed the use of metaphors for anatomy education and chose the metaphor of a

3D puzzle, where students compose an anatomic model themselves to learn the spatial relations.

For metaphorical design, several approaches have been described (e.g., by [75, 156, 175]). Generally, various candidate metaphors need to be considered with respect to their suitability for a specific application. To be appropriate, a metaphor needs to be known to the audience and should evoke associations that are useful in the design of the user interface.

Within the source domain, the metaphor has a set of associations, e.g., possible actions. Typically, not all of these actions will be transferred to the target domain, and often, additional actions are possible that are not part of the source domain. For the evaluation of a metaphor, the amount of overlap between the actions in the source and target domain is essential. If this overlap is too low, the metaphor may not match the user's assumptions regarding functionality, and thus may be misleading.

For our project, we had identified the system functionality as will be described in the following paragraph. Next, we generated possible metaphors matching the intended functionality and thus arrived at the two metaphors *shelf* and *display*. According to the requirements, aspects of both metaphors are used and in a combination of the two metaphors, the *virtual data shelf* arose.

## Requirements and Functionalities of a VR concept for CBR for IAs

Discussions with neurosurgeons revealed that they organize patient data in simple table structures on a desktop PC, which makes getting an overview or a meaningful comparison of multiple cases with many parameters difficult. Given the specific use case, the following requirements regarding the layout and functionalities were derived from previous discussions with neurosurgeons:

- R1) The shelf should provide a good overview of the database. As many cases as possible should be displayed at the same time and large layouts were used for the study. Therefore, occlusion should be avoided.
- R2) The shelf should provide interactions to explore the whole database as well as single cases.
- R3) The underlying database and thus the shelf should be scalable.

To meet these requirements, we used a metaphorical design to create an intuitive user experience [176]. Accordingly, the characteristics size, purpose, functionalities, and visual area of the two candidate metaphors *shelf* and *displays* were compared and discussed and finally combined into a *virtual data shelf*.

SIZE The first characteristic is *size*. Interactive displays tend to be smaller than shelves, and even when using a very large display like in cinemas, we are used to

having the whole screen in view. Shelves instead can be very large, like in warehouses. To meet R1, the size of the proposed visualization is based on the shelf metaphor. Consequently, the size is too large to have the whole shelf in the field of view. Thus, it is more difficult to get a quick overview of the currently displayed cases. However, displaying more cases simultaneously shows a larger subset, leading to a better overview of the whole database.

PURPOSE AND FUNCTIONALITIES When looking at the *purpose*, a display is typically used for visualizing and interacting by clicking on it, whereas a shelf is used for structuring (searching and sorting) cases. However, once a shelf is full, it is usually not changed or restructured frequently.

For the shelf, functionalities and interactions are limited to taking out and adding cases. A display is much more flexible and interactive than a shelf. Taking a data table, different software usually support the user with interactions such as sorting and filtering are usually available. To meet  $R_2$ , both interactions are combined, resulting in the following interaction possibilities: filtering, sorting, and finding similar cases and highlighting, grabbing, and taking out. For the first three functionalities, the user must interact with the user interface (see Fig. 8.1 A and B). Highlighting (see Fig. 8.1 F) an item can be performed by using the trigger button of the VR controller. To grab and take out an item, the user must point to the item and press the grab button. If the grabbed item is released within the grab area (see Fig. 8.1 C), it is automatically returned to its position on the shelf. To leave an item outside the shelf, it must be released outside of the grab area.

When clicking on a user interface button, the similarity between the currently selected item and all other cases is calculated according to the CBR functionality described in Section 7.1 and visualized via colored circles (similarity is encoded in saturation). This similarity is calculated as Euclidean distance over morphological and hemodynamic parameters as well as the metadata of the cases saved in the database. The user can choose to predict the results of any parameter based on the most similar cases to the selected item. This could for example be used for rupture risk assessment for intracranial aneurysms [224].

To further support the detailed exploration mentioned in *R*<sub>2</sub>, there is an information panel that pops up next to each item when hovering over it (see Fig. 8.1 G). Inside it, the item's ID is displayed, as well as its value of the parameter the shelf is currently sorted by. If the similarity between the selected items and all other items was just calculated, the items will be sorted and additionally visualized according to it.

Similarity values range from 0 to 1, with 0 meaning no similarity, and 1 being the highest possible similarity when calculating the similarity of a case to itself. To inspect all parameters of cases in detail, a button can be pressed to show a list view of all parameters and the values of the selected and highlighted cases as a list.

VISUAL AREA Regarding the *visual area*, the shelf can only hold a limited number of cases. Although the visual space of a display is limited as well, the number of cases is unlimited due to scrolling or going to the next page. Since the *data shelf* should use a large database, we enable the use of several pages to fulfill *R*<sub>3</sub>.

For immersion, a semi-realistic room environment was chosen for a feeling of familiarity, as well as to avoid discomfort. The *virtual data shelf* and all its functionalities are displayed and summarized in Figure 8.1.

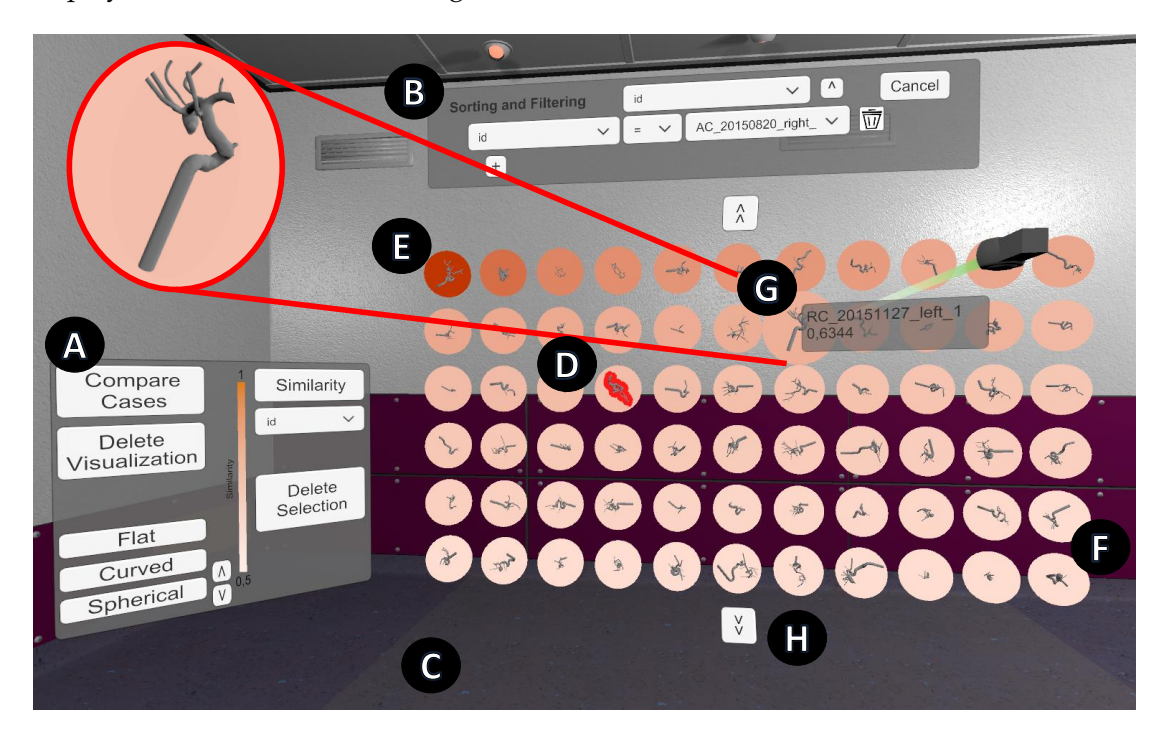


Figure 8.1: The *virtual data shelf* (*flat*) after similarity calculation. A) Main Menu, B) filtering and sorting menu, C) grab area, D) selected case, E) case used for similarity, F) similarity visualization, G) info panel, H) next page. A detailed view of a 3D aneurysm model of the case by G) with relevant surrounding vessels is in the left-hand corner. Image from Allgaier\* et al. [7] and available under a CC BY 4.0 license. No changes were made.

## Implementation of Layouts

The three layouts are *flat*, *curved*, and *spherical* (depicted in Figure 8.2). The *flat* layout arose due to the shelf metaphor and the benefit of providing a clear grid alignment enhancing spatial memory [139]. However, sizes are perceived differently and there is perspective distortion at the edges. The second layout is *curved* horizontally, resulting in no perspective distortion and the same distances per row if the user is in the center.

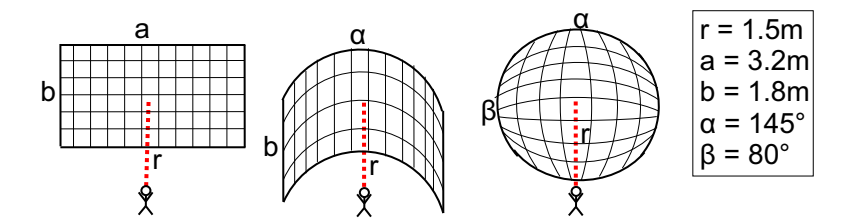


Figure 8.2: Three layouts: flat, curved, and spherical. Image from Allgaier\* et al. [7] and available under a CC BY 4.0 license. No changes were made.

The third layout is *spherical* and thus curved horizontally and vertically, resulting in all cases having the same distance from the center.

To ensure the same conditions for all three layouts, they all show the same number of equally scaled items. The gap between the items along straight directions, as well as curved directions, is consistent across all layouts. For both *curved* and *spherical*, the items are oriented towards the center of the layout, always facing the user, whereas for *flat* they face forward.

All three layouts, their parameters, and their final sizes were determined in a preliminary pilot study (*Eo*).

The *virtual data shelf* was implemented with the game engine Unity (Unity Technologies, San Francisco U.S.). For the implementation as well as the evaluation an HTC Vive Pro Eye (HTC Corporation, Taiwan) was used.

## 8.1.3 Evaluation of a VR concept for CBR for IAs

For the evaluation, two distances between the user and the shelf and a shelf size of  $6 \times 11$  cases were chosen based on a preliminary pilot study with nine participants using the think-aloud method [82]. We used two fixed distances  $d_1 = r = 1.5 \, \text{m}$  and  $d_2 = 2r = 3 \, \text{m}$  as the distance determines how much of the shelf lies within the field of view and how small the objects are. Because of the two tasks, the distance might either support the overview (large distances) or exploration (small distances). Therefore, a small and a large distance was used. However, we made sure that the relevant texture and shape differences of the items were still recognizable when using the large distance.

In the studies, the users were instructed to sit to keep them from moving (for consistent distances), though results are not expected to change if users stand since the center of the shelf was always placed at the same height as the user's head. After the preliminary pilot study, the evaluation includes two studies. As a large number of medical experts are not available for quantitative analysis, we did a small qualitative feedback round with medical experts, and a larger study open to non-medical participants for quantitative analysis.

## Preliminary pilot study (Eo)

This study served to get a general feedback regarding the different layouts, the user interactions, and usability. Thereby, nine participants qualitatively assessed the *virtual data shelf* using the *think-aloud* method [82]. All of the participants had used a VR headset before. Three participants were visceral surgeons, the other participants were computer scientists or engineers.

The main focus of Eo was on the comparison of three sizes per layout. The results can be summarized as follows: The preferred size and distance between user and shelf depend on the task. To get a quick overview, a small shelf is better, whereas for exploration a larger shelf is more suitable. The flat layout is preferred most to get an overview, as the whole shelf was within the field of view. However, for detailed exploration, the curved and spherical layout is preferred. All sizes only differ in their width (amount of columns). A maximum height of six rows was chosen and columns were added according to the user's field of view and common head movement, which is horizontal and not vertical. Due to R1, the largest version that was still rated as appropriate by most participants of each layout was chosen for subsequent studies, resulting in displaying 66 items (6 × 11) at the same time. As a consequence of the received feedback, two user positions with different distances to the shelf were considered in the broad audience study E1. The resulting layouts and their properties are displayed in Figure 8.2.

Table 8.2: Characteristics of participants (n = 61) in E1. VR Exp. is experience with VR, VG Exp. is the frequency of playing video games per month. # is the number of participants with a quality, and % is the relative amount of the total number of participants.

Age	#	%	Sex	#	%	VR Exp	#	%	VG Exp	#	%
15-25	19	47.5	M	34	55.74	None	24	39.3	Never	16	26.2
26-35	21	34.4	F	27	44.26	< 15	30	49.2	< 1	12	19.7
36-45	2	3.3				> 15	7	11.5	1-3	7	11.5
46-55	2	3.3							More	26	42.6
56-65	6	9.8									

#### *Broad Audience Study (E1)*

In this study, 61 participants (see Tab. 8.2) compared the layouts to assess their suitability for exploration and overview tasks using a limited version of the *virtual data shelf*. In this version, only simplified geometries are displayed, and all functionalities are removed. Thus, not the target audience, e.g., medical researchers and clinicians, was used as participants, but a broad audience without medical background, to assess general overview and exploration capacities. The study consisted of two tasks (see

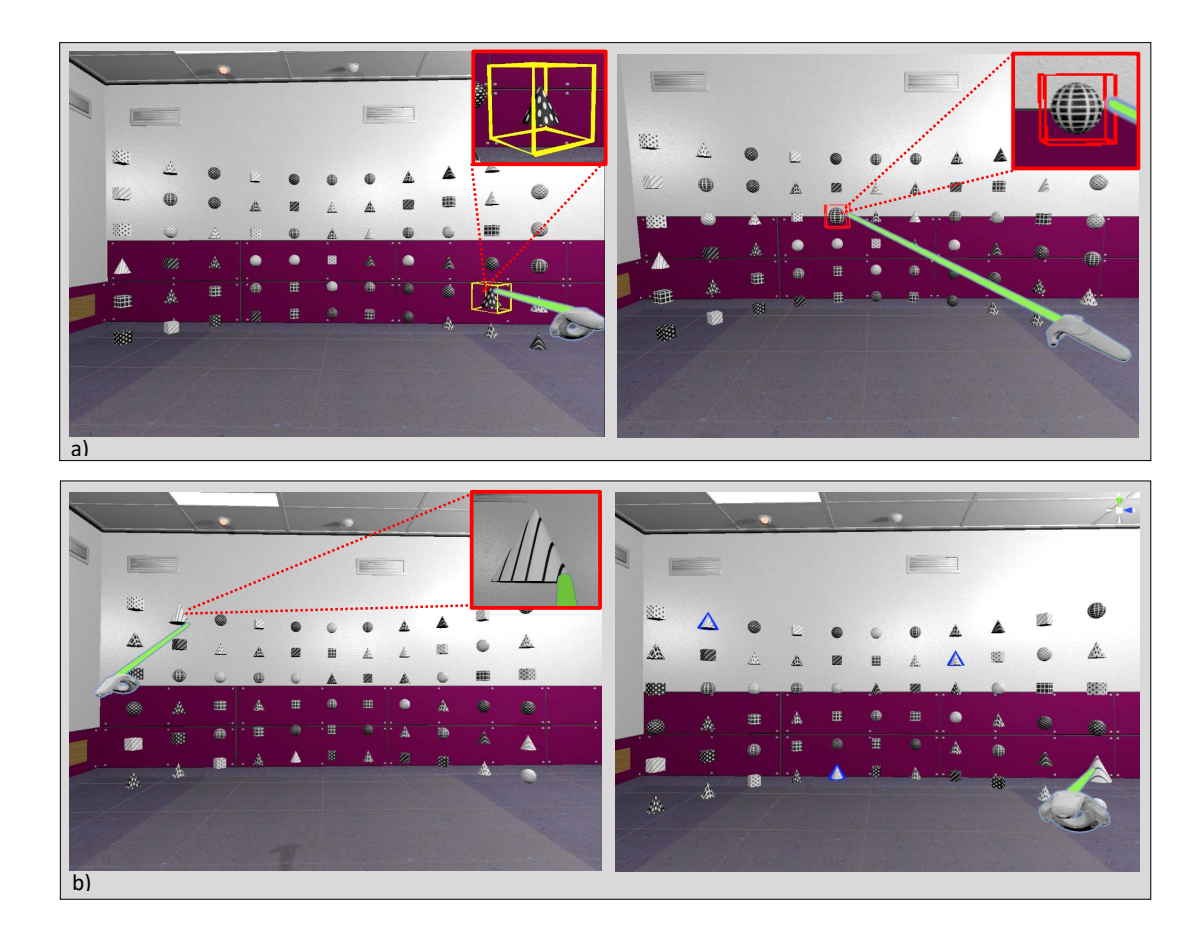


Figure 8.3: Study procedure: a) Task 1: pre-attentive search (yellow: first item, red: second item) and b) Task 2: attentive search. The search items are white cones with black lines. Selected items are highlighted in blue. Image from Allgaier\* et al. [7] and available under a CC BY 4.0 license. No changes were made.

Fig. 8.3): one for pre-attentive search to assess overview and one for attentive search to assess exploration. After the tasks were explained to the participant using a rehearsal with one layout, one distance, and a pattern which are not used in the study, they had one trial.

After starting the first task, a randomly highlighted object near the border must be selected. Afterwards, a randomly determined object within a specific Manhattan distance ( $d_{Manhattan} = 7$ ) is highlighted and must be selected. Thereby, the time between selecting the first and the second object as well as errors were captured. This was done twice per layout with the two distances in randomized order. The order of layouts was arranged according to a balanced latin square, a method that reduces

order effects by ensuring an even spread of options across every trial and across the whole study.

In the second task, the participants had to select multiple objects attentively by finding all cones with black lines (see Fig. 8.3). Here, again, the layouts were ordered according to a balanced latin square and for each layout, the two user positions were used in a randomized order. For this task, the duration and error were measured. Errors include selecting the wrong item and missing correct items. Since for each subtask a different arrangement was used, two similar arrangements were created and flipped horizontally and vertically, yielding six different but similar arrangements. The order of arrangements also underlies a balanced latin square.

E1 was completed by filling out two questionnaires. The first one was directly included into the VR tool and served to compare the layouts subjectively. For each distance, the participants could change between the three layouts and had to rate them via a five-point Likert scale regarding their appropriateness to get an overview and to explore the items in detail (not at all appropriate, not appropriate, neutral, appropriate, very appropriate). Lastly, the participants' demographics were gathered via a small questionnaire. Here, we also asked about experience with video games and VR, as familiarity with virtual spaces, controllers, and their interactions might be a factor in how a layout is rated. We chose definite cutoff values where we expected confident differences in experience to avoid user uncertainty.

#### Medical Expert Evaluation (E2)

Finally, we evaluated the *virtual data shelf* qualitatively with possible users using the think-aloud method. We used a database of 76 IAs with up to 34 metadata and morphological and hemodynamic parameters per aneurysm. The focus of *E2* was on investigating concrete use cases where such a tool could be supportive, including requirements and adaptations that would be necessary to implement. The usability in general, the visualization of similar aneurysms, and the possibility to examine and compare cases were also assessed. The layouts were additionally evaluated for the aneurysm-specific use case. Two neuroradiologists and two neurosurgeons participated. The two male neuroradiologists were in the age ranges [36-40] and [46-50] and experienced VR less than 15 times, one plays video games several times a week and the other one never plays video games. The neurosurgeons, [46-50] and [51-55] years, have experienced VR less than 15 times and never, and one surgeon plays video games one to three times a month, whereas the other one plays video games less than once a month.

## 8.1.4 Results of a VR concept for CBR for IAs

#### Quantitative results

The quantitative data from *E1* such as errors and time were statistically analyzed using the Kruskal-Walis test. This test was chosen as the data does not underlie a normal distribution. To further analyze statistical differences, a pairwise Wilcoxon test with Bonferroni correction was used as post-hoc analysis. In total, one data point from the first task, two data points from the second task, and one data point from the VR questionnaire were removed due to technical problems and accidentally skipping a subtask. The following results are structured according to the different tasks.

The first task shows significant differences between the layouts when using the short distance (p < 0.001). The post-hoc analysis revealed statistically significant differences between the curved and flat layouts as well as the spherical and flat layouts regarding time. The effect size is f = 0.46 and thus indicates a strong effect. The descriptive results show that regarding time the flat layout has the smallest median, mean, and interquartile range. This is followed by the curved layout when using the short distance. However, regarding the long distance, the differences are very small. The exact values are summarized in Table 8.3. That the flat layout is faster coincides with the results of the study by Takashina et al.'s [238].

Table 8.3: Measured time and error for all three layouts (F = flat, C = curved and S = spherical) and both tasks. The color saturation indicates the order of the results with high saturation equalling the best result.

Task 1													
Time (in seconds)									Eı	rror			
		Short			Long			Short Long			Long		
	F	C	S	F	C	S		F	C	S	F	C	S
Median	1.02	1.43	1.68	0.93	0.99	0.98	Median	0	0	O	0	0	0
Mean	1.37	1.66	1.97	1.05	1.04	1.14	Mean	0.13	0.02	0.03	0.07	0.03	0.02
IQR	0.47	0.67	1.18	0.32	0.27	0.24	IQR	O	O	O	0	O	O
						Task 2	2						
		Time (	in seco	nds)					Eı	rror			
		Short			Long				Short			Long	
	F	C	S	F	C	S		F	C	S	F	C	S
Median	10.11	10.98	10.18	8.65	9.25	10.03	Median	О	0	0	0	О	0
Mean	11.73	12.97	12.43	9.9	10.97	11.14	Mean	0.28	0.18	0.08	0.05	0.05	О
IQR	6.12	3.78	4.42	3.39	4	4.56	IQR	0	0	0	o	O	0

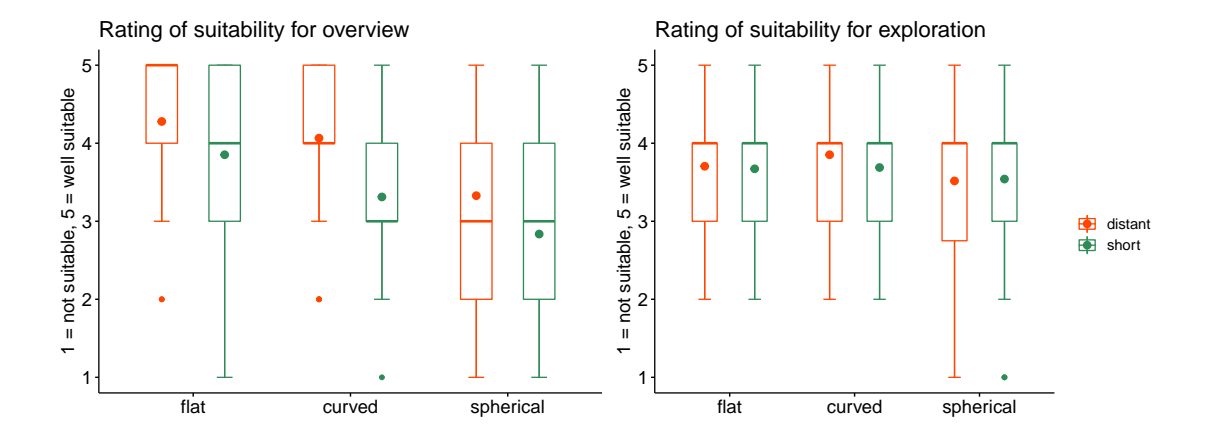


Figure 8.4: Rating of the layouts from E1 regarding their suitability to get an overview and for exploration. Image from Allgaier\* et al. [7] and available under a CC BY 4.0 license. No changes were made.

Regarding the second task, there are no significant differences between the layouts regarding time and error (for both distances).

Concerning the questionnaire, the statistical analysis revealed significant differences regarding the suitability to get an overview for short and long distances (both p <0.001). The post-hoc analysis shows differences for short distances (f =0.35) between flat and spherical, and for long distances (f =0.39) between flat and spherical as well as curved and spherical. The descriptive results (see Fig. 8.4) show that, regarding overview, the flat layout is always perceived as the best one and the spherical as the worst. For flat and curved, the short distance is rated as not as good as the long distance. Regarding exploration no significant differences could be found.

## Qualitative results

The feedback from E2 (and from E0) is categorized into applications and layouts.

APPLICATIONS For neuroradiologists, such an application would be very useful if it is extended by data about the patient-specific treatment. The treatment of similar cases can guide the treatment decision for a new case, resulting in a more objective decision. Usually, this decision is based on experience and subjective intuition, which can be incomplete, incorrect, or biased. Especially since the database contains medical data from various institutions, comparing treatment decisions and results is beneficial. If treatment data is included, the neuroradiologists stated that the shelf can be explored using the described functionalities while also exploring the 3D anatomy of interesting cases. Thereby, they can generate and possibly verify hypotheses such as:

- All aneurysms that were similar (morphologically and/or hemodynamically) before the treatment were treated similarly.
- All similarly treated aneurysms have a similar outcome.
- Different treatment methods of similar aneurysms lead to different outcomes.

One can also expand the *virtual data shelf* and include not only the treatment data of previous cases, but also the possibility to virtually treat the aneurysm and examine the results, e.g., based on the blood flow or include MRI data to highlight inflammations.

Treatment decision scenario aside, the *virtual data shelf* in its current state could be good for anatomical understanding for medical students and can be enhanced by adding more surrounding structures (e.g., CoW, eyes). They also need more surrounding structures and would like to explore head data with aneurysms starting from the outside and removing single parts step by step. When the aneurysm is reached, it would be helpful to scale it.

The neurosurgeons mentioned that the tool in its current state is not applicable to gain new insights into surgery preparation, but a collaborative VR application for patient education might be useful. For this, other anatomical structures such as the skull must be included to show access planning and describe the surgery. However, one must examine acceptance among patients. Besides patient education, the *virtual data shelf* is useful to explore an aneurysm prior to surgery and to get a better understanding of the anatomical structures. For this, more models including more vessels, the optical nerve, and bones, would be helpful. Furthermore, they mentioned that exploring an aneurysm in VR is much better than exploring it via 3D images.

In general, they emphasized that having this database and the 3D models is very valuable. Filtering and sorting is helpful, but depends on the specific question or purpose (e.g., anatomical education or treatment decision). Generally, finding similar aneurysms would be very useful in combination with the treatment decision, blood flow and virtually simulating different treatment strategies.

For the neurosurgeons, filtering was particularly relevant because only one aneurysm location is relevant at a time. Regarding usability, the neuroradiologists mentioned two aspects. First, it would be helpful to have a default orientation of the aneurysm models that coincides with the view they normally have in their 2D image data. Even if they look at 3D models, they use this default orientation as starting point for searching specific vascular structures and thus always return to this default. Alternatively, a CoW could be added to which the aneurysm models are automatically registered to provide a better orientation and anatomical understanding. Another option would be to include a small head which indicates the current rotation. Alternatively, surrounding structures can support the orientation.

Second, they mentioned that in contrast to neurosurgeons, neuroradiologists mostly work with 2D data and the transfer from 3D model to 2D data is difficult for them. Therefore, 2D image data could be included to facilitate this transfer. Besides this

medicine-related feedback, they mentioned that instead of a controller a data glove would probably be a more intuitive way of interacting with the 3D model, especially for grabbing and rotating. However, they mentioned that it was easy and fast to become familiar with the controller.

LAYOUTS After trying out all three layouts, both neuroradiologists stated that they preferred the spherical layout, although a larger distance (larger than the radius) is necessary to get an overview. With the spherical layout, the models seem to be more tangible due to equal distances, thus enclosing the user. Because of this, the participants stated that it is more intuitive. Some surgeons emphasized that for detailed exploration, the curved and spherical layout is much more intuitive and appropriate since all objects have the same distance. One of them also recognized that the spherical layout has the benefit that objects above each other can be differentiated more easily as they differ in their depth. Consequently, it is easier to concentrate on one single item. One slightly preferred the flat layout. Overall, there was no favorite layout.

## 8.1.5 Discussion of a VR concept for CBR for IAs

E1 revealed that the flat layout is the best and fastest to get an overview, especially for small distances. With short distances, all three layouts are too large to be completely in the field of view. However, with the flat layout, the head does not have to be rotated as much (recall Fig. 8.2). This coincides with the questionnaire results which rated flat as the best regarding overview. This could be explained by the fact that we are used to working with displays in front of us, being entirely in our field of view. We did not include a questionnaire regarding comfort, which is recommended in future studies to reveal correlations between comfort and layout. VR provides the possibility to use more space and thus to display and interact with models that are distributed around the user. Movement is therefore required to fully exploit the potential of VR. Since a lot of our participants had never used VR (39%) or just a couple of times (49%, see Tab. 8.2), the lack of familiarity with the medium might have influenced the result. To avoid this, a long-term evaluation is recommended and might provide additional insights. Concerning both the VR experience as well as the frequency of playing video games, no differences regarding the ranking in the questionnaire could be found. One limitation here is the number of participants in each of the subgroups which does not allow proper statistical analysis.

When looking at the error rate, the flat layout has more errors than the other two layouts. This might be due to the flat interaction angle when selecting objects at the edges.

In contrast to  $E_1$ , where only slight differences occurred regarding exploration,  $E_2$ , the qualitative feedback, shows that medical professionals prefer the curved or spherical layout for a detailed exploration. This also confirms the results of Liu et al. [148].

We hypothesize that medical experts appreciated being closer to the 3D models, as they were interested in and familiar with the anatomy and thus wanted to inspect individual cases more closely. This is facilitated by the curved and spherical layouts since they enable a closer distance between the user and all models as compared to the flat layout. Experience levels with VR and video games across the experts were varied, and we had too few participants for a statistical evaluation, though we found no correlation between performance and experience in general participants in *E1*. Thus, based on our comparison using non-experts and experts, all layouts should be provided, and the user should be allowed to change them based on the current task and preferences.

In general, the *virtual data shelf* is a good basis for medical research. However, for hypothesis generation, our tool must be further refined and extended. In the case of treatment decision, treatment properties have to be identified and quantified to compare and find similar cases. Once these have been included and the database has been enlarged considerably, neuroradiologists would consider actively using the tool for the mentioned tasks. It can also be extended by including virtual treatment possibilities or combining it with virtual training and treatment applications. Other applications mentioned by the experts are medical education and training anatomical understanding. Hence, not just the affected structure but additional surrounding structures to provide the necessary anatomical context are required.

However, no matter for which use case the *virtual data shelf* shall be specialized, additional interactions and functionalities would be relevant and it is not applicable in its current form.

In contrast to previous works, we proposed a design combining benefits from the shelf and display metaphor. Furthermore, in our comparison of different layouts, we used much more complex objects under our goal of displaying and working with a large database. In contrast to other studies comparing different layouts [238], we could not find statistically significant evidence showing that interacting on a curved layout is faster.

#### Limitations and Future Work

E1 was conducted with non-experts and therefore a lot of functionalities had to be removed. However, the focus was on the layouts. Furthermore, the basic principle of our *virtual data shelf* can be applied to other use cases. Although a specific use case was selected based on previous feedback from neurosurgeons, the evaluation with neurosurgeons and neuroradiologists as well as the feedback from visceral surgeons emphasized that for clinical use the tool has to be expanded and specialized according to the discipline and objective.

Accordingly, in the future, we want to adapt the shelf to one of the identified medical use cases. Then, a more precise evaluation in which the ability of the shelf regarding data exploration, hypotheses generation, and decision-making can be evaluated. Therefore, specialized evaluation tasks must be created. To investigate the benefit of

such a *virtual data shelf*, an evaluation over time with more respective experts is highly recommended.

No matter which use case is chosen, it is important that new cases can be added. Although it is no problem to extend the data table, the models first have to be generated. Since it is not always feasible to manually create and prepare the models and include them, especially in a surgeon's busy schedule, an automatic approach including segmentation and preprocessing would be beneficial.

Another possible extension would be a focus on arrangement and grouping of models in relation to each other, making use of distances and depth, thus exploiting the entirety of the VR space.

Since our focus was the comparison of the layouts, we used a fixed number of items based on  $R_1$  and the pilot study. However, a larger evaluation regarding information overload and the preferred number of items could give more insights.

There are studies highlighting the advantages of VR over desktop when dealing with complex anatomical 3D structures [107, 114, 258]. We did not include a comparison of the two modalities as our focus was on the comparison of different layouts within VR, however, a future study to investigate the new and the conventional modality might be interesting. Other future studies could address ergonomics, where the virtual shelf's position, height, width, and orientation are specifically scaled to each user's individual needs and comfort based on their size and preference.

## 8.1.6 Conclusion on a VR concept for CBR for IAs

Our studies show that an appropriate arrangement of 3D objects in an immersive virtual reality environment depends on the user and task objectives. If getting an overview as well as an exploration is required in an application, the users should have the possibility to change the layouts according to their needs.

The proposed *virtual data shelf*, which combines benefits of virtual shelves and displays, serves as a good basis for various applications such as in the medical field and can easily be extended by additional functionalities.

#### 8.2 EXCERPT: A VR CONCEPT FOR COW EXPLORATION

Beyond the exploration of a database for cohort-based research, VR has many benefits in the medical field. The immersion and spatial freedom offer particular opportunities in the field of education. This excerpt presents a glimpse into future work by presenting a prototype for the exploration of the CoW in VR and shows that the computer support for cohort-based research can extend even further than the previously discussed approaches that answered RQ 3. The CoW is taught in medical education, but is always depicted as a 2D diagram in schooling books, and even most technologically enhanced materials are limited to 2D [128]. This limits the understanding of the

## Publication

Section 8.2 is based on:

[220] L. Spitz, M. Allgaier, and A. Mpotsaris, D. Behme, B. Preim, and S. Saalfeld. "Segmentation of Circle of Willis from 7T TOF-MRI data and immersive exploration using VR." In: Curr Dir Biomed Eng 8.1 (2022), 129-132. doi: 10.1515/cdbme-2022-0033. The work was conceptualized, designed, and implemented by L. Spitz. M. Allgaier supported the VR development.

CoW's natural alignment and its connections in a real brain. Additionally, a standard CoW does not depict pathologies or prepares for the particularities of patient-specific anatomy, where entire segments or vessels may be missing. Given that understanding anatomy spatially is one of the most challenging areas for medical students [12], exploring a 3D CoW in VR could thus enhance the learning experience.

FUNCTIONALITIES OF A VR PROTOTYPE FOR COW EXPLORATION For the VR prototype we used the CoW model segmented via the methods in Chapter 3. A VR environment developed by Allgaier et al. [6] was used in the Unity game engine and the XR Interaction Toolkit as a base for the prototype. The aneurysm selection scene was used as a base for a medical environment for the CoW exploration. The CoW model was placed in the middle of the otherwise empty VR OR environment with a menu panel to its left (see Figure 8.5). The menu contained a slider for transparency and a slider for scale. Transparency refers to the opaqueness of the vessel walls, beneath which the centerline becomes visible (see Figure 8.6). This can help to show the base structure of the CoW without particularities of the vessels and their texture and material in the way. The scale slider can be used to make the CoW and centerline bigger or smaller.

The user can interact with the CoW by grabbing it with the controller. Once grabbed, it can be rotated and placed freely around the room. This way the CoW can be viewed from different angles that would not otherwise be possible.

FIRST IMPRESSION OF A VR PROTOTYPE FOR COW EXPLORATION Two experienced neuroradiologists explored the prototype and discussed their first impressions.

They expressed that exploration in VR was a new way for them to see the CoW from arbitrary angles and scales. They remarked that the 3D model illustrated the connections between anterior and posterior circulations of the CoW very well.

For anatomical teaching, they could imagine a VR CoW model not only helpful for general anatomical education, but also for demonstration of specific pathologies. This is in line with the positive effects noted in surveys on virtual anatomy systems [114, 194].

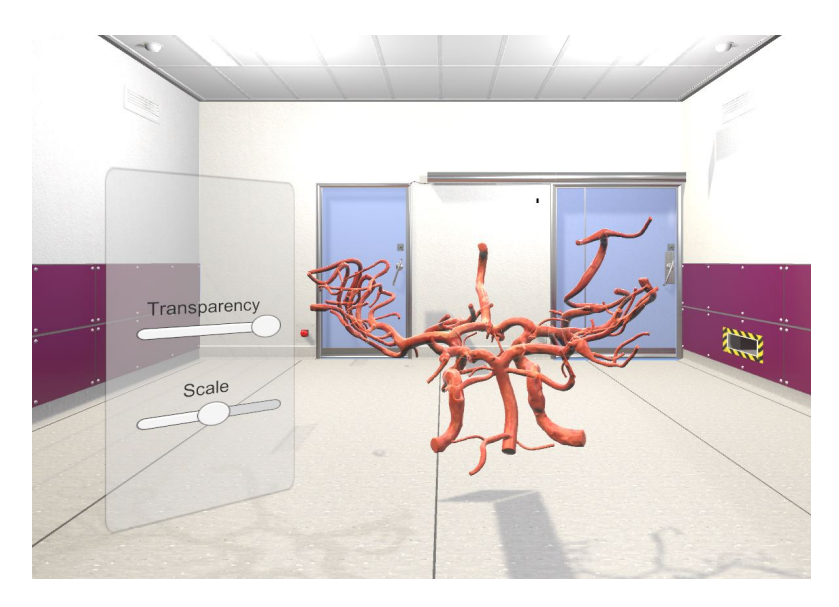


Figure 8.5: CoW model in the VR prototype with maximum opacity and default scale. Image from **Spitz** et al. [220] and available under a CC BY 4.0 license. No changes were made.

Additional inclusions would be adding a skull and brain toggle to see orientation of the CoW, and according to the radiologists the eyes to see the distance to them.

FUTURE WORK FOR A VR PROTOTYPE FOR COW EXPLORATION In the future, a study to compare how teaching CoW anatomy to medical students with a VR application performs in contrast to the standard education with 2D diagrams would be feasible. While the CoW is a very specialized structure, it is argued that introducing imaging scans much earlier in the medical curriculum than it is currently might help with general anatomical and spatial understanding of anatomy and could have positive consequences [128]. This can help with the mental translation between 2D and 3D, 2D being provided by imaging, and 3D by a VR application like our tool.

Another functionality of the application could be a puzzle of complex anatomical structures that can be assembled and disassembled to examine and understand the connections between the parts. This could be done for the CoW, but for other organs too, like the inner ear. Other prototypes for different parts of anatomy already exist and have received first positive feedback [192].

In conclusion, this excerpt presents a VR prototype that enables exploration of a detailed CoW model, including the centerline, in a free 3D environment with a medical OR backdrop. As VR systems have become increasingly affordable in recent years, they have become more widespread. The prototype includes options for transparency of the vessel walls and scale of the entire CoW model, as well as the freedom to rotate the CoW around all axes and place it within the room.

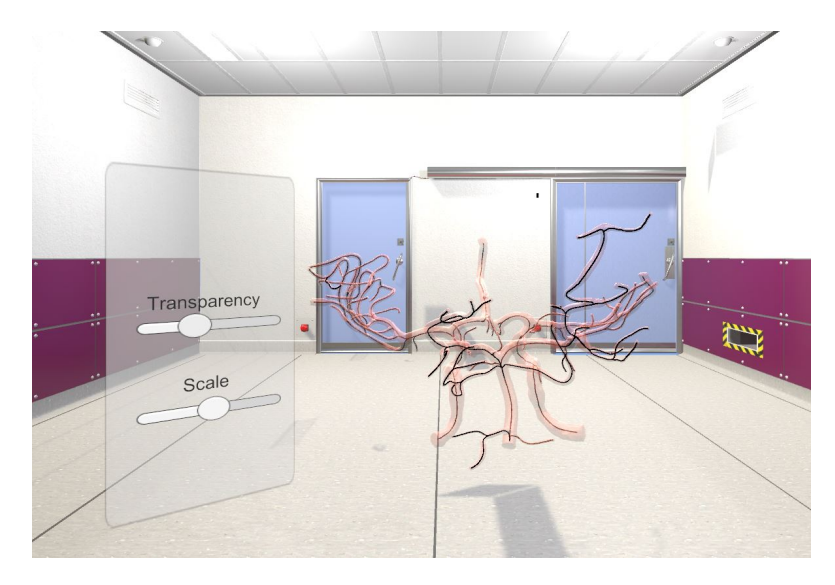


Figure 8.6: CoW model in the VR prototype with lowered opacity, showing the centerline. Image from **Spitz** et al. [220] and available under a CC BY 4.0 license. No changes were made.

The prototype was rated very positively by neuroradiologists, who commented on the educational possibilities of such a VR application and saw further potential for other use cases. This extends the answer to RQ 3, to what extent can morphology-driven analysis support cohort-based research, to the patient-specific education use-case.

#### 8.3 CONCLUSION ON VR CONCEPTS FOR MORPHOLOGIC ANALYSIS

In this chapter we aimed to extend the answer to RQ 3, which asked to what extent morphology-driven analysis can support cohort-based research, which we already answered in Chapter 7. We expanded the answer by proposing VR concepts for the analysis tasks.

The virtual data shelf demonstrated the benefit of VR for morphological analysis and beyond. The excerpt further showed the potential of analysis not only supporting cohort-based research, but also more individual cases and in education in VR. It does so by presenting a 3D CoW with patient-specific morphology, which is not available in textbooks, thus offering opportunities for better spatial understanding for medical students, as well as for patient education and thus a better understanding and trust in physicians.

Whereas the VR Prototype primarily offers education opportunities, the virtual data shelf offers an immersive arrangement of IAs for cohort-based research, though the exact layout depends on the individual use case. While the virtual data shelf and the underlying data were not sufficient to support treatment decisions in its current

state, with the appropriate underlying data and adaptions for specific use cases, it could feasibly be used for treatment decision support, virtual treatment, and research question generation. Thus, VR offers a whole new range of possibilities for analysis support of cohort-based research.

# Part V

CONCLUSIONS ON MORPHOLOGY-DRIVEN ANALYSIS OF NEUROVASCULAR PATHOLOGIES

Finally, the thesis is summarized, and its limitations and future work are discussed.

The thesis introduces computer support for the morphology-driven analysis of neurovascular pathologies, with a focus on IAs. Brain function is reliant on a steady blood supply, and any pathology of the neurovasculature can lead to immediate deficits, and, eventually, death, if not treated. Further, a disruption of blood flow can lead to thrombosis and strokes, which often end deadly. Computational support for analysis can aid in the research of not yet understood mechanisms of the pathologies, in closing research gaps of existing treatment methods, in the decision of how to treat the pathology, and in risk assessment.

Specifically, the thesis focused on morphology-driven analysis, as the morphology of the vasculature plays an important role in the progression of pathologies and in how they are treated. It presents analysis for preprocessing of the neurovasculature, patient-specific analysis, and cohort-based analysis.

PREPROCESSING Before analysis, the morphology must be extracted from medical imaging scans. For this, Chapter 3 presents a segmentation pipeline that, while originally conceptualized for the segmentation of TOF-MRI, can easily be adapted to segment vasculature from other modalities by adjusting the preprocessing steps.

In some cases, combining information of multiple modalities is necessary, for example for data assimilation for CSVD research. Here, the morphology, meaning a detailed segmentation, from 7T TOF-MRI, combined with the blood flow measurements from 7T PC-MRI, can be used to explore blood flow in small vessels of the CoW to research CSVD. Co-registration, the process of combining two models or images, can be used for this case. However, co-registrations are highly specific and need to be tailored to the specific use case. Vascular registration is particularly challenging, as the voxels that make up the vessels in the imaging only make up a small percentage of the entire volume. No co-registration method exists yet for the registration of 7T TOF-MRI and 7T PC-MRI. From this need, *RQ 1* arises:

RQ 1: How can information about vascular pathologies from multiple 7T MRI scans be combined?

To answer RQ 1: Vascular information from 7T MRI scans can be combined with a sophisticated, specialized co-registration method, as introduced in Chapter 4. To address the difference in detail of the modalities and the specific challenges of vascular coregistration, the approach is hybrid and hierarchical, utilizing a metric that fits the centerline of the TOF-MRI segmentation to the intensity ridges that make up the vessels within the PC-MRI voxel volume. The hierarchical nature in which the method traverses the vessel tree, as well as the decoupling of the parameters of the affine transformation, address the challenges of optimizing the registration. As a result of answering RQ 1, this thesis presents a hybrid co-registration approach that utilizes the topological information of the vasculature and gives a solution for the research gap of combining of vascular pathologies from 7T MRI scans.

For patient-specific analysis, the thesis first illustrates PATIENT-SPECIFIC ANALYSIS how morphology can drive analysis and affect hemodynamics with a study of mirror aneurysms in Chapter 5. Patients with this rare IA subgroup have IAs at the same location in the left and right hemispheres, meaning these IAs had the same patient-specific and location-based risk factors. At the time of data collection, some patients also had mirror aneurysms with different rupture states. Using morphology, differences in mirror aneurysms were analyzed. To analyze the influence of morphology, the IA domes were stitched on the parent vessels of the other hemisphere, and blood flow was simulated in both the original and the stitched cases. A difference between left and right hemisphere IAs was found, with left IAs being larger and more concave, having higher hemodynamic parameters, and a higher chance of being ruptured. The stitched cases revealed that both the morphology of the IA dome as well as of the parent vessels influence hemodynamics, with size, concavity, and vessel angle having the strongest influence. This study highlights the importance of patient-specific, morphology-driven analysis and of morphology as an important risk factor for IAs, as well as the impact of changes in morphology.

The mirror aneurysm example used scans of patients at one specific moment. However, morphology may change over time. This longitudinal change should be analyzed, because IAs growth is a risk factor for rupture and because deformation is a relevant aspect to be considered for treatment. Implants affect their surrounding structures, and the implants themselves may deform over time, e.g., the compression phenomenon observed in the WEB. Analysis of changes in morphology, and deformations, are therefore essential for IA treatment. This raises *RQ* 2:

RQ 2: How can longitudinal morphological deformation be analyzed?

The more novel the treatment or implant, the less researched the potential deformation caused by it is. The CNS is a relatively novel implant for the treatment of IAs, specifically the difficult-to-treat WNBAs. No studies have yet assessed the influence of the CNS on IA morphology, and whether there is a deformation of the CNS itself, over time. From this need, RQ 2 arose. In Chapter 6, the thesis presents the first studies that assess the longitudinal deformation of the IA, specifically its ostium, after CNS deployment. Additionally, the deformation of the CNS was assessed.

To assess deformation, the IAs from patients taken at multiple steps before and after treatment were segmented and registered, and the ostium and morphologic pa-

rameters were extracted semi-automatically. Various shape and size parameters were calculated and assessed. A preliminary study with seven patients assessed longitudinal deformation, meaning change over a certain amount of time, of the ostium. A pre-treatment scan was compared to the latest follow-up scan available. The preliminary study found a shrinking of the ostia after treatment, which may be explained by the healing process induced by CNS deployment. A second study with 13 patients also took scans taken between the first pre-treatment and the last follow-up scan into account. It also assessed CNS deformation by size parameters, and by size and shape of the edge ring, the upper rim of the CNS that was identified automatically.

Analysis of deformation was carried out in six groups, among them an intra-patient assessment to act as a control group, a longitudinal assessment that measured deformation over the maximum amount of time between scans, postprocedural changes, and assessments that approximated a specific amount of time passing, like six months or one year after treatment. Correlations with recurrence and spatial changes were assessed as well.

No statistically significant changes over time were found for the IA ostium or ostium. Neither did morphology correlate with recurrence or spatial change. This may, after confirmation in a bigger study, show the potential of the CNS robustness to deformation over time.

To answer RQ 2: The longitudinal deformation of morphology can be assessed by careful extraction, evaluation, and analysis of morphological parameters from different timesteps, followed by careful grouping and comparison of the observed changes. Correlation with the outcome and assessment of overall spatial change are also crucial. The analysis supports physicians beyond rupture risk and treatment decision support, as it can, with more cases, give new insights into why some patients may have a good outcome while others have a bad outcome.

COHORT-BASED ANALYSIS Next, the thesis addressed the opportunity morphology-driven analysis offers for cohort-based research. While the previous projects also assessed groups of patients, they assessed the morphology of the patients individually, and this was the area where the computational support was provided. The projects presented in Chapter 7 and Chapter 8 instead want to support the finding and matching of cohorts, rather than focusing on the individual patients.

The wide variety of parameters, morphologic or otherwise, that can be derived from IAs and that determine their risk factors and treatment decisions, pose a significant challenge for physicians. Their large number makes it impossible to keep an overview, especially when many aneurysms are considered. The concept of what makes cases similar, and how to define similarity with such a huge variety of parameters, is another challenge. Here, computer support can potentially aid physicians in keeping that overview for treatment decisions, but also for research question generation or cohort-matching. The thesis thus considers *RQ* 3:

RQ 3: To what extent can morphology-driven analysis support cohort-based research?

First, the question of how to select subgroups was considered. Subgroups, or cohorts, can be relevant for IAs in the case of finding similar cases to determine how they were treated, or for finding a subset of cases that are representative of the whole to train physicians, or to prepare them for a specific kind of case.

For research and cohort-matching, a tool was designed that with the help of CBR identifies similar cases within a database. It assesses rupture risk via classification and provides different visualizations of the results and the similarity within the underlying database of IA cases. The tool received positive results in a quantitative assessment with a phantom database and in a qualitative survey with doctors and experienced IA researchers. The tool is currently actively being used by neurosurgeons for cohort matching in rupture, risk factors, and treatment research, leading to joint clinical research papers [231–234].

Another application for subgroup selection is for reducing the size of a database, to get an IA training set for trainee neurosurgeons. Using IS, a representative subgroup can be found, and the thesis presents RIS, which, inspired by IS, finds a subgroup that along with the variance of the database also takes similarity to a specified case into account. It thus selects a subgroup that could be used to train a certain range of cases with specific traits, without being too similar. A framework for the evaluation of RIS was presented as well.

When utilizing these subgroup tools, the actual morphology of the cases can, however, get somewhat lost. As the exploration of the IA and its surrounding vasculature, and vasculature in general, is also valuable, the thesis further presents concepts for VR for morphology-driven analysis, as VR offers improved spatial perception through depth perception and immersion.

Cohorts necessarily include a large number of cases, thus this thesis presents a comparison of different layouts for a virtual data shelf that aims to optimally display a large amount of 3D IA models. The virtual data shelf further has the same CBR functionality as the previously presented tool and offers the opportunity to explore individual cases. After a pilot study, a broad audience study for quantitative assessment and a medical expert study for qualitative feedback was performed. Both studies found that the arrangement of IAs depends on the use case of the virtual data shelf.

Lastly, the thesis gives a brief excerpt into the exploration of the vasculature, specifically the CoW, for education purposes. VR offers novel opportunities to understand the complex vasculature of the CoW, as well as potentially heightening motivation and drive to learn. A prototype received positive feedback from neurosurgeons.

To answer RQ 3: Analysis can support cohort-based research to the extent that it can, via computer support, match cohorts and identify subgroups from a large number of IAs and their parameters, where a human would quickly get confused. The developed approaches find similarity and define subgroups from an arbitrary number of cases and parameters and present new insights from the provided data. The tool the thesis

presents can match cohorts and is actively being used in clinical research. Analysis can further be supported by visualizations, including VR, that gain insight into how the results of the subgroups or cohorts were matched, and thus aid in the generation of research questions, or, with the addition of appropriate data, even treatment decisions.

The thesis thus presents computation support for the morphology-driven analysis of neurovascular pathologies. It showed that, after specialized preprocessing, patient-specific and cohort-based analysis can facilitate new insights for research.

## 9.1 LIMITATIONS

IA RESEARCH BEYOND MORPHOLOGY Aneurysm research largely relies on imaging scans. However, every scan is a snapshot of a moment in time, meaning every IA listed as unruptured at the time of scan may have ruptured in the meantime. For an unruptured aneurysm to be considered stable, no change or progression must have been observed at follow-ups. For this thesis, follow-up data beyond the moment of the used scan was not available for most of the presented projects.

While this thesis focuses on IA morphology, it does not mean to downplay the importance of clinical parameters for rupture risk, treatment decisions, and research. The ranking of which parameters, clinical or morphologic, are the most reliable to predict rupture, or which parameters predict success for which treatment, are not fully understood yet. This is part of what drove RQ 3. That it is important to look beyond morphology and consider clinical metadata, e.g., IA location, patient age, or patient sex, is highlighted by the inclusion of those parameters in clinical scores such as the PHASES and ELAPSS scores, as well as the Triple-S risk prediction models (recall Section 2.6.4) [17, 124]. While morphology is included in all of these scores as well, the thesis does not give the same attention to those other parameters.

MANUAL STEPS A limitation of the thesis is the manual steps in the segmentation pipeline from Section 3.2, which is used in almost all other projects of the thesis, and the landmark selection from Section 4.4. Manual steps always mean potential for human error and inconsistencies, especially in areas like segmentation with no available ground truth. As mentioned in Section 6.3, there is ambiguity in how to segment, e.g., where to set a threshold. Segmenting (or setting landmarks) manually, even when done by the same experienced person, opens the segmentation to subjectivity and inconsistencies, both in individual segmentations and a series of segmentations. This could have been solved with DL, however, due to the lack of ground truth, data shortage, and data imbalance, there was no way to train a DL network, or to evaluate an automatic segmentation. Due to the specificity of the data, pathologies, and use cases, no pre-trained networks existed to supplement the segmentation, registration, or classification tasks.

Further, the goal of segmentation was detailed morphologic analysis and, in some cases, blood flow simulations. Both cases need high-quality surface meshes, for which DL results are not yet sufficient, meaning manual postprocessing would have to follow DL segmentation as well. The lack of sufficient data and approach may be solved in the future and will be discussed in Section 9.2. Developing specific and more advanced segmentation algorithms was not within the scope of this thesis

THE MEANING OF NO STATISTICAL SIGNIFICANCE In Section 6.3, the thesis found no statistically significant deformation of the IA ostium or the CNS itself and no correlation with pre-treatment IA morphology and recurrence. However, a lack of statistical significance does not equal a lack for deformation. While some of the observed deformations may indeed be due to imaging resolution or segmentation ambiguity, deformation was observed in individual patients. The study the thesis presents, however, did not find any observable or statistically significant patterns. This may be due to the small number of patients analyzed. Part of the lack of correlation with recurrence may the that of the thirteen patients, only three had a recurrence, which was too few to find correlations. A study with more patients is necessary to find causes for deformation and potentially existing correlations with recurrence or to confirm if deformation cases are outliers. Outliers or not, multiple studies about the efficacy of the CNS show its safety, deformation or not [99, 117].

LACK OF TREATMENT DATA The CBR tool presented in Section 7.1 and its VR concept from Section 8.1 were mentioned to potentially aid in treatment decisions, as well as in research purposes like cohort matching and research question generation. However, the lack of treatment data in the database, meaning that there is no information available about how the cases in the database were treated, is a significant limitation, according to the neurosurgeons who evaluated the tool. With that information, they would conceivably use the tool during the decision-making process for how to treat a newly diagnosed or found IA. Information about the treatment of the individual IAs used in the database for the CBR tool was not available. Further, the database used IAs from multiple clinics, meaning that there may not have been standardized ways of recording the treatment options. This also raises the question of how to record treatment success over time in a database.

Another issue is data availability in general. Data security and patient privacy are concerns and have to be driven forward by the clinics. Additionally, imaging scans for follow-ups are expensive, and radiation doses from imaging should be minimized.

## 9.2 FUTURE WORK

There remains much to be done in the field of morphology-driven analysis for neurovascular pathologies.

PREPROCESSING A fully automatic segmentation of the neurovasculature would be desirable, as a consistent and speedy segmentation would aid in facilitating morphological analysis. Due to the range of imaging modalities available, there is likely no one-size-fits-all approach, but for individual modalities, a segmentation may feasibly be derived. The artifacts in the imaging that necessitate the manual post-processing mentioned in Section 3.2 are a challenge, however. Similarly, focusing on the pathology when segmentation of the entire vasculature is not desirable may also pose a challenge. These may be possible to overcome with DL, as approaches exist that automatically identify a region of interest, anatomical structures, or pathologies. At this point, DL alone cannot produce high-quality meshes and would need postprocessing. In the future, such approaches may however be developed.

Whether to be solved with DL or not, another improvement of the segmentation pipeline is to combine it into a single tool, as its current state uses five different kinds of software.

The presented co-registration approach from Section 4.4 can in the future be improved in multiple ways. It currently uses affine transformations, which may be able to approximate non-rigid deformations when done locally, but a deformable transformation may lead to further improvements. A non-iterative optimizer could reduce the runtime, as could GPU acceleration. Here, too, DL could potentially offer a solution, though there is the issue of lack of ground truth and available data. As registration is a common preprocessing step for morphology-driven analysis, making it available and accessible would help facilitate analysis tasks.

PATIENT-SPECIFIC ANALYSIS For patient-specific analysis, Section 9.1 already discussed the need of larger studies to confirm the robustness of the CNS against deformation or to find definite patterns in what causes IA deformation or recurrence after CNS deployment. While several studies have assessed its safety and efficacy, the CNS is still a novel implant in comparison to IA treatments like clipping and coiling. It shows much promise, but more long-term studies with more patients will further cement its value and benefits to patients. Cases of CNS failure need to be studied more, and how these failed cases can be optimally retreated. Other studies could assess the CNS outside of its intended use, meaning for non-WNBAs, or it being placed non-symmetrically. Another yet unexplored field is the best placement of the CNS. As the placement of any implant is based on IA morphology, analysis must be driven by the morphology to gain insights into best practices. Computational support for this morphology-driven analysis can aid physicians in answering these unsolved research questions.

The analysis can easily be adapted to other implants in the future. To gain further insights, the patient-specific analysis could further be combined with the cohort-based similarity analysis presented in this thesis, once more patients are available. A large multicenter study could give insights not just into the morphological deformation

of the implant and the vasculature, but also into similarities between patients with successful or failed outcomes.

COHORT-BASED ANALYSIS For cohort-based analysis, Section 9.1 discussed the added value of treatment data to the CBR tool and how that addition could conceivably be used for treatment decisions. DL could also be added to support rupture risk assessment, and integrate automatic segmentation and morphology extraction [204]. In regard to its value of generating research questions, the visualization of the impact of weighing of individual parameters could add further clarity for clinicians. This could extend its use beyond the cohort matching it is already being used for.

The VR concept for the CBR tool would benefit from the addition of treatment data in the same way. It, however, could benefit from the inclusion of a treatment simulation as well, where the physician could treat the IA in VR with different methods and see the simulated results, thus gaining insight into what the best treatment method is. This is out of the scope of morphology-driven analysis but would in turn not be possible without the prior analysis that gives insights into treatment of similar aneurysms. Outside of analysis, VR applications of neurovasculature offer opportunities in education and training that can be explored in the future as well, in studies with trainee physicians. The IS framework for selecting a representative subgroup would benefit from qualitative feedback from neurosurgeons.

DL SUPPORT As mentioned above, many of the analysis steps presented in this thesis could be supported by DL networks. Further, the use of DL may even address some of the individual projects' limitations, e.g. the manual steps of the segmentation from Section 3.2 that are used in several of the thesis projects.

In the future, the following steps steps need to be addressed to make DL support feasible:

- Data shortage: DL, needs a large amount of data to train. While data augmentation methods are available, several projects had less than ten cases on hand, and augmentation is limited and does not solve overfitting, especially for clinical data [56, 70, 103]. A general rule of thumb is to use at least ten times the data as the number of features [164], and 300 datasets is mentioned as a small dataset [70].
- *Lack of ground truth*: while unsupervised approaches exist, training and evaluation of a network for segmentation or co-registration require a ground truth [56, 103]. No ground truth exists for the presented projects, so the ground truth first must be created (semi-)manually by experts, which is time-consuming.
- *Data imbalance*: the data that was available was largely unbalanced. The thesis either worked with healthy patients or patients with pathologies, and the pathologies were largely unbalanced in their features. As a network will always take

over any bias present in the training set [56, 70], care should be taken when expanding datasets to address data shortage to select a balanced set of data.

- Ethical concerns: the use of DL in the medical field is not free of ethical concerns. The already mentioned bias of unbalanced training sets may extend to bias against groups of patients. Further, the privacy of sensitive patient data is a concern, as well as the explainability of DL networks. This refers to the lack of trust of medical professionals into DL networks due to the black box nature of DL, where DL's reasoning for its results is untransparent and hard to track [70, 198].
- Competitiveness of iterative methods: iterative methods remain competitive in many areas, particularly co-registration [103]. While DL methods are often considered faster and less computationally expensive (after training), some iterative methods are on par in terms of performance [103], meaning that the benefit of DL, with all the listed requirements, must be established first.

In conclusion, this thesis presents computational support for the morphology-driven analysis of neurovascular pathologies, especially for IAs. The thesis contributes:

- a specialized, hybrid hierarchical co-registration method was developed to combine high-resolution 7T MRI data
- studies that, for the first time, analyze the longitudinal deformation of the novel implant CNS and how it affects the IA in which it is employed over time
- tools for the automatic selection of subgroups and cohort matching from a large database of cases and parameters, that also facilitate visual exploration of the underlying cases, enabling research question generation

The analyses introduced by the thesis give new insights into IA research, and have much potential with respect to their limitations, and with improving imaging and DL, as well as more available data in the future.

- [1] A. Aamodt and E. Plaza. "Case-based reasoning: foundational issues, methodological variations, and system approaches." In: *AI Commun* 7.1 (1994), pp. 39–59. DOI: 10.3233/AIC-1994-7104.
- [2] T. Abboud, J. Rustom, M. Bester, P. Czorlich, E. Vittorazzi, H. O. Pinnschmidt, M. Westphal, and J. Regelsberger. "Morphology of ruptured and unruptured intracranial aneurysms." In: *World Neurosurg* 99 (2017), pp. 610–617. ISSN: 1878-8750. DOI: 10.1016/j.wneu.2016.12.053.
- [3] A. Ajam, A. A. Aziz, V. S. Asirvadam, A. S. Muda, I. Faye, and S. J. Safdar Gardezi. "A review on segmentation and modeling of cerebral vasculature for surgical planning." In: *IEEE Access* 5 (2017), pp. 15222–15240. DOI: 10.1109/ACCESS.2017.2718590.
- [4] C. Y. Akhunbay-Fudge, K. Deniz, A. K. Tyagi, and T. Patankar. "Endovascular treatment of wide-necked intracranial aneurysms using the novel Contour Neurovascular System: a single-center safety and feasibility study." In: *J Neurointerv Surg* 12.10 (2020), pp. 987–992. DOI: 10.1136/neurintsurg-2019-015628.
- [5] A. M. Algra, A. Lindgren, M. D. I. Vergouwen, J. P. Greving, I. C. van der Schaaf, T. P. C. van Doormaal, and G. J. E. Rinkel. "Procedural clinical complications, case-fatality risks, and risk factors in endovascular and neurosurgical treatment of unruptured intracranial aneurysms: a systematic review and meta-analysis." In: *JAMA Neurol* 76.3 (2019), pp. 282–293. ISSN: 2168-6149. DOI: 10.1001/jaman eurol.2018.4165.
- [6] M. Allgaier, A. Amini, B. Neyazi, I. E. Sandalcioglu, B. Preim, and S. Saalfeld. "VR-based training of craniotomy for intracranial aneurysm surgery." In: *Int J Comput Assist Radiol Surg* 17 (2022), 449–456. DOI: 10.1007/s11548-021-02538-3.
- [7] M. Allgaier\*, L. Spitz\*, D. Behme, A. Mpotsaris, P. Berg, B. Preim, and S. Saalfeld. "Design of a virtual data shelf to effectively explore a large database of 3D medical surface models in VR." In: *Int J Comput Assist Radiol Surg* 18.1 (2023). \*These authors contributed equally, pp. 2013–2022. DOI: 10.1007/s11548-023-02851-z.
- [8] E. Anderson. "The species problem in iris." In: *Ann Mo Bot Gard* 23 (1936), pp. 457–509.

- [9] M. Ankerst, M. M. Breunig, H.-P. Kriegel, and J. Sander. "OPTICS: ordering points to identify the clustering structure." In: *Proc. ACM SIGMOD Int Conf Manag Data*. Association for Computing Machinery, 1999, pp. 49–60. DOI: 10. 1145/304182.304187.
- [10] L. Antiga, M. Piccinelli, L. Botti, B. Ene-Iordache, A. Remuzzi, and D. Steinman. "An image-based modeling framework for patient-specific computational hemodynamics." In: *Med Biol Eng Comput* 46.11 (2008), 1097–1112. DOI: 10.1007/s11517-008-0420-1.
- [11] A. S. Arthur, A. Molyneux, A. L. Coon, I. Saatci, I. Szikora, F. Baltacioglu, et al. "The safety and effectiveness of the Woven EndoBridge (WEB) system for the treatment of wide-necked bifurcation aneurysms: final 12-month results of the pivotal WEB Intrasaccular Therapy (WEB-IT) Study." In: *J Neurointerv Surg* 11.9 (2019), pp. 924–930. DOI: 10.1136/neurintsurg-2019-014815.
- [12] A. B. Awadh, S. Lindsay, J. Clark, G. Clowry, and I. Keenan. "Student perceptions of challenging topics and concepts in anatomy education." In: *Anatomical Society summer meeting, University of Oxford, Oxford.* 2018, pp. 392–418. DOI: 10.1002/ase.2045.
- [13] S. Aylward, J. Jomier, S. Weeks, and E. Bullitt. "Registration and analysis of vascular images." In: *Int J Comput Vis* 55.2 (2003), pp. 123–138. DOI: 10.1023/A: 1026126900358.
- [14] S. R. Aylward, S. Weeks, and E. Bullitt. "Analysis of the parameter space of a metric for registering 3D vascular images." In: *Med Image Comput Comput Assist Interv*. Springer Berlin Heidelberg, 2001, pp. 932–939.
- [15] C. E. Baccin, T. Krings, H. Alvarez, A. Ozanne, and P. Lasjaunias. "Multiple mirror-like intracranial aneurysms. Report of a case and review of the literature." In: *Acta Neurochir (Wien)* 148.10 (2006), pp. 1091–1095. DOI: 10 . 1007 / s00701-006-0860-z.
- [16] D. Backes, G. J. Rinkel, J. P. Greving, B. K. Velthuis, Y. Murayama, H. Takao, et al. "ELAPSS score for prediction of risk of growth of unruptured intracranial aneurysms." In: *Neurology* 88.17 (2017), pp. 1600–1606. DOI: 10.1212/WNL.000000000003865.
- [17] D. Backes, M. D. I. Vergouwen, A. T. T. Groenestege, A. S. E. Bor, B. K. Velthuis, J. P. Greving, et al. "PHASES score for prediction of intracranial aneurysm growth." In: *Stroke* 46.5 (2015), pp. 1221–1226. DOI: 10.1161/STROKEAHA.114.008198.
- [18] M. K. Bakker and Y. M. Ruigrok. "Genetics of intracranial aneurysms." In: *Stroke* 52.9 (2021), pp. 3004–3012. DOI: 10.1161/STR0KEAHA.120.032621.

- [19] T. Becske, D. Kallmes, I. Saatci, C. McDougall, I. Szikora, G. Lanzino, et al. "Pipeline for uncoilable or failed aneurysms: results from a multicenter clinical trial." In: *Radiology* 267.3 (2013), pp. 858–68. DOI: 10.1148/radiol.13120099.
- [20] R. Belavadi, S. V. R. Gudigopuram, C. C. Raguthu, H. Gajjela, I. Kela, C. L. Kakarala, M. Hassan, and I. Sange. "Surgical clipping versus endovascular coiling in the management of intracranial aneurysms." In: *Cureus* 13.12 (2021), e20478. DOI: 10.7759/cureus.20478.
- [21] E. Beller, D. Klopp, J. Göttler, J. Kaesmacher, C. Zimmer, J. S. Kirschke, and S. Prothmann. "Closed-cell stent-assisted coiling of intracranial aneurysms: evaluation of changes in vascular geometry using digital subtraction angiography." In: *PLoS One* 11.4 (2016), pp. 1–11. DOI: 10.1371/journal.pone.0153403.
- [22] A. Benaissa, C. Tomas, F. Clarençon, N. Sourour, D. Herbreteau, L. Spelle, S. Gallas, A.-C. Januel, A. Gaultier, and L. Pierot. "Retrospective analysis of delayed intraparenchymal hemorrhage after flow-diverter treatment: presentation of a retrospective multicenter trial." In: *AJNR Am J Neuroradiol* 37.3 (2016), pp. 475–480. DOI: 10.3174/ajnr.A4561.
- [23] A. Benaissa, C. Barbe, and L. Pierot. "Analysis of recanalization after endovascular treatment of intracranial aneurysm (ARETA trial): presentation of a prospective multicenter study." In: *J Neuroradiol* 42.2 (2015), pp. 80–85. ISSN: 0150-9861. DOI: 10.1016/j.neurad.2014.04.003.
- [24] H. E. Bennink, H. C. van Assen, G. J. Streekstra, R. ter Wee, J. A. E. Spaan, and B. M. ter Haar Romeny. "A novel 3D multi-scale lineness filter for vessel detection." In: *Med Image Comput Comput Assist Interv.* 2007, pp. 436–443. DOI: 10.1007/978-3-540-75759-7\_53.
- [25] D. Bera, R. Pratap, and B. D. Verma. "Dimensionality Reduction for Categorical Data." In: *IEEE Transactions on Knowledge and Data Engineering* 35.4 (2023), pp. 3658–3671. DOI: 10.1109/TKDE.2021.3132373.
- [26] P. Berg, D. Stucht, G. Janiga, O. Beuing, O. Speck, and D. Thévenin. "Cerebral blood flow in a healthy circle of Willis and two intracranial aneurysms: computational fluid dynamics versus four-dimensional phase-contrast magnetic resonance imaging." In: *J Biomech Eng* 136.4 (2014), pp. 55–66. DOI: 10.1115/1.4026108.
- [27] P. Berg, S. Saalfeld, S. Voß, O. Beuing, and G. Janiga. "A review on the reliability of hemodynamic modeling in intracranial aneurysms: why computational fluid dynamics alone cannot solve the equation." In: *Neurosurg Focus* 47.1 (2019). DOI: 10.3171/2019.4.FOCUS19181.

- [28] P. Berg, S. Voß, G. Janiga, S. Saalfeld, A. W. Bergersen, K. Valen-Sendstad, et al. "Multiple Aneurysms AnaTomy CHallenge 2018 (MATCH)—phase II: rupture risk assessment." In: *Int J Comput Assist Radiol Surg.* (2019), pp. 1–10. DOI: 10. 1007/s11548-019-01986-2.
- [29] P. Bhogal, I. Lylyk, J. Chudyk, N. Perez, C. Bleise, and P. Lylyk. "The Contour early human experience of a novel aneurysm occlusion device." In: *Clin Neuro-radiol* 31.1 (2021), pp. 147–154. DOI: 10.1007/s00062-020-00876-4.
- [30] P. Bhogal, S. Udani, C. Cognard, M. Piotin, P. Brouwer, N.-A. Sourour, et al. "Endosaccular flow disruption: where are we now?" In: *J Neurointerv Surg* 11.10 (2019), pp. 1024–1025. DOI: 10.1136/neurintsurg-2018-014623.
- [31] Z. Bian, J. Zhong, C. R. Hatt, and N. S. Burris. "A deformable image registration based method to assess directionality of thoracic aortic aneurysm growth." In: *Proc. Medical Imaging: Image Processing*. Vol. 11596. 2021, 115962P. DOI: 10.1117/12.2581937.
- [32] F. Bing, T. E. Darsaut, I. Salazkin, A. Makoyeva, G. Gevry, and J. Raymond. "Stents and flow diverters in the treatment of aneurysms: device deformation in vivo may alter porosity and impact efficacy." In: *Neuroradiology* 55.1 (2012), pp. 85–92. DOI: 10.1007/s00234-012-1082-0.
- [33] A. Biondi, P. Primikiris, G. Vitale, and G. Charbonnier. "Endosaccular flow disruption with the Contour Neurovascular System: angiographic and clinical results in a single-center study of 60 unruptured intracranial aneurysms." In: *J Neurointerv Surg* 15.9 (2023), pp. 838–843. DOI: 10.1136/jnis-2022-019271.
- [34] Žiga Bizjak, T. Jerman, B. Likar, F. Pernuš, A. Chien, and Žiga Špiclin. "Registration based detection and quantification of intracranial aneurysm growth." In: *Proc. Medical Imaging: Computer-Aided Diagnosis*. Vol. 10950. 2019, p. 1095007. DOI: 10.1117/12.2512781.
- [35] J. Bock, B. Kreher, J. Hennig, and M. Markl. "Optimized pre-processing of time-resolved 2D and 3D phase-contrast MRI data." In: *Proc. of the International Society for Magnetic Resonance in Medicine (ISMRM)*. 2007, p. 3138.
- [36] F. Bonneville, N. Sourour, and A. Biondi. "Intracranial aneurysms: an overview." In: *Neuroimaging Clin N Am* 16.3 (2006), pp. 371–382. DOI: 10.1016/j.nic.2006.05.001.
- [37] M. M. Breunig, H.-P. Kriegel, R. T. Ng, and J. Sander. "LOF: identifying density-based local outliers." In: *Proc. ACM SIGMOD Int Conf Manag Data*. Association for Computing Machinery, 2000, pp. 93–104. DOI: 10.1145/342009.335388.
- [38] W. Brinjikji, M. H. Murad, G. Lanzino, H. J. Cloft, and D. F. Kallmes. "Endovascular treatment of intracranial aneurysms with flow diverters." In: *Stroke* 44.2 (2013), pp. 442–447. DOI: 10.1161/STROKEAHA.112.678151.

- [39] J.-H. Buhk. "Po36 Three unusual cases with TRENZA." In: *J Neurointerv Surg* 16.Suppl 2 (2024), A42–A43. DOI: 10.1136/jnis-2024-ESMINT.73.
- [40] F. Cagnazzo, H. J. Cloft, G. Lanzino, and W. Brinjikji. "WEB (Woven Endo-Bridge) device for intracranial aneurysm treatment: technical, radiological, and clinical findings in a consecutive North American cohort." In: *Acta Neurochir* (*Wien*) 165.8 (2023), 2077–2086. DOI: 10.1007/s00701-023-05668-6.
- [41] A. Can and R. Du. "Association of hemodynamic factors with intracranial aneurysm formation and rupture: systematic review and meta-analysis." In: *Neurosurgery* 78.4 (2016), pp. 510–520. DOI: 10.1227/NEU.0000000000001083.
- [42] L. Cao, C. Peng, and J. T. Hansberger. "A large curved display system in Virtual Reality for immersive data interaction." In: *Proc. of the IEEE GEM*. 2019, pp. 1–4. DOI: 10.1109/GEM.2019.8811550.
- [43] J. Caroff, H. Neki, C. Mihalea, F. D'Argento, H. Abdel Khalek, L. Ikka, J. Moret, and L. Spelle. "Flow-diverter stents for the treatment of saccular middle cerebral artery bifurcation aneurysms." In: *AJNR Am J Neuroradiol* 37.2 (2016), pp. 279–284. DOI: 10.3174/ajnr.A4540.
- [44] M. V. Casimiro, A. W. McEvoy, L. D. Watkins, and N. D. Kitchen. "A comparison of risk factors in the etiology of mirror and nonmirror multiple intracranial aneurysms." In: *Surg Neurol* 61.6 (2004), pp. 541–545. DOI: 10.1016/j.surneu. 2003.08.016.
- [45] N. Cavasin, U. A. Gava, S. Magrini, and E. Cagliari. "Treatment of a ruptured fetal-type posterior communicating aneurysm with a combined approach using the new contour neurovascular system." In: *BMJ Case Rep* 15.4 (2022). DOI: 10.1136/bcr-2021-248065.
- [46] J. R. Cebral, M. A. Castro, O. Soto, R. Löhner, and N. Alperin. "Blood-flow models of the circle of Willis from magnetic resonance data." In: *J Eng Math* 47.3 (2003), pp. 369–386. DOI: 10.1023/B:ENGI.0000007977.02652.02.
- [47] J. Cebral, B. Chung, F. Mut, J. Chudyk, C. Bleise, E. Scrivano, P. Lylyk, R. Kadirvel, and D. Kallmesd. "Analysis of flow dynamics and outcomes of cerebral aneurysms treated with intrasaccular flow-diverting devices." In: *AJNR Am J Neuroradiol* 40.9 (2019), pp. 1511–1516. DOI: 10.3174/ajnr.A6169.
- [48] J. Cebral, F. Mut, J. Weir, and C. Putman. "Association of hemodynamic characteristics and cerebral aneurysm rupture." In: *AJNR Am J Neuroradiol* 32.2 (2011), pp. 264–270. DOI: 10.3174/ajnr.A2274.
- [49] H.-M. Chan and A. C. S. Chung. "Efficient 3D-3D vascular registration based on multiple orthogonal 2D projections." In: *Proc. of the 2nd International Workshop on Biomedical Image Registration (WBIR)*. 2003, pp. 301–310. DOI: 10.1007/978-3-540-39701-4\_32.

- [50] H. M. Chan, A. C. S. Chung, S. C. H. Yu, and W. M. Wells. "2D-3D vascular registration between digital subtraction angiographic (DSA) and magnetic resonance angiographic (MRA) images." In: *Proc. of the 2nd IEEE International Symposium on Biomedical Imaging: From Nano to Macro.* 2004, pp. 708–711. DOI: 10.1109/ISBI.2004.1398636.
- [51] A. Chandra, W. A. Li, C. R. Stone, X. Geng, and Y. Ding. "The cerebral circulation and cerebrovascular disease I: anatomy." In: *Brain Circ* 3.2 (2017), pp. 45–56. DOI: 10.4103/bc.bc\_10\_17.
- [52] G. Charbonnier, J.-P. Desilles, S. Escalard, B. Maier, G. Ciccio, S. Smajda, et al. "Timing and spectrum of neurological complications after flow diverter implantation for intracranial aneurysms." In: *Front neurol* 12 (2021). DOI: 10.3389/fneur.2021.590383.
- [53] Y. Chau, L. Mondot, M. Sachet, J. Gaudart, D. Fontaine, M. Lonjon, and J. Sédat. "Modification of cerebral vascular anatomy induced by Leo stent placement depending on the site of stenting: A series of 102 cases." In: *Interv Neuroradiol* 22.6 (2016), pp. 666–673. DOI: 10.1177/1591019916660867.
- [54] T. Chen and C. Guestrin. "XGBoost: a scalable tree boosting system." In: *Proc. ACM SIGKDD Int Conf Knowl Discov Data Min.* 2016, pp. 785–794. DOI: 10.1145/2939672.2939785.
- [55] A. Chien, J. Sayre, and F. Viñuela. "Comparative morphological analysis of the geometry of ruptured and unruptured aneurysms." In: *Neurosurgery* 69.2 (2011), pp. 349–356. DOI: 10.1227/NEU.0b013e31821661c3.
- [56] T. Ching, D. S. Himmelstein, B. K. Beaulieu-Jones, A. A. Kalinin, B. T. Do, G. P. Way, et al. "Opportunities and obstacles for deep learning in biology and medicine." In: *Interface Focus* 15.141 (2018), p. 20170387. DOI: 10.1098/rsif. 2017.0387.
- [57] J. Chojdak-Łukasiewicz, E. Dziadkowiak, A. Zimny, and B. Paradowski. "Cerebral small vessel disease: a review." In: *Adv Clin Exp Med* 30.3 (2021), pp. 349–356. DOI: 10.17219/acem/131216.
- [58] C. L. Chuang. "Case-based reasoning support for liver disease diagnosis." In: *Artif Intell Med* 53.1 (2011), pp. 15–23. DOI: 10.1016/j.artmed.2011.06.002.
- [59] P. Cignoni, M. Callieri, M. Corsini, M. Dellepiane, F. Ganovelli, and G. Ranzuglia. "MeshLab: an open-source mesh processing tool." In: *Eurographics Italian Chapter Conference*. The Eurographics Association, 2008. ISBN: 978-3-905673-68-5. DOI: 10.2312 / LocalChapterEvents / ItalChap / ItalianChapConf2008/129-136.

- [60] C. Cognard, L. Pierot, R. Anxionnat, and F. Ricolfi. "Results of embolization used as the first treatment choice in a consecutive nonselected population of ruptured aneurysms: clinical results of the Clarity." In: *Neurosurgery* 69.4 (2011), pp. 837–41. DOI: 10.1227/NEU.0b013e3182257b30.
- [61] C. Cognard and A. C. Januel. "Remnants and recurrences after the use of the WEB intrasaccular device in large-neck bifurcation aneurysms." In: *Neurosurgery* 76.5 (2015), pp. 522–530. DOI: 10.1227/NEU.0000000000000669.
- [62] M. Dabagh, P. Nair, J. Gounley, D. Frakes, L. F. Gonzalez, and A. Randles. "Hemodynamic and morphological characteristics of a growing cerebral aneurysm." In: *Neurosurg Focus FOC* 47.1 (2019), E13. DOI: 10.3171/2019.4. F0CUS19195.
- [63] N. N. Dange and J. M. Roy. "Initial experience with the Contour Device in the treatment of ruptured intracranial wide-necked bifurcation aneurysms: A single-operator, multicenter Study." In: *Neurol India* 70.5 (2022), pp. 2059–2064. DOI: 10.4103/0028-3886.359281.
- [64] T. M. De Silva and F. M. Faraci. "Microvascular dysfunction and cognitive impairment." In: *Cell Mol Neurobiol* 36.2 (2016), pp. 241–258. DOI: 10.1007/s10571-015-0308-1.
- [65] F. Detmer, D. Fajardo-Jiménez, F. Mut, N. Juchler, S. Hirsch, V. M. Pereira, P. Bijlenga, and J. R. Cebral. "External validation of cerebral aneurysm rupture probability model with data from two patient cohorts." In: *Acta Neurochir* 160 (2018), pp. 2425–2434. DOI: 10.1007/s00701-018-3712-8.
- [66] F. J. Detmer, B. J. Chung, C. Jimenez, F. Hamzei-Sichani, D. Kallmes, C. Putman, and J. R. Cebral. "Associations of hemodynamics, morphology, and patient characteristics with aneurysm rupture stratified by aneurysm location." In: *Neuroradiology* 61.3 (2019), pp. 275–284. DOI: 10.1007/s00234-018-2135-9.
- [67] F. J. Detmer, B. J. Chung, F. Mut, M. Slawski, F. Hamzei-Sichani, C. Putman, C. Jiménez, and J. R. Cebral. "Development and internal validation of an aneurysm rupture probability model based on patient characteristics and aneurysm location, morphology, and hemodynamics." In: *Int J Comput Assist Radiol Surg.* 13.11 (2018), pp. 1767–1779. DOI: 10.1007/s11548-018-1837-0.
- [68] F. J. Detmer, S. Hadad, B. J. Chung, F. Mut, M. Slawski, N. Juchler, et al. "Extending statistical learning for aneurysm rupture assessment to Finnish and Japanese populations using morphology, hemodynamics, and patient characteristics." In: *Neurosurg Focus* 47.1 (2019), E16. DOI: 10.3171/2019.4.F0CUS19145.
- [69] S. Dhar, M. Tremmel, J. Mocco, M. Kim, J. Yamamoto, A. H. Siddiqui, L. N. Hopkins, and H. Meng. "Morphology parameters for intracranial aneurysm rupture risk assessment." In: *Neurosurgery* 63.2 (2008), pp. 185–197. DOI: 10.1227/01.NEU.0000316847.64140.81.

- [70] T. Dhar, N. Dey, S. Borra, and R. S. Sherratt. "Challenges of deep learning in medical image analysis improving explainability and trust." In: *IEEE Trans Technol Soc* 4.1 (2023), pp. 68–75. DOI: 10.1109/TTS.2023.3234203.
- [71] M. R. Diagbouga, S. Morel, P. Bijlenga, and B. R. Kwak. "Role of hemodynamics in initiation/growth of intracranial aneurysms." In: *Eur J Clin Invest* 48.9 (2018), e12992. DOI: 10.1111/eci.12992.
- [72] F. Diana, M. de Dios Lascuevas, S. Peschillo, E. Raz, S. Yoshimura, M. Requena Ruiz, D. Hernández Morales, and A. Tomasello. "Intrasaccular flow disruptorassisted coiling of intracranial aneurysms using the novel Contour Neurovascular Systems and NEQSTENT: A single-center safety and feasibility study." In: *Brain Sci* 12.8 (2022), p. 991. DOI: 10.3390/brainsci12080991.
- [73] T. Dwyer, K. Marriott, T. Isenberg, K. Klein, N. Riche, F. Schreiber, W. Stuerzlinger, and B. H. Thomas. "Immersive analytics: an introduction." In: *Immersive Analytics*. Cham, 2018, pp. 1–23. ISBN: 978-3-030-01388-2. DOI: 10.1007/978-3-030-01388-2\_1.
- [74] B. M. Ens, R. Finnegan, and P. P. Irani. "The personal cockpit: A spatial interface for effective task switching on head-worn displays." In: *Proc. of the SIGCHI Conf Hum Factors Comput Syst.* 2014, pp. 3171–3180. DOI: 10.1145/2556288.2557058.
- [75] T. D. Erickson. "Working with interface metaphors." In: *Readings in Human-Computer Interaction*. 1995, pp. 147–151. DOI: 10.1016/B978-0-08-051574-8.50018-2.
- [76] M. Ester, H.-P. Kriegel, J. Sander, and X. Xu. "A density-based algorithm for discovering clusters in large spatial databases with noise." In: *Proc. of KDD*. AAAI Press, 1996, pp. 226–231.
- [77] S. P. Ferns, M. E. Sprengers, W. J. van Rooij, G. J. Rinkel, J. C. van Rijn, S. Bipat, M. Sluzewski, and C. B. Majoie. "Coiling of intracranial aneurysms." In: *Stroke* 40.8 (2009), e523–e529. DOI: 10.1161/STROKEAHA.109.553099.
- [78] D. Fiorella, A. Molyneux, A. Coon, I. Szikora, I. Saatci, F. Baltacioglu, et al. "Safety and effectiveness of the Woven EndoBridge (WEB) system for the treatment of wide necked bifurcation aneurysms: final 5 year results of the pivotal WEB Intra-saccular Therapy study (WEB-IT)." In: *J Neurointerv Surg* 15.12 (2023), pp. 1175–1180. DOI: 10.1136/jnis-2023-020611.
- [79] D. Fiorella, A. Molyneux, A. Coon, I. Szikora, I. Saatci, F. Baltacioglu, et al. "Safety and effectiveness of the Woven EndoBridge (WEB) system for the treatment of wide necked bifurcation aneurysms: final 5 year results of the pivotal WEB Intra-saccular Therapy study (WEB-IT)." In: *J Neurointerv Surg* 15.12 (2023), pp. 1175–1180. DOI: 10.1136/jnis-2023-020611.
- [80] R. A. Fisher. "The use of multiple measurements in taxonomic problems." In: *Ann Eugen* 7.2 (1936), pp. 179–188. DOI: 10.1111/j.1469-1809.1936.tb02137.x.

- [81] O. Fluck, C. Vetter, W. Wein, A. Kamen, B. Preim, and R. Westermann. "A survey of medical image registration on graphics hardware." In: *Comput Methods Programs Biomed* 104.3 (2011), e45–e57. DOI: 10.1016/j.cmpb.2010.10.009. Epub2010Nov26..
- [82] M. E. Fonteyn, B. Kuipers, and S. J. Grobe. "A description of think aloud method and protocol analysis." In: *Qual Health Res* 3.4 (1993), pp. 430–441. DOI: 10.1177/104973239300300403.
- [83] A. Y. Fouda, S. C. Fagan, and A. Ergul. "Brain vasculature and cognition." In: *Arterioscler Thromb Vasc Biol* 39.4 (2019), pp. 593–602. DOI: 10.1161/ATVBAHA. 118.311906.
- [84] A. F. Frangi, W. J. Niessen, K. L. Vincken, and M. A. Viergever. "Multiscale vessel enhancement filtering." In: *Med Image Comput Comput Assist Interv*. Ed. by W. M. Wells, A. Colchester, and S. Delp. Springer Berlin Heidelberg, 1998, pp. 130–137. DOI: 10.1007/BFb0056195.
- [85] A. M. Frölich, M. T. Nawka, M. Ernst, I. Frischmuth, J. Fiehler, and J.-H. Buhk. "Intra-aneurysmal flow disruption after implantation of the Medina Embolization device depends on aneurysm neck coverage." In: *PLOS ONE* 13.2 (2018), pp. 1–10. DOI: 10.1371/journal.pone.0191975.
- [86] F. Gaidzik, S. Pathiraja, S. Saalfeld, D. Stucht, O. Speck, D. Thévenin, and G. Janiga. "Hemodynamic data assimilation in a subject-specific circle of Willis geometry." In: *Clin Neuroradiol* (2020). DOI: 10.1007/s00062-020-00959-2.
- [87] F. Gaidzik, C. Stucht D. Roloff, O. Speck, D. Thévenin, and G. Janiga. "Transient flow prediction in an idealized aneurysm geometry using data assimilation." In: *Comput Biol Med* 115.103507 (2019). DOI: 10.1016/j.compbiomed.2019.103507.
- [88] F. Gaidzik, J. Korte, S. Saalfeld, G. Janiga, and P. Berg. "Image-based hemodynamic simulations for intracranial aneurysms: the impact of complex vasculature." In: *Int J Comput Assist Radiol Surg* 19.4 (2024), pp. 687–697. DOI: 0.1007/s11548-023-03045-3.
- [89] F. Gaidzik, S. Pathiraja, S. Saalfeld, D. Stucht, O. Speck, D. Thévenin, and G. Janiga. "Hemodynamic data assimilation in a subject-specific circle of Willis geometry." In: *Clin Neuroradiol* 31.3 (2021), pp. 643–651. DOI: 10.1007/s00062-020-00959-2.
- [90] F. Gallo-Pineda, M. Fernández-Gómez, C. Domínguez-Rodríguez, J. I. Gallego-León, C. Hidalgo-Barranco, T. Díaz-Martí, and A. Romance-García. "Evaluating efficacy and complications of Contour Intrasaccular Device in cerebral aneurysm management: A multicenter analysis." In: *World Neurosurg* 183.1 (2024), e738–e746. DOI: 10.1016/j.wneu.2024.01.017.

- [91] B. Gao, B. Kim, J.-I. Kim, and H. Kim. "Amphitheater layout with egocentric distance-based item sizing and landmarks for browsing in virtual reality." In: *Int J Hum-Comput Interact* 35 (2018), pp. 1–15. DOI: 10.1080/10447318.2018.1498654.
- [92] S. García, J. Luengo, and F. Herrera. *Data preprocessing in data mining*. Intelligent Systems Reference Library. Springer International Publishing, 2014. ISBN: 9783319102474.
- [93] M. Garland and P. S. Heckbert. "Surface simplification using quadric error metrics." In: *Seminal Graphics Papers: Pushing the Boundaries, Volume* 2. 2023. ISBN: 9798400708978. DOI: 10.1145/3596711.3596727.
- [94] R. Gasparotti and R. Liserre. "Intracranial aneurysms." In: *Eur Radiol* 15.3 (2005), pp. 441–447. DOI: 10.1007/s00330-004-2614-8.
- [95] S. Ghozy, B. I. Lashin, M. Elfil, C. Bilgin, H. Kobeissi, M. Shehata, R. Kadirvel, and D. F. Kallmes. "The safety and effectiveness of the Contour Neurovascular System for the treatment of wide-necked aneurysms: a systematic review and meta-analysis of early experience." In: *Interv Neuroradiol* (2022). DOI: 10.1177/15910199221139546.
- [96] R. Gondar, O. P. Gautschi, J. Cuony, F. Perren, M. Jägersberg, M.-V. Corniola, et al. "Unruptured intracranial aneurysm follow-up and treatment after morphological change is safe: observational study and systematic review." In: *J Neurol Neurosurg Psychiatry* 87.12 (2016), pp. 1277–1282. DOI: 10.1136/jnnp-2016-313584.
- [97] M. R. Goni, N. I. R. Ruhaiyem, M. Mustapha, A. Achuthan, and C. M. N. Che Mohd Nassir. "Brain vessel segmentation using deep learning a review." In: *IEEE Access* 10 (2022), pp. 111322–111336. DOI: 10.1109/ACCESS.2022.3214987.
- [98] N. Goyal, D. Hoit, J. DiNitto, L. Elijovich, D. Fiorella, L. Pierot, et al. "How to WEB: a practical review of methodology for the use of the Woven EndoBridge." In: *J Neurointerv Surg* 12.5 (2020), pp. 512–520. DOI: 10.1136/neurintsurg-2019-015506.
- [99] C. J. Griessenauer, S. Ghozy, A. Biondi, C. Hecker, F. Wodarg, T. Liebig, et al. "Contour Neurovascular System for endovascular embolization of cerebral aneurysms: a multicenter cohort study of 10 European neurovascular centers." In: *J Neurointerv Surg* (2024). DOI: 10.1136/jnis-2023-021378.
- [100] A. Guédon, F. Clarençon, F. D. Maria, C. Rosso, A. Biondi, J. Gabrieli, P. Rojas, J. Chiras, and N. Sourour. "Very late ischemic complications in flow-diverter stents: a retrospective analysis of a single-center series." In: *J Neurosurg* 125.4 (2016), pp. 929 –935. DOI: 10.3171/2015.10.JNS15703.

- [101] F. Gärtner, T. Klintz, S. Peters, F. B. Neves, K. Mostafa, J. Mahnke, et al. "Intracranial aneurysm treatment with contour or WEB a single center comparison of intervention times and learning curves." In: *Interv Neuroradiol* 0.0 (2023). DOI: 10.1177/15910199231179512.
- [102] P. Han, D. Jin, W. Wei, C. Song, X. Leng, L. Liu, J. Yu, and X. Li. "The prognostic effects of hemodynamic parameters on rupture of intracranial aneurysm: A systematic review and meta-analysis." In: *Int J Surg* 86 (2021), pp. 15–23. ISSN: 1743-9191. DOI: 10.1016/j.ijsu.2020.12.012.
- [103] L. Hansen and M. P. Heinrich. "Revisiting iterative highly efficient optimisation schemes in medical image registration." In: *Med Image Comput Comput Assist Interv.* 2021, pp. 203–212. DOI: 10.1007/978-3-030-87202-1\\_20.
- [104] M. Hartung, T. Grist, and C. François. "Magnetic resonance angiography: current status and future directions." In: *J Cardiovasc Magn Reson* 13.1 (2011), p. 19. DOI: 10.1186/1532-429X-13-19.
- [105] C. Hecker, E. Broussalis, J. A. R. Pfaff, S. Pikija, C. J. Griessenauer, and M. Killer-Oberpfalzer. "Comparison of the Contour Neurovascular System and Woven EndoBridge device for treatment of wide-necked cerebral aneurysms at a bifurcation or sidewall." In: *J Neurosurg* 139.2 (2023), pp. 563–572. DOI: 10.3171/2022.12.JNS222268.
- [106] D. M. Heiferman, N. Goyal, V. Inoa, C. Nickele, and A. S. Arthur. "A new era in the treatment of wide necked bifurcation aneurysms: intrasaccular flow disruption." In: *Interv Neuroradiol* 30.1 (2024), pp. 31–36. DOI: 10.1177/15910199221094390.
- [107] F. Heinrich, V. Apilla, K. Lawonn, C. Hansen, B. Preim, and M. Meuschke. "Estimating depth information of vascular models: A comparative user study between a virtual reality and a desktop application." In: *Comp & Graph* 98 (2021), pp. 210–217. ISSN: 0097-8493. DOI: https://doi.org/10.1016/j.cag.2021.05.014.
- [108] D. Herbreteau, R. Bibi, A. Narata, K. Janot, C. Papagiannaki, S. Soize, and L. Pierot. "Are anatomic results influenced by WEB shape modification? Analysis in a prospective, single-center series of 39 patients with aneurysms treated with the WEB." In: *AJNR Am J Neuroradiol* 37.12 (2016), pp. 2280–2286. DOI: 10.3174/ajnr.A4918.
- [109] S. Hetts, A. Turk, J. English, C. Dowd, J. Mocco, C. Prestigiacomo, et al. "Stent-assisted oiling versus coiling alone in unruptured intracranial aneurysms in the matrix and platinum science trial: safety, efficacy, and mid-term outcomes." In: *AJNR Am J Neuroradiol* 35.4 (2014), pp. 698–705. DOI: 10.3174/ajnr.A3755.

- [110] C.-C. Hsu and W.-H. Huang. "Integrated dimensionality reduction technique for mixed-type data involving categorical values." In: *Applied Soft Computing* 43 (2016), pp. 199–209. ISSN: 1568-4946. DOI: 10.1016/j.asoc.2016.02.015.
- [111] W.-C. Hsu, M. Meuschke, A. F. Frangi, B. Preim, and K. Lawonn. "A survey of intracranial aneurysm detection and segmentation." In: *Med Image Anal* 101 (2025), p. 103493. ISSN: 1361-8415. DOI: 10.1016/j.media.2025.103493.
- [112] M.-W. Huang, C.-F. Tsai, and W.-C. Lin. "Instance selection in medical datasets: A divide-and-conquer framework." In: *Comput Electr Eng* 90 (2021), p. 106957. DOI: 10.1016/j.compeleceng.2020.106957.
- [113] Q.-H. Huang, Y.-F. Wu, Y. Xu, B. Hong, L. Zhang, and J.-M. Liu. "Vascular geometry change because of endovascular stent placement for anterior communicating artery aneurysms." In: *AJNR Am J Neuroradiol* 32.9 (2011), pp. 1721–1725. DOI: 10.3174/ajnr.A2597.
- [114] F. Huettl, P. Saalfeld, C. Hansen, B. Preim, A. Poplawski, W. Kneist, H. Lang, and T. Huber. "Virtual reality and 3D printing improve preoperative visualization of 3D liver reconstructions-results from a preclinical comparison of presentation modalities and user's preference." In: *Ann Transl Med* 9.13 (2021), p. 1074. DOI: 10.21037/atm-21-512.
- [115] T. Ishibashi, Y. Murayama, M. Urashima, T. Saguchi, M. Ebara, H. Arakawa, K. Irie, H. Takao, and T. Abe. "Unruptured intracranial aneurysms incidence of rupture and risk factors." In: *Stroke* 40(1) (2008), pp. 313–316. DOI: 10.1161/STROKEAHA.108.521674.
- [116] F. I. Islim, N. Saleem, and T. Patankar. "Large single-center experience with short-term follow-up of Neqstent-assisted coiling." In: *AJNR Am J Neuroradiol* 45.5 (2024), pp. 605–611. DOI: 10.3174/ajnr.A8187.
- [117] P. Jagtiani, G. S. Sioutas, J. Vivanco-Suarez, J.-K. Burkhardt, and V. M. Srinivasan. "An updated meta-analysis on the safety and effectiveness of the Contour Neurovascular system." In: *Interv Neuroradiol* (2024). DOI: 10.1177/15910199231226280.
- [118] M. Jenkinson and S. Smith. "A global optimisation method for robust affine registration of brain images." In: *Med Image Anal* 5.2 (2001), 143–156. DOI: 10. 1016/s1361-8415(01)00036-6.
- [119] W. Jeong, M. Han, and K. Rhee. "The hemodynamic alterations induced by the vascular angular deformation in stent-assisted coiling of bifurcation aneurysms." In: *Comput Methods Programs Biomed* 53 (2014), pp. 1–8. DOI: 10. 1016/j.compbiomed.2014.07.006.
- [120] S. Jirjees, Z. M. Htun, I. Aldawudi, P. C. Katwal, and S. Khan. "Role of morphological and hemodynamic factors in predicting intracranial aneurysm rupture: a review." In: *Cureus* 12.7 (2020), e9178. DOI: 10.7759/cureus.9178.

- [121] J. Jomier and S. Aylward. "Rigid and deformable vasculature-to-image registration: a hierarchical approach." In: *Med Image Comput Comput Assist Interv.* 2004, pp. 829–836. DOI: 10.1007/978-3-540-30135-6\\_101.
- [122] F. J. Joseph, H. E. R. Vanluchene, and D. Bervini. "Simulation training approaches in intracranial aneurysm surgery—a systematic review." In: *Neurosurg Rev* 46.1 (2023), p. 101. DOI: 10.1007/s10143-023-01995-5.
- [123] A. Joshi, X. Qian, D. Dione, K. Bulsara, C. Breuer, A. Sinusas, and X. Papademetris. "Effective visualization of complex vascular structures using a non-parametric vessel detection method." In: *IEEE Trans Vis Comput Graph* 14.6 (2008), pp. 1603–1610. DOI: 10.1109/TVCG.2008.123.
- [124] L. T. van der Kamp, G. J. E. Rinkel, D. Verbaan, R. van den Berg, W. P. Vandertop, Y. Murayama, et al. "Risk of rupture after intracranial aneurysm growth." In: *JAMA Neurol* 78.10 (2021), pp. 1228–1235. DOI: 10.1001/jamaneurol.2021. 2915.
- [125] M. Kaps, G.-M. von Reutern, E. P. Stolz, and H. J. von Büdingen. *Sonografie in der neurologie*. *3rd ed*. Stuttgart: Georg Thieme Verlag, 2016. ISBN: 978-3-13-136773-0.
- [126] W. Kaspera, K. Ćmiel Smorzyk, W. Wolański, E. Kawlewska, A. Hebda, M. Gzik, and P. Ładziński. "Morphological and hemodynamic risk factors for middle cerebral artery aneurysm: a case-control study of 190 patients." In: *Sci Rep* 10.1 (2020), p. 2016. DOI: 10.1038/s41598-019-56061-2.
- [127] A. Keedy. "An overview of intracranial aneurysms." In: *Mcgill J Med* 9.2 (2006), pp. 141–146.
- [128] I. D. Keenan and M. Powell. "Interdimensional travel: visualisation of 3D-2D transitions in anatomy learning." In: *Biomedical Visualisation: Volume 6.* Springer International Publishing, 2020, pp. 103–116. ISBN: 978-3-030-37639-0. DOI: 10. 1007/978-3-030-37639-0\_6.
- [129] Y. Kim, E. Riloff, and S. M. Meystre. "Exploiting unlabeled texts with clustering-based instance selection for medical relation Classification." In: *AMIA Annu Symp Proc.* 2018, pp. 1060–1069.
- [130] Y. D. Kim, J. S. Bang, S. U. Lee, W. J. Jeong, O.-K. Kwon, S. P. Ban, T. K. Kim, S. B. Kim, and C. W. Oh. "Long-term outcomes of treatment for unruptured intracranial aneurysms in South Korea: clipping versus coiling." In: *J Neurointerv Surg* 10.12 (2018), pp. 1218–1222. DOI: 10.1136/neurintsurg-2018-013757.
- [131] R. King, J.-Y. Chueh, I. van der Bom, C. Silva, S. Carniato, G. Spilberg, A. Wakhloo, and M. Gounis. "The effect of intracranial stent implantation on the curvature of the cerebrovasculature." In: *AJNR Am J Neuroradiol* 33.9 (2012), pp. 1657–1662. DOI: 10.3174/ajnr.A3062.

- [132] S. Kobashi, K. Kondo, and Y. Hata. "Computer-aided diagnosis of intracranial aneurysms in MRA images with case-based reasoning." In: *IEICE Trans Inf Syst* 89 (2006), pp. 340–350. DOI: 10.1093/ietisy/e89-d.1.340.
- [133] J. Korte, F. Gaidzik, N. Larsen, E. Schütz, T. Damm, F. Wodarg, et al. "In vitro and in silico assessment of flow modulation after deploying the Contour Neurovascular System in intracranial aneurysm models." In: *J NeuroIntervent Surg* 16.8 (2023), pp. 815–823. DOI: 10.1136/jnis-2023-020403.
- [134] M. A. Kramer. "Nonlinear principal component analysis using autoassociative neural networks." In: *AIChE J* 37.2 (1991), pp. 233–243. DOI: 10.1002/aic. 690370209.
- [135] N. Larsen, C. Flüh, J. Madjidyar, M. Synowitz, O. Jansen, and F. Wodarg. "Visualization of aneurysm healing: Enhancement patterns and reperfusion in intracranial aneurysms after embolization on 3T vessel wall MRI." In: *Clin Neuro-radiol* 30.4 (2020), pp. 811–815. DOI: 10.1007/s00062-019-00854-5.
- [136] K. Lawonn, M. Meuschke, R. Wickenhöfer, B. Preim, and K. Hildebrandt. "A geometric optimization approach for the detection and segmentation of multiple aneurysms." In: *Comput Graph Forum* 38.3 (2019), pp. 413–425. DOI: 10.1111/cqf.13699.
- [137] Y. LeCun, Y. Bengio, and G. Hinton. "Deep learning." In: *Nature* 521.7553 (2015), pp. 436–444. DOI: 10.1038/nature14539.
- [138] S Lewallen and P Courtright. "Epidemiology in practice: case-control studies." In: *Community Eye Health* 11.28 (1998), pp. 57–58.
- [139] F. C. Y. Li, D. Dearman, and K. N. Truong. "Virtual shelves: interactions with orientation aware devices." In: *Proc. of the ACM Trans Program Lang Syst.* 2009, pp. 125–128. ISBN: 9781605587455. DOI: 10.1145/1622176.1622200.
- [140] H. Li, R. Pan, H. Wang, X. Rong, Z. Yin, D. P. Milgrom, X. Shi, Y. Tang, and Y. Peng. "Clipping versus coiling for ruptured intracranial aneurysms." In: *Stroke* 44.1 (2013), pp. 29–37. DOI: 10.1161/STROKEAHA.112.663559.
- [141] J. Li and G. Lee. "DeepI2P: image-to-point cloud registration via deep classification." In: *Proc. of the IEEE/CVF Conference on Computer Vision and Pattern Recognition (CVPR)*. 2021, pp. 15960–15969. DOI: 10.48550/ARXIV.2104.03501.
- [142] Q. Li, Y. Yang, C. Reis, T. Tao, W. Li, X. Li, and J. H. Zhang. "Cerebral small vessel disease." In: *Cell Transplant* 27.12 (2018), pp. 1711–1722. DOI: 10.1177/0963689718795148.

- [143] T. Liebig, G. Gal, C. O'Kelly, F. Wodarg, M. Killer-Oberpfalzer, Y. Ozpeynirci, et al. "Neqstent coil-assisted flow diverter (NQS) for the treatment of bifurcation aneurysms: the coil-assisted flow diversion safety and performance study (CAFI)." In: *J Neurointerv Surg* 16.7 (2024), pp. 721–725. DOI: 10.1136/jnis-2022-020056.
- [144] T. Liebig, M. Killer-Oberpfalzer, G. Gal, P. Schramm, A. Berlis, F. Dorn, O. Jansen, and F. Fiehler Jens and; Wodarg. "The safety and effectiveness of the Contour Neurovascular System (Contour) for the treatment of bifurcation aneurysms: The CERUS Study." In: *Neurosurgery* 90.3 (2022), pp. 270–277. DOI: 10.1227/NEU.000000000001783.
- [145] R. H. Lin and C. L. Chuang. "A hybrid diagnosis model for determining the types of the liver disease." In: *Comput Biol Med* 40.7 (2010), pp. 665–670. DOI: 10.1016/j.compbiomed.2010.06.002.
- [146] J. Litak, M. Mazurek, B. Kulesza, P. Szmygin, J. Litak, P. Kamieniak, and C. Grochowski. "Cerebral small vessel disease." In: *Int J Mol Sci* 21.24 (2020). DOI: 10.3390/ijms21249729.
- [147] F. T. Liu, K. M. Ting, and Z.-H. Zhou. "Isolation forest." In: *Proc. of the IEEE Int Conf Data Min.* 2008, pp. 413–422. DOI: 10.1109/ICDM.2008.17.
- [148] J. Liu, A. Prouzeau, B. Ens, and T. Dwyer. "Design and evaluation of interactive small multiples data visualisation in immersive spaces." In: *Proc. of the IEEE Conf Virtual Real 3D User Interfaces*. 2020, pp. 588–597. DOI: 10.1109/VR46266. 2020.00081.
- [149] S. Liu, P. Liu, Z. Li, Y. Zhang, W. Li, and X. Tang. "A 3D/2D registration of the coronary arteries based on tree topology consistency matching." In: *Biomed Signal Process Control* 38 (2017), pp. 191–199. ISSN: 1746–8094. DOI: 10.1016/j.bspc.2017.06.001.
- [150] S. Liu, P. Liu, Z. Li, Y. Zhang, W. Li, and X. Tang. "A 3D/2D registration of the coronary arteries based on tree topology consistency matching." In: *Biomed Signal Process Control* 38 (2017), 191–199. DOI: doi:10.1016/j.bspc.2017.06.001.
- [151] X. Lv, Y. Zhang, and W. Jiang. "Systematic review of Woven EndoBridge for wide-necked bifurcation aneurysms: complications, adequate occlusion rate, morbidity, and mortality." In: *World Neurosurg* 110.1 (2018), pp. 20–25. DOI: 10.1016/j.wneu.2017.10.113.
- [152] M. Lyu, R. Torii, C. Liang, T. W. Peach, P. Bhogal, L. Makalanda, Q. Li, Y. Ventikos, and D. Chen. "Treatment for middle cerebral artery bifurcation aneurysms: in silico comparison of the novel Contour device and conventional flow-diverters." In: *Biomech Model Mechanobiol* (2024). DOI: 10.1007/s10237-024-01829-3.

- [153] B. Ma, R. E. Harbaugh, and M. L. Raghavan. "Three-dimensional geometrical characterization of cerebral aneurysms." In: *Ann Biomed Eng* 32.2 (2004), pp. 264–273. DOI: 10.1023/b:abme.0000012746.31343.92.
- [154] J. B. MacQueen. "Some methods for classification and analysis of multivariate observations." In: *Proc. of the Berkeley Symp on Math Statist and Prob.* Ed. by L. M. Le Cam and J. Neyman. University of California Press, 1967, pp. 281–297.
- [155] I. R. Macdonald and J. J. S. Shankar. "Delayed parent artery occlusions following use of SILK flow diverters for treatment of intracranial aneurysms." In: J Neurointerv Surg 11.7 (2019), pp. 690–693. DOI: 10.1136/neurintsurg-2018-014354.
- [156] K. H. Madsen. "A guide to metaphorical design." In: *Commun ACM* 37.12 (1994), pp. 57–62.
- [157] M. Markl, A. Frydrychowicz, S. Kozerke, M. Hope, and O. Wieben. "4D flow MRI." In: *J Magn Reson Imaging* 36.5 (2012), pp. 1015–1036. DOI: 10.1002/jmri. 23632.
- [158] H. S. Markus and F. E. de Leeuw. "Cerebral small vessel disease: recent advances and future directions." In: *Int J Stroke* 18.1 (2023), pp. 4–14. DOI: 10. 1177/17474930221144911.
- [159] S. Matl, R. Brosig, M. Baust, N. Navab, and S. Demirci. "Vascular image registration techniques: a living review." In: *Med Image Anal* 35.1 (2017), pp. 1–17. DOI: 10.1016/j.media.2016.05.005.
- [160] C. McDougall, S. C. Johnston, A. Gholkar, S. Barnwell, J. Vazquez Suarez, J. Massó Romero, et al. "Bioactive versus bare platinum coils in the treatment of intracranial aneurysms: the MAPS (matrix and platinum science) trial." In: *AJNR Am J Neuroradiol* 35.5 (2014), pp. 935–942. DOI: 10.3174/ajnr.A3857.
- [161] R. A. McLaughlin, J. Hipwell, D. J. Hawkes, J. Noble, J. V. Byrne, and T. Cox. "A Comparison of 2D-3D Intensity-Based Registration and Feature-Based Registration for Neurointerventions." In: *Med Image Comput Comput Assist Interv*. Ed. by T. Dohi and R. Kikinis. 2002, pp. 517–524.
- [162] I. Meissner, J. Torner, J. Huston, M. L. Rajput, D. O. Wiebers, L. K. Jones, and R. D. Brown. "Mirror aneurysms: a reflection on natural history: clinical article." In: *J Neurosurg* 116.6 (2012), pp. 1238 –1241. DOI: 10.3171/2012.1. JNS11779.
- [163] C. Meng, Q. Wang, S. Guan, K. Sun, and B. Liu. "2D-3D Registration With Weighted Local Mutual Information in Vascular Interventions." In: *IEEE Access* 7 (2019), pp. 162629–162638. DOI: 10.1109/ACCESS.2019.2905345.

- [164] R. Miotto, F. Wang, S. Wang, X. Jiang, and J. T. Dudley. "Deep learning for healthcare: review, opportunities and challenges." In: *Brief Bioinform* 19.6 (2017), pp. 1236–1246. DOI: 10.1093/bib/bbx044.
- [165] S. Mittenentzwei, O. Beuing, B. Neyazi, I. E. Sandalcioglu, N. Larsen, B. Preim, and S. Saalfeld. "Definition and extraction of 2D shape indices of intracranial aneurysm necks for rupture risk assessment." In: *Int J Comput Assist Radiol Surg* 16.11 (21), pp. 1977–1984. DOI: 10.1007/s11548-021-02469-z.
- [166] S. Moccia, E. De Momi, S. El Hadji, and L. S. Mattos. "Blood vessel segmentation algorithms review of methods, datasets and evaluation metrics." In: *Comput Methods Programs Biomed* 158 (2018), pp. 71–91. ISSN: 0169-2607. DOI: 10.1016/j.cmpb.2018.02.001.
- [167] J. Modersitzki. *Numerical methods for image registration*. Oxford University Press, Dec. 2003. ISBN: 9780198528418. DOI: 10.1093/acprof:0s0/9780198528418.001. 0001.
- [168] A. J. Molyneux, R. S. Kerr, L.-M. Yu, M. Clarke, M. Sneade, J. A. Yarnold, and P. Sandercock. "International subarachnoid aneurysm trial (ISAT) of neurosurgical clipping versus endovascular coiling in 2143 patients with ruptured intracranial aneurysms: a randomised comparison of effects on survival, dependency, seizures, rebleeding, subgroups, and aneurysm occlusion." In: *Lancet* 366.9488 (2005), pp. 809–817. ISSN: 0140-6736. DOI: 10.1016/S0140-6736(05)67214-5.
- [169] K. Mostafa, F. Bueno Neves, F. Gärtner, S. Peters, J. Hensler, N. Larsen, T. Klintz, J. Mahnke, O. Jansen, and F. Wodarg. "Contour device implantation versus coil embolization for treatment of narrow neck intracranial aneurysms." In: *Sci Rep* 13.1 (2023), p. 4904. DOI: 10.1038/s41598-023-31877-1.
- [170] V. Muoio, P. B. Persson, and M. M. Sendeski. "The neurovascular unit concept review." In: *Acta Physiol* 210.4 (2014), pp. 790–798. DOI: 10.1111/apha.12250.
- [171] S. J. Murphy and D. J. Werring. "Stroke: causes and clinical features." In: *Medicine (Abingdon)* 48.9 (2020), pp. 561–566. ISSN: 1357-3039. DOI: 10.1016/j.mpmed.2020.06.002.
- [172] A. Nader-Sepahi, M. Casimiro, J. M. B. Sen, and N. D. Kitchen. "Is aspect ratio a reliable predictor of intracranial aneurysm rupture?" In: *Neurosurgery* 54.6 (2004), pp. 1343–1348. DOI: 10.1227/01.NEU.0000124482.03676.8B.
- [173] Y. Nagai, M. K. Kemper, C. J. Earley, and E. J. Metter. "Bloodflow velocities and their relationships in carotid and middle cerebral arteries." In: *Ultrasound Med Biol* 24.8 (1998), pp. 1131–1136. DOI: 10.1016/S0301-5629(98)00092-1.
- [174] M. T. Nawka, G. Broocks, R. McDonough, J. Fiehler, and M. Bester. "Woven EndoBridge (WEB) width at the aneurysm neck level affects early angiographic aneurysm occlusion." In: *Clin Neuroradiol* 32.1 (2022), pp. 89–97. DOI: 10.1007/s00062-021-01034-0.

- [175] D. C. Neale and J. M. Carroll. "The role of metaphors in user interface design." In: *Handbook of human-computer interaction*. 1997, pp. 441–462. DOI: 10.1016/B978-044481862-1.50086-8.
- [176] D. C. Neale and J. M. Carroll. "The role of metaphors in user interface design." In: *Handbook of Human-Computer Interaction (Second Edition)*. Amsterdam: North-Holland, 1997, pp. 441–462. DOI: https://doi.org/10.1016/B978-044481862-1.50086-8.
- [177] M. Neugebauer, K. Lawonn, O. Beuing, P. Berg, G. Janiga, and B. Preim. "AmniVis A system for qualitative exploration of near-wall hemodynamics in cerebral aneurysms." In: *Comput Graph Forum* 32.3pt3 (2013), pp. 251–260. DOI: 10.1111/cgf.12112.
- [178] B. Neyazi, V. M. Swiatek, M. Skalej, O. Beuing, K.-P. Stein, J. Hattingen, B. Preim, P. Berg, S. Saalfeld, and I. E. Sandalcioglu. "Rupture risk assessment for multiple intracranial aneurysms: why there is no need for dozens of clinical, morphological and hemodynamic parameters." In: *Ther Adv Neurol Disord* 13 (2020), p. 1756286420966159. DOI: 10.1177/1756286420966159.
- [179] U. Niemann, P. Berg, A. Niemann, O. Beuing, B. Preim, M. Spiliopoulou, and S. Saalfeld. "Rupture status classification of intracranial aneurysms using morphological parameters." In: *Proc. IEEE Int Symp Comput Based Med Syst.* 2018, pp. 48–53. DOI: 10.1109/CBMS.2018.00016.
- [180] S. Oeltze-Jafra, M. Meuschke, M. Neugebauer, S. Saalfeld, K. Lawonn, G. Janiga, H.-C. Hege, S. Zachow, and B. Preim. "Generation and visual exploration of medical flow data: survey, research trends and future challenges." In: *Comput Graph Forum* 38.1 (2019), pp. 87–125. DOI: 10.1111/cgf.13394.
- [181] S. Oeltze and B. Preim. "Visualization of vasculature with convolution surfaces: method, validation and evaluation." In: *IEEE Trans Med Imaging* 24.4 (2005), pp. 540–548. DOI: 10.1109/TMI.2004.843196.
- [182] OpenStax. File:1314 Circle of WillisN.jpg. Online; accessed February 24, 2025. This file is licensed under the Creative Commons Attribution 4.0 International license. Version 8.25 from the Textbook OpenStax Anatomy and Physiology, arrangement slightly edited. 2016. URL: https://upload.wikimedia.org/wikipedia/commons/6/6b/1314\_Circle\_of\_WillisN.jpg.
- [183] B Pabón, V Torres, S Zaidi, H Salahuddin, M Patiño, F Peláez, et al. "LB-oo4 Novel saccular endovascular aneurysm lattice (SEAL device) PRE-SEAL IT early clinical feasibility trial: procedural, 24-hours, and 3-month safety and effectiveness independent core lab adjudicated outcomes." In: *J Neurointerv Surg* 15.Suppl 1 (2023), A244–A244. DOI: 10.1136/jnis-2023-SNIS.378.

- [184] L. Pierot, J. Moret, F. Turjman, D. Herbreteau, H. Raoult, X. Barreau, et al. "WEB treatment of intracranial aneurysms: clinical and anatomic results in the French observatory." In: *AJNR Am J Neuroradiol* 37.4 (2016), pp. 655–659. DOI: 10.3174/ajnr.A4578.
- [185] L. Pierot, C. Barbe, H. A. Nguyen, D. Herbreteau, J.-Y. Gauvrit, A.-C. Januel, et al. "Intraoperative complications of endovascular treatment of intracranial aneurysms with coiling or balloon-assisted coiling in a prospective multicenter cohort of 1088 participants: analysis of recanalization after endovascular treatment of intracranial aneurysm (ARETA) study." In: *Radiology* 295.2 (2020), pp. 381–389. DOI: 10.1148/radiol.2020191842.
- [186] L. Pierot, C. Barbe, A. Thierry, F. Bala, F. Eugene, C. Cognard, et al. "Patient and aneurysm factors associated with aneurysm recanalization after coiling." In: *J Neurointerv Surg* 14.11 (2022), pp. 1096–1101. DOI: 10.1136/neurintsurg-2021-017972.
- [187] L. Pierot and A. Biondi. "Endovascular techniques for the management of wideneck intracranial bifurcation aneurysms: a critical review of the literature." In: *J Neuroradiol* 43.3 (2016), pp. 167–175. DOI: 10.1016/j.neurad.2016.02.001.
- [188] L. Pierot, L. Spelle, C. Cognard, and I. Szikora. "Wide neck bifurcation aneurysms: what is the optimal endovascular treatment?" In: *J Neurointerv Surg* 13.5 (2021), e9–e9. DOI: 10.1136/neurintsurg-2021-017459.
- [189] L. Pierot, I. Szikora, X. Barreau, M. Holtmannspoetter, L. Spelle, J. Klisch, et al. "Aneurysm treatment with the Woven EndoBridge (WEB) device in the combined population of two prospective, multicenter series: 5-year follow-up." In: *J Neurointerv Surg* 15.6 (2023), pp. 552–557. DOI: 10.1136/neurintsurg-2021-018414.
- [190] M. Piotin, A. Biondi, N. Sourour, C. Mounayer, M. Jaworski, S. Mangiafico, et al. "The LUNA aneurysm embolization system for intracranial aneurysm treatment: short-term, mid-term and long-term clinical and angiographic results." In: J Neuroint Surg 10.12 (2018), e34–e34. DOI: 10.1136/neurintsurg-2018-013767.
- [191] M. Piotin, R. Fahed, H. Redjem, S. Smajda, J. P. Desilles, S. Escalard, et al. "The ARTISSE intrasaccular device for intracranial aneurysm treatment: short-term, mid-term and long-term clinical and angiographic results." In: *J Neurointerv Surg* 14.10 (2022), pp. 957–961. DOI: 10.1136/neurintsurg-2021-017806.
- [192] D. Pohlandt, B. Preim, and P. Saalfeld. "Supporting anatomy education with a 3D puzzle in a VR environment results from a pilot study." In: *Proc. of Mensch Und Computer* 2019. 2019, pp. 91–102. DOI: 10.1145/3340764.3340792.

- [193] M. J. D. Powell. "An efficient method for finding the minimum of a function of several variables without calculating derivatives." In: *Comput J* 7.2 (1964), pp. 155–162. DOI: 10.1093/comjnl/7.2.155.
- [194] B. Preim and P. Saalfeld. "A survey of virtual human anatomy education systems." In: *Comp & Graph* 71 (2018), pp. 132–153. DOI: 10.1016/j.cag.2018.01.005.
- [195] B. Preim and P. Saalfeld. "A survey of virtual human anatomy education systems." In: *Comput & Graph* 71 (2018), pp. 132–153. ISSN: 0097-8493. DOI: 10.1016/j.cag.2018.01.005.
- [196] M. L. Raghavan, B. Ma, and R. E. Harbaugh. "Quantified aneurysm shape and rupture risk." In: *J Neurosurg* 102.2 (2005), pp. 355 –362. DOI: 10.3171/jns.2005. 102.2.0355.
- [197] R. Raj and J. Numminen. "Initial experiences with the Trenza Embolization device for the treatment of wide-neck intracranial aneurysms: a 12-patient case series." In: *AJNR Am J Neuroradiol* 45.4 (2024), pp. 418–423. DOI: 10.3174/ajnr. A8153.
- [198] M. I. Razzak, S. Naz, and A. Zaib. "Deep learning for medical image processing: overview, challenges and the future." In: *Classification in BioApps: Automation of Decision Making*. Cham: Springer International Publishing, 2018, pp. 323–350. ISBN: 978-3-319-65981-7. DOI: 10.1007/978-3-319-65981-7\_12.
- [199] T. A. Reinartz. "A unifying view on instance selection." In: *Data Min Knowl Discov* 6 (2002), pp. 191–210. DOI: 10.1023/A:1014047731786.
- [200] S. Renowden and R. Nelson. "Management of incidental unruptured intracranial aneurysms." In: *Pract Neurol* 20.5 (2020), pp. 347–355. DOI: 10.1136/practneurol-2020-002521.
- [201] F. Ritter, T. Boskamp, A. Homeyer, H. Laue, M. Schwier, F. Link, and H.-O. Peitgen. "Medical image analysis." In: *IEEE Pulse* 2.6 (2011), 60–70. DOI: 10. 1109/MPUL.2011.942929.
- [202] F. Ritter, B. Preim, O. Deussen, and T. Strothotte. "Using a 3d puzzle as a metaphor for learning spatial relations." In: *Proc. Graph Interface*. 2000, pp. 171–178. DOI: 10.20380/GI2000.23.
- [203] D. Rivest-Henault, H. Sundar, and M. Cheriet. "Nonrigid 2D/3D registration of coronary artery models with live fluoroscopy for guidance of cardiac interventions." In: *IEEE Trans Med Imaging* 31.8 (2012), pp. 1557–1572. DOI: 10.1109/ TMI.2012.2195009.

- [204] X. Ru, Z. Zhang, X. Wang, J.-Y. Liu, Y.-C. Zhu, and Z. Wu. "Automatic geometric quantification and rupture risk evaluation of 3D intracranial aneurysms." In: *Proc. IEEE Int Conf Acoust Speech Signal Process.* 2025, pp. 1–5. DOI: 10.1109/ICASSP49660.2025.10888305.
- [205] D. Rueckert, P. Aljabar, R. Heckemann, J. Hajnal, and A. Hammers. "Diffeomorphic Registration Using B-Splines." In: *Med Image Comput Comput Assist Interv.* 2006, pp. 702–709. DOI: 10.1007/11866763\\_86.
- [206] R. Russo, S. Molinaro, and M. Ergui. "Cerus Endovascular Contour Neurovascular System Protrusion into parent artery successfully managed with post-detachment bail-out PTA." In: *Clin Neuroradiol* 33.2 (2023), pp. 561–564. DOI: 10.1007/s00062-022-01257-9.
- [207] S. Saalfeld, S. Voß, B. Beuing O. Preim, and P. Berg. "Flow-splitting-based computation of outlet boundary conditions for improved cerebrovascular simulation in multiple intracranial aneurysms." In: *Int J Comput Assist Radiol Surg* 14.10 (2019), 1805–1813. DOI: 10.1007/s11548-019-02036-7.
- [208] S. Saalfeld, P. Berg, M. Neugebauer, and B. Preim. "Reconstruction of 3D Surface Meshes for Blood Flow Simulations of Intracranial Aneurysms." In: *Proceedings of the computer- and robot-assisted surgery (CURAC)*. 2015, pp. 163–168.
- [209] S. Saalfeld, P. Berg, A. Niemann, M. Luz, B. Preim, and O. Beuing. "Semiautomatic neck curve reconstruction for intracranial aneurysm rupture risk assessment based on morphological parameters." In: *Int J Comput Assist Radiol Surg* 13.11 (2018), pp. 1781–1793. DOI: 10.1007/s11548-018-1848-x.
- [210] K. A. Satriadi, B. Ens, M. Cordeil, T. Czauderna, and B. Jenny. "Maps Around Me: 3D Multiview Layouts in Immersive Spaces." In: *Proc. of the ACM Hum Comput Interact* 4.ISS (2020). DOI: 10.1145/3427329.
- [211] W. I. Schievink. "Intracranial aneurysms." In: *N Engl J Med* 336.1 (1997), pp. 28–40. DOI: 10.1056/NEJM199701023360106.
- [212] D. Schott, P. Saalfeld, G. Schmidt, F. Joeres, C. Boedecker, F. Huettl, H. Lang, T. Huber, B. Preim, and C. Hansen. "A VR/AR environment for multi-user liver anatomy education." In: *Proc IEEE Conf Virtual Real 3D User Interfaces*. 2021, pp. 296–305. DOI: 10.1109/VR50410.2021.00052.
- [213] C. Schumann, M. Neugebauer, R. Bade, B. Preim, and H.-O. Peitgen. "Implicit vessel surface reconstruction for visualization and CFD simulation." In: *Int J Comput Assist Radiol Surg* 2 (Mar. 2008), pp. 275–286. DOI: 10.1007/s11548-007-0137-x.
- [214] M. M. Shao, T. G. White, J. B. Bassett, E. Dowlati, S. H. Mehta, C. Werner, et al. "Intrasaccular treatment of intracranial aneurysms: a comprehensive review." In: *J Clin Med* 13.20 (2024). DOI: 10.3390/jcm13206162.

- [215] Y. Shi, M. J. Thrippleton, G. W. Blair, D. A. Dickie, I. Marshall, I. Hamilton, F. N. Doubal, F. Chappell, and J. M. Wardlaw. "Small vessel disease is associated with altered cerebrovascular pulsatility but not resting cerebral blood flow." In: *J Cereb Blood Flow Metab* 40.1 (2020), pp. 85–99. DOI: 10.1177/0271678X18803956.
- [216] Y. Shi and J. M. Wardlaw. "Update on cerebral small vessel disease: a dynamic whole-brain disease." In: *Stroke Vasc Neurol* 1.3 (2016). DOI: 10.1136/svn-2016-000035.
- [217] Y. Song, J. Totz, S. Thompson, S. Johnsen, D. Barratt, C. Schneider, et al. "Locally rigid, vessel-based registration for laparoscopic liver surgery." In: *Int J Comput Assist Radiol Surg* 10.12 (2015), pp. 1951–1961. DOI: 10.1007/s11548-015-1236-8
- [218] L. Spelle, D. Herbreteau, J. Caroff, X. Barreau, J.-C. Ferré, J. Fiehler, et al. "CLinical assessment of WEB device in ruptured aneurYSms (CLARYS): results of 1-month and 1-year assessment of rebleeding protection and clinical safety in a multicenter study." In: *J Neurointerv Surg* 14.8 (2022), pp. 807–814. DOI: 10.1136/neurintsurg-2021-017416.
- [219] L Spitz. *Multi-modal co-registration of high-resolution 7T MRI vessel data*. Master Thesis, Otto-von-Guericke University Magdeburg. 2020.
- [220] L. Spitz, M. Allgaier, A. Mpotsaris, D. Behme, B. Preim, and S. Saalfeld. "Segmentation of Circle of Willis from 7T TOF-MRI data and immersive exploration using VR." In: *Curr Dir Biomed Eng* 8.1 (2022), pp. 129–132. DOI: 10.1515/cdbme-2022-0033.
- [221] L. Spitz, F. Gaidzik, D. Stucht, H. Mattern, B. Preim, and S. Saalfeld. "A hybrid hierarchical strategy for registration of 7T TOF-MRI to 7T PC-MRI intracranial vessel data." In: *Int J Comput Assist Radiol Surg* 18.1 (2023), 837–844. DOI: 10.1007/s11548-023-02836-y.
- [222] L. Spitz, J. Korte, F. Gaidzik, N. Larsen, D. Behme, B. Preim, and S. Saalfeld. *Deformation analysis of intracranial aneurysms after treatment with the contour neurovascular system*. Manuscript submitted for publication. Institute of Simulation and Graphics, Otto-von-Guericke University Magdeburg. 2025.
- [223] L. Spitz, J. Korte, F. Gaidzik, N. Larsen, B. Preim, and S. Saalfeld. "Assessment of intracranial aneurysm neck deformation after contour deployment." In: *Int J Comput Assist Radiol Surg* 19 (2024), pp. 2321–2327. DOI: 10.1007/s11548-024-03189-w.
- [224] L. Spitz, U. Niemann, O. Beuing, B. Neyazi, I. E. Sandalcioglu, B. Preim, and S. Saalfeld. "Combining visual analytics and case-based reasoning for rupture risk assessment of intracranial aneurysms." In: *Int J Comput Assist Radiol Surg* 15.9 (2020), pp. 1525–1535. DOI: 10.1007/s11548-020-02217-9.

- [225] L. Spitz, J. Schmidt, J. Korte, P. Berg, D. Behme, B. Neyazi, B. Preim, and S. Saalfeld. "Morphologic and hemodynamic analysis of intracranial mirror aneurysms." In: *Curr Dir Biomed Eng* 10.2 (2024), pp. 87–90. DOI: 10.1515/cdbme-2024-1074.
- [226] L. Spitz, V. M. Swiatek, B. Neyazi, I. E. Sandalcioglu, B. Preim, and S. Saalfeld. "An interactive tool for identifying patient subgroups based on arbitrary characteristics for medical research." In: *Curr Dir Biomed Eng* 7.1 (2021), pp. 43–46. DOI: 10.1515/cdbme-2021-1010.
- [227] L. Spitz, S. C. Umeh, D. Behme, B. Neyazi, I. E. Sandalcioglu, B. Preim, and S. Saalfeld. "Subset selection for intracranial aneurysms for training simulations." In: *Curr Dir Biomed Eng* 10.1 (2024), pp. 73–76. DOI: 10.1515/cdbme-2024-0119.
- [228] Z. Stankovic, B. Allen, J. Garcia, K. Jarvis, and M. Markl. "4D flow imaging with MRI." In: *Cardiovasc Diagn Ther* 4.2 (2014), pp. 173–192. DOI: 10.3978/j.issn.2223-3652.2014.01.02.
- [229] K. Sun, Z. Chen, S. Jiang, and Y. Wang. "Morphological multiscale enhancement, fuzzy filter and watershed for vascular tree extraction in angiogram." In: *J Med Syst* 35.5 (2011), pp. 811–824. DOI: 10.1007/s10916-010-9466-3.
- [230] D. E. Sunny, M. Amoo, M. Al Breiki, E. D. W. Teng, J. Henry, and M. Javadpour. "Prevalence of incidental intracranial findings on magnetic resonance imaging: a systematic review and meta-analysis." In: *Acta Neurochir (Wien)* 164.10 (2022), pp. 2751–2765. DOI: 10.1007/s00701-022-05225-7.
- [231] V. M. Swiatek, A. Amini, M. Marinescu, C. A. Dumitru, L. Spitz, K.-P. Stein, S. Saalfeld, A. Rashidi, I. E. Sandalcioglu, and B. Neyazi. "Sex differences in intracranial aneurysms: a matched cohort study." In: *J Pers Med* 14.10 (2024), p. 1038. DOI: 10.3390/jpm14101038.
- [232] V. M. Swiatek, A. Amini, C. E. Sandalcioglu Ortuño, L. Spitz, K. Hartmann, A. Rashidi, K.-P. Stein, S. Saalfeld, I. E. Sandalcioglu, and B. Neyazi. "Unveiling rupture risk and clinical outcomes in midline aneurysms: A matched cohort analysis investigating the impact of localization within the anterior or posterior circulation." In: *Neurosurg Rev* 47.1 (2024), p. 76. DOI: 10.1007/s10143-024-02310-6.
- [233] V. M. Swiatek, A. Amini, L. Spitz, A. Rashidi, C. A. Dumitru, K.-P. Stein, S. Saalfeld, I. E. Sandalcioglu, and B. Neyazi. "Anterior interhemispheric vs. pterional approach in the microsurgical management of anterior communicating artery aneurysms: a comparative analysis employing a novel multidimensional matching-tool." In: *Neurosurg Rev* 47.1 (2024), p. 366. DOI: 10.1007/s10143-024-02592-w.

- [234] V. M. Swiatek, A. Amini, C. A. Dumitru, L. Spitz, K.-P. Stein, S. Saalfeld, A. Rashidi, I. E. Sandalcioglu, and B. Neyazi. "Multidimensional Comparison of Microsurgical Clipping and Endovascular Techniques for Anterior Communicating Artery Aneurysms: Balancing Occlusion Rates and Periprocedural Risks." In: Medicina (Kaunas) 61.3 (2025). DOI: 10.3390/medicina61030498.
- [235] C. Symonds. "The circle of Willis." In: *Br Med J* 1.4906 (1955), pp. 119–124. DOI: 10.1136/bmj.1.4906.119.
- [236] D. Säring, J. Fiehler, T. Ries, and N. D. Forkert. "Rigid 3D-3D registration of TOF MRA integrating vessel segmentation for quantification of recurrence volumes after coiling cerebral aneurysm." In: *Neuroradiology* 54.2 (2012), pp. 171–176. DOI: 10.1007/s00234-011-0836-4.
- [237] F. Taher and N. Prakash. "Automatic cerebrovascular segmentation methods a review." In: *IAES International Journal of Artificial Intelligence* 10.3 (2021), pp. 576–583. DOI: 10.11591/ijai.v10.i3.pp576-583.
- [238] T. Takashina, M. Ito, H. Nagaura, and E. Wakabayashi. "Evaluation of curved raycasting-based interactive surfaces in virtual environments." In: *Proc. of the IEEE Conf Virtual Real 3D User Interfaces Abstr Workshops*. 2021, pp. 534–535. DOI: 10.1109/VRW52623.2021.00149.
- [239] S. Tateshima, A. Chien, J. Sayre, J. Cebral, and F. Viñuela. "The effect of aneurysm geometry on the intra-aneurysmal flow condition." In: *Neuroradiol-*08y 52.12 (2010), pp. 1135–1141. DOI: 10.1007/s00234-010-0687-4.
- [240] R. G. Tawk, T. F. Hasan, C. E. D'Souza, J. B. Peel, and W. D. Freeman. "Diagnosis and treatment of unruptured intracranial aneurysms and aneurysmal subarachnoid hemorrhage." In: *Mayo Clin Proc* 96.7 (2021), pp. 1970–2000. ISSN: 0025-6196. DOI: 10.1016/j.mayocp.2021.01.005.
- [241] A. ter Telgte, E. M. C. van Leijsen, K. Wiegertjes, C. J. M. Klijn, A. M. Tuladhar, and F.-E. de Leeuw. "Cerebral small vessel disease: from a focal to a global perspective." In: *Nat Rev Neurol* 14.7 (2018), pp. 1759–4766. DOI: 10.1038/s 41582-018-0014-y.
- [242] G. Tetteh, V. Efremov, N. D. Forkert, M. Schneider, J. Kirschke, B. Weber, C. Zimmer, M. Piraud, and B. H. Menze. "DeepVesselNet: vessel segmentation, centerline prediction, and bifurcation detection in 3-D angiographic volumes." In: *Front Neurosci* 14 (2020). DOI: 10.3389/fnins.2020.592352.
- [243] M. Thormann, A. Mpotsaris, and D. Behme. "Treatment of a middle cerebral artery bifurcation aneurysm with the novel Contour Neurovascular System compatible with 0.021 inch catheters." In: *Neuroradiol J* 35.3 (2022), pp. 396–398. DOI: 10.1177/19714009211041523.

- [244] D. A. Tonetti, B. T. Jankowitz, and B. A. Gross. "Antiplatelet therapy in flow diversion." In: *Neurosurgery* 86. Supplement 1 (2020), S47–S52. DOI: 10.1093/neuros/nyz391.
- [245] S. Voß, P. Berg, G. Janiga, M. Skalej, and O. Beuing. "Variability of intraaneurysmal hemodynamics caused by stent-induced vessel deformation." In: *Curr Dir Biomed Eng* 3.2 (2017), pp. 305–308. DOI: doi:10.1515/cdbme-2017-0063.
- [246] Z. Vrselja, H. Brkic, S. Mrdenovic, R. Radic, and G. Curic. "Function of circle of Willis." In: *J Cereb Blood Flow Metab* 34.4 (2014), pp. 578–584. DOI: 10.1038/jcbfm.2014.7.
- [247] R. Wang, D. Zhang, J. Zhao, S. Wang, Y. Zhao, and H. Niu. "A comparative study of 43 patients with mirror-like intracranial aneurysms: risk factors, treatment, and prognosis." In: *Neuropsychiatr Dis Treat* 10 (2014), pp. 2231–2237. DOI: 10.2147/NDT.S70515.
- [248] J. M. Wardlaw, C. Smith, and M. Dichgans. "Mechanisms of sporadic cerebral small vessel disease: insights from neuroimaging." In: *Lancet Neurol* 12.5 (2013), pp. 1474–4422. DOI: 10.1016/S1474-4422(13)70060-7.
- [249] J. M. Wardlaw, C. Smith, and M. Dichgans. "Small vessel disease: mechanisms and clinical implications." In: *Lancet Neurol* 18.7 (2019), pp. 684–696. DOI: S1474-4422(19)30079-1.
- [250] M. J. Wermer, I. C. van der Schaaf, A. Algra, and G. J. Rinkel. "Risk of rupture of unruptured intracranial aneurysms in relation to patient and aneurysm characteristics." In: *Stroke* 38.4 (2007), pp. 1404–1410. DOI: 10.1161/01.STR. 0000260955.51401.cd.
- [251] D. O. Wiebers, J. P. Whisnant, J. Huston 3rd, I. Meissner, R. D. Brown Jr, D. G. Piepgras, et al. "International study of unruptured intracranial aneurysms investigators. Unruptured intracranial aneurysms: natural history, clinical outcome, and risks of surgical and endovascular treatment." In: *Lancet* 362.9378 (2003), pp. 103–110. DOI: 10.1016/s0140-6736(03)13860-3.
- [252] F. Wodarg, F. Gärtner, and J. Mahnke. "The CONTOUR device for the treatment of ruptured aneurysms results, learnings and limits." In: *J Neurointerv Surg* 14.Suppl 2 (2022), A13. DOI: 10.1136/neurintsurg-2022-ESMINT.31.
- [253] F. Wodarg, Y. Ozpeynirci, J. Hensler, O. Jansen, and T. Liebig. "Contour-assisted coiling with jailed microcatheter may result in better occlusion (CoCoJaMBO) in wide-necked intracranial aneurysms: proof of principle and immediate angiographic results." In: *Interv Neuroradiol* 29 (2023), pp. 79–87. DOI: 10.1177/15910199211069782.

- [254] J. Xiang, S. K. Natarajan, M. Tremmel, D. Ma, J Mocco, L. N. Hopkins, A. H. Siddiqui, E. I. Levy, and H. Meng. "Hemodynamic-morphologic discriminants for intracranial aneurysm rupture." In: *Stroke* 42.1 (2011), pp. 144–152. DOI: 10. 1161/STROKEAHA.110.592923.
- [255] J. Yuan, C. Huang, N. Lai, Z. Li, X. Jiang, X. Wang, et al. "Hemodynamic and morphological analysis of mirror aneurysms prior to rupture." In: *Neuropsychiatr Dis Treat* 16 (2020), pp. 1339–1347. DOI: 10.2147/NDT.S254124.
- [256] S.-M. Zhang, L.-X. Liu, P.-W. Ren, X.-D. Xie, and J. Miao. "Effectiveness, safety and risk factors of Woven EndoBridge device in the treatment of wide-neck intracranial aneurysms: systematic review and meta-analysis." In: *World Neuro-surg* 136 (2020), e1–e23. ISSN: 1878-8750. DOI: 10.1016/j.wneu.2019.08.023.
- [257] J. Zhao, H. Lin, R. Summers, M. Yang, B. G. Cousins, and J. Tsui. "Current treatment strategies for intracranial aneurysms: an overview." In: *Angiology* 69.1 (2018), pp. 17–30. DOI: 10.1177/0003319717700503.
- [258] Y. Zinchenko, P. Khoroshikh, S. Alexandr, A. Smirnov, A. Tumyalis, A. Kovalev, S. Gutnikov, and K. Golokhvast. "Virtual reality is more efficient in learning human heart anatomy especially for subjects with low baseline knowledge." In: *New Ideas Psychol* 59 (Dec. 2020), p. 100786. DOI: 10.1016/j.newideapsych.2020. 100786.